*materials*

Special Issue Reprint

# Advanced Manufacturing Technologies of Thermoplastic Composites

Edited by
Tian Zhao

mdpi.com/journal/materials

MDPI

# Advanced Manufacturing Technologies of Thermoplastic Composites

# Advanced Manufacturing Technologies of Thermoplastic Composites

Guest Editor

**Tian Zhao**

*Guest Editor*
Tian Zhao
Institute of Advanced
Structure Technology
Beijing Institute of Technology
Beijing
China

This is a reprint of the Special Issue, published open access by the journal *Materials* (ISSN 1996-1944), freely accessible at: www.mdpi.com/journal/materials/special_issues/Thermoplastic_Composites.

For citation purposes, cite each article independently as indicated on the article page online and using the guide below:

Lastname, A.A.; Lastname, B.B. Article Title. *Journal Name* **Year**, *Volume Number*, Page Range.

# Contents

# About the Editor

**Tian Zhao**

Dr. Tian Zhao is a Special Researcher/Associate Professor and Ph.D. Supervisor at the Institute of Advanced Structural Technology of the Beijing Institute of Technology. He serves as a Standing Director of the SAMPE Society of Committee and a member of Youth Working Committee of the Chinese Society for Composite Materials. Meanwhile, he is the sole guest editor for the Special Issue of the scientific journal *Materials*, a youth editorial board member for the *Journal of Aeronautical Materials and Materials Engineering*, and a reviewer for several top SCI journals including *Composites Part A*.

He has led research projects including the National Natural Science Foundation of China, Aviation Science Foundation and Aerospace Basic Research Project. He was selected as the first "Postdoctoral International Exchange Program" Fellowship at the Beijing Institute of Technology. He has published over 30 SCI papers as the first/ corresponding author and has applied to 15 national invention patents, accompanied by one industry process specification. His research achievements have been successfully applied to the European composite materials project "Clean Sky 2", supporting the development of the world's first thermoplastic composite aircraft fuselage structure.

*Editorial*

# Advanced Manufacturing Technologies of Thermoplastic Composites

Tian Zhao

Institute of Advanced Structure Technology, Beijing Institute of Technology, Beijing 100081, China;
t.zhao@bit.edu.cn

Thermoplastic composites are becoming increasingly attractive to the aerospace and automotive industries owing to their outstanding mechanical properties and cost-effective manufacturing processes. Some advanced manufacturing techniques, e.g., 3D printing, filament winding and welding, are particularly well-suited for this type of composites. However, high temperatures and pressures are normally required during the fabrication due to the intrinsic properties of thermoplastic resin, e.g., a relatively high Tg and viscosity, which introduce additional difficulties and challenges for the manufacturing process. Numerous researchers have worked to gain insights into the mechanisms that underlie different manufacturing processes of thermoplastic composites in order to promote their applications in engineering structures.

This Special Issue is titled "Advanced Manufacturing Technologies of Thermoplastic Composites" and is dedicated to providing readers with an overview of the current research progress on different manufacturing techniques of thermoplastic composites. The Special Issue includes ten high-quality research articles, the collection of which covers a period of almost two years, while more than 60 authors from different institutions participated to contribute their scientific outputs.

Geng et al. [1] investigated the influence of process parameters on the mechanical properties of thermoplastic composite materials (CFRPs) using laser-assisted CF/PPS winding forming technology. A numerical model was established to simulate the heat transfer that occurs during the winding process, as well as the tensile behavior of the composite specimens. Yu et al. [2] analyzed the effects of surface treatment on the resistance welding process for unidirectional carbon fiber/PPS composites. A quantitative processing window was proposed for resistance welding to achieve the best weld strength. Yao et al. [3] reported research on the interfacial enhancement of CF/PA6T composites with pre ultrafine PA6T powder as an emulsion sizing agent. It was found that the mechanical performance, including the tensile, shear and interlaminar strength, was obviously improved for the processed composites. Li et al. [4] optimized the formulation design and foaming processes and achieved mechanical property enhancement using a carbon-fiber-reinforced PVC composite foam (CF/PVC). The results indicated a reduction in VOC emission in automotive interior leather applications. The influence of thermal parameters on the self-nucleation behavior of a PPS during secondary thermoforming was systematically studied by Ren et al. [5]. Different mechanisms were found for the two thermal cycles, while it was shown that they will both generate self-nucleation behavior. To achieve efficient and strong connections between the metal and polymer components, Zhou et al. [6] used a hot pressure-welding technique to join AA6061 and CF/PA66 composites and found that the aluminum alloy's surface morphology has the greatest impact on the mechanical property of the welded joint. Wu et al. [7] quantitatively investigated the typical manufacturing defects, e.g., fiber bundle bias distribution and void contents, in 3D-printed CF/PLA specimens using a micro-CT technique. Wang et al. [8] performed a detailed analysis of prepreg trajectories in relation to the shell geometry, accompanied by an in-depth investigation of the underlying

causes of wrinkling on dome surfaces. Zhao et al. [9] explored the possibility of combining the compression-molding of CCF-PAEK and injection of SCF-PEEK. The interfacial behavior was significantly affected by the processing temperature. A parametric study, considering the lap length, adhesive layer thickness, adhesive layer shape, adhesive layer overflow length and laminate lay-up, was conducted by Chen et al. [10] to characterize the shear strength of adhesively bonded composite joints by using both numerical and experimental methods.

As is known, the "advanced manufacturing technologies of thermoplastic composites" is a comprehensive topic, and therefore, it is not possible to include research on all aspects of this research area. However, we believe that the collected papers provide a further understanding of the physical mechanisms of different manufacturing technologies and the mechanical behavior of thermoplastic composites. We hope that further progress can be achieved based on the ideas introduced in this Special Issue.

**Conflicts of Interest:** The author declares no conflicts of interest.

## References

1. Geng, H.B.; Cao, X.W.; Zu, L.; Pan, H.L.; Zhang, G.M.; Zhang, Q.; Fu, J.H.; Zhou, L.C.; Wu, Q.G.; Jia, X.L.; et al. The Effects of Laser-Assisted Winding Process Parameters on the Tensile Properties of Carbon Fiber/Polyphenylene Sulfide Composites. *Materials* **2024**, *17*, 4664. [CrossRef] [PubMed]
2. Yu, D.W.; Qing, X.T.; Lin, H.Y.; Yang, J.; Yang, J.C.; Wang, X.J. Response Surface Methodology Optimization of Resistance Welding Process for Unidirectional Carbon Fiber/PPS Composites. *Materials* **2024**, *17*, 2176. [CrossRef] [PubMed]
3. Yao, J.H.; Wang, Z.; Yang, J.C.; Wang, X.J.; Yang, J. Interfacial Enhancement and Composite Manufacturing of Continuous Carbon-Fiber-Reinforced PA6T Composites via PrePA6T Ultrafine Powder. *Materials* **2024**, *17*, 1557. [CrossRef] [PubMed]
4. Li, H.F.; Wu, Y.; Wu, L.Y.; Cui, C.W.; Niu, K.M. Innovative CF/PVC Foam Applicated for Automotive Synthetic Leather with High-Performance and Reduced VOC Emissions. *Materials* **2024**, *17*, 1076. [CrossRef] [PubMed]
5. Ren, Y.; Li, Z.Y.; Li, X.G.; Su, J.Y.; Li, Y.; Gao, Y.; Zhou, J.F.; Ji, C.C.; Zhu, S.; Yu, M.H. The Influence of Thermal Parameters on the Self-Nucleation Behavior of Polyphenylene Sulfide (PPS) during Secondary Thermoforming. *Materials* **2024**, *17*, 890. [CrossRef] [PubMed]
6. Zhou, H.P.; Li, Y.; Liu, W.D.; Luo, Y.; Ao, S.S.; Luo, Z. Effect of Process Parameters on Joint Performance in Hot Pressure Welding of 6061 Aluminum Alloy to CF/PA66. *Materials* **2024**, *17*, 329. [CrossRef] [PubMed]
7. Wu, H.T.; Chen, X.Y.; Xu, S.H.; Zhao, T. Evolution of Manufacturing Defects of 3D-Printed Thermoplastic Composites with Processing Parameters: A Micro-CT Analysis. *Materials* **2023**, *16*, 6521. [CrossRef] [PubMed]
8. Wang, B.; Wen, L.H.; Xiao, J.Y.; Wang, S.Y.; Ren, P.; Wang, L.Q.; Zu, L.; Hou, X. Automated Fiber Placement Path Planning and Analysis of Pressure Vessels. *Materials* **2023**, *16*, 6187. [CrossRef] [PubMed]
9. Zhao, Z.Y.; Zhang, J.D.; Bi, R.; Chen, C.H.; Yao, J.N.; Liu, G. Study on the Overmolding Process of Carbon-Fiber-Reinforced Poly (Aryl Ether Ketone) (PAEK)/Poly (Ether Ether Ketone) (PEEK) Thermoplastic Composites. *Materials* **2023**, *16*, 4456. [CrossRef] [PubMed]
10. Chen, Q.L.; Du, B.; Zhang, X.D.; Zhong, H.; Ning, C.G.; Bai, H.M.; Li, Q.; Pan, R.Q.; Zhou, B.C.; Hu, H.J. Parametric Investigation into the Shear Strength of Adhesively Bonded Single-Lap Joints. *Materials* **2022**, *15*, 8013. [CrossRef] [PubMed]

*Article*

# Evolution of Manufacturing Defects of 3D-Printed Thermoplastic Composites with Processing Parameters: A Micro-CT Analysis

**Hantai Wu [1], Xinyu Chen [1], Shuaiheng Xu [1] and Tian Zhao [1,2,\*]**

[1] Beijing Key Laboratory of Lightweight Multi-Functional Composite Materials and Structures, Institute of Advanced Structure Technology, Beijing Institute of Technology, Beijing 100081, China; 3220212078@bit.edu.cn (H.W.)

[2] Beijing Institute of Astronautical System Engineering, Beijing 100076, China

\* Correspondence: t.zhao@bit.edu.cn

**Abstract:** Owing to the melting and healing properties of thermoplastic resin, additive manufacturing or 3D printing is considered one of the most promising technologies for fiber-reinforced thermoplastic composites. However, manufacturing defects are still the main concern, which significantly limits the application of 3D-printed composite structures. To gain an insight into the effects of different processing parameters on the typical manufacturing defects, a micro-scale analysis was carried out via Micro-CT technology on the 3D-printed continuous carbon fiber-reinforced polylactic acid (PLA) composite specimens. The bias distribution of the fiber in the deposited filament was found. Moreover, when the feed rate of the filament was reduced from 100% to 50%, the a/b value was closer to 3.33, but the porosity increased from 7.077% to 25.352%. When the layer thickness was 0.2 mm, the increased nozzle pressure reduced the porosity but also increased the risk of fiber bundle breakage. The research provides an effective approach for analyzing the micro-structure of 3D printed composite structures and thus offers guidance for the processing control.

**Keywords:** 3D printing; fiber-reinforced thermoplastic composites; process parameters; micro-CT; microstructural analysis

## 1. Introduction

Benefiting from their excellent mechanical properties and cost-effective manufacturing methods, thermoplastic composites (TPCs) have gained an increasing attraction in many industrial fields, such as aerospace, automotive and medical engineering, etc. [1–3]. Thermoplastic resin can be heated and melted when given an increased temperature and retains the original properties after consolidation [4]. Therefore, a number of rapid manufacturing techniques, e.g., automatic fiber laying (AFP) [5], automatic tape layering (ATL) [6], compression molding [7], pultrude molding [8], etc., can be applied on TPCs to form structures with complex configurations within a short processing time [9]. Among them, additive manufacturing (AM), or 3D printing, is considered one of the most advanced techniques, which significantly improves structural design flexibility [10,11]. Three-dimensional printing technology is based on 2D slices deposited layer upon layer into a 3D object, without molds, and reducing material waste [12]. Extensive research has been conducted on the 3D printing technique of thermoplastic resin and their composites [13,14], which greatly promotes the development of this manufacturing technology.

Nevertheless, the development of 3D printing techniques for continuous fiber-reinforced thermoplastic composites (CFRTPCs) has been slow. For example, Fused Deposition Modeling (FDM) is the most widely used and promising 3D printing technique for CFRTPCs [15]. In the FDM technology, the continuous fiber bundle is fed into the extrusion head, impregnated by a heated thermoplastic resin, and then deposited onto the printing platform

via a small diameter nozzle to print the part layer by layer [16], whereas typical defects always exist within the FDM technology of CFRTPC structures, which prevents further application of this technology. Rahmatabadi et al. [17] studied the compression, bending, and tensile properties of PVC manufactured by FDM and demonstrated that the presence of high-density cavities in FDM-manufactured parts is the source area of crack growth and failure. Tian et al. [18] systematically studied the influence of 3D printing process parameters on the interface and properties of printed composite materials and found that temperature and pressure are the key parameters of the molding process. By optimizing the process parameters, the maximum bending strength of 3D printing continuous fiber-reinforced PLA with 27% fiber content reached 335 MPa, and the bending modulus was 30 GPa. Geng et al. [19] found that melt pressure (controlled by printing speed and extrusion speed) directly affects the surface morphology and extrusion diameter of the filament in the FDM process of PEEK. Therefore, it can be inferred that the mechanical properties of FDM technology for CFRTPCs are significantly influenced by the microscopic defects introduced during the printing process. Simultaneously, ensuring the reliability of printed filaments is crucial to meet the demands of manufacturing complex 3D configurations.

To overcome these problems, many scholars have carried out relevant investigations. Zhang et al. [20] studied the effect of layer thickness on the void distribution of continuous carbon fiber-reinforced PLA composites. They found that decreasing the layer thickness effectively improved the ironing force, thus minimizing the formation of void age and improving the surface quality of the printed specimens. Shuto et al. [21] studied the influence of nozzle temperature on the porosity and filament deformation and concluded that nozzle temperature had little influence on porosity, while filament area fraction was higher at both ends of the printable temperature range. Liao et al. [22] used high-resolution X-ray microscopy to quantitatively count the number of voids in different printing directions and obtained results that the void volume of the sample with the 0° printing direction was much higher than that with the printing path of 45/−45 or 0/90.

High-resolution X-ray micro-computed tomography (denoted as Micro-CT hereafter) is a very interesting non-destructive testing technology that can be used to reconstruct internal structural details, hence becoming an effective method that is increasingly used for the quantitative analysis of manufacturing defects within composite structures [23,24]. Yamamoto et al. [25] observed the inside of the samples printed under different path-planning algorithms by Micro-CT and suppressed the voids in the actual printing process by adjusting the parameters of the algorithm. He et al. [26] quantitatively measured the number of voids in 3D-printed continuous fiber-reinforced Polyamide6 specimens via Micro-CT. Zhang et al. [27] observed the Micro-CT images of the printing-induced defects such as fiber wrinkling, twisting, and folding at different turning angles (30°~180°). Yu et al. [28] used Micro-CT to characterize the position, length, and direction of short-fiber in basalt–fiber-reinforced PLA composites and statistically analyzed the changes in the number of two types of voids under the influence of different fiber contents.

In this study, the microstructure characteristics of CFRTPCs prepared by FDM technology were characterized by Micro-CT, focusing on the morphology and porosity of the printed filaments. The deformation of filaments, void volume distribution, and void distribution in space under different parameters were quantified, and the influence of printing parameters on the morphology and printing defects of the specimen was discussed. Provided a reference for the parameter selection and process optimization during the preparation of CFRTPCs by FDM technology.

## 2. Materials and Experiments

### 2.1. Materials and Printing Equipment

In this study, a T300-1 K carbon fiber bundle, provided by Toray Co., Tokyo, Japan, with an average single-fiber diameter of 7 μm was used as the reinforcement. PLA filament with a diameter of 1.75 mm, produced from PolyLite™., Suzhou, China, was used as the thermoplastic resin. All specimens were fabricated using a COMBOT-200 FDM 3D printer

provided by Shaanxi Fibertech Technology Development Co., Ltd., Shaanxi, China. The nozzle diameter was 1.0 mm. The geometry of the 3D-printed sample was modeled and then was cut into thin layers using the slicing software. The main size and printing path of the specimen are schematically shown in Figure 1a. The filaments along the X and Y directions were defined as the 'layer' and the 'column', respectively. After slicing, the G-code [29] was saved and transferred to the FDM printer to carry out the printing process.
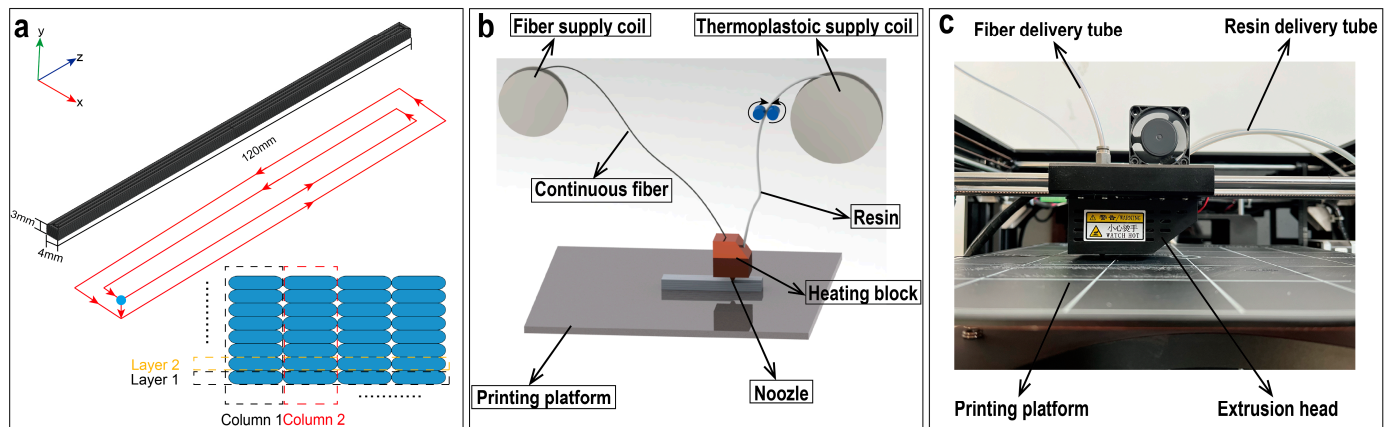


**Figure 1.** (**a**) Schematic of the size and printing path of the printed composite specimen; (**b**) simulation diagram of the in situ fusion technology; (**c**) diagram of the printing equipment used in the experiment.

The 3D printer used in situ fusion technology, which means during the printing process, the fiber bundle and resin filament were separately transported through different fed tubes and were mixed in the heating block. The moving extrusion head deposited the filament on the unheated printing platform in accordance with the set print path, as illustrated in Figure 1b. After a certain layer was deposited, the print head was raised to continue to deposit the next layer, and the printing path of all layers was the same.

### 2.2. Process Conditions and Parameters

In this research, a series of typical printing parameters, i.e., nozzle temperature (T), printing speed (S), Feed rate of the filament (F) (related to the unit volume of resin fed into the printing head), and layer thickness (H) were selected to analyze their effects on the quality of the as-manufactured specimens. The design matrix of the experimental study is listed in Table 1.

**Table 1.** Experimental design of the parametric analysis of the 3D printing process.

| Specimen | T (°C) | S (mm/min) | F (%) | H (mm) |
|---|---|---|---|---|
| T210 | **210** | 100 | 100 | 0.3 |
| T220 | **220** | 100 | 100 | 0.3 |
| T230 | **230** | 100 | 100 | 0.3 |
| T240 | **240** | 100 | 100 | 0.3 |
| S150 | 230 | **150** | 100 | 0.3 |
| S200 | 230 | **200** | 100 | 0.3 |
| F75 | 230 | 100 | **75** | 0.3 |
| F50 | 230 | 100 | **50** | 0.3 |
| H0.2 | 230 | 100 | 100 | **0.2** |
| H0.4 | 230 | 100 | 100 | **0.4** |

The bold part represents the printing parameters of interest, e.g., T210 represents printing temperature as the printing parameter of concern; 210 is the specific value.

### 2.3. Characterization Methods

The filament morphologies and void contents of the 3D-printed composite specimens were acquired to assess the effects of different parameters on the quality of the specimens. Cross-sectional slices of the specimens were gathered via a Diondo-D2 Micro-CT scanner (Diondo, Hattingen, Nordrhein-Westfalen, Germany) with a 90 kV accelerating voltage and a 90 µA current. The Micro-CT resolution was approximately 5 µm. Each specimen was rotated in equal increments over 360°, and 1860 projections were collected. Subsequently, 2D slices were imported into Avizo (FEI, Hillsboro, OR, USA) software, and 3D models of the specimens were reconstructed. The analysis process is shown in Figure 2.
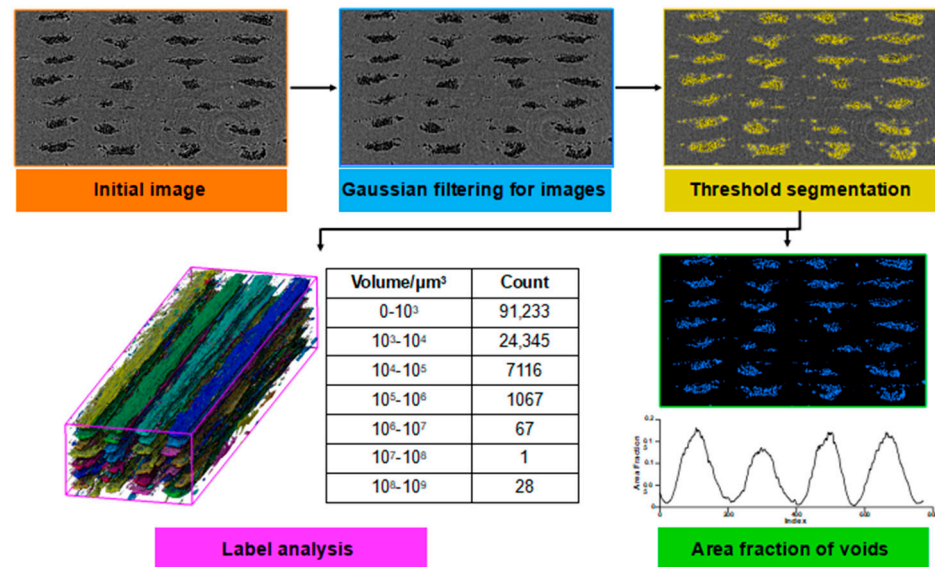


**Figure 2.** Steps of void extraction and quantitative analysis.

## 3. Results and Discussion

### 3.1. Morphology Characterization of Filaments

Cross-sectional images of the T230 printed specimen reconstructed from the CT scanning results and the light microscopy are illustrated in Figure 3. Due to the similar density of PLA resin and carbon fiber, the colors of these two are similar in the CT scan results. Therefore, the gray pixels correspond to the fiber and resin, and the black pixels correspond to the voids. Two interesting points were observed with respect to filament morphology. Firstly, the cross-sectional area of the deposited filament is shown as a rounded rectangle instead of a circular shape. This is likely a result of the contact pressure of the nozzle during the printing process. More importantly, an offset distribution at the top part of the entire filament was found for the voids; at the same time, the fiber bundle is concentrated in the top area of the filament. The same phenomenon was observed in [30].

A possible explanation for the offset distribution of the fiber bundles in the entire filament is illustrated in Figure 4. During the printing process, the unimpregnated dry carbon fiber bundle and PLA thermoplastic resin filament were independently fed from different inlet tubes and mixed in the heating block. The resin tube was distributed in front of the one for the fiber bundle with respect to the printing direction, which formed an initial spatial distribution of these two components. Subsequently, the PLA resin was heated and melted, thus immersing the fiber bundle. Due to the inertia effect of the printing head movement, the fiber bundle constantly laid on the back side of the nozzle, which finally resulted in a concentrated distribution of the fiber bundle on the upper part of the deposited filament.

In order to quantitatively characterize the effects of printing parameters on the filament morphology, three geometrical parameters for the filament were defined: $a$ and $b$ are the length and the width of the rounded rectangle, respectively, and $h$ is the vertical distance

from the position where the voids begin to appear to the bottom of the filament, as indicated in Figure 3a. Therefore, the ratios a/b and h/b were selected to characterize the morphology of the deposited filament and the offset magnitude of the fiber bundle during the printing processes with different parameters.
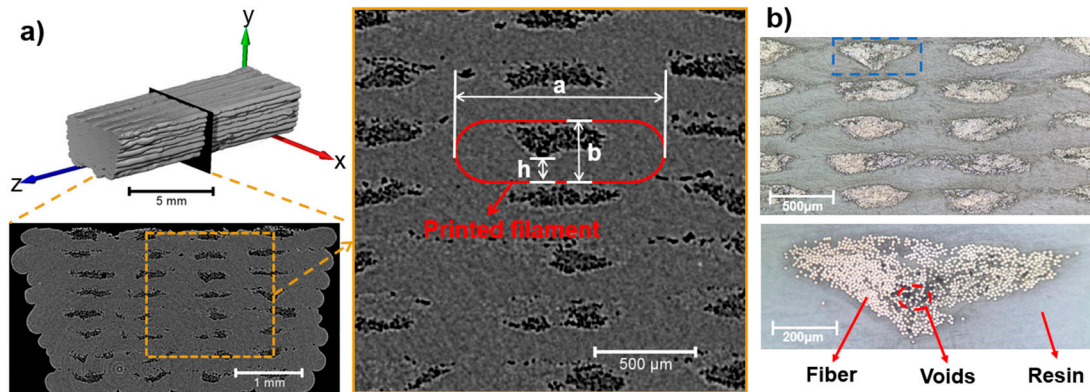


**Figure 3.** (**a**) Reconstructed cross-sectional image of the printed specimen T230 based on Micro-CT scan, magnification of the part inside the rectangular frame: the profile of the deposited filament is outlined by the red line; and (**b**) optical microscopy images of the specimen T230 at different magnifications.
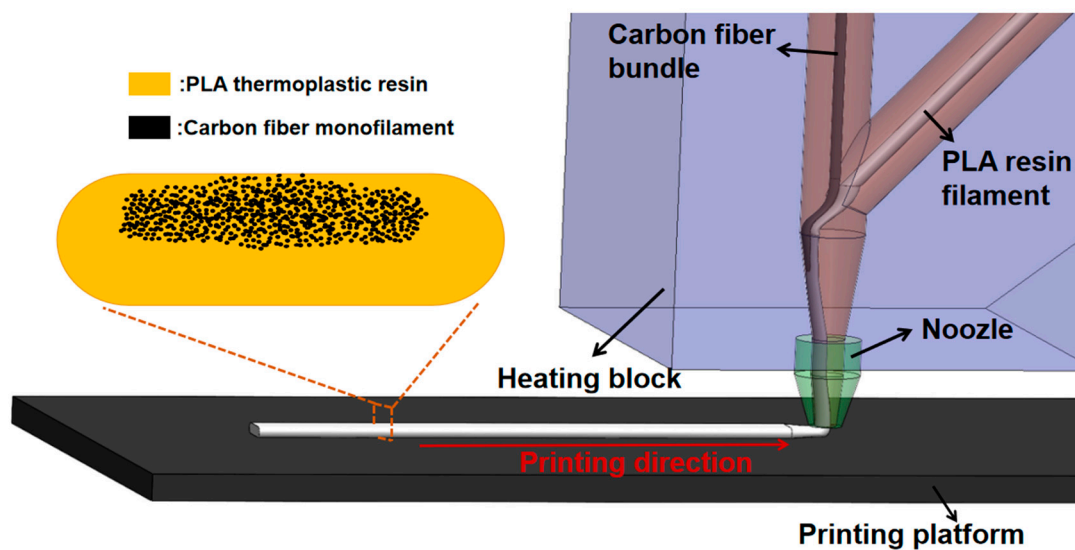


**Figure 4.** A schematic diagram of the spatial distribution of the fiber bundle and PLA resin filament in the heating block tube and nozzle during the printing process.

3.1.1. Effect of Printing Parameters on a/b

Figures 5–8 show the evolution of the parameter a/b as the layers are superimposed within different columns. The horizontal dotted lines in the figures represent the theoretical values of a/b, which are 5, 3.33, and 2.5 for the layer thicknesses of 0.2 mm, 0.3 mm, and 0.4 mm, respectively. In Figures 5–7, it is interesting to find that the ratio a/b of the first and the fourth columns gradually increases, and the major part is greater than the theoretical value, while the curves of the second and third columns basically float around the horizontal dotted line. As shown in Figure 7, when the feed rate of the filament is 50% and 75%, the a/b of each column fluctuates around the theoretical value but with higher amplitudes. This tends to indicate that when the feed rate of the filament is reduced, the shape of the filament is more inclined to the theoretical shape, but the possibility of the filament deformation is also increased. Regarding the layer thicknesses of 0.3 mm and 0.4 mm, the curves show a similar trend. In comparison, the ratio a/b for the thickness of

0.2 mm is obviously higher, and more significant oscillations are observed in the curves, as shown in Figure 8. This is likely due to the fiber breakage, which is caused by the increase in nozzle pressure when the layer thickness is reduced [20].
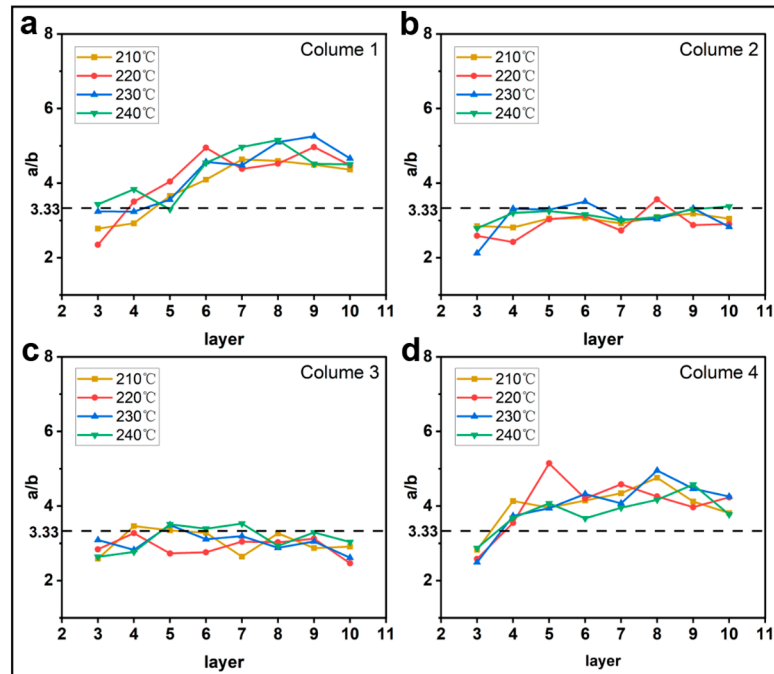


**Figure 5.** Influence of printing temperature on the filament morphology index a/b. The four sub-diagrams in (**a**–**d**) correspond to the four columns of the printed specimens, respectively (see Figure 1a).
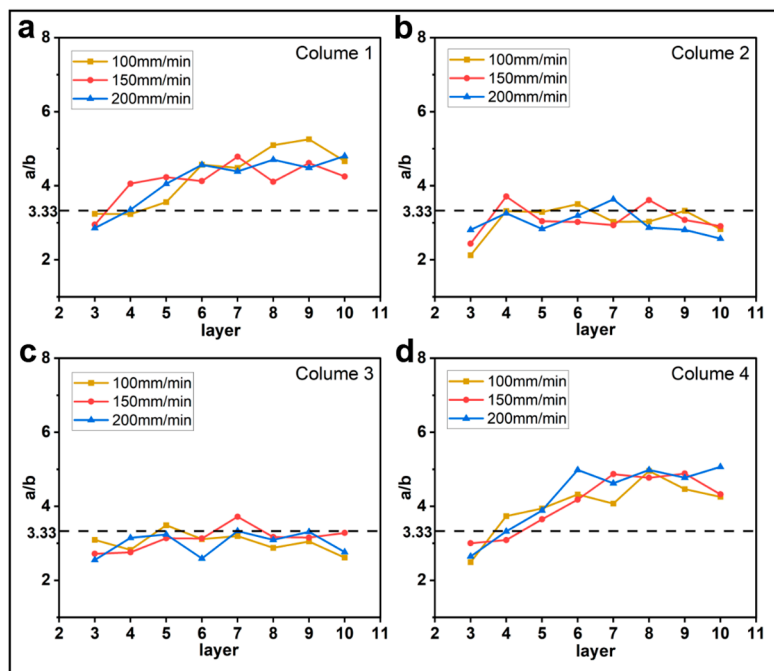


**Figure 6.** Influence of printing speed on the filament morphology index a/b. The four sub-diagrams in (**a**–**d**) correspond to the four columns of the printed specimens, respectively.
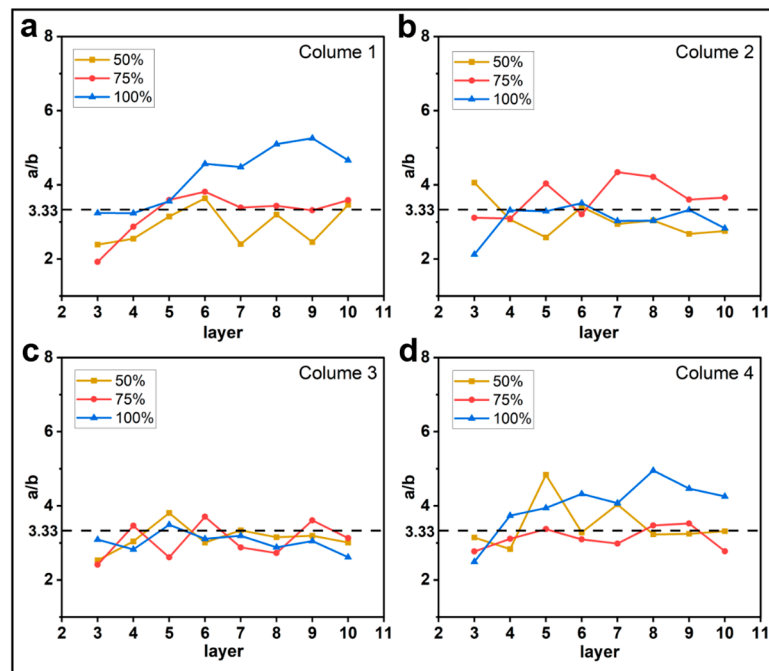
**Figure 7.** Influence of feed rate of the filament on the filament morphology index a/b. The four sub-diagrams in (**a**–**d**) correspond to the four columns of the printed specimens, respectively.
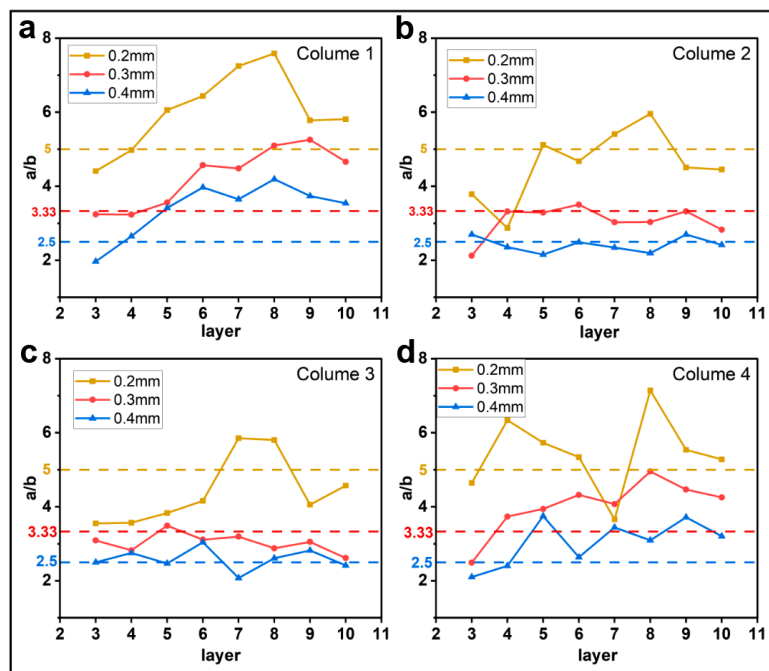


**Figure 8.** Influence of layer thickness on the filament morphology index a/b. The four sub-diagrams in (**a**–**d**) correspond to the four columns of the printed specimens, respectively.

### 3.1.2. Effect of Printing Parameters on h/b

Figures 9–12 plot the variation of parameter h/b as the layers are superimposed. According to Figures 9 and 10, neither printing temperature nor printing speed have an apparent influence on the curve trend. Generally, the curves are constantly leveling at around the ratio h/b of 0.4. In the direction of the thickness of a single deposited filament bundle, the fibers are basically clustered in the upper half area. When the feed rate of the filament decreases, it is found that the value of h/b possibly drops to 0, as shown

in Figure 11. This can be explained by the fact that owing to the reduced contents of thermoplastic resin in the nozzle, the fiber bundle has more flexibility and thus is more inclined to disperse throughout the entire filament instead of gathering in the upper part. This possibility is greatly increased when the feed rate of the filament is reduced. Regarding the effects of layer thickness, another extreme case is that the value of h/b is equal to 1 occurs once given a 0.2 mm thickness. This indicates that there are almost no voids in the filament, which is most likely because the fiber bundle was broken in this part, hence the filament was filled with pure resin.
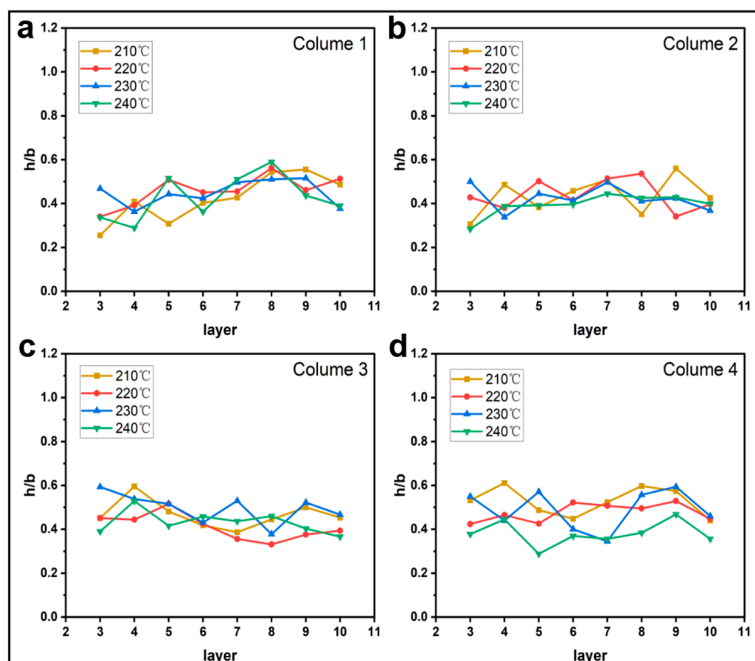


**Figure 9.** Influence of printing temperature on the filament morphology index h/b. The four sub-diagrams in (**a**–**d**) correspond to the four columns of the printed specimens, respectively.
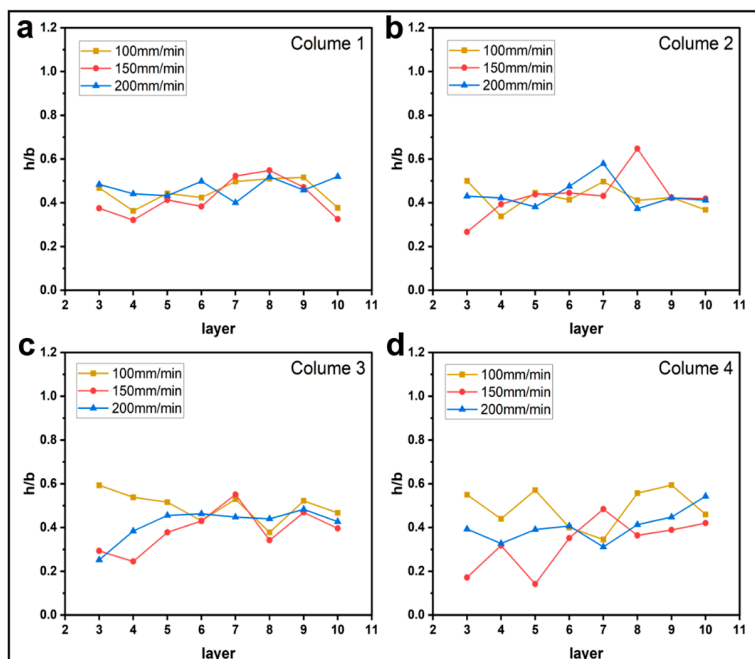


**Figure 10.** Influence of printing speed on the filament morphology index h/b. The four sub-diagrams in (**a**–**d**) correspond to the four columns of the printed specimens, respectively.
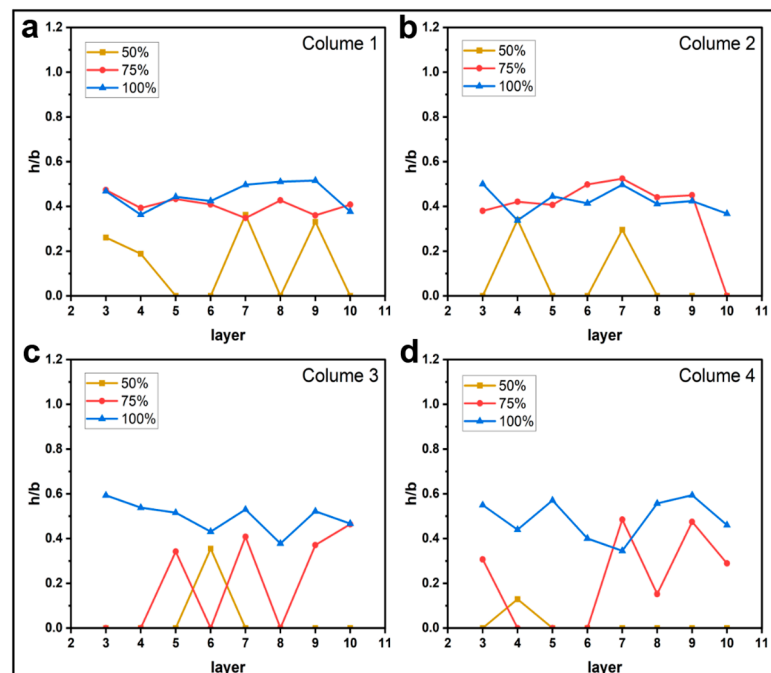
**Figure 11.** Influence of feed rate of the filament on the filament morphology index h/b. The four sub-diagrams in (**a**–**d**) correspond to the four columns of the printed specimens, respectively.
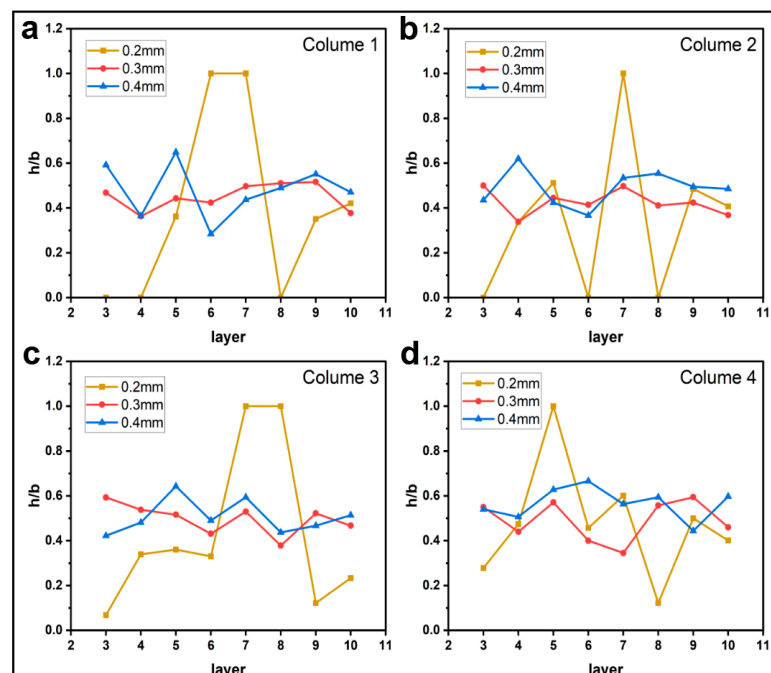


**Figure 12.** Influence of layer thickness on the filament morphology index h/b. The four sub-diagrams in (**a**–**d**) correspond to the four columns of the printed specimens, respectively.

*3.2. Characterization of Porosity Content*

Due to the improper impregnation between resin and fiber and the lack of consolidation pressure, porosity or void is a typical manufacturing defect of printed composite structures. As illustrated in Figure 13, voids can basically be divided into two categories based on their spatial distribution: (i) intra-bead voids: the voids mainly distributed inside the fiber bundles, indicated by the red lines, which is caused by the incomplete impregnation between the thermoplastic resin and the fibers; and (ii) inner-bead voids: the voids mainly distributed in between the printed filaments, indicated by the blue lines, which

is caused by the insufficient flow of the pre-deposited filament due to the cold filament interface combined with low consolidation pressure [20].
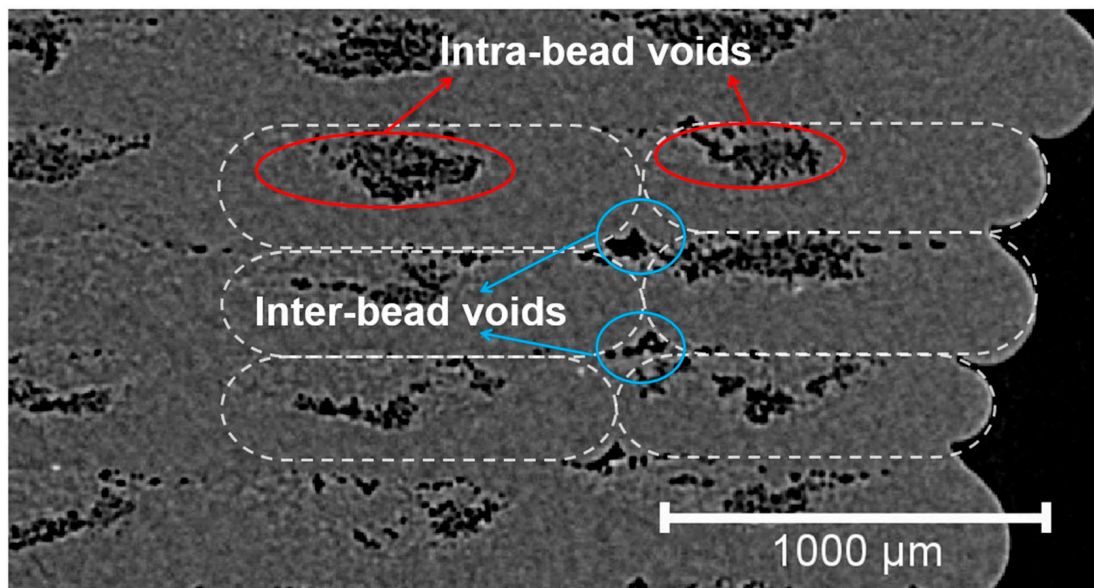


**Figure 13.** A typical Micro-CT image of printed composite Specimen T230 containing different types of voids.

In this research, the printed samples were mainly divided into two categories according to the size of the maximum void volume: Case 1 indicates the samples with the maximum void volume in the range of $1 \times 10^8$~$1 \times 10^9$ μm$^3$, represented by the Specimen T230 (see Figure 14a); and Case 2 indicates the samples with the maximum void volume greater than or equal to $1 \times 10^9$ μm$^3$, represented by the Specimen H0.4 (see Figure 14b). Figure 14c–j illustrate the distribution of the voids with different volume magnitudes. Obviously, the voids with a volume range of $1 \times 10^8$~$1 \times 10^9$ μm$^3$ are all intra-bead voids, which are distributed alongside the printing direction. The voids with a volume range of $1 \times 10^9$~$1 \times 10^{10}$ μm$^3$ are a result of the connection of intra-bead voids and inter-bead voids. Other smaller voids ($\leq 1 \times 10^8$ μm$^3$) are randomly distributed between the filaments, which therefore belong to inter-bead voids. As observed from Figure 14a,b, for both cases, the voids with volume size higher than $1 \times 10^6$ μm$^3$ account for the major proportion, higher than 93% of the entire void content inside the specimens. Therefore, the subsequent discussion will only focus on voids with a volume greater than or equal to $1 \times 10^6$ μm$^3$ since the rest part has little effect on the mechanical performance of the samples.

### 3.2.1. Effect of Printing Parameters on Void Dimension

A quantitative statistic on the distribution of voids at different volume magnitudes as a function of different printing parameters is illustrated in Figure 15. It can be observed that the count of voids in the volume size of $1 \times 10^8$~$1 \times 10^9$ μm$^3$ is approximately 28, corresponding to the number of printed filaments. The printing temperature and printing speed barely have any effect on the distribution of void numbers at different volume levels (see Figure 15a,b). On the contrary, when the feed rate of the filament decreases, voids with larger volume segments appear, and the number of voids within the range of $1 \times 10^8$~$1 \times 10^9$ μm$^3$ gradually decreases, which implies that the connection between the intra-bead voids and the inter-bead voids. A large void with a volume range of $1 \times 10^{10}$~$1 \times 10^{11}$ μm$^3$ was found once given a feed rate of the filament of 50%, which connected most filaments inside the specimen. Regarding Figure 15d, it is found that an obvious decrease in the voids within the range of $1 \times 10^8$~$1 \times 10^9$ μm$^3$ while an increase in the ones within $1 \times 10^7$~$1 \times 10^8$ μm$^3$ when given a decreased layer thickness (i.e., 0.2 mm),

which is owing to the increased ironing pressure between the nozzle and the deposited filament [17].
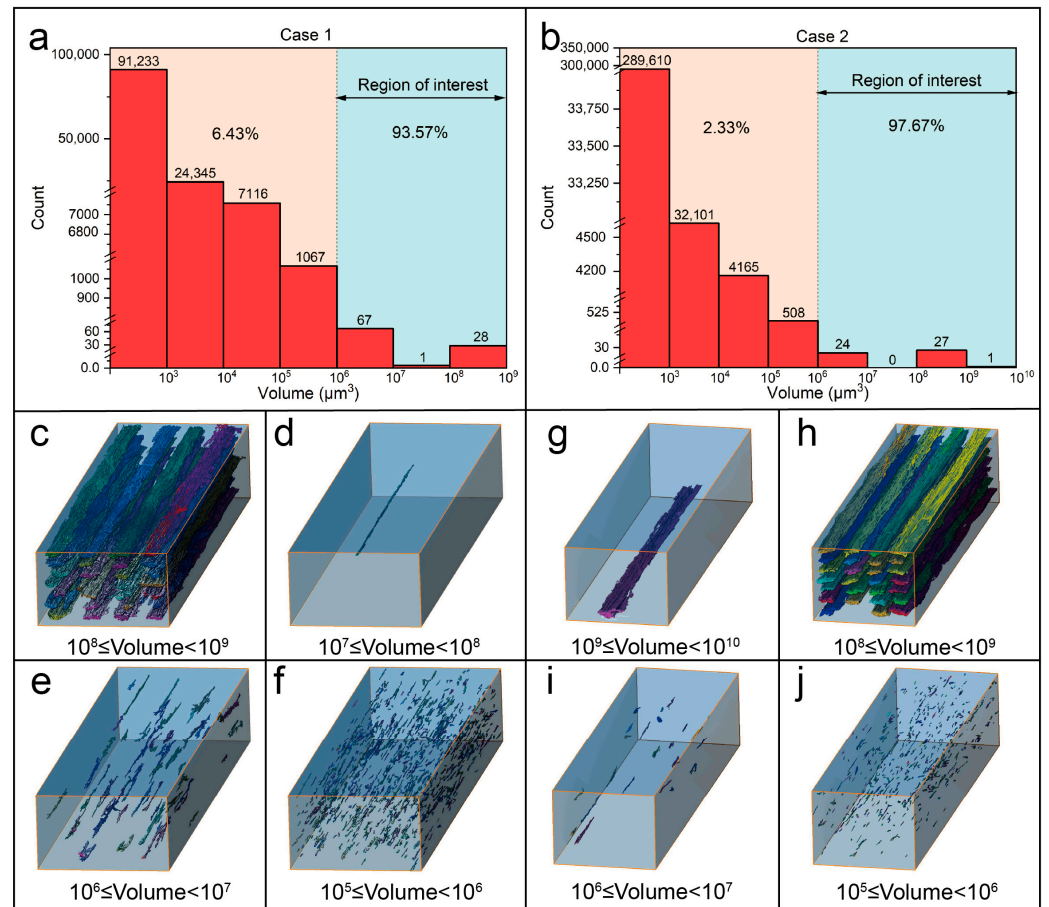


**Figure 14.** Statistical diagram of the number of voids at different volume levels within two representative printed specimens: (**a**) T230 and (**b**) H0.4. Three-dimensional reconstructions and visualization of voids for the Specimen T230 with different volume ranges: (**c**) $1 \times 10^8 \sim 1 \times 10^9$ μm$^3$, (**d**) $1 \times 10^7 \sim 1 \times 10^8$ μm$^3$, (**e**) $1 \times 10^6 \sim 1 \times 10^7$ μm$^3$, and (**f**) $1 \times 10^5 \sim 1 \times 10^6$ μm$^3$. Three-dimensional reconstructions and visualization of voids for the Specimen H0.4 with different volume ranges: (**g**) $1 \times 10^9 \sim 1 \times 10^{10}$ μm$^3$, (**h**) $1 \times 10^8 \sim 1 \times 10^9$ μm$^3$, (**i**) $1 \times 10^6 \sim 1 \times 10^7$ μm$^3$, and (**j**) $1 \times 10^5 \sim 1 \times 10^6$ μm$^3$.

### 3.2.2. Porosity Distribution in X Direction

In addition to analyzing the void distribution at different volume magnitudes, an investigation of the spatial distribution of the voids within the specimen was conducted. Figure 16 shows the void fraction of the printed specimen along the transverse direction. For simplification, the void contents at different directions are labeled with three different axes, i.e., X, Y, and Z axis (direction). One should note that the statistics index is the sum of the porosity of the A-A slice at the Y-Z plane, as indicated by the schematic in Figure 16a. Four peaks generally correspond to the central line of the four printed filament columns. The effects of printing temperature and printing speed on the porosity distribution are similar and insignificant; the maximum value is leveling at around 0.2, and the minimum value remains close to 0. A lower feed rate of the filament results in an apparent increase in both the maximum and minimum values of the void fraction, as illustrated in Figure 16c. The maximum values reach 0.3~0.4, and the minimum values are around 0.1~0.25 once given a feed rate of the filament of 50%. The increase in the maximum void fraction results from a higher dispersion of fibers, which is due to the reduction in internal pressure within the printing head and the less effective impregnation of the resin with the fiber [18], while the increase in the minimum values indicates the connection of the voids along the X

direction, corresponding to the large void formation in the F50 Specimen (see Figure 15c), which can be explained by the lack of resin to fill in the gaps between different columns. Observing Figure 16d, the void content is increased when given a higher layer thickness, which is likely a consequence of the reduction in ironing force between the nozzle and the deposited filament [20].
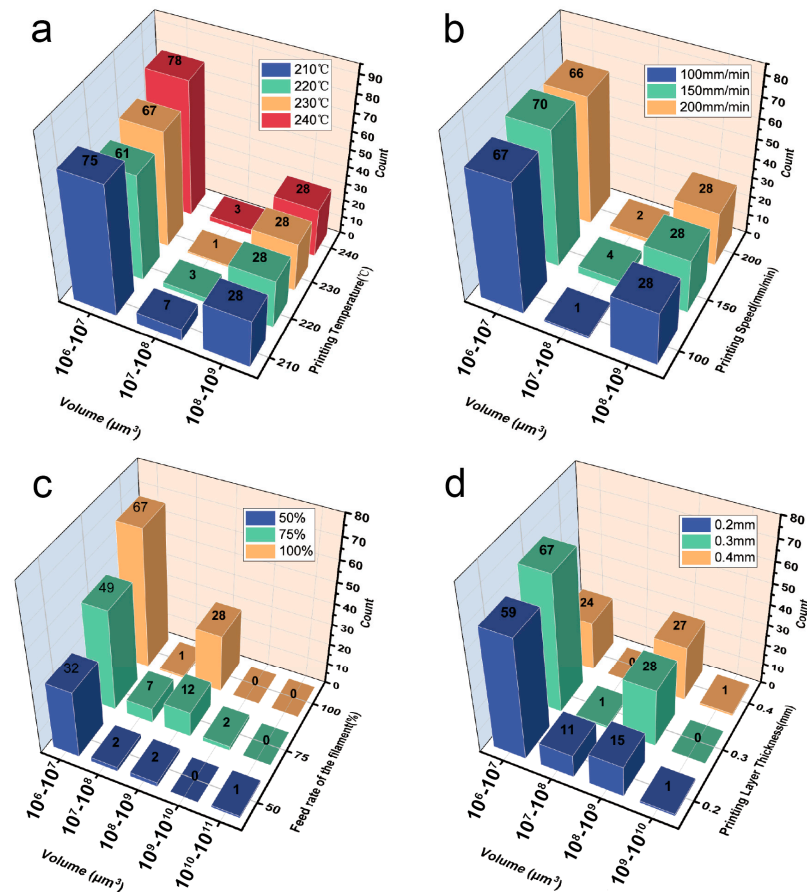


**Figure 15.** The bar chart statistics of the number of voids at different volume magnitudes based on the effects of different printing parameters: (**a**) printing temperature, (**b**) printing speed, (**c**) feed rate of the filament, and (**d**) layer thickness.

### 3.2.3. Porosity Distribution in Y Direction

Figure 17 plots the evolution of the sum of porosity of the B-B slice at the X-Z plane with a varying thickness value in the Y direction. The curve peaks correspond to the number of layers. Differently, the peak values are located at 5/6-layer thickness from bottom to top, indicating the offset of the voids in the direction of each filament thickness. Figure 17a,b both show that the peak value decreases first and then increases gradually, and the positions of the second and third layers are the lowest, causing the initial print layers to be under continuous pressure until the end of printing. Similar to Figure 16, changing the printing temperature or printing speed has little effect on the porosity values in the Y direction. However, the changes in the feed rate of the filament and layer thickness have more significant impacts on the porosity distribution. When the feed rate of the filament decreases, both the maximum and minimum values of the curves increase, as shown in Figure 17c. Similar to the observations in Figure 16c, the maximum void fraction reaches 0.4 and the minimum void fraction reaches 0.2 when given a feed rate of the filament of 50%, indicating that the voids along the Y direction are no longer independent of each other. Figure 17d shows that when the layer thickness is 0.4 mm, the peak porosity values of different layers are basically the same. When the layer thickness is 0.2 mm, the maximum

value decreases while the minimum one increases, which is similar to the observation in Figure 16d.
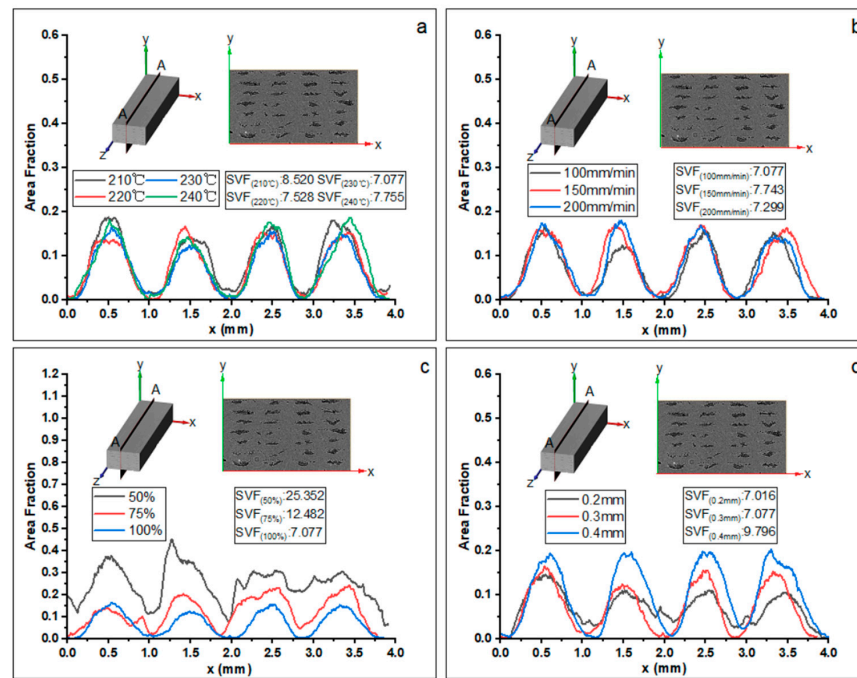


**Figure 16.** Evolution of the porosity content of the A-A plane slice along the *X*-axis with different printing parameters: (**a**) printing temperature, (**b**) printing speed, (**c**) feed rate of the filament, and (**d**) layer thickness. SVF represents the total porosity content inside the specimen within three-dimensional space. The lower corner mark represents the corresponding printing parameters.
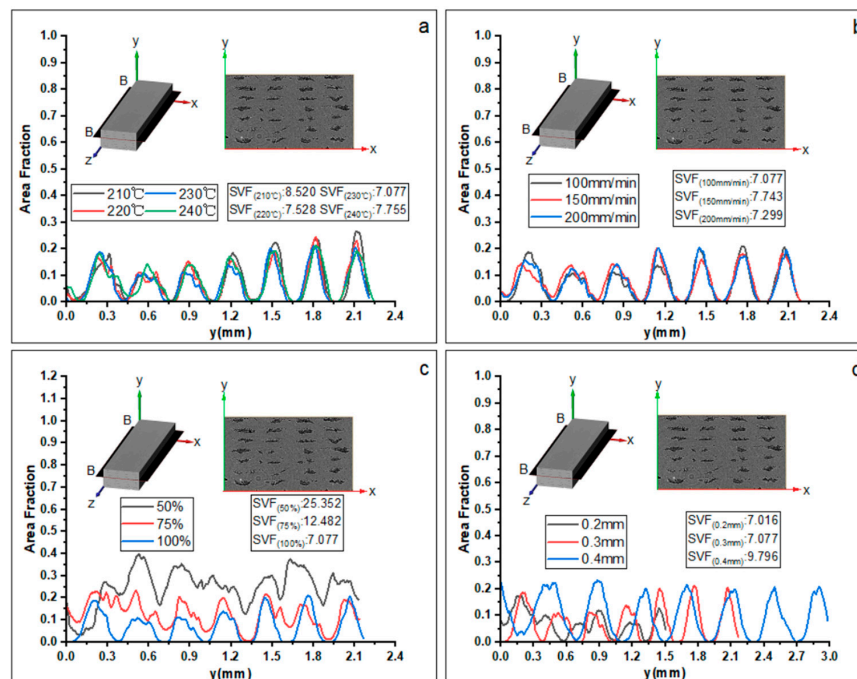


**Figure 17.** Evolution of the porosity content of the B-B plane slice along the *Y*-axis with different printing parameters: (**a**) printing temperature, (**b**) printing speed, (**c**) feed rate of the filament, and (**d**) layer thickness. SVF represents the total porosity content inside the specimen within three-dimensional space. The lower corner mark represents the corresponding printing parameters, and the statistical range is from the first layer to the seventh layer.

15

### 3.2.4. Porosity Distribution in Z Direction

As shown in Figure 18, the curve describes the evolution of the porosity of the C-C slice at the X-Y plane with a varying value at the Z axis. Basically, the porosity is constantly leveling around 0.07 when given different printing temperatures (Figure 18a) and printing speeds (Figure 18b). Decreasing the feed rate of the filament significantly increases the porosity from 0.07 to 0.25, as illustrated in Figure 18c. Figure 18d shows that the porosity is maximum when the layer thickness is 0.4 mm.
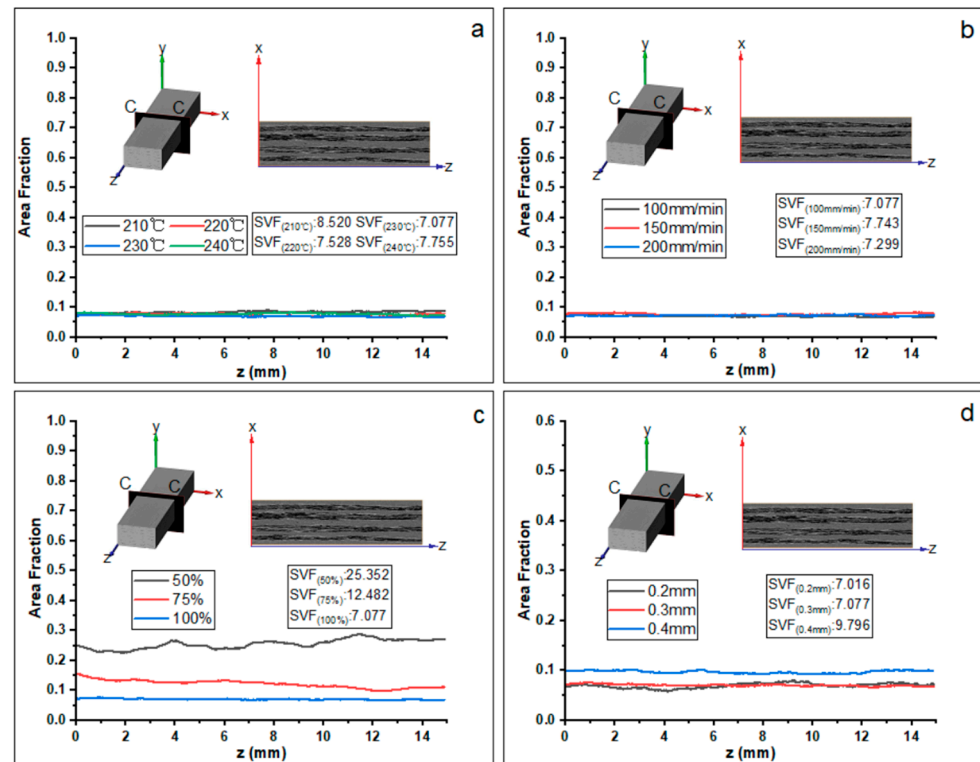


**Figure 18.** Evolution of the porosity content of the C-C plane slice along the Z-axis with different printing parameters: (**a**) printing temperature, (**b**) printing speed, (**c**) feed rate of the filament, and (**d**) layer thickness. SVF represents the total porosity content inside the specimen within three-dimensional space. The lower corner mark represents the corresponding printing parameters.

### 4. Conclusions

In this paper, Micro-CT technology was used to quantitatively analyze the influence of several typical printing parameters on the filament morphologies and printing voids of 3D-printed carbon fiber-reinforced PLA composite specimens. The effects of different processing parameters, i.e., printing temperature, printing speed, feed rate of the filament, and layer thickness on the micro-structures of the printed specimens were systematically investigated. In comparison, the effects of printing temperature and printing speed were not significant. Some conclusion points are drawn:

1. Due to the geometric position of the fiber bundle and resin filament in the heating block and the inertial action during the printing processes, the fiber bundle was mainly distributed in the upper part of the deposited filament, which led to the offset distribution of the voids within the filament. The printing voids within the 3D-printed composite specimens can basically be divided into two types: intra-bead voids with a general volume of $1 \times 10^8 \sim 1 \times 10^9$ μm$^3$ and inter-bead voids with a volume normally less than $1 \times 10^8$ μm$^3$.

2. When the feed rate of the filament decreased, the filament shape was more likely to be the ideal shape. However, due to the weak constraints of resin, fibers could be distributed throughout the filament, which resulted in a high dispersion of the

filament shape. Given a low layer thickness, the size of the filament was smaller than the theoretical shape, and the deposited filament was likely filled with pure resin due to the fracture of the fiber bundle.

3. The reduction in the feed rate of the filament led to an increase in both the maximum and minimum void values, while the decrease in the layer thickness caused an increase in the minimum value but a decrease in the maximum ones.

4. This study primarily focuses on the impact of the printing process on filament size and microscopic defects. However, the evaluation of mechanical properties under different printing parameters is lacking, which could be considered for further investigation in subsequent research.

**Author Contributions:** Conceptualization, H.W. and T.Z.; Methodology, X.C.; Investigation, S.X.; Writing—Original Draft Preparation, H.W.; Writing—Review and Editing, T.Z. All authors have read and agreed to the published version of the manuscript.

**Institutional Review Board Statement:** Not applicable.

**Informed Consent Statement:** Not applicable.

**Data Availability Statement:** Not applicable.

## References

1. Basgul, C.; Yu, T.; MacDonald, D.W.; Siskey, R.; Marcolongo, M.; Kurtz, S.M. Does annealing improve the interlayer adhesion and structural integrity of FFF 3D printed PEEK lumbar spinal cages? *J. Mech. Behav. Biomed. Mater.* **2020**, *102*, 103455. [CrossRef]

2. Laux, C.J.; Villefort, C.; Ehrbar, S.; Wilke, L.; Guckenberger, M.; Muller, D.A. Carbon Fiber/Polyether Ether Ketone (CF/PEEK) Implants Allow for More Effective Radiation in Long Bones. *Materials* **2020**, *13*, 1754. [CrossRef] [PubMed]

3. Penumakala, P.K.; Santo, J.; Thomas, A. A critical review on the fused deposition modeling of thermoplastic polymer composites. *Compos. Part B Eng.* **2020**, *201*, 108336. [CrossRef]

4. Dai, G.; Zhan, L.; Ma, B.; Guan, C.; Huang, M. Effect of process parameters on interlaminar properties of thermoplastic composite: Molecular dynamics simulation and experimental verification. *Polymer* **2023**, *280*, 126062. [CrossRef]

5. Donough, M.J.; Shafaq; St John, N.A.; Philips, A.W. Gangadhara Prusty, B. Process modelling of In-situ consolidated thermoplastic composite by automated fibre placement—A review. *Compos. Part A Appl. Sci. Manuf.* **2022**, *163*, 107179. [CrossRef]

6. Yadav, N.; Schledjewski, R. Inline tape width control for thermoplastic automated tape layup. *Compos. Part A Appl. Sci. Manuf.* **2022**, *163*, 107267. [CrossRef]

7. Doppelbauer, L.K.; Rienesl, K.; Stelzer, P.S.; Zulueta, K.; Chang, L.-Y.; Major, Z. A macroscopic model of the compaction process during compression molding of carbon fiber sheet molding compounds. *Compos. Part A Appl. Sci. Manuf.* **2023**, *169*, 107535. [CrossRef]

8. Elchalakani, M.; Higgoda, T.M.; Kimiaei, M.; Yang, B. Pultruded FRP tubular section members, connections, and frames: A review on experimental studies. *Structures* **2023**, *56*, 104986. [CrossRef]

9. Frketic, J.; Dickens, T.; Ramakrishnan, S. Automated manufacturing and processing of fiber-reinforced polymer (FRP) composites: An additive review of contemporary and modern techniques for advanced materials manufacturing. *Addit. Manuf.* **2017**, *14*, 69–86. [CrossRef]

10. Cheng, P.; Peng, Y.; Li, S.; Rao, Y.; Le Duigou, A.; Wang, K.; Ahzi, S. 3D printed continuous fiber reinforced composite lightweight structures: A review and outlook. *Compos. Part B Eng.* **2023**, *250*, 110450. [CrossRef]

11. Huang, Y.; Tian, X.; Zheng, Z.; Li, D.; Malakhov, A.V.; Polilov, A.N. Multiscale concurrent design and 3D printing of continuous fiber reinforced thermoplastic composites with optimized fiber trajectory and topological structure. *Compos. Struct.* **2022**, *285*, 115241. [CrossRef]

12. Soleyman, E.; Aberoumand, M.; Soltanmohammadi, K.; Rahmatabadi, D.; Ghasemi, I.; Baniassadi, M.; Abrinia, K.; Baghani, M. 4D printing of PET-G via FDM including tailormade excess third shape. *Manuf. Lett.* **2022**, *33*, 1–4. [CrossRef]

13. Ahmad, M.N.; Mohamad, A.R. Analysis on dimensional accuracy of 3D printed parts by Taguchi approach. In *Advances in Mechatronics, Manufacturing, and Mechanical Engineering*; Springer: Singapore, 2021; pp. 219–231. [CrossRef]

14. Osman, A.; Lu, J. 3D printing of polymer composites to fabricate wearable sensors: A comprehensive review. *Mater. Sci. Eng. R Rep.* **2023**, *154*, 100734. [CrossRef]

15. Ahmad, M.N.; Ishak, M.R.; Mohammad Taha, M.; Mustapha, F.; Leman, Z. A Review of Natural Fiber-Based Filaments for 3D Printing: Filament Fabrication and Characterization. *Materials* **2023**, *16*, 4052. [CrossRef] [PubMed]

16. Rahmatabadi, D.; Soltanmohammadi, K.; Pahlavani, M.; Aberoumand, M.; Soleyman, E.; Ghasemi, I.; Baniassadi, M.; Abrinia, K.; Bodaghi, M.; Baghani, M. Shape memory performance assessment of FDM 3D printed PLA-TPU composites by Box-Behnken response surface methodology. *Int. J. Adv. Manuf. Technol.* **2023**, *127*, 935–950. [CrossRef]

17. Rahmatabadi, D.; Soltanmohammadi, K.; Aberoumand, M.; Soleyman, E.; Ghasemi, I.; Baniassadi, M.; Abrinia, K.; Bodaghi, M.; Baghani, M. Development of Pure Poly Vinyl Chloride (PVC) with Excellent 3D Printability and Macro- and Micro-Structural Properties. *Macromol. Mater. Eng.* **2022**, *308*, 2200568. [CrossRef]

18. Tian, X.; Liu, T.; Yang, C.; Wang, Q.; Li, D. Interface and performance of 3D printed continuous carbon fiber reinforced PLA composites. *Compos. Part A Appl. Sci. Manuf.* **2016**, *88*, 198–205. [CrossRef]

19. Geng, P.; Zhao, J.; Wu, W.; Ye, W.; Wang, Y.; Wang, S.; Zhang, S. Effects of extrusion speed and printing speed on the 3D printing stability of extruded PEEK filament. *J. Manuf. Process.* **2019**, *37*, 266–273. [CrossRef]

20. Zhang, Z.; Long, Y.; Yang, Z.; Fu, K.; Li, Y. An investigation into printing pressure of 3D printed continuous carbon fiber reinforced composites. *Compos. Part A Appl. Sci. Manuf.* **2022**, *162*, 107162. [CrossRef]

21. Shuto, R.; Norimatsu, S.; Arola, D.D.; Matsuzaki, R. Effect of the nozzle temperature on the microstructure and interlaminar strength in 3D printing of carbon fiber/polyphenylene sulfide composites. *Compos. Part C Open Access* **2022**, *9*, 100328. [CrossRef]

22. Liao, B.; Yang, H.; Ye, B.; Xi, L. Microscopic void distribution of 3D printed polymer composites with different printing direction. *Mater. Lett.* **2023**, *341*, 134236. [CrossRef]

23. Dou, H.; Ye, W.; Zhang, D.; Cheng, Y.; Huang, K.; Yang, F.; Rudykh, S. Research on drop-weight impact of continuous carbon fiber reinforced 3D printed honeycomb structure. *Mater. Today Commun.* **2021**, *29*, 102869. [CrossRef]

24. Liu, F.; Ferraris, E.; Ivens, J. Mechanical investigation and microstructure performance of a two-matrix continuous carbon fibre composite fabricated by 3D printing. *J. Manuf. Process.* **2022**, *79*, 383–393. [CrossRef]

25. Yamamoto, K.; Luces, J.V.S.; Shirasu, K.; Hoshikawa, Y.; Okabe, T.; Hirata, Y. A novel single-stroke path planning algorithm for 3D printers using continuous carbon fiber reinforced thermoplastics. *Addit. Manuf.* **2022**, *55*, 102816. [CrossRef]

26. He, Q.; Wang, H.; Fu, K.; Ye, L. 3D printed continuous CF/PA6 composites: Effect of microscopic voids on mechanical performance. *Compos. Sci. Technol.* **2020**, *191*, 108077. [CrossRef]

27. Zhang, H.; Chen, J.; Yang, D. Fibre misalignment and breakage in 3D printing of continuous carbon fibre reinforced thermoplastic composites. *Addit. Manuf.* **2021**, *38*, 101775. [CrossRef]

28. Yu, S.; Hwang, Y.H.; Hwang, J.Y.; Hong, S.H. Analytical study on the 3D-printed structure and mechanical properties of basalt fiber-reinforced PLA composites using X-ray microscopy. *Compos. Sci. Technol.* **2019**, *175*, 18–27. [CrossRef]

29. Voříšek, J.; Patzák, B. GPAMS: A G-code processor for advanced additive manufacturing simulations. *Addit. Manuf.* **2023**, *65*, 103279. [CrossRef]

30. Le Duigou, A.; Barbé, A.; Guillou, E.; Castro, M. 3D printing of continuous flax fibre reinforced biocomposites for structural applications. *Mater. Des.* **2019**, *180*, 107884. [CrossRef]

*Article*

# Automated Fiber Placement Path Planning and Analysis of Pressure Vessels

**Bo Wang [1], Lihua Wen [1,\*], Jinyou Xiao [1], Shiyu Wang [1], Ping Ren [2,3], Liqiang Wang [2,3], Lei Zu [4] and Xiao Hou [1]**

[1] School of Astronautics, Northwestern Polytechnical University, Xi'an 710072, China; wang_bo@mail.nwpu.edu.cn (B.W.); xiaojy@nwpu.edu.cn (J.X.); wangsy@nwpu.edu.cn (S.W.); houxiaoht@163.com (X.H.)
[2] Xi'an Institute of Aerospace Propulsion Technology, Xi'an 710025, China
[3] The 41st Institute of the Fourth Academy of China Aerospace Science and Technology Corporation National Key Lab of Combustion, Flow and Thermo-Structure, Xi'an 710025, China
[4] School of Mechanical Engineering, Hefei University of Technology, Hefei 230000, China; zulei@hfut.edu.cn
\* Correspondence: lhwen@nwpu.edu.cn

**Abstract:** The automated fiber placement (AFP) process faces a crucial challenge: the emergence of out-of-plane buckling in thermoplastic prepreg tows during steering, significantly impeding the quality of composite layup. In response, this study introduces a novel approach: the development of equations for wrinkle-free fiber placement within composite pressure vessels. The investigation encompasses a detailed analysis of prepreg trajectories in relation to shell geometry, accompanied by an in-depth understanding of the underlying causes of wrinkling on dome surfaces. Moreover, a comprehensive model for shell coverage, grounded in placement parameters, is meticulously established. To validate the approach, a simulation tool is devised to calculate press roller motions, ensuring the uniform fiber dispersion on the mandrel and achieving flawless coverage of the shell without wrinkles. This innovative strategy not only optimizes the AFP process for composite layup but also remarkably enhances the overall quality of composite shells. As such, this research carries significant implications for the advancement of composite manufacturing techniques and the concurrent improvement in material performance.

**Keywords:** composite pressure vessel; automated fiber placement; placement path planning; graphic visualization

## 1. Introduction

Composite pressure vessels have been utilized for several decades as a lightweight solution for containing gas or fluid under pressure, being widely used in aerospace, military, and aquatic sector industries [1,2]. The cutting-edge technology of automated fiber placement (AFP) has revolutionized the fabrication of diverse composite products, including large storage tanks, pipeline systems, pressure vessels, and rocket motor casings. Different from other methods [3,4], AFP does not rely on tension to fix the prepreg position, but instead, it cooperates with the robot's movement to create the prepreg placement path. Moreover, AFP's in situ technology can effectively enhance the molding rate of products without relying on secondary curing molding equipment, which can reduce the equipment investment and decrease the product production cycle. Due to its myriad benefits, AFP stands as the progressive direction in pressure vessel preparation [5–7]. The generation of the placement path is one of the most crucial processes in the placement process, which including placement path generation [8–11], placement path evaluation [12–16], and motion simulation [17–19]. An ideal placement path can effectively prevent the occurrence of wrinkle defects during the prepreg-forming process. This can be achieved by placing fiber tows onto the mandrel surface of a desired shape with designed placing patterns to ensure uniform fiber distribution, to prevent defect accumulation, and to enhance the mechanical properties of composite pressure vessels.

In recent years, many researchers have investigated the placement path planning of AFP. Belnoue et al. [20] introduced the formation of out-of-plane wrinkles in the debulking and autoclave curing processes of laminates with embedded gaps and overlaps between the deposited tapes. Predictions were made using a novel modeling framework and validated against micro-scale geometry characterization of artificially manufactured samples. This study provided valuable insights to guide defect modeling within AFP processes. Christopher et al. [21] utilized finite element simulation and an optimization algorithm to design the prepreg placement path of a flat structure and employed the sensitivity optimization method of the level set function to plan the prepreg placement path of the flat structure. The simulation results showed that this approach effectively increased the laminate's stiffness by 41.5% and 23.4% under two boundary conditions. Bijan et al. [22] proposed a novel uniform fiber placement path planning algorithm for robotics. The algorithm formulates a set of surface curves representing the path of the composite sheet to ensure the uniform laying of subsequent streamers without gaps or overlaps. The algorithm was a numerical validation and an industrial implementation that substantiated the algorithm's efficacy. Cong et al. [23] evaluated the laying quality of the fiber trajectory by examining the tow deformation characteristics of prepreg on freeform surfaces and suggested an AFP path evaluation algorithm based on prepreg tow deformability. Pierre et al. [24] presented a tool path smoothing method applied to the AFP process. The smoothing method aims to minimize the curvature and rotational axis order variations. The algorithm was based on a robust filtering method that ensures a short computing time, was adapted to redundant machine tool, and finally took into account the difference in the dynamic characteristics of each axis in the objective function to generate the fastest tool path. Qu et al. [25] contributed a wrinkle defect criterion for prepreg forming on curved surfaces, capitalizing on the analysis of the filament deformation characteristics of prepreg on free-form surfaces. As the results show, the laying of curved parts demonstrated that placement path planning incorporating this criterion could effectively suppress defects such as wrinkles and bridging.

The mechanical properties of composite pressure vessels are greatly affected by the prepreg laying angle, making placement path planning crucial in their manufacturing process. The prepreg is shaped in situ on the mandrel surface according to the planned path under the action of the press roller mechanism, with a specific bond strength required between the layers. However, limitations in the AFP technology and the prepreg's forming characteristics could result in an unsuitable placement path that does not meet the design requirements. To reduce the need for costly modifications during placement path planning, this study introduces an innovative approach that harmonizes the prepreg suitability analysis with pressure vessel placement readiness. Specifically, this paper incorporates the wrinkle-free laying trajectory criterion of prepreg on curved surfaces with the shell surface curve equation to derive the laying trajectory equations that comply with the process requirements. This approach maximizes the utilization of the composite material strength and expands the design space of laying patterns. Ultimately, the proposed method offers invaluable insights into the preparation of pressure vessels with irregular pole holes and streamlines the efficiency of placement path planning.

## 2. Placement Path Planning of Pressure Vessel

The pressure vessel is composed of two domes at each end and a cylinder section in the middle. Both ends have different geometric forms that require distinct considerations for the design of the placement path. As a result, equations for the placement path are derived with slight variations to account for the differences in geometrical parameters between the two sections.

### 2.1. Placement Path Planning for Wrinkle-Free Defects in the Ellipsoidal Dome Section

Figure 1 depicts that ellipsoidal dome sections can be modeled as a curved surface that rotates counterclockwise around the Z axis. The pressure vessel's surface can be described

using the cylindrical coordinate system {r, θ, z}, and the relevant constitutive equations are shown as follows:

$$r(\theta, z) = (r\cos\theta, r\sin\theta, Z) \tag{1}$$

where r and z represent the radius and axial distance of the rotary body, and θ is the mandrel rotation angle.
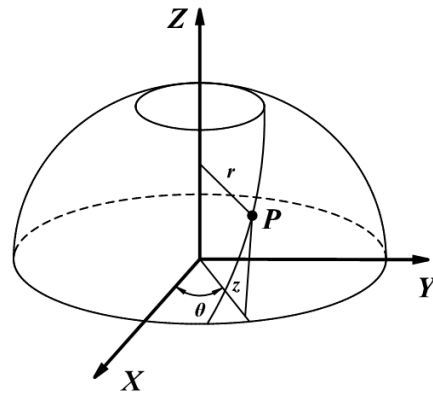


**Figure 1.** Placement path on a surface of revolution.

In order to prevent the occurrence of wrinkle defects resulting from the accumulation of defects during prepreg placement on a curved surface, Qu et al. [25] investigated the strain variation of prepreg during surface placement of a specific width and established a criterion condition for wrinkle-free placement of prepreg on the curved surface.

$$\left| \frac{W}{2} \times K_g - \frac{W^2}{8} \times K \right| \leq \frac{W}{2 \times R_{min}} \tag{2}$$

where W is the width of the prepreg; $K_g$ is the geodesic curvature of the placement path; K is the Gaussian curvature of the surface; and $R_{min}$ is the minimum forming radius at which the prepreg can be laid on a flat surface without wrinkle defects.

From the Liouville formula for differential geometry, the geodesic curvature $K_g$ of the curve on the surface of the slalom and the Gaussian curvature K of the surface can be expressed as follows:

$$K_g = \frac{d\alpha}{ds} + \frac{r'\sin\alpha}{r\sqrt{1 + r'^2}} \tag{3}$$

$$K = \frac{-r''}{r\left(1 + r'^2\right)^2} \tag{4}$$

where α is the angle between the curve on the surface and the surface meridian, called the laying angle; s is the coordinate of the corresponding arc length of the curve; r′ is the derivative of r with respect to z; and r″ is the second derivative of r with respect to z. Meanwhile, the parameters z, s, α, θ, and r′ on the surface of the slalom satisfy the following differential equation relations [26,27]:

$$\frac{dz}{ds} = \frac{\cos\alpha}{\sqrt{1 + r'^2}} \tag{5}$$

$$\frac{d\theta}{dz} = \frac{\tan\alpha\sqrt{1 + r'^2}}{r} \tag{6}$$

Since the Gaussian curvature of the surface and the prepreg width W is constant values, Equation (2) expresses the relationship between $K_g$ and $R_{min}$ in the absence of wrinkle defects in the prepreg. The absolute value exists on Equation (3)'s left-hand side.

Hence, two cases exist. In case I, ($K_g - \frac{W^2}{8} * K \geq 0$), when the prepreg is laid on the surface, the strain reaches a critical state, and Equation (3) is deformed as follows:

$$K_g = \frac{1}{R_{min}} + \frac{W \times K}{4} \tag{7}$$

Similarly, in case II, ($\frac{W}{2} * K_g - \frac{W^2}{8} * K < 0$), Equation (2) is deformed as follows:

$$K_g = \frac{W \times K}{4} - \frac{1}{R_{min}} \tag{8}$$

According to Equations (7) and (8), the geodesic curvature of the without wrinkle placement path on the surface with constant geometry and prepreg width depends on $R_{min}$. As $R_{min}$ tends toward infinity, Equations (7) and (8) can be calculated to obtain the range of values of $K_g$. Moreover, according to the combination of Equations (3)–(6), Equations (7) and (8)'s deformation can obtain Equations (9) and (10) as follows:

$$\frac{d\alpha}{dz} = \frac{\sqrt{1 + r'^2}}{R_{min} \cos \alpha} + \frac{-Wr'' \sqrt{1 + r'^2}}{4r \left(1 + r'^2\right)^2 \cos \alpha} - \frac{r'}{r} \tan \alpha \tag{9}$$

$$\frac{d\alpha}{dz} = \frac{Wr'' \sqrt{1 + r'^2}}{4r \left(1 + r'^2\right)^2 \cos \alpha} - \frac{\sqrt{1 + r'^2}}{R_{min} \cos \alpha} - \frac{r'}{r} \tan \alpha \tag{10}$$

In the case of laying the prepreg on the dome of the pressure vessel without wrinkle defects, the differential equation relationship for the change in laying angle along the axial direction is given by Equations (9) and (10). These are non-linear differential equations, which can be solved numerically using the Runge–Kutta formula to determine the range of variation in $\alpha$ along the dome axis, given the geometrical parameters of the pressure vessel and the width of the prepreg.

To verify the universality of placement path planning, this study selects an unequal pole hole pressure vessel as the object of study. The meridian curve equation is $\frac{z^2}{b^2} + \frac{r^2}{R^2} = 1$, where b and R are the semi-minor and semi-major axes, respectively, of the ellipse with values of 50 mm and 53 mm, as shown in Figure 2. The left and right head heights are h1 = 46 mm and h2 = 42 mm, respectively; the cylindrical length is L = 200 mm; the prepreg width is W = 6.35 mm; and $R_{min}$ = 300 mm. The initial laying angle of the left dome is set to 60°. By applying Equations (9) and (10), the end laying angle variation of prepreg without wrinkle defects of the left ellipsoidal dome near the cylinder section is calculated to be [8.03°, 18.04°] ∪ [21.54°, 31.55°], and the laying angle variation along the axial direction of the ellipsoidal dome is shown in Figure 3. Combined with Equation (6), the Runge–Kutta formula is used to calculate the mandrel rotation angle θ of the placement path under the corresponding laying angle, and the three-dimensional placement path of the ellipsoidal dome is shown in Figure 4. As the minimum forming radius $R_{min}$ tends toward infinity (with a value of $10^{25}$ mm selected as infinite in this paper), the placement path of the dome section will approximate the geodesic curve with an initial angle of 60° but will not coincide with it, as shown in Figures 3 and 4. The analysis of Equations (9) and (10) indicates that the influence of the Gaussian curvature of the dome surface and the geodesic curvature of the placement path makes it impossible to place the prepreg on certain geodesic lines on the surface without wrinkle defects, regardless of the value of $R_{min}$, which also explains why, as described in the literature [28], prepregs with a certain width may sometimes produce wrinkle defects even when placed on the geodesic path of a curved surface. The wrinkle-free laying angle range at an ellipsoidal dome section is enlarged by reducing the $R_{min}$ value of a preform plane placement, the selection of deployment placement path parameters at the ellipsoidal dome section is expanded, and the optimal deployment

placement path parameters are subsequently optimized to use an optimization algorithm and a finite element analysis.
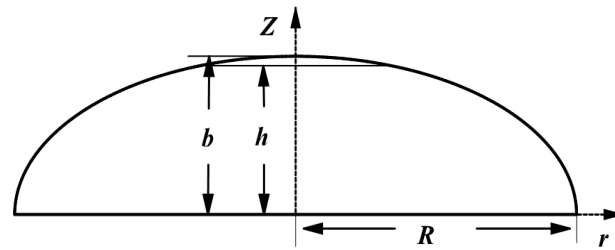


**Figure 2.** Geometry of an ellipsoidal dome.
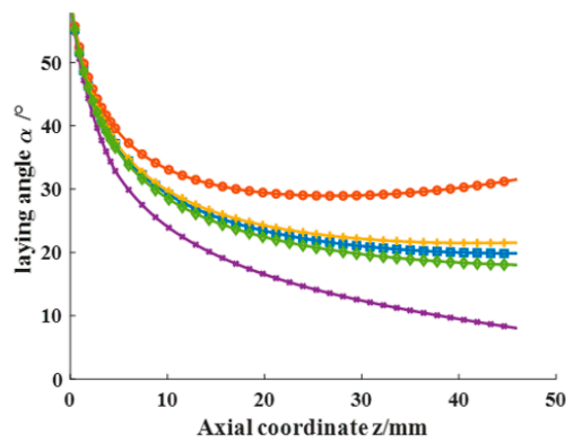


**Figure 3.** Range of laying angle for the prepreg place placement without wrinkle defects in the left ellipsoidal dome section.
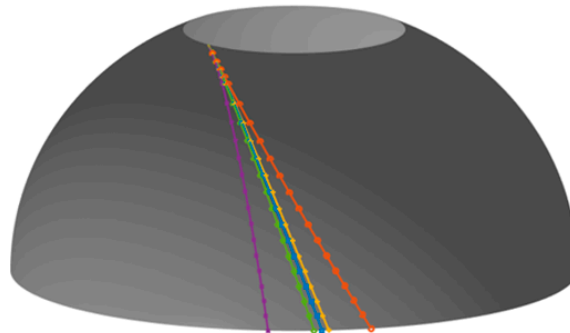


**Figure 4.** Actual placement path of the ellipsoidal dome section.

### 2.2. Placement Path Planning for Defect-Free Algorithm in the Ellipsoidal Dome Section

For composite plies formed using AFP, gaps and overlaps can frequently occur between two adjacent prepregs in the same ply due to the mandrel's shape and placement path planning algorithm. These gaps and overlaps have negative impacts on the entire placement

process and the structural integrity of composite layers, including reduced laying efficiency and increased material losses due to more shearing and re-feeding operations of the filament bundle. Moreover, the gaps and overlaps can affect the uniformity of layer thickness and the dimensional accuracy of the composite component shape, and also result in mechanical property variations at different locations, leading to damage and failure of the layers where gaps exist.

To address these challenges, a defect-free placement path planning algorithm is proposed for the dome section that combines wrinkle-free placement paths with prepreg and dome geometry to achieve gap-free, overlap-free, and wrinkle-free placement of the prepreg. Pressure vessels are rotary structures characterized by a straight axis, a circular interface perpendicular to the axis, and a spline curve bus. To illustrate the specific implementation steps of the no defect placement path planning algorithm for the ellipsoidal dome of the pressure vessels, the schematic depiction of a pressure vessel is showcased in Figure 5 to elucidate the precise steps involved in the defect-free placement path planning algorithm.
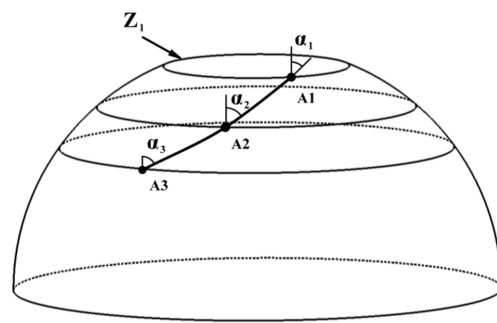


**Figure 5.** Schematic diagram of the prepreg placement path on the dome surface of the pressure vessel.

The prepreg placement path in the ellipsoidal dome can be discretized into m points (A1, A2, . . ., Am); a plane perpendicular to the axis is made over each point; and the resulting plane is defined as the cross-section of the pressure vessels with the cross-section circle corresponding to a perimeter of $C_m$, where the cross-section circle at the pole hole of the ellipsoidal dome is the smallest and the corresponding perimeter is $C_1$.

The crux of designing an ellipsoidal dome section with no defects lies in accurately determining the laydown angle of the prepreg. Figure 6 illustrates that the width covered by the prepreg at the laydown angle $\alpha$ is denoted as $W_L$.

$$W_L = \frac{W}{\cos \alpha} \tag{11}$$
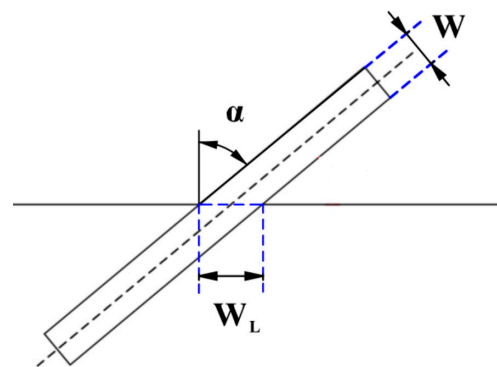


**Figure 6.** Schematic diagram for calculating the actual cover width for prepreg laying.

Based on the analysis of the actual coverage width of the prepreg described above, it is feasible to achieve continuous, defect-free placement of prepreg along a certain laying angle without any gaps or overlapping defects. This approach is now being applied to

the mandrel surface. As the mandrel cross-section undergoes continuous change, the laying angle of the prepreg can also be adjusted accordingly for the purpose of forming a placement path that is free of gaps and defects, with continuously changing laying angles. The design of this placement path can be divided into three steps. The first step involves setting the initial laying angle and calculating the number of laps of prepreg laying. For example, when studying the left ellipsoidal dome, the pole hole with the smallest circumference of the section is designated as the starting point of laying, the initial laying angle is set to $\alpha_1$, and the number of laps of laying N is calculated.

$$N = \left\lceil \frac{2\pi r_{Z_1}}{WL} \right\rceil \tag{12}$$

where $r_{Z_1}$ is the radius of the cross-sectional circle at the pole hole.

The second step involves correcting the actual initial forming angle $\alpha_c$ and calculating the laying angle of the placement path. The number of laps N required to achieve even and defect-free coverage of the dome region with prepreg is determined through Equation (12). As N is obtained by rounding up, further correction and calculation are required to determine the actual initial laying angle $\alpha_c$.

$$\alpha_c = \sin^{-1}\left( \frac{WN}{2\pi r_{Z_1}} \right) \tag{13}$$

Similarly, the laying angle $\alpha_m$ at the other intersections of the placement path can be expressed as follows:

$$\alpha_m = \sin^{-1}\left( \frac{WN}{2\pi r_{Z_m}} \right) \tag{14}$$

The third step involves conducting a wrinkle detection analysis of the placement path. By combining the wrinkle-free criterion, the placement path obtained in the second step is evaluated for the presence of wrinkle defects. Taking the right ellipsoidal dome of the mandrel as an example, the minimum forming radius $R_{min}$ is set to 30 mm for the prepreg plane lay-up without wrinkle defects. With the initial laying angle analysis range set to $[0°, 90°]$, the maximum prepreg strain corresponding to different initial lay-up angle paths of the right ellipsoidal dome is calculated by using Equations (2)–(4) and compared with the selected prepreg limit strain without wrinkle defects. As depicted in Figure 7, since corrections must be made according to the number of placement paths after a given initial laying angle, a specific range of initial lay-up angles corresponds to the same actual initial laying angle and placement path. Hence, step-like fold strain values will appear in Figure 8. Based on the calculation results, the range of initial angle selection for the right ellipsoidal dome without defects is determined to be $[60.56°, 90°]$. As the initial angle of the laying curve increases gradually, the variation in strain values during the placement of prepreg exhibits a progressively gentle trend. Furthermore, the placement path pattern of the ellipsoidal dome depicted in Figure 7 can also be employed for reinforcement structures of the pressure vessels. The construction of ellipsoidal dome structures using a multi-layered deposition approach enables precise reinforcement of vulnerable regions within the pressure vessels. This precise reinforcement leads to an effective enhancement in the strength utilization efficiency of the fiber material, concurrently reducing the superfluous mass of the vessels. This reinforcement strategy not only contributes to the optimization of structural performance in pressure vessels but also unveils broader prospects for practical engineering applications.

| Initial laying angle: 0° | Initial laying angle: 45° | Initial laying angle: 90° |
|---|---|---|
| Actual initial laying angle after correction: 10.25° | Actual initial laying angle after correction: 45.34° | Actual initial laying angle after correction: 88° |
| Laying envelope number: 28 | Laying envelope number: 20 | Laying envelope number: 1 |
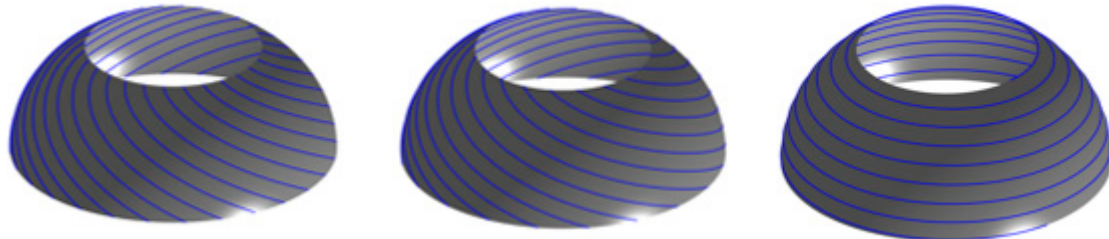
**Figure 7.** Defect-free ellipsoidal dome sections' placement path pattern.
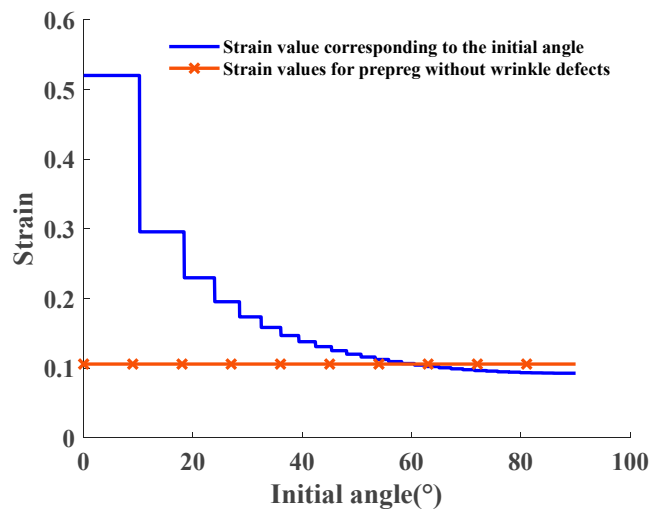
**Figure 8.** Variation in strain in the placement path of the ellipsoidal dome regions with variable initial laying angle.

By means of simulation analysis and verification, the proposed defect-free placement path calculation method for the dome section of the mandrel structure, which integrates the analysis of mandrel and prepreg geometry and incorporates the prepreg wrinkle criterion, has been demonstrated to be highly effective in guiding the prepreg to achieve gap-free, overlap-free, and wrinkle-free placement in the dome section.

### 2.3. Placement Path Planning for Wrinkle-Free Defects in the Cylinder Section

The cylinder section is a rotary structure with equal sections, characterized by K, $r'$, and $r''$ values of 0. By combining Equations (9) and (10) with the geometrical characteristics of the cylinder section, the wrinkle-free placement path equation for the cylinder section is analytically derived as follows:

$$\frac{\mathrm{d}\alpha}{\mathrm{d}z} = \frac{1}{R_{min}\cos\alpha} \tag{15}$$

$$\frac{\mathrm{d}\alpha}{\mathrm{d}z} = -\frac{1}{R_{min}\cos\alpha} \tag{16}$$

Using the aforementioned cylinder section as an example, with the initial laying angle set at 20° and the minimum forming radius $R_{min} = 1800$ mm of the prepreg adjusted, the range of prepreg laying angles that result in wrinkle-free placement for the cylinder section is calculated using Equations (15) and (16) as [13.35°, 26.94°]. The axial variation of the laying angle is illustrated in Figure 9, while the actual placement trajectory of the cylindrical portion is depicted in Figure 10. Equations (15) and (16) serve as the theoretical underpinnings for the AFP process designed for variable-angle placement paths devoid of any wrinkle defects on the surface of the cylinder. These equations establish the foundational framework for achieving precise and controlled fiber deposition on the cylindrical surface, ensuring the production of defect-free composite structures. Their seamless integration into the fabrication procedure facilitates the realization of optimized fiber configurations, ushering in amplified mechanical properties and heightened structural integrity within the resultant composite materials.
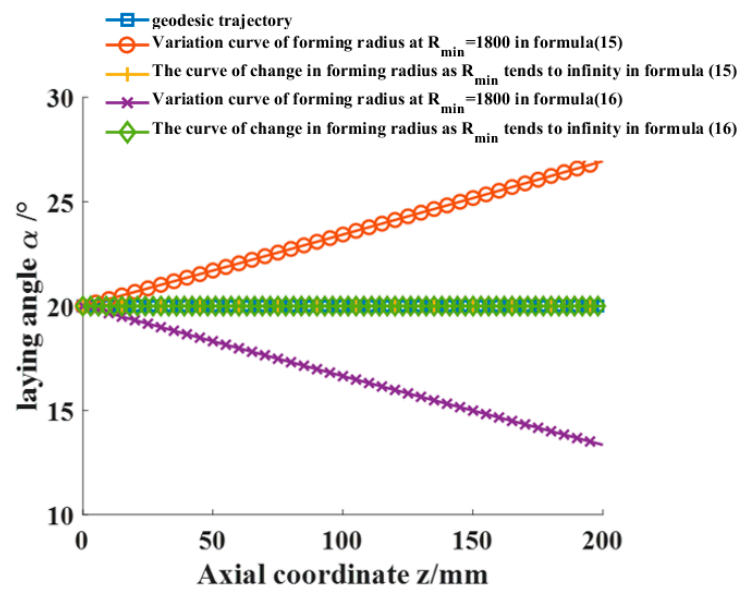


**Figure 9.** Range of angles for laying prepreg without wrinkle defects in the cylinder section.
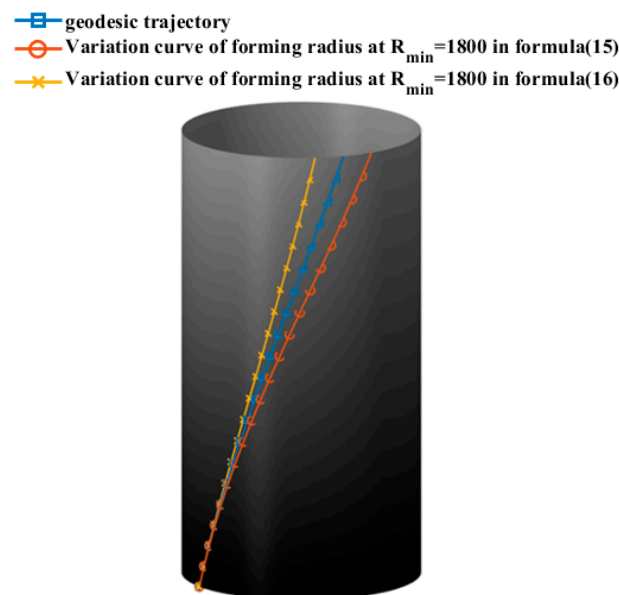


**Figure 10.** Placement path in the cylinder section.

As the minimum forming radius of the prepreg $R_{min}$ approaches infinity, the wrinkle-free placement path of the cylinder section converges to the geodesic curve. This implies that a prepreg with a certain width can be placed on the surface of a rotating body with a constant cross-section without any wrinkle defects, following the geodesic trajectory.

Deforming and integrating Equations (15) and (16) give

$$\int_0^L dz = \pm \int_{\alpha_0}^{\alpha} R_{min} \cos \alpha \, d\alpha \tag{17}$$

The equation for the axial length corresponding to the change in the laying angle of the cylinder section is obtained:

$$L = |R_{min}(\sin \alpha - \sin \alpha_0)| \tag{18}$$

where $\alpha_0$ is the initial laying angle, $\alpha$ is the termination laying angle, and L is the axial length of the cylinder corresponding to the without-wrinkle-defect lay of the prepreg required for the transition between the two laying angle changes.

## 3. Full Coverage

To ensure uniform coverage of the mandrel with prepreg without wrinkle defects, the prepreg laying process starts from the left head pole hole, extends to the right pole hole, and returns. A complete cycle involves staggering the prepreg width at the cylinder equator, followed by multiple cycles to achieve full coverage. However, not all mandrel rotation angles allow for even filling, but rather only when the mandrel rotation angle reaches a specific value can conditions for even filling be met.

During the AFP process, the mandrel rotates one cycle of roundtrip movement of the press roller, denoted by $\sum \theta$. The total mandrel rotation angle can be expressed as follows:

$$\sum \theta = \theta_a + \theta_b + \Delta\theta = 360 \left( M \pm \frac{k}{Y} \right) \tag{19}$$

where $\theta_a$ and $\theta_b$ represent the ellipsoidal dome and cylinder section placement path corresponding to the mandrel rotation angle, respectively; $\Delta\theta$ is a tiny angle; and M is the number of revolutions of the mandrel when the prepreg is covered. Y is similar to N in Equation (12) and represents the number of cycles required for the mandrel to be uniformly covered by prepreg. The laying angle $\alpha$ involved in the calculation of the actual laying coverage width is the minimum laying angle of the cylinder section. K is an integer number that satisfies the requirement that k/Y is the simplest true fraction.

The process of analyzing the full coverage of the placement path is illustrated in Figure 11. The mandrel and prepreg described above are analyzed for placement path coverage. The prepreg minimum forming radius is set to $R_{min}$ = 300 mm. The initial laying angles of the left and right ellipsoidal domes are 60° and 30°, and the final laying angles of the left and right ellipsoidal domes are calculated to be within the range of [8.03°, 18.039°] ∪ [21.54°, 31.55°] and [5.71°, 14.19°] ∪ [17.27°, 26.03°], respectively. The final laying angles of the left and right ellipsoidal domes are set as 25° and 10°, respectively, to obtain a constant laying angle range of [0°, 39.15°] for the cylinder section. A constant laying angle of 30° is selected for the cylinder section. The value of M is chosen as 2, and the value of k is chosen as 37, resulting in a tiny angle of $\Delta\theta$ = 97.39°. Based on the above data, the effect of prepreg forming for different laying paths is shown in Figure 12. The minimum laying angle for the cylinder section is 10°, and the minimum coverage fraction of prepreg on the cylinder section is as follows:

$$T = \frac{WY}{2\pi R \cos \alpha} \times 100\% = \frac{6.35 \times 52}{106\pi \cos(10°)} = 100.69\%$$
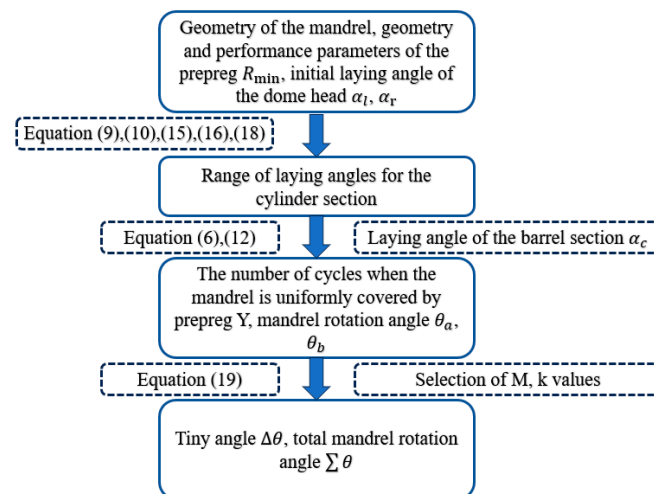
**Figure 11.** Flow chart of the optimal design procedure for determining the placement process parameters.
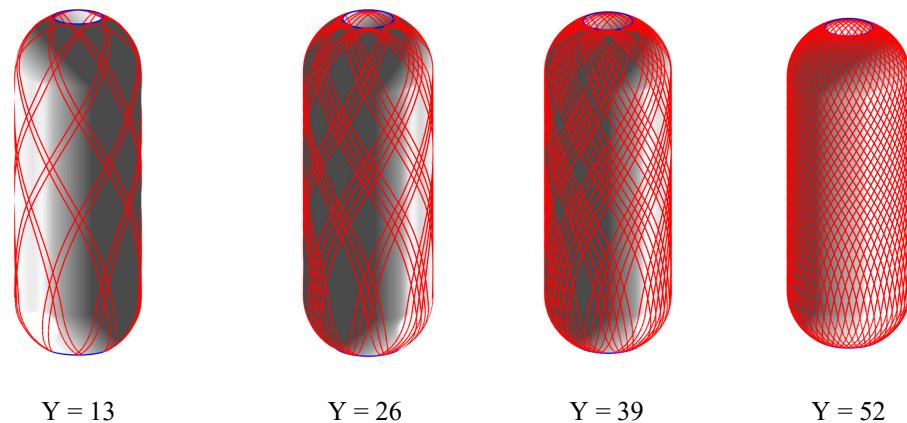


| Y = 13 | Y = 26 | Y = 39 | Y = 52 |

**Figure 12.** Placement path patterns for the Y = 13, Y = 26, Y = 39, and the final placed circuit.

In the actual placement of prepared pressure vessels, it is acceptable for the coverage fraction to be greater than 100% due to the parameter Y in the cylinder section typically being rounded upwards.

## 4. Motion Control Analysis for the Placement Path of Pressure Vessel

Based on the results of the placement path solution, the coordinate position of the prepreg laying point can be determined. However, to validate the accuracy of the placement path planning method, it is essential to conduct actual laying verification on the machine, involving examining the trajectory of the press roller and the mandrel rotation axis. During the prepreg placement process on the mandrel surface for pressure vessel preparation, the press roller mechanism is only required to move within the red area illustrated in Figure 13a to ensure complete coverage of the pressure vessel.

During the preparation of pressure vessels using AFP, the accuracy of the prepreg's laying angle plays a crucial role in determining the accuracy of the placement path. The press roller is responsible for controlling the laying angle, and as the mandrel rotates, the press roller moves axially within the red area of the mandrel surface. The laying angle of the prepreg is precisely controlled by regulating the $\varphi_1$ and $\varphi_2$ angles of the press roller and mandrel, respectively. In Figure 13b, $\varphi_1$ represents the angle between the projection of the contact plane of the press roller and the mandrel in the XZ plane and the YZ plane. In Figure 13c, $\varphi_2$ takes on the mantle of the angle linking the press roller's radial direction with the mandrel's axial trajectory—a magnitude synonymous with the prepreg's laying angle $\alpha$ within the contours of placement path analysis.
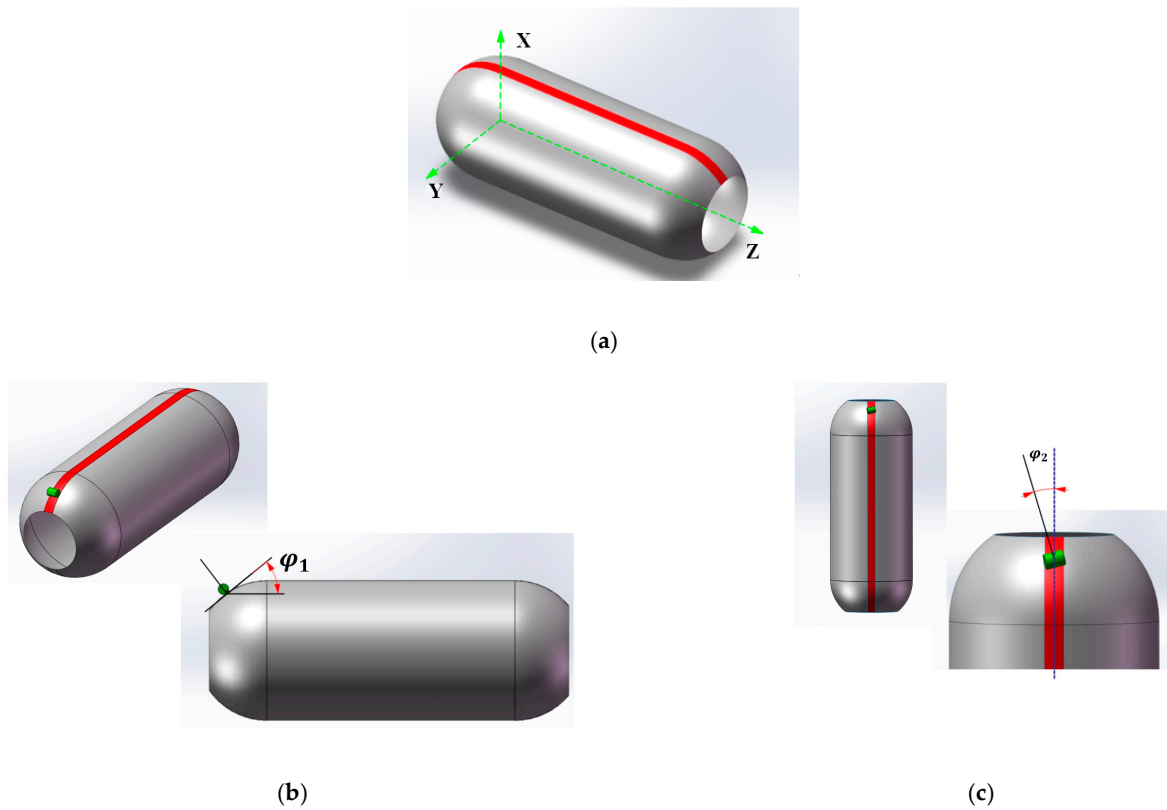
**Figure 13.** The coordinate system for the layering head motion and its trajectory on the vessel surface: (**a**) the movement zone; (**b**) the angle $\varphi_1$ and (**c**) the angle $\varphi_2$.

From Figure 13b, $\varphi_1$ is the angle between the tangent path of the dome surface and the axis of the mandrel, which can be expressed as follows:

$$\varphi_1 = \tan^{-1}(r') \tag{20}$$

The accuracy of the prepreg's laying angle plays a crucial role in the AFP process for pressure vessel preparation. The press roller mechanism, controlling the laying angle, moves axially on the mandrel surface within the red area (as shown in Figure 13a) as the mandrel rotates. The laying angle is precisely controlled via the angles $\varphi_1$ and $\varphi_2$ of the press roller and the mandrel, respectively. Setting the left ellipsoidal dome parameter $\varphi_1$ as positive, the change in $\varphi_1$ during the laying of the press roller mechanism from left to right is illustrated in Figure 14a. The $\varphi_1$ of the cylinder section is 0 since the laying head is parallel to the mandrel axis in that region. The laying angle $\alpha$, equivalent to $\varphi_2$ of the press roller, is shown in Figure 14b for the placement path of the mandrel, which is divided into five areas, namely, I and V (the laying angle change sections of the left and right dome regions), II and IV (the laying angle transition sections of the cylinder section), and III (the cylinder constant laying angle section). Similarly, the mandrel rotation angle change curve corresponding to the direction of the axis length of the prepreg placed from left to right via the press roller is shown in Figure 14c. The change curves of $\varphi_1$, $\varphi_2$, and the axial displacement of the press roller based on the mandrel rotation angle are illustrated in Figure 14d, which can effectively guide the press roller mechanism and the mandrel rotation axis to coordinate and control the precise and smooth in situ forming of prepreg on the mandrel surface. To validate the placement path planning method, actual laying verification on the machine is necessary, which requires investigating the trajectory of the press roller and the mandrel rotation axis.

(a)



(b)



(c)



(d)
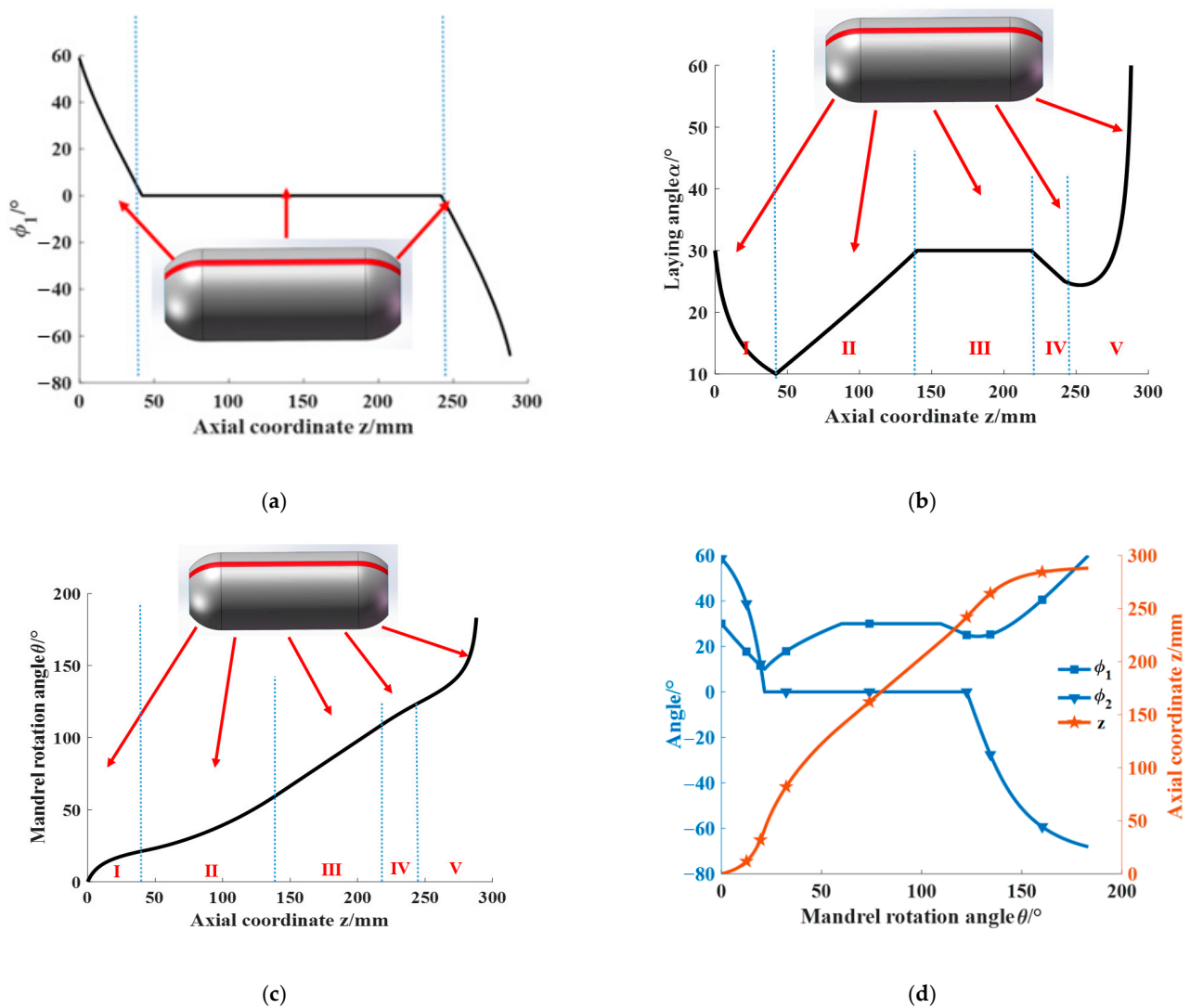
**Figure 14.** Variation curve of the placement process parameters: (**a**) variation curve of $\varphi_1$; (**b**) variation curve of the laying angle $\alpha$; (**c**) variation curve of mandrel rotation angle $\theta$; (**d**) variation curves for each process parameter based on the mandrel rotation angle $\theta$.

The laying speed plays a crucial role in the forming quality and efficiency of composite components and is influenced by other process parameters. Thus, studying the stable regulation of prepreg laying speed via the robot and mandrel rotation axis is of great significance in producing high-quality and efficient composite components. As depicted in Figure 15, the prepreg laying speed $V_Z$ comprises the axial shift speed of the laying head ($V_a$) and the mandrel rotation speed ($V_b$). The values of $V_a$ and $V_b$ can be calculated based on the laying angle at different moments.

The presented Figure 16 illustrates the press roller shift speed and mandrel rotation speed curve when the prepreg laying speed is set to 40 mm/s using the laying angle curve in Figure 14b as a reference. Based on the research findings in this section, the robot and mandrel rotation axis can collaboratively generate G codes, which is used as a common input for the robot control system. Furthermore, the AFP system can be efficiently controlled to prepare pressure vessels of superior quality and productivity by combining the results of placement path analysis with the motion parameter analysis.
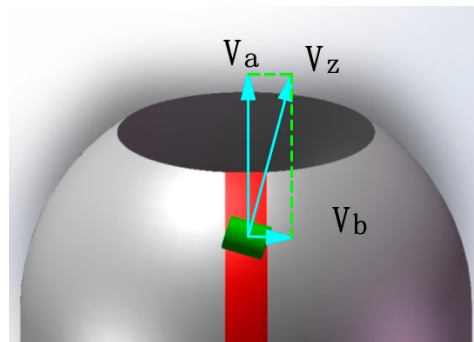
**Figure 15.** Schematic diagram of the breakdown of the prepreg laying speed.
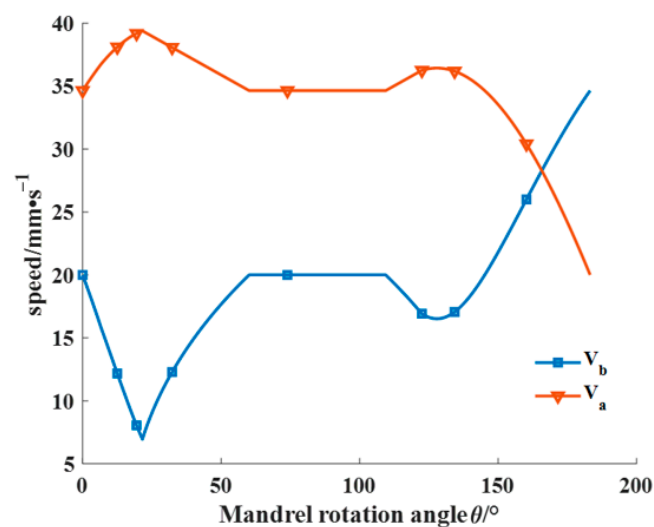


**Figure 16.** Speed curve of the press roller shift speed and mandrel rotation speed based on the mandrel rotation angle.

## 5. Conclusions

This paper introduces a novel method for calculating the AFP placement path within pressure vessels. The approach is rooted in the wrinkle defect criterion governing prepreg forming on curved surfaces and leverages principles from differential geometry. The goal is to generate placement paths that sidestep both wrinkle and overlap defects. Different from traditional path planning strategies that mainly consider initial paths, the proposed method can directly obtain the laying range in the domain of the rotating surface, determine the placement path by selecting the laying angle, significantly improving the efficiency of placement path planning, reducing the trial-and-error costs, and facilitating the combination with optimization methods for placement path optimization analysis. In addition, the uniform laying envelope shell model of prepreg is simulated to obtain suitable process parameters. Finally, combining the motion characteristics of the AFP equipment, the motion status of the press roller is decomposed to obtain the motion parameters of the press roller, which guides the AFP equipment to complete the laying action.

**Institutional Review Board Statement:** Not applicable.

**Informed Consent Statement:** Not applicable.

**Data Availability Statement:** All data, models, or code that support the conclusions of this study are available from the corresponding author upon reasonable request.

**Conflicts of Interest:** The authors declare no conflict of interest.

## References

1. Lin, L.; Wang, X.; Yang, B.; Zhang, L.; Zhao, Z.; Qu, X.; Lu, Y.; Jiang, X.; Lu, S. Conditionmonitoring of composite overwrap pressure vessels based on buckypaper sensor and MXene sensor. *Compos. Commun.* **2021**, *25*, 100699. [CrossRef]
2. Daghighi, S.; Weaver, P.M. Three-dimensional effects influencing failure in bend-free, variable stiffness composite pressure vessels. *Compos. Struct.* **2021**, *262*, 113346. [CrossRef]
3. Zu, L.; Xu, H.; Jia, X.; Zhang, Q.; Wang, H.; Zhang, B. Winding path design based on mandrel profile updates of composite pressure vessels. *Compos. Struct.* **2020**, *235*, 111766. [CrossRef]
4. Li, H.; Li, M. Constant Winding Angle Curve on Revolution Surface and its Application. *Comput. Des.* **2022**, *144*, 103160. [CrossRef]
5. Xiao, R.; Shi, J.; Xiao, J. Study of Allowable Interlaminar Normal Stress Based on the Time–Temperature Equivalence Principle in Automated Fiber Placement Process. *Polymers* **2021**, *13*, 4180. [CrossRef] [PubMed]
6. Jiang, J.; He, Y.; Wang, H.; Ke, Y. Modeling and experimental validation of compaction pressure distribution for automated fiber placement. *Compos. Struct.* **2021**, *256*, 113101. [CrossRef]
7. Matsuzaki, R.; Mitsui, K.; Hirano, Y.; Todoroki, A.; Suzuki, Y. Optimization of curvilinear fiber orientation of composite plates and its experimental validation. *Compos. Struct.* **2021**, *255*, 112956. [CrossRef]
8. Yan, L.; Chen, Z.C.; Shi, Y.; Mo, R. An accurate approach to roller path generation for robotic fibre placement of free-form surface composites. *Robot. Comput. Manuf.* **2014**, *30*, 277–286. [CrossRef]
9. Bruyneel, M.; Zein, S. A modified Fast Marching Method for defining fiber placement trajectories over meshes. *Comput. Struct.* **2013**, *125*, 45–52. [CrossRef]
10. Wang, X.; An, L.; Zhang, L.; Zhou, L. Uniform coverage of fibres over open-contoured freeform structure based on arc-length parameter. *Chin. J. Aeronaut.* **2008**, *21*, 571–577. [CrossRef]
11. Shirinzadeh, B.; Cassidy, G.; Oetomo, D.; Alici, G. Trajectory generation for open-contoured structures in robotic fibre placement. *Robot. Comput. Manuf.* **2007**, *23*, 380–394. [CrossRef]
12. Zhao, C.; Xiao, J.; Huang, W.; Huang, X.; Gu, S. Layup quality evaluation of fiber trajectory based on prepreg tow deformability for automated fiber placement. *J. Reinf. Plast. Compos.* **2016**, *35*, 1576–1585. [CrossRef]
13. Wehbe, R.; Tatting, B.; Rajan, S.; Harik, R.; Sutton, M.; Gürdal, Z. Geometrical modeling of tow wrinkles in automated fiber placement. *Compos. Struct.* **2020**, *246*, 112394. [CrossRef]
14. Belhaj, M.; Hojjati, M. Wrinkle formation during steering in automated fiber placement: Modeling and experimental verification. *J. Reinf. Plast. Compos.* **2018**, *37*, 396–409. [CrossRef]
15. Brasington, A.; Sacco, C.; Halbritter, J.; Wehbe, R.; Harik, R. Automated fiber placement: A review of history, current technologies, and future paths forward. *Compos. Part C Open Access* **2021**, *6*, 100182. [CrossRef]
16. Zhang, L.; Wang, X.; Pei, J.; Zhou, Y. Review of automated fibre placement and its prospects for advanced composites. *J. Mater. Sci.* **2020**, *55*, 7121–7155. [CrossRef]
17. Mu, Z.; Xu, W.; Liang, B. Avoidance of multiple moving obstacles during active debris removal using a redundant space manipulator. *Int. J. Control Autom. Syst.* **2017**, *15*, 815–826. [CrossRef]
18. Doan, N.C.N.; Lin, W. Optimal robot placement with consideration of redundancy problem for wrist-partitioned 6R articulated robots. *Robot. Comput. Manuf.* **2017**, *48*, 233–242. [CrossRef]
19. Wu, B.; Zhang, D.; Luo, M.; Zhang, Y. Collision and interference correction for impeller machining with non-orthogonal four-axis machine tool. *Int. J. Adv. Manuf. Technol.* **2013**, *68*, 693–700. [CrossRef]
20. Belnoue, J.P.-H.; Mesogitis, T.; Nixon-Pearson, O.J.; Kratz, J.; Ivanov, D.S.; Partridge, I.K.; Potter, K.D.; Hallett, S.R. Understanding and predicting defect formation in automated fibre placement pre-preg laminates. *Compos. Part A Appl. Sci. Manuf.* **2017**, *102*, 196–206. [CrossRef]
21. Brampton, C.J.; Wu, K.C.; Kim, H.A. New optimization method for steered fiber composites using the level set method. *Struct. Multidiscip. Optim.* **2015**, *52*, 493–505. [CrossRef]
22. Zucco, G.; Rouhi, M.; Oliveri, V.; Cosentino, E.; O'higgins, R.M.; Weaver, P.M. Continuous tow steering around an elliptical cutout in a composite panel. *AIAA J.* **2021**, *59*, 5117–5129. [CrossRef]
23. Gurdal, Z.; Tatting, B.; Wu, K. Tow-placement technology and fabrication issues for laminated composite structures. In Proceedings of the 46th AIAA/ASME/ASCE/AHS/ASC Structures, Structural Dynamics and Materials Conference, Austin, TX, USA, 18–21 April 2005. [CrossRef]
24. Debout, P.; Chanal, H.; Duc, E. Tool path smoothing of a redundant machine: Application to Automated Fiber Placement. *Comput. Des.* **2011**, *43*, 122–132. [CrossRef]

25. Qu, W.; He, R.; Cheng, L.; Yang, D.; Gao, J.; Wang, H.; Yang, Q.; Ke, Y. Placement suitability analysis of automated fiber placement on curved surfaces considering the influence of prepreg tow, roller and AFP machine. *Compos. Struct.* **2021**, *262*, 113608. [CrossRef]

26. Zu, L.; Xu, H.; Wang, H.; Zhang, B.; Zi, B. Design and analysis of filament-wound composite pressure vessels based on non-geodesic winding. *Compos. Struct.* **2019**, *207*, 41–52. [CrossRef]

27. Zu, L.; Xu, H.; Zhang, Q.; Jia, X.; Zhang, B.; Li, D. Design of filament-wound spherical pressure vessels based on non-geodesic trajectories. *Compos. Struct.* **2019**, *218*, 71–78. [CrossRef]

28. Zhang, P.; Sun, R.; Zhao, X.; Hu, L. Placement suitability criteria of composite tape for mould surface in automated tape placement. *Chin. J. Aeronaut.* **2015**, *28*, 1574–1581. [CrossRef]

# The Effects of Laser-Assisted Winding Process Parameters on the Tensile Properties of Carbon Fiber/Polyphenylene Sulfide Composites

Hongbo Geng [1], Xuewen Cao [1], Lei Zu [1,2,3], Helin Pan [1,*], Guiming Zhang [1,*], Qian Zhang [1], Jianhui Fu [1], Lichuan Zhou [1], Qiaoguo Wu [4], Xiaolong Jia [5] and Honghao Liu [1]

1 School of Mechanical Engineering, Hefei University of Technology, Hefei 230009, China; 2022020005@mail.hfut.edu.cn (H.G.); zulei@hfut.edu.cn (L.Z.)
2 Anhui Province Key Lab of Aerospace Structural Parts Forming Technology and Equipment, Hefei University of Technology, Hefei 230009, China
3 Engineering Research Center of Advanced Composite Materials Design & Application of Anhui Province, Hefei 230051, China
4 School of Civil and Hydraulic Engineering, Hefei University of Technology, Hefei 230009, China
5 State Key Laboratory of Organic-Inorganic Composites, College of Materials Science and Engineering, Beijing University of Chemical Technology, Beijing 100029, China
* Correspondence: 11625024@zju.edu.cn (H.P.); zhanggm20@hfut.edu.cn (G.Z.)

**Abstract:** Currently, there is limited research on the in situ forming process of thermoplastic prepreg tape winding, and the unclear impact of process parameters on mechanical properties during manufacturing is becoming increasingly prominent. The study aimed to investigate the influence of process parameters on the mechanical properties of thermoplastic composite materials (CFRP) using laser-assisted CF/PPS winding forming technology. The melting point and decomposition temperature of CF/PPS materials were determined using DSC and TGA instruments, and based on the operating parameters of the laser-assisted winding equipment, the process parameter range for this fabrication technology was designed. A numerical model for the temperature of laser-heated CF/PPS prepreg was established, and based on the filament winding process setup, the heating temperature and tensile strength were simulated and tested. The effects of process parameters on the heating temperature of the prepreg and the tensile strength of NOL rings were then analyzed. The non-dominated sorting genetic algorithm (NSGA-II) was employed to globally optimize the process parameters, aiming to maximize winding rate and tensile strength. The results indicated that core mold temperature, winding rate, laser power, and their interactions significantly affected mechanical properties. The optimal settings were 90 °C, 418.6 mm/s, and 525 W, achieving a maximum tensile strength of 2571.51 MPa. This study provides valuable insights into enhancing the forming efficiency of CF/PPS-reinforced high-performance engineering thermoplastic composites.

**Keywords:** CF/PPS; laser heating; winding molding; process parameters; optimization analysis

## 1. Introduction

Due to their excellent mechanical properties, carbon fiber-reinforced polymer composites (CFRP) with thermoplastic resins have become a hot research topic. Compared to common composites, thermoplastic composites offer significant advantages such as being lightweight, and having high strength, fatigue resistance, and design flexibility. Additionally, they have a longer storage life at room temperature and can be repeatedly recycled and reprocessed [1]. However, the high viscosity and melting points of thermoplastic resins pose considerable challenges during the in situ molding process, requiring careful optimization to achieve high-performance results.

In order to obtain high-performance thermoplastic composites, researchers have conducted studies on the effects of process parameters on the mechanical properties of structures for some common molding processes, such as lay-up molding [2–6]. Oromiehie E. et al. [7] examined how automated fiber placement (AFP) process parameters including compaction force, heat source temperature, and filament laying speed affect laminate interlaminar shear strength (ILSS) using a hot gas torch. They found that these parameters affected laminate fiber damage and resin-rich areas, emphasizing the necessity of selecting optimal processing conditions for mechanical qualities. Xiaolong M. et al. [8] used hand lay-up molding to study how processing conditions affected thermoplastic composites' crystalline and fracture morphology. Processing parameters affected mechanical and crystalline qualities, according to their findings. Dai G. et al. [9] studied how molding temperature, pressure, and holding time affected CF/PEEK cross-laminates' ILSS. A 20 min holding duration and 400–420 °C temperature range were ideal for molding.

Laser-assisted molding CF/PEEK laminates with different consolidation forces were examined by Qiuyu M. et al. [10]. They found that raising the pressure roller force lowered the void ratio and improved the ILSS, with an average ILSS of 49.95 MPa at 109 N, 9.08% higher than 48 N. Comer A.J. et al. [11] found that AFP laminates had lower ILSS but higher toughness than hot-pressed laminates. This was due to AFP laminates' high cooling rate and molecular chain movement restrictions. Hu J. et al. [12] examined hot-pressed flat woven carbon fiber fabric-reinforced polyether ether ketone (CFF/PEEK) thermoplastic composites. They studied how molding temperature, pressure, and holding time affect CFF/PEEK composite mechanical properties. A molding temperature of 390 °C reduced resin viscosity and increased fluidity, enabling fiber impregnation and improving composite characteristics.

Kim S.H. and Park C.K. [13] examined how process temperature affects FFR-PP resin impregnation quality. Higher temperatures enhanced resin impregnation but destroyed flax fibers, lowering product quality. Vahid Z. et al. [14] examined how processing temperature (160–240 °C) affected GF-PVC composite strength and microstructure. They found that PVC matrix degradation at 240 °C weakened the fiber-matrix link and reduced flexural characteristics to 39.3 MPa. Jonas B. et al. [15] tested process parameters on consolidation quality. Temperature affected forming quality most, followed by holding time and pressure. Fujihara K. et al. [16] found that lowering the molding temperature and holding time reduced matrix deterioration and improved bending performances in micro-woven CF/PEEK composites. According to Lessard H. et al. [6,17] increasing the mold temperature reduces the cooling rate, improving matrix crystallinity and component mechanical properties.

McCool R. et al. [18] observed that rapid cooling during forming lowers matrix crystallinity, which lowers macroscopic mechanical parameters including bending and interlaminar shear strength. Guangming Dai et al. [19] suggested an all-atom interlayer interface model for unidirectional carbon fiber-reinforced polyether ether ketone (CF/PEEK) composites. MD simulations and experimental validation showed that increasing the forming temperature improves polymer molecular mobility, interlayer diffusion, and bond strength. They also found that interlayer characteristics vary more with temperature than pressure. High-speed filament winding and direct-fired quasi-axial helical filament winding utilizing laser-assisted prepreg thermoplastic tape were shown by Funck R., and Neitzel M. [20]. Heat sources and preheating procedures for winding and molding were compared. In laser-assisted tape winding, stacking layers increase consolidation pressure and contact length, which Amin Hosseini S.M. et al. [21] investigated. Donough M.J. et al. [22] evaluated modeling approaches, material models, predictive analysis, and process parameter optimization for the in situ consolidation of automated fiber placement with thermoplastic prepreg tapes. Present limits and future directions for modeling in situ consolidation processes were reviewed. Flexural properties were used to optimize molding temperature and holding time for continuous CF/PEEK composite laminates by Fujihara K. et al. [16]. High molding temperatures and long holding durations degrade PEEK and diminish mechanical characteristics. Grouve W.J. et al. [23] examined how process factors, material

characteristics, and interlaminar bond strength affect laser-assisted tape deployment. The available experimental evidence suggests that the optimal bond quality can be achieved at high speeds and low input power when the laser beam irradiates the tape with a significant portion of the spot area, resulting in a temperature increase in the prepreg that exceeds the substrate temperature, which is below the melt temperature of the PPS.

In the aforementioned study, the automated fiber placement (AFP) technique, despite its flexibility and capacity for producing intricate structures, encountered difficulties in maintaining a continuous fiber lay on the mandrel. This resulted in the deterioration of the mechanical properties of the carbon fiber-reinforced plastic (CFRP). Furthermore, it is challenging to enhance the layup velocity when working with composites that possess cylindrical or axisymmetric geometries.

In order to mitigate these shortcomings, this paper employs the laser-assisted fiber winding and molding process of CF/PPS as the subject of investigation (shown in Figure 1). A numerical model of laser-heated CF/PPS is established based on the analysis of the thermodynamic properties of CF/PPS. NOL ring tensile tests at different process levels are carried out to explore the influence laws of process parameters on the heating temperature of CF/PPS and the tensile strength of CFRP. The process parameters were optimized using a non-dominated sorting genetic algorithm (NSGA-II) to identify the optimal combination of maximum winding rate and highest tensile strength.
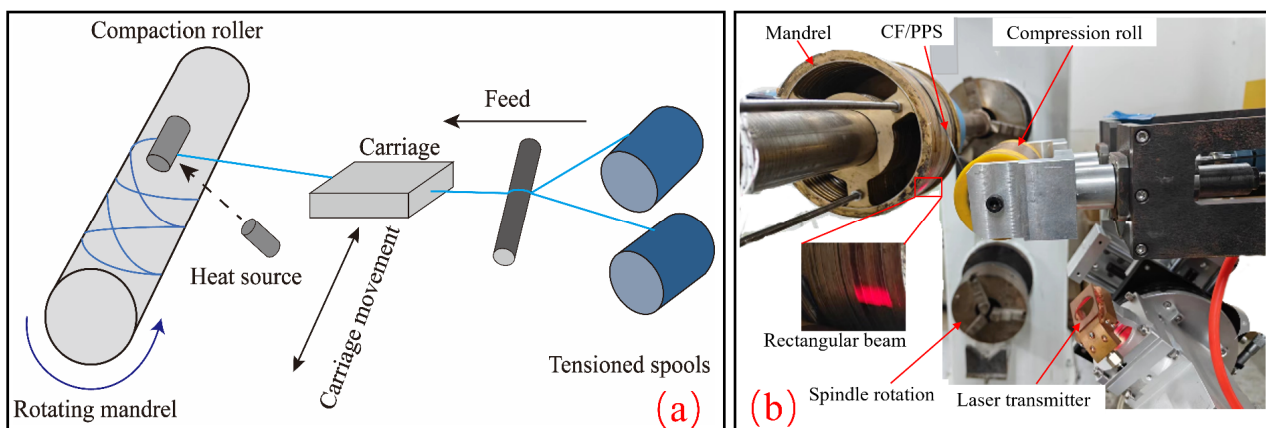


**Figure 1.** Laser-assisted fiber winding and molding process: (**a**) molding process schematic; (**b**) actual molding process diagram.

## 2. Materials and Methods

### 2.1. CF/PPS Materials and Thermal Properties Measurement

In this study, T700/PPS unidirectional thermoplastic prepreg (resin mass fraction of $34\% \pm 3\%$) produced by Jiangsu Hengbo Composite Materials Co., Ltd. (Danyang, Jiangsu, China) was selected as the material of interest. The thermodynamic properties were measured using a differential scanning calorimeter (DSC214, NETZSCH, Selb, Germany) and a thermogravimetric analyzer (TG209F1, NETZSCH, Germany). In accordance with the stipulations set forth in the GB/T 19466.5-2004 standard [24], differential scanning calorimetry (DSC) was employed to ascertain the melting point temperature of the samples across a temperature range of 25 °C to 400 °C, with varying heating rates of 5 °C/min, 10 °C/min, 15 °C/min, and 20 °C/min. According to the GB/T 19466.4-2004 standard [25], TGA testing was conducted to determine the decomposition temperature of the samples within the range of room temperature to 600 °C at the same heating rates.

### 2.2. Designing Process Solutions

In the laser-assisted CF/PPS prepreg tape winding and molding process, three principal process variables are of consequence: laser power, winding speed, and core mold temperature. Based on the results of the measurements of the melting and decomposition

points of CF/PPS, and given that it is challenging for PPS to melt and bond at lower temperatures, while higher temperatures will lead to the degradation of the PPS matrix, this study employs the response surface Box–Behnken design (BBD) to create the three-parameter, three-level winding and molding process of CF/PPS prepregs. The specific levels of the aforementioned process parameters are presented in Table 1.

**Table 1.** Parameter levels of thermoplastic prepreg winding process.

| Parameter Level | Laser Power/(W) | Winding Speed/(mm/s) | Mold Temperature/(°C) |
|---|---|---|---|
| High level | 525 | 510.5 | 90 |
| Low level | 375 | 204.2 | 30 |

Note: The maximum laser power is 1500 W; the maximum winding rate is 130 r/min.

During laser heating, the laser beam transfers thermal energy to the surface of the thermoplastic composite (CF/PPS), which then spreads via thermal conduction (Equation (1)). The energy distribution is influenced by the laser spot shape, power, movement speed, and material surface properties. The laser power density $Q$ varies over time and space, creating a dynamic heat source that rapidly increases the temperature in the laser focal area, forming a high-temperature region. To optimize computing performance and minimize processing, this work uses a two-dimensional model for simulation. Equation (2) defines the power density $Q$ of the heat source [26].

$$\rho C_p \frac{\partial T}{\partial t} = \frac{\partial}{\partial x}\left(k_x \frac{\partial T}{\partial x}\right) + \frac{\partial}{\partial y}\left(k_y \frac{\partial T}{\partial y}\right) + Q \tag{1}$$

$$Q(x, y, t) = \frac{P}{a \cdot b} \cdot \chi(x, y, t) \tag{2}$$

where $\rho$, $C_p$, $k_x$, $k_y$ denote the density, specific heat capacity, and anisotropic heat transfer coefficient of the composite material varying with temperature or degree of cure, respectively; $Q$ is the laser heating source term. $a$ and $b$ are the dimensions of the rectangular laser spot, $p$ is the laser power, and $\chi(x, y, t)$ is a function describing the spot's position and shape over time and space.

For the accurate representation of the heat transfer process, the boundary conditions for convective heat transfer between the surface of the composite material and the surrounding air must be defined (Equation (3)). The convection coefficient is then calculated using Equation (4).

$$-k\nabla T \cdot \boldsymbol{n} = h(T - T_\infty) \tag{3}$$

$$\begin{cases} Re = \frac{\rho u L}{v}, \ \mathrm{Pr} = \frac{c_p \mu}{k} \\ Nu = 0.23 Re^{0.8} Pr^{0.4}, h = \frac{Nu \cdot k}{L} \end{cases} \tag{4}$$

where $T_\infty$ is the ambient temperature and $h$ is the convective heat transfer coefficient. The Reynolds number ($Re$), Nusselt number ($Nu$), and Prandtl number (Pr) are defined as follows: $Re$ (m/s), $Nu$ (m²/s), and Pr (J/(kg·K)). The characteristic length ($L$) is in meters, viscosity (μ) in Pa/s, and thermal conductivity ($k$) in W/(m²J). CF/PPS related material properties are shown in Table 2.

**Table 2.** CF/PPS key material properties.

| $\rho$ | $k_x$ | $k_y$ | $C_p$ | Wavelength | Actual Laser Spot Size |
|---|---|---|---|---|---|
| 1570 kg/m³ | 6.0 W/(m·K) | 0.7 W/(m·K) | 1260 J/(kg·K) | 960 nm | 6.35 × 10 mm² |

*2.3. Testing of Specimens and Determination of Tensile Properties*

Following the guidelines of GB/T 1458-2023 [27], we created ring-shaped samples by wrapping CF/PPS prepreg using a DAC500 fiber laser heating system. The samples had a

diameter of $150 \pm 0.2$ mm and a breadth of $6 \pm 0.2$ mm. The tensile tests were conducted at an ambient temperature using a universal tensile testing machine (model ETM105D, Shenzhen Wance Experimental Equipment Co., Ltd., Shenzhen, China) with a loading rate of 3.0 mm/min. Every batch of samples consisted of six specimens to conduct tensile tests. The unidirectional tensile strength was determined by applying the formula specified in Equation (5).

$$\sigma_t = \frac{P_b}{2b \cdot h} \tag{5}$$

where $\sigma_t$ reinforced composite tensile strength (unit: MPa); $P_b$ breaking load (unit: N); $b$ specimen width (unit: mm); and $h$ specimen thickness (unit: mm).

*2.4. Methods for Optimization*

This study employs the non-dominated sorting genetic algorithm (NSGA-II) to enhance the laser-assisted prepreg tape winding process, addressing the issues of nonlinearity and discontinuity in the design space. The algorithm maximizes tensile strength and rotation rate, thereby demonstrating superior global solution capability and efficiency compared to traditional genetic algorithms.

The optimization process comprises several steps. Initially, objectives and variables must be defined. Then, the population is initialized with combinations of laser power, rotational speed, mandrel temperature, and winding stress. Subsequently, a mathematical model is developed to predict tensile and shear strengths. Finally, the optimization is performed to identify the optimal values. Subsequently, the most efficacious combinations are identified and displayed. The objective of this study is to optimize the material's tensile strength by adjusting the laser power, rotational speed, mandrel temperature, and winding tension in accordance with Equations (6) and (7).

$$Min[-f_{Tensile} - WR] \tag{6}$$

$$s.t. \begin{cases} 375\,W \leq LP \leq 525\,W \\ 204.2\,\text{mm/s} \leq WR \leq 510.5\,\text{mm/s} \\ 30\,°C \leq MT \leq 90\,°C \end{cases} \tag{7}$$

where $f_{Tensile}$ is the maximum tensile strength objective function; $WR$ is the rotational speed; $LP$ is the laser power; and $MT$ is the core mold temperature.

## 3. Results and Discussion

*3.1. CF/PPS Melting Point and Thermal Decomposition Temperature*

Differential scanning calorimetry research demonstrates that the melting point temperature of composites made from carbon fiber-reinforced polyphenylene sulfide increases in proportion to the rate at which they are heated. More precisely, the temperature at which the substance melted increased from 246 °C to 259 °C when the pace at which it was heated was increased from 5 °C/min to 20 °C/min, as shown in Figure 2. The thermal decomposition temperatures of CF/PPS composites also exhibit variations depending on the heating rate, as established through TGA testing. Decomposition initiated within the temperature range of around 450 °C to 505 °C, with heating rates ranging from 5 °C/min to 20 °C/min, as depicted in Figure 3.

The results suggest that the melting point and thermal breakdown temperature of CF/PPS composites are influenced by the pace at which the temperature is increased. This study establishes the CF/PPS melting point at 246 °C and the decomposition temperature at 450 °C to verify the quality of laser-assisted fiber winding molded parts and determine the forming processing window.
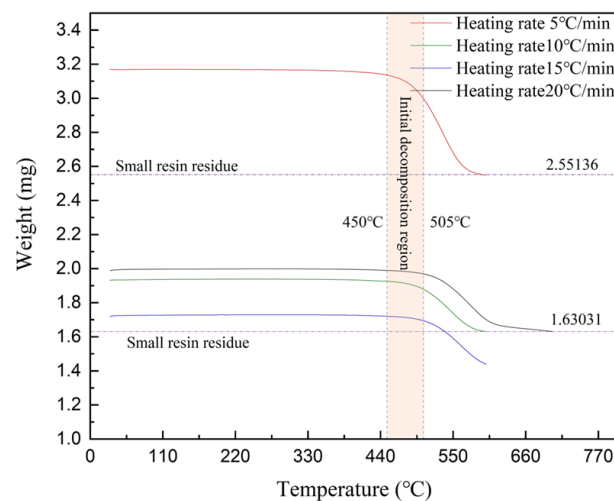
**Figure 2.** The melting point of CF/PPS under different heating rates.
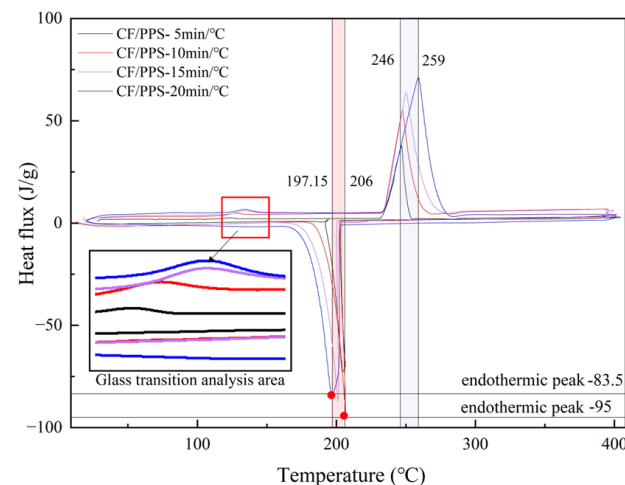


**Figure 3.** Thermal decomposition temperature of CF/PPS under different heating rates.

### 3.2. Computational Modeling of Laser-Induced Heating in CF/PPS

The present work utilized the COMSOL Multiphysics finite element software Version 6.2 to describe the laser-assisted heating and molding process for CF/PPS winding. The simulation entailed the emission of a laser beam in a homogeneous manner from a rectangular surface, which then proceeded to irradiate both the prepreg tape and the substrate.

It is notable that the power and winding speed of the laser and winding apparatus are expressed as percentages. To ensure consistency with the control of process parameters in actual production, the laser power and winding speed parameters in the BBD scheme are also expressed as percentage values. The winding rates of 20%, 35%, and 50% correspond to linear speeds of 204.2 mm/s, 357.35 mm/s, and 510.5 mm/s, respectively. The convection coefficients for these rates were calculated using Equation (4). The company conducted tests on the laser, which had a power output of 1500 W, and irradiated an area measuring 20 mm × 10 mm. Analysis revealed that 31.75% of the entire beam surface area, equivalent to 6.35 mm × 10 mm, was responsible for effectively heating the prepreg material. Therefore, the laser's starting intensity was determined to be $5.95 \times 10^5$ W/mm$^2$, $7.14 \times 10^5$ W/mm$^2$, and $8.33 \times 10^5$ W/mm$^2$ at the various rates. The heating duration for the core mold was determined by considering the starting temperature of the solid components, the rate at which the winding was carried out, and the size of the specific area being heated. The heating times corresponding to the winding rates of 20%, 35%, and 50% were 49 ms, 28 ms, and 20 ms, respectively.

As illustrated in Figure 4, the CF/PPS prepreg tape is capable of reaching a maximum local heating temperature of 332 °C under specific conditions: a laser power of 30%, a winding rate of 35%, and a core mold temperature of 60 °C. It is crucial to acknowledge that the aforementioned temperature does not account for any potential reduction at the point of contact. A series of simulations were conducted in order to investigate the laser-assisted fiber winding process, with the variables being the laser power, winding rate, and core mold temperature. The Box–Behnken Design response surface method was employed to ascertain the parameter combinations that result in optimal molding effectiveness. The results of the CF/PPS heating temperature calculations are presented in Table 3 for the reader's convenience.
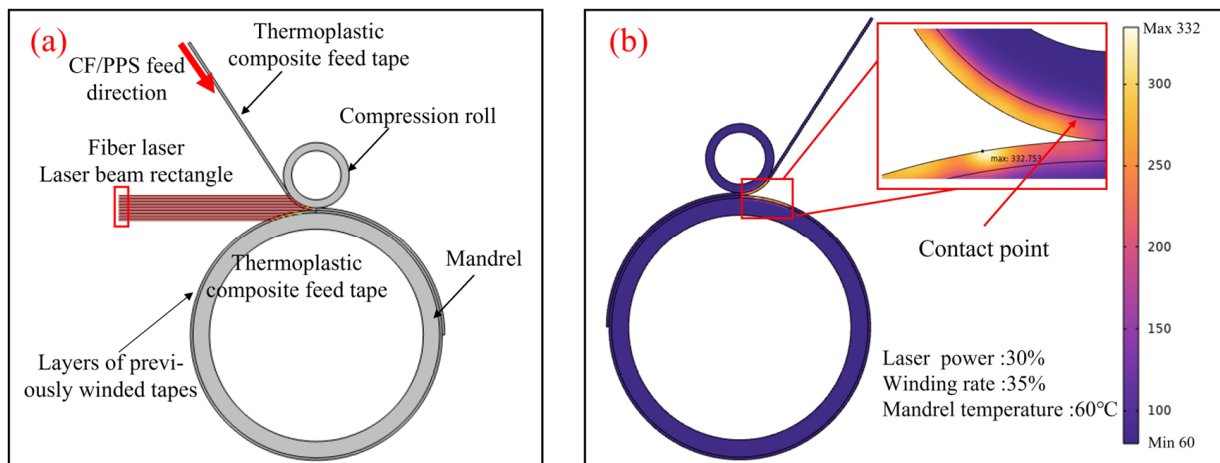


**Figure 4.** Simulation of laser-assisted CF/PPS wrap-around molding process. (**a**) Numerical modeling; (**b**) temperature analysis.

**Table 3.** CF/PPS heating temperature and NOL ring tensile test results.

| Order | Laser Power Percentage/% | Percent Winding Rate/% | Mandrel Heating Temperature/°C | Heating Temperature/°C | Tensile Strength/MPa | Coefficient of Variation% |
|---|---|---|---|---|---|---|
| 1 | 30 | 50 | 90 | 307.40 | 2194.77 | 9.70 |
| 2 | 35 | 20 | 60 | 511.39 | 1633.83 | 7.94 |
| 3 | 35 | 50 | 60 | 310.30 | 2342.89 | 3.58 |
| 4 | 25 | 35 | 90 | 320.63 | 2308.31 | 7.66 |
| 5 | 30 | 35 | 60 | 332.75 | 2352.64 | 6.98 |
| 6 | 25 | 35 | 30 | 260.63 | 2185.23 | 3.50 |
| 7 | 30 | 35 | 60 | 332.75 | 2322.68 | 6.17 |
| 8 | 30 | 20 | 30 | 419.77 | 1656.85 | 8.16 |
| 9 | 35 | 35 | 90 | 404.88 | 2558.46 | 6.61 |
| 10 | 25 | 50 | 60 | 244.50 | 1729.04 | 4.65 |
| 11 | 30 | 20 | 90 | 479.77 | 1773.57 | 9.61 |
| 12 | 30 | 35 | 60 | 332.75 | 2298.38 | 7.69 |
| 13 | 25 | 20 | 60 | 388.14 | 1849.45 | 9.56 |
| 14 | 30 | 35 | 60 | 332.75 | 2299.93 | 7.61 |
| 15 | 35 | 35 | 30 | 344.88 | 2492.17 | 8.09 |
| 16 | 30 | 35 | 60 | 332.75 | 2428.98 | 7.08 |
| 17 | 30 | 50 | 30 | 247.40 | 2029.85 | 8.28 |

Figure 5 exhibits the graphical representation of the response surface and contour plots obtained from the computer simulations of laser-induced heating on CF/PPS material. These simulations were conducted using the BBD process scheme. The charts investigate the influence of various parameters, such as laser power, winding rate, and core mold temperature, on the surface temperature of CF/PPS. In Figure 5a, when the winding rate remains constant, the surface temperature shows a nearly linear increase with laser power. The temperature reaches its highest point at 35% laser power. On the other hand, when the laser power remains constant, the effect of the winding rate on the surface temperature

demonstrates a progressive rise. Figure 5d demonstrates that the contour plot depicting the relationship between laser power and winding rate is not perfectly circular. The increased ellipticity suggests a substantial interaction between these two parameters.
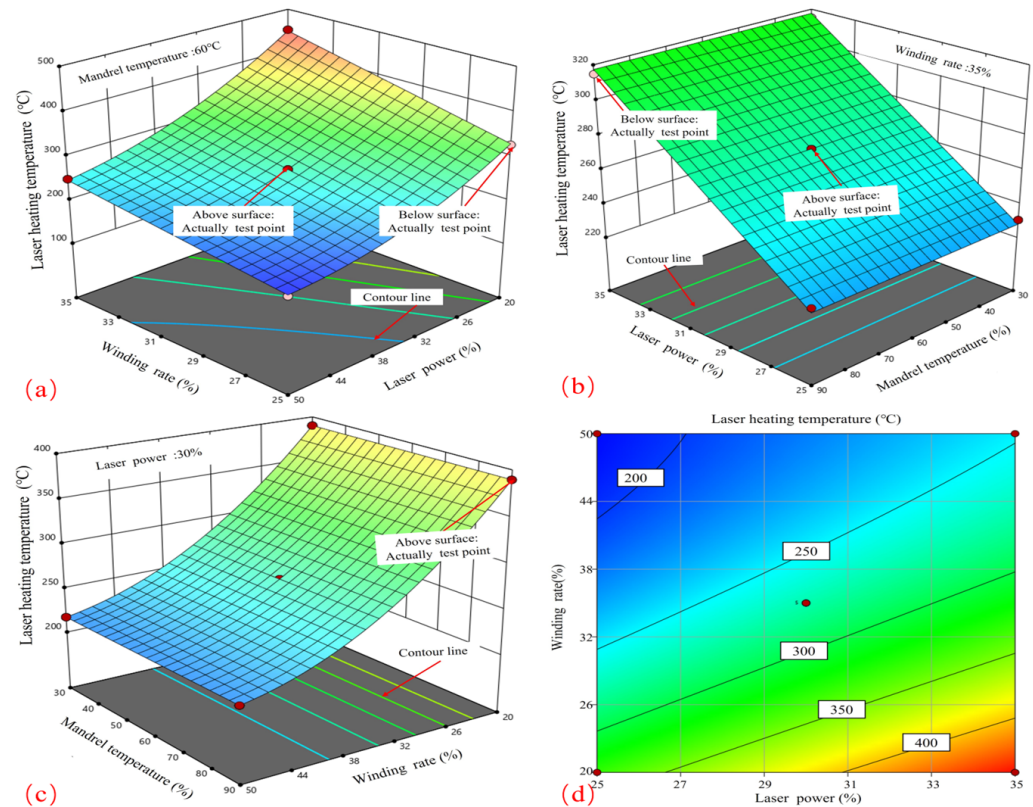


**Figure 5.** Process coupling effect law on CF/PPS prepreg strip temperature. (**a**) Effect of LP-WR interaction on laser heating temperature; (**b**) Effect of LP-MT interaction on laser heating temperature; (**c**) Effect of WR-MT interaction on laser heating temperature; (**d**) Contours of LP-WR interaction on laser heating temperature.

Figure 5b demonstrates that when the core mold temperature remains constant, the surface temperature increases linearly when the laser power is increased, reaching its highest point at 35% power. Figure 5c demonstrates that the impact of winding rate on surface temperature becomes more significant as the core mold temperature remains constant, but the effect of core temperature increases linearly at a consistent winding rate. To attain the maximum surface temperature, it is important to employ a combination of increased laser power and a swifter winding rate. Considering that the CF/PPS material starts to degrade at a minimum temperature of 450 °C, it is essential to carefully control these parameters to avoid the surface temperature going beyond this limit, particularly when using greater winding rates.

### 3.3. Influence of Process Parameters on Tensile Strength of CF/PPS Composites

3.3.1. Examination of Response Surface Test Results

The results of the NOL ring tests' tensile strength are displayed in Table 3. In addition, the coefficient of variation (i.e., the ratio of the standard deviation to the mean) was obtained by calculating the data from six valid tests under each group of process combinations. The results show that the maximum coefficient of variation is about 10% and the minimum coefficient of variation is about 4%. Thus, it can be seen that the overall experimental data have a small degree of dispersion and the test data have good reliability. The findings were examined using a comprehensive binomial regression approach with Design Expert 10.0 software, resulting in the creation of a dependable predictive model (refer to Table 4).

Figure 6 presents comprehensive information regarding the sample, the methodology employed for testing, and the typical modes of failure. Furthermore, it provides a visual representation of the distribution of projected tensile strength values in comparison to the actual values. The strong correlation and linear association between these values indicate that the prediction model obtained from the response surface analysis is highly reliable. The correspondence between the model predictions and the actual experimental results is exceptionally strong and reliable.

**Table 4.** Response surface regression model.

| | Forecasting Function | Mean Square | F-Value | *p*-Value |
|---|---|---|---|---|
| Stretch fitting equation | $f1 = 2017.18 - 99.38x_1 + 71.48x_2 2.08x_3 + 2.76x_1x_2 - 0.061x_1x_3 - 0.027x_2x_3 + 0.51x_1{}^2 - 2.06x_2{}^2 + 0.04x_3{}^2$ | $1.634 \times 10^5$ | 52.84 | <0.0001 |
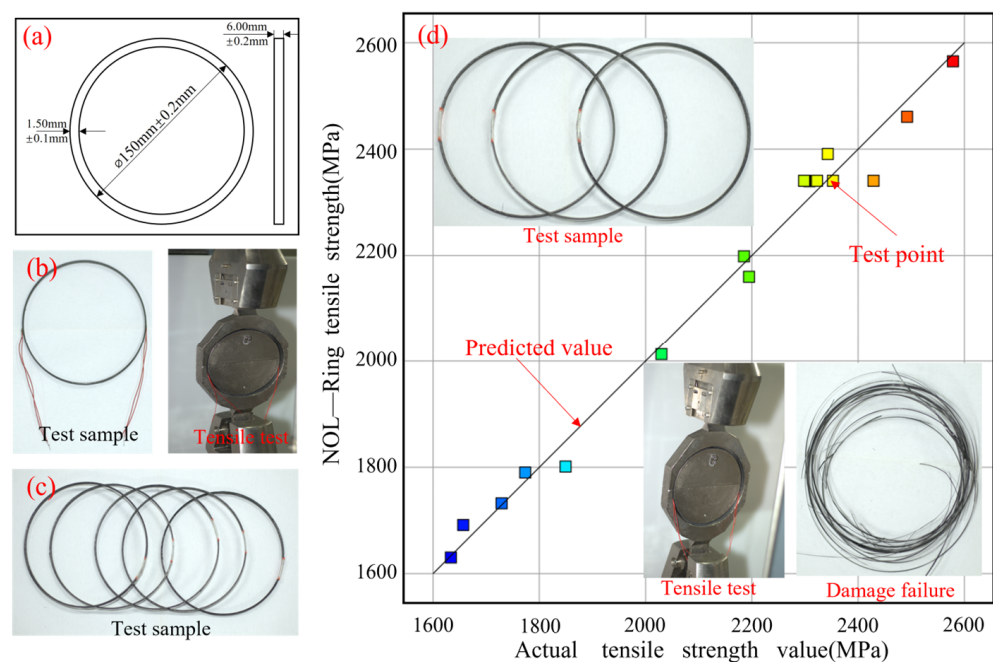


**Figure 6.** Distribution of predicted and actual values. (**a**) NOL ring standard sample size; (**b**) NOL ring standardized samples and stretching process; (**c**) NOL ring standard sample; (**d**) Typical damage states, tensile values, and predicted results for NOL ring stretching, where the color of the test point changes from blue to red representing progressively larger values.

### 3.3.2. Effect of Single Factors on Tensile Strength

As illustrated in Figure 7a, there is a linear correlation between laser power and tensile strength. The data indicate that an increase in laser power results in an enhancement of tensile strength. At a laser power of 25%, the tensile strength is observed to be 2038.31 MPa. A 35% increase in power results in a tensile strength of 500 MPa. As a consequence of the elevated laser intensity, the melting of the resin and the bonding of the fiber to the resin are enhanced, thereby reinforcing the composite.

Figure 7b depicts a parabolic relationship between winding rate and tensile strength. At a winding rate of 20%, the tensile strength is observed to be 250 MPa. At a winding rate of 35%, the tensile strength reaches a maximum of 400 MPa, subsequently declining to 200 MPa at a winding rate of 50%. Higher winding rates initially result in improved fiber alignment and resin distribution, leading to enhanced tensile strength. The application of high winding rates has the potential to increase fiber strain or reduce resin penetration, which in turn may affect the strength of the composite material.
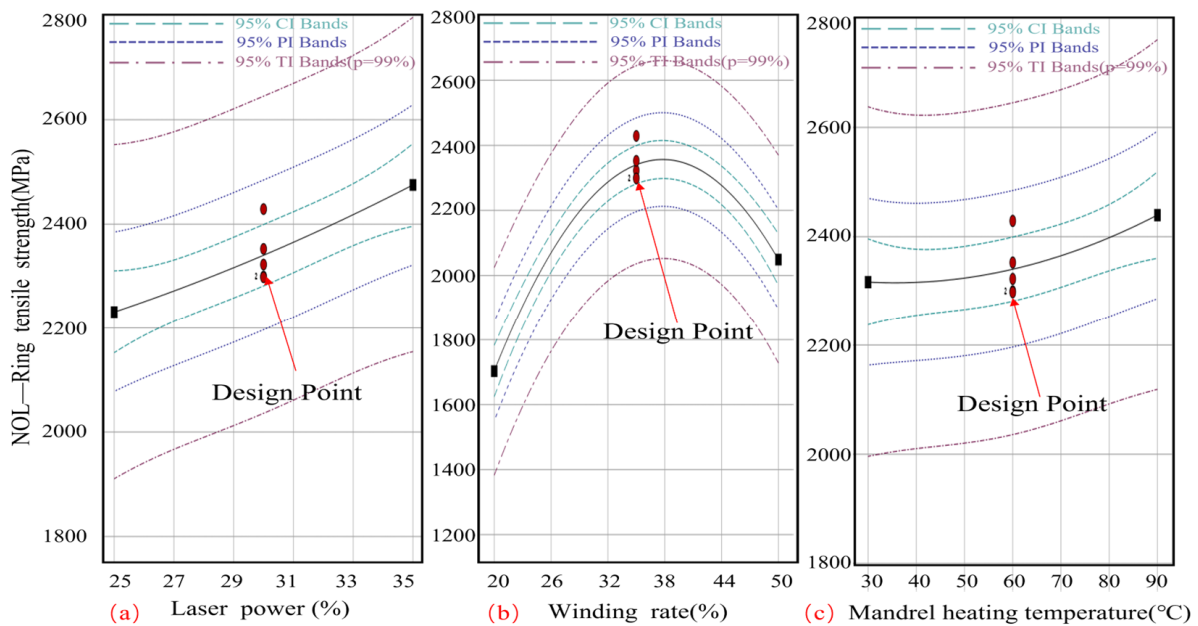
**Figure 7.** Influence law of single process parameter variation on tensile strength of NOL ring. (**a**) Curve of the effect of LR on the tensile strength of NOL rings; (**b**) Curve of the effect of WR on the tensile strength of NOL rings; (**c**) Curve of the effect of MT on the tensile strength of NOL rings.

Figure 7c exhibits a concave core mold temperature-tensile strength relationship. The tensile strength is 200 MPa at 30 °C and 350 MPa at 90 °C. Maintaining an optimal core mold temperature is crucial for ensuring homogeneous resin melting and curing, which in turn facilitates enhanced fiber–resin contact. However, elevated temperatures can result in resin degradation, while insufficient temperatures may impede the melting process, thereby impairing the mechanical qualities of the composite. Additionally, the figure illustrates 95% confidence intervals, forecasts, and tolerance intervals as dotted lines. The bands illustrate the probable range of actual and forecast values, confirming the statistical significance of the observed trends and demonstrating the dependability and accuracy of the data.

### 3.3.3. Process Parameter Interaction

Figure 8 shows the response surface and contour plots that illustrate the relationship between laser power and winding rate in relation to tensile strength. Figure 8a demonstrates that when the laser power is maintained at a constant level, the relationship between the winding rate and tensile strength exhibits a parabolic curve, reaching its maximum value at 35%. Conversely, when the winding rate is maintained at a constant level, the tensile strength will increase in proportion to the laser power, although the rate of growth will be less pronounced. Therefore, in order to achieve the highest possible tensile strength, the optimal combination of process parameters is a winding rate of 35% in conjunction with a higher laser power, both of which fall within the specified process boundaries.

Figure 8b depicts elliptical contours, which indicate a significant correlation between winding tension and curing temperature. The contours display a higher density in proximity to the winding rate axis in comparison to the laser power axis, indicating that the winding rate exerts a more significant influence on tensile strength than the laser power. This finding is in accordance with the observed effects of laser heating on the surface temperature of the core mold. In addition, the results are consistent with the effect of molding rate on the porosity of the product and its quality during CF/PPS placement [28].
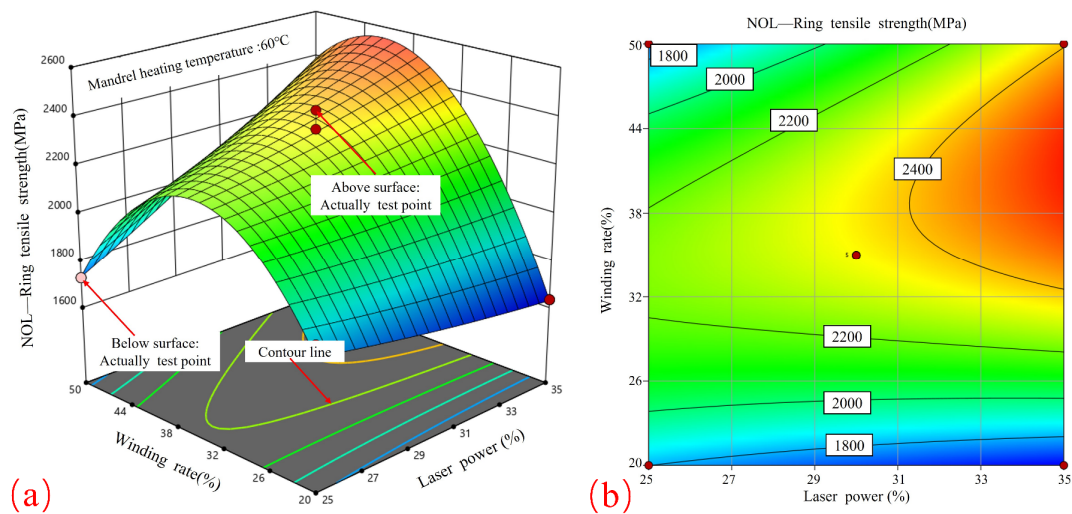
**Figure 8.** Effect of laser power and winding rate on tensile strength: (**a**) response surface; (**b**) contour plot.

Figure 9 illustrates the response surface and contour plots that elucidate the influence of laser power and core mold temperature on tensile strength. Figure 9a illustrates that, when the core mold temperature is maintained at a constant level, the influence of laser power on tensile strength exhibits a nearly linear increase, reaching its maximum at 35%. When the laser power is maintained at a constant level, the impact of the core mold temperature on the tensile strength demonstrates a gradual and consistent increase, reaching its peak at 90 °C. Therefore, the optimal process parameters for attaining the highest tensile strength are an increased laser power and an elevated core mold temperature. The contour plots in Figure 9b exhibit a nearly circular shape, indicating that the relationship between laser power and core mold temperature is relatively insignificant.
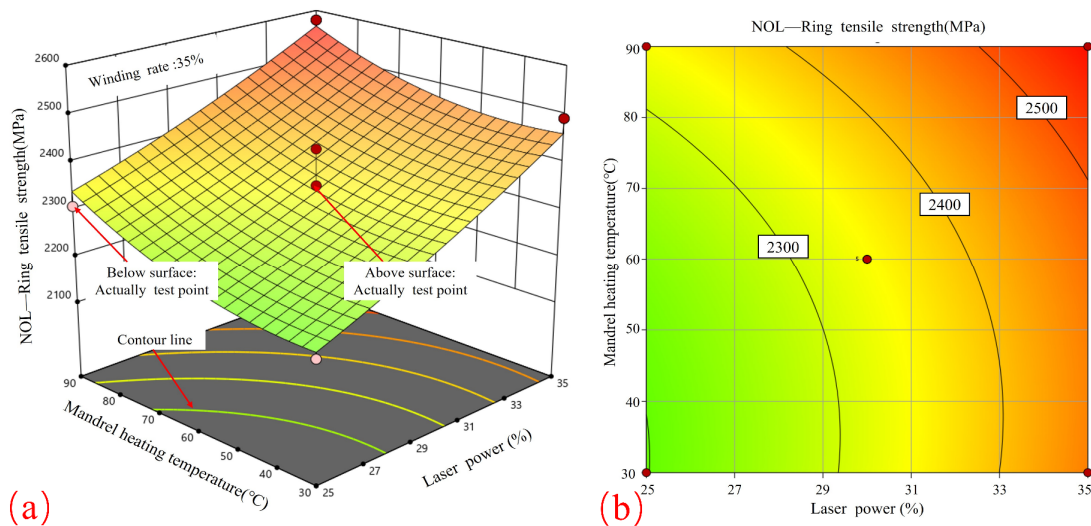


**Figure 9.** Effect of laser power and core mold temperature on tensile strength: (**a**) response surface; (**b**) contour plot.

Figure 10 depicts the impact of the winding rate and core mold temperature on tensile strength, as illustrated through the use of response surface and contour plots. Figure 10a illustrates that when the winding rate is maintained at a constant level, the tensile strength demonstrates a predominantly linear increase with the core mold temperature, reaching its maximum value at 90 °C. Conversely, when the core mold temperature is held constant,

the effect of the winding rate on tensile strength displays a parabolic pattern, with an initial increase followed by a decrease.
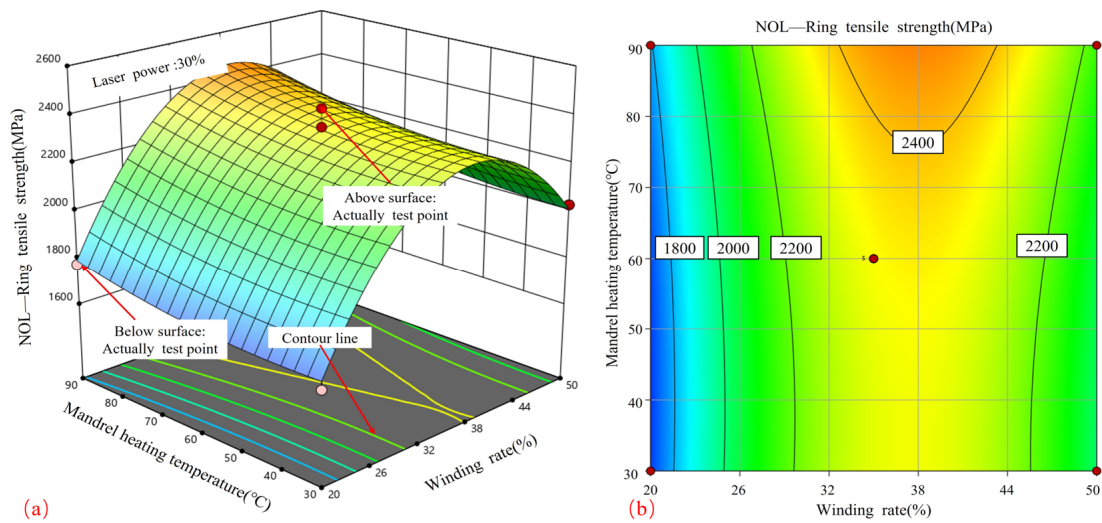


**Figure 10.** Effect of winding rate and core mold temperature on tensile strength; (**a**) response surface; (**b**) contour plot.

Figure 10b illustrates elliptical contour graphs, which indicate a significant correlation between the winding rate and core mold temperature. The greater density of contour lines surrounding the winding rate axis in comparison to those situated near the core mold temperature axis suggests that the winding rate exerts a more pronounced influence on tensile strength than the core mold temperature. In order to achieve the highest possible tensile strength, it is recommended that a curing temperature of 90 °C and a winding rate ranging from 33% to 45% be employed. Tensile strengths in excess of 2400 MPa were attained using these values.

*3.4. Composite Process Optimization*

3.4.1. Process Parameter Significance Analysis

An analysis of variance and a correlation analysis were conducted to evaluate the impact of laser-assisted winding and molding process parameters on the tensile strength of NOL rings. The results are presented in Table 5, which demonstrates that the effects of different process parameters on tensile strength vary. The results indicate that MT, WR, and LP are significant parameters ($p < 0.05$) for the tensile strength model. The influence is rated as being greatest for WR, followed by LP and then MT. The correlation values for the tensile strength of the NOL ring are 0.28 for LP, 0.4 for WR, and 0.14 for MT.

**Table 5.** Analysis of variance results of NOL ring tensile strength fitting model.

| Model | Tensile Strength/MPa | | Correlation Coefficient |
|---|---|---|---|
| | **F-Value** | **$p$-Value** | |
| LP | 38.45 | 0.0004 | 0.28 |
| WR | 77.30 | <0.0001 | 0.40 |
| MT | 9.75 | 0.0168 | 0.14 |
| LP*WR | 55.62 | 0.0001 | 0.51 |
| LP*MT | 0.11 | 0.7505 | 0.22 |
| WR*MT | 0.19 | 0.6778 | 0.36 |
| $LP^2$ | 0.22 | 0.6515 | --- |
| $WR^2$ | 293.78 | <0.0001 | --- |
| $MT^2$ | 1.94 | 0.2064 | --- |

This ranking is a consequence of the direct correlation between winding speed and the heating time of the CF/PPS at a constant laser power. A reduction in winding speed results in an extended heating period, which increases the temperature of the prepreg tape and may ultimately approach the pyrolysis temperature of the thermoplastic resin PPS. This can lead to a weakening of the bond. Conversely, a higher winding speed reduces the heating time, preventing the surface temperature from reaching the melt temperature and consequently reducing the adhesion of the prepreg layer, which in turn reduces the tensile strength of the NOL ring. Moreover, fluctuations in laser power have a lesser impact than variations in winding rate due to the constrained process window.

The correlation coefficient for the interaction between LP and WR is 0.51, indicating that enhancing this interaction could significantly enhance material strength. In order to achieve the greatest enhancement in material properties, it is essential to devote considerable attention to the winding rate and its synergistic effect with laser power during process optimization.

### 3.4.2. Molding Process Parameter Validation and Optimization

For the optimization procedure, Isight's non-dominated sorting genetic algorithm (NSGA-II) was employed. The parameters were as follows: a variance distribution index of 20.0, a crossover chance of 0.9, a population size of 60, and several generations of 100. In ensuring the highest winding rate and tensile strength, the optimization results after 6001 iterations show a laser power of 525 W, a winding rate of 424.6 mm/s, a mandrel temperature of 90.0 °C, and a tensile strength of 2647.8 MPa.

The Pareto fronts for laser power vs winding rate, laser power versus core temperature, and core temperature versus winding rate are shown in Figure 11a, 11b, and 11c, respectively. The impacts of these parameter combinations on tensile strength and the optimization process are clearly shown by these figures and projections on the xy and xz planes. The results show that by carefully modifying these process parameters, the material's tensile strength may be greatly increased.
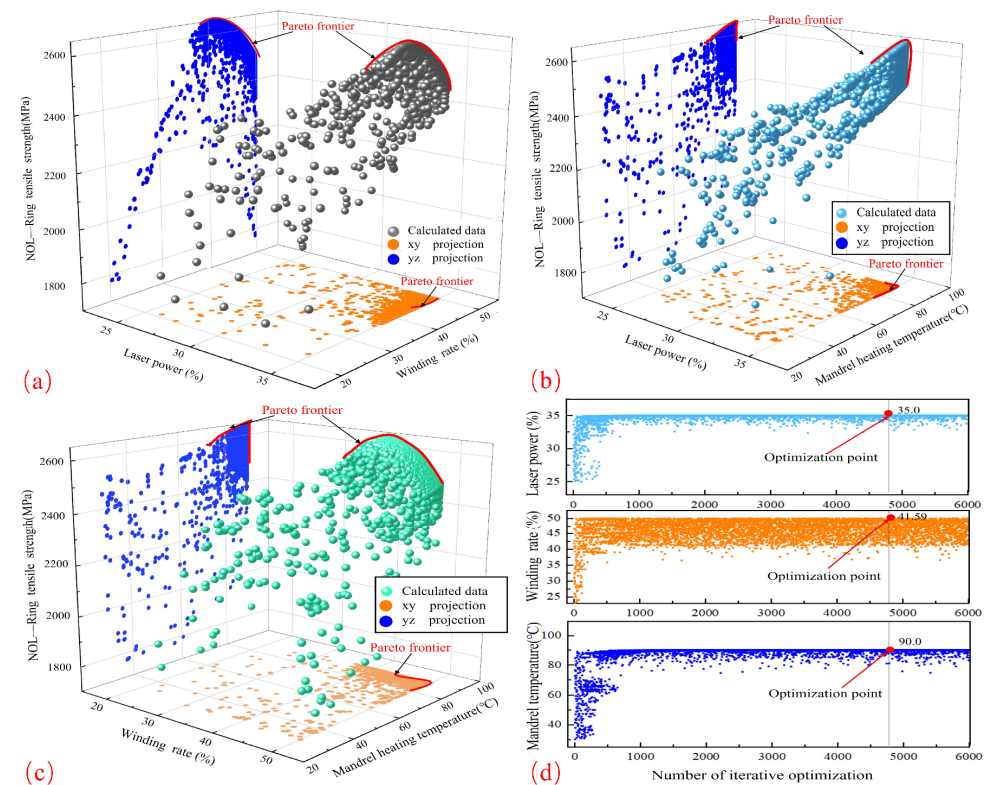


**Figure 11.** Pareto frontiers for the response variables: (**a**) LP vs. WR vs. NTS; (**b**) LP vs. MT vs. NTS; (**c**) WR vs. MT vs. NTS; (**d**) LP, WR, and MT iterations.

The laser power, winding rate, and mandrel temperature were tuned, and experiments were carried out using these optimized parameters to confirm the accuracy of the tensile strength predictions for NOL rings produced by response surface optimization. Table 6 records the test outcomes. An excellent fit of the model is indicated by the minor relative errors in the tensile strength between the actual and projected values (3.2% vs. 2.8%, respectively).

**Table 6.** Optimization results and comparison of non-optimal solutions.

|  | Laser Power Percentage/% | Percent Winding Rate/% | Mandrel Heating Temperature/°C | Tensile Strength/MPa | Relative Error/% |
| --- | --- | --- | --- | --- | --- |
| Optimization solution | 35.0 | 41.6 | 90.0 | 2647.80 | —— |
| Measured value#1 | 35.0 | 41.0 | 90.0 | 2564.23 | 3.2% |
| Measured value#2 | 35.0 | 41.0 | 90.0 | 2571.51 | 2.8% |

The results of the experiment show that, under optimized conditions, the tensile properties of NOL rings meet the expected levels, indicating the validity of the optimal process parameters determined by the satisfaction function method. Any detected differences could be the result of flaws in the experimental data or constraints in the optimization model. In real-world applications, the optimization model algorithm, the experimental design technique, or a larger sample size can all be improved to increase the dependability of the optimization results.

## 4. Conclusions

To enhance the tensile properties of thermoplastic composites, this study explored the relationship between laser-assisted fiber winding process parameters—laser power, winding rate, and core mold temperature—and the tensile strength of NOL rings using the Box–Behnken design response surface methodology. A numerical model was developed to analyze the influence of process variables on CF/PPS surface temperature during molding. Additionally, a mathematical model was constructed to predict the mechanical properties of NOL rings, identifying significant interactions between different process parameters through response surface and contour plots. Experimental validation confirmed the optimization results, demonstrating that the optimized process parameters significantly improved the tensile strength of NOL rings. Specifically, the optimal parameters were 525 W laser power, 424.7 mm/s winding speed, and 90 °C core mold temperature. The tensile strength of the optimized NOL ring reached 2647.80 MPa, significantly higher than the non-optimized result, underscoring the effectiveness and practicality of this optimization method.

The principal findings can be summarized as follows:

1. The objective of this study is to investigate the influence of process parameters on surface temperature. The surface temperature of the prepreg tape is significantly affected by the laser power, winding rate, and core mold temperature. The order of influence is as follows: the interaction between laser power and winding rate is the most significant factor, followed by winding rate, laser power, and core mold temperature.

2. The effect of process parameters on tensile strength is as follows: The tensile strength of NOL rings is significantly influenced by the laser power, winding rate, and core mold temperature. The response surface and contour plots revealed a correlation coefficient of 0.51 for the interaction between laser power and winding rate, indicating that optimizing their combination is crucial for enhancing tensile strength.

3. The optimization results are as follows: The optimized parameters, which consisted of 35% laser power (525 W), 41% winding rate (418.6 mm/s), and 90 °C core mold temperature, resulted in the highest tensile strength for NOL rings, exhibiting a significant improvement over the unoptimized process parameters.

## References

1. Van Hoa, S.; Duc Hoang, M.; Simpson, J. Manufacturing procedure to make flat thermoplastic composite laminates by automated fiber placement and their mechanical properties. *J. Thermoplast. Compos. Mater.* **2017**, *30*, 1693–1712. [CrossRef]

2. Wanigasekara, C.; Oromiehie, E.; Swain, A.; Prusty, B.G.; Nguang, S.K. Machine learning based predictive model for AFP-Based unidirectional composite laminates. *IEEE Trans. Ind. Inform.* **2020**, *16*, 2315–2324. [CrossRef]

3. Oromiehie, E.; Garbe, U.; Gangadhara Prusty, B. Porosity analysis of carbon fiber reinforced polymer laminates manufactured using automated fiber placement. *Compos. Mater.* **2020**, *54*, 1217–1231. [CrossRef]

4. Qureshi, Z.; Swait, T.; Scaife, R.; El-Dessouky, H.M. In situ consolidation of thermoplastic prepreg tape using automated tape placement technology: Potential and possibilities. *Compos. Part B Eng.* **2014**, *66*, 255–267. [CrossRef]

5. Zheng, B.; Li, M.; Deng, T.; Zhou, H.; Huang, Z.; Zhou, H.; Li, D. Process-structure-property relationships of thermoformed woven carbon-fiber-reinforced polyether ether ketone composites. *Polym. Compos.* **2019**, *40*, 3823–3834. [CrossRef]

6. Lessard, H.; Lebrun, G.; Benk, A.; Pham, X.T. Influence of process parameters on the thermostamping of a $[0/90]_{12}$ carbon/polyether ether ketone laminate. *Compos. Part A Appl. Sci. Manuf.* **2015**, *70*, 59–68. [CrossRef]

7. Oromiehie, E.; Gain, A.K.; Prusty, B.G. Processing parameter optimisation for automated fibre placement (AFP) manufactured thermoplastic composites. *Compos. Struct.* **2021**, *72*, 114223. [CrossRef]

8. Ma, X.L.; Wen, L.H.; Wang, S.Y.; Xiao, J.Y.; Li, W.H.; Hou, X. Inherent relationship between process parameters, crystallization and mechanical properties of continuous carbon fiber reinforced PEEK composites. *Def. Technol.* **2023**, *24*, 269–284. [CrossRef]

9. Dai, G.; Zhan, L.; Guan, C.; Huang, M. The effect of moulding process parameters on interlaminar properties of CF/PEEK composite laminates. *High Perform. Polym.* **2020**, *32*, 835–841. [CrossRef]

10. Miao, Q.; Dai, Z.; Ma, G.; Niu, F.; Wu, D. Effect of consolidation force on interlaminar shear strength of CF/PEEK laminates manufactured by laser-assisted forming. *Compos. Struct.* **2021**, *266*, 113779. [CrossRef]

11. Comer, A.J.; Ray, D.; Obande, W.O.; Jones, D.; Lyons, J.; Rosca, I.; O'higgins, R.M.; McCarthy, M.A. Mechanical characterisation of carbon fibre–PEEK manufactured by laser-assisted automated-tape-placement and autoclave. *Compos. Part A Appl. Sci. Manuf.* **2015**, *69*, 10–20. [CrossRef]

12. Hu, J.; Zhang, H.; Li, S.; Ji, C.; Chen, S.; Zhou, Z.; Wang, B. Process parameter–mechanical property relationships and influence mechanism of advanced CFF/PEEK thermoplastic composites. *Polym. Compos.* **2022**, *43*, 5119–5132. [CrossRef]

13. Kim, S.H.; Park, C.K. Direct impregnation of thermoplastic melt into flax textile reinforcement for semi-structural composite parts. *Ind. Crops Prod.* **2017**, *95*, 651–663. [CrossRef]

14. Vahid, Z.; Moslemi Naeini, H.; Bahramian, A.R.; Abdollahi, H.; Behravesh, A.H. Investigation of the effect of processing temperature on the elastic and viscoelastic properties of PVC/fiberglass composite laminates. *Modares Mech. Eng.* **2016**, *15*, 9–16.

15. Jonas, B.; Roshan, S. Effect of processing parameters on consolidation quality of GF/PP commingled yarn based composites. *J. Thermoplast. Compos. Mater.* **2000**, *13*, 292–313.

16. Fujihara, K.; Huang, Z.; Ramakrishna, S.; Hamada, H. Influence of processing conditions on bending property of continuous carbon fiber reinforced PEEK composites. *Compos. Sci. Technol.* **2004**, *64*, 2525–2534. [CrossRef]

17. McCool, R.; Murphy, A.; Wilson, R.; Jiang, Z.; Price, M.; Butterfield, J.; Hornsby, P. Thermoforming carbon fibre-reinforced thermoplastic composites. *Proc. Inst. Mech. Eng. Part L J. Mater. Des. Appl.* **2012**, *226*, 91–102. [CrossRef]

18. Gao, S.L.; Kim, J.K. Cooling rate influences in carbon fibre/PEEK composites. Part 1. Crystallinity and interface adhesion. *Compos. Part A Appl. Sci. Manuf.* **2015**, *31*, 517–530. [CrossRef]

19. Dai, G.; Zhan, L.; Ma, B.; Guan, C.; Huang, M. Effect of process parameters on interlaminar properties of thermoplastic composite: Molecular dynamics simulation and experimental verification. *Polymer* **2023**, *280*, 126062. [CrossRef]

20. Funck, R.; Neitzel, M.P. Improved thermoplastic tape winding using laser or direct-flame heating. *Compos. Part A Appl. Sci. Manuf.* **1995**, *6*, 189–192. [CrossRef]

21. Hosseini, S.A.; Baran, I.; van Drongelen, M.; Akkerman, R. On the temperature evolution during continuous laser-assisted tape winding of multiple C/PEEK layers: The effect of roller deformation. *Int. J. Mater. Form.* **2021**, *14*, 203–221. [CrossRef]

22. Donough, M.J.; Shafaq, S.; John, N.A.; Philips, A.W.; Prusty, B.G. Process modelling of In-situ consolidated thermoplastic composite by automated fibre placement a review. *Compos. Part A Appl. Sci. Manuf.* **2022**, *163*, 107179. [CrossRef]

23. Grouve, W.J.; Warnet, L.L.; Rietman, B.; Visser, H.A.; Akkerman, R. Optimization of the tape placement process parameters for carbon–PPS composites. *Compos. Part A Appl. Sci. Manuf.* **2013**, *50*, 44–53. [CrossRef]

24. *GB/T 19466.5-2004*; Plastics Thermal Analysis Part 5: Differential Scanning Calorimetry (DSC). National Standard of the People's Republic of China: Beijing, China, 2004.

25. *GB/T 19466.4-2004*; Plastics Thermal Analysis Part 4: Thermogravimetric Analysis (TGA). National Standard of the People's Republic of China: Beijing, China, 2004.

26. Esselink, F.S.; Hosseini, S.M.; Baran, I.; Akkerman, R. Optimization of laser-assisted tape winding/placement process using inverse optical model. *Scope Procedia Manuf.* **2020**, *47*, 182–189. [CrossRef]

27. *GB/T 1458-2023*; Test Method for Mechanical Properties of Ring of Filament-Winding Reinforced Composites. National Standard of the People's Republic of China: Beijing, China, 2023.

28. Zhao, D.; Chen, J.; Zhang, H.; Liu, W.; Yue, G.; Pan, L. Effects of processing parameters on the performance of carbon fiber reinforced polyphenylene sulfide laminates manufactured by laser-assisted automated fiber placement. *J. Compos. Mater.* **2022**, *56*, 427–439. [CrossRef]

*Article*

# Response Surface Methodology Optimization of Resistance Welding Process for Unidirectional Carbon Fiber/PPS Composites

**Da-Wei Yu [1], Xiao-Ting Qing [1], Hong-Yu Lin [1], Jie Yang [2,3], Jia-Cao Yang [3,*] and Xiao-Jun Wang [3,*]**

[1] College of Polymer Science and Engineering, Sichuan University, Chengdu 610065, China;
yudawei0515@163.com (D.-W.Y.); qingxt@stu.scu.edu.cn (X.-T.Q.); linhy@stu.scu.edu.cn (H.-Y.L.)
[2] State Key Laboratory of Polymer Materials Engineering, Sichuan University, Chengdu 610065, China;
ppsf@scu.edu.cn
[3] Institute of Materials Science and Technology, Analysis and Testing Center, Sichuan University,
Chengdu 610065, China
* Correspondence: jiacaoyang@outlook.com (J.-C.Y.); wangxj@scu.edu.cn (X.-J.W.)

**Abstract:** The use of thermoplastic composites (TPCs) as one of the lightweight solutions will inevitably encounter problems in connection. Resistance welding has the characteristics of high strength, simplicity, and high reliability, and is considered a very potential hot-melt connection technology. The resistance welding technology of unidirectional carbon fiber-reinforced polyphenylene sulfide composites (UCF/PPS) was systematically studied. The experimental results show that the 100-mesh brass mesh has the best resin wetting effect and heating efficiency, and the PPS/oxidized 100-mesh brass mesh composite resistance element (Ox-RE/PPS) has the highest welding strength. The welding failure mode changes from interface failure and RE failure to interlayer structure damage and fiber fracture. The single-factor experimental results show that the maximum welding strength is reached at 310 °C, 1.15 MPa, and 120 kW/m$^2$. According to the conclusion of the single-factor experiment, the Box–Behnken method was further used to design a three-factor, three-level experiment, and a quadratic regression model was established according to the test results. The results of variance analysis, fitting curve analysis, and perturbation plot analysis proved that the model had high fitting and prediction abilities. From the 3D surface diagram analysis, the influence of power density is the largest, and the interaction between welding temperature and power density is the most significant. Combined with the analysis of Design Expert 13 software, the optimal range of process parameters was obtained as follows: welding temperature 313–314 °C, welding pressure 1.04–1.2 MPa, and power density 124–128 kW/m$^2$. The average strength of resistance welding joints prepared in the optimal range of process parameters was 13.58 MPa.

**Keywords:** resistance welding; UCF/PPS; response surface method (RSM); lap shear strength (LSS); optimal process parameters

## 1. Introduction

TPCs are composites composed of thermoplastic resins and various different materials combined by physical or chemical processes [1,2]. The strength of the material can be enhanced, and the economic benefits can be improved, by utilizing various combinations of reinforcement materials. TPCs have excellent mechanical properties, as well as being lightweight, rapid prototyping, easy repair, and having strong design ability [3,4]. With the research of many scholars in recent years, the composite materials of high-performance thermoplastic resins, such as polyphenylene sulfide (PPS), polyetheretherketone (PEEK), polyetheretherketone ketone (PEKK), and polyetheretherimide (PEI), have developed rapidly [5–7]. TPCs are replacing thermosetting composites (TSCs) in defense, military industry, aerospace, rail transportation, civil, and other fields [8]. However, the increase in usage and the expansion of market share also bring a series of problems and challenges, such

as the connection methods of TPC components [1,9]. At present, high-performance thermoplastic resin composites are mainly used in secondary load-bearing structures and some primary load-bearing structures. It is of great significance to explore ways to improve joint performance and find solutions that meet the connection standards of primary load-bearing structures to promote innovation and progress in the field of industrial manufacturing.

Nowadays, the most mature connection methods are still the traditional connection methods, such as mechanical connection and bonding [10,11]. The disadvantage of the former is that the use of rivets or bolts can cause local stress concentration in the parts or cause defects in the composite material. The disadvantage of the latter is that it requires high pretreatment of the bonding surface, and the performance of the bonding is greatly affected by the environment. To address the mismatch between the development of connection technology and materials, it is necessary to explore effective and reliable methods of connection. According to the current practical application needs, appropriate connection methods should be selected to ensure the reliability and convenience of composite part connections [12,13]. Due to the remelting property of the thermoplastic resin matrix, TPCs can be heated for shape change and retreatment [14]. Therefore, in addition to traditional connection methods, hot-melt connection technology can also be used to connect. Hot-melt connection technology contains many subcategories, but the three most promising ones are resistance welding (RW), induction welding (IW), and ultrasonic welding (UW) [15–19]. These three technologies solve problems that are difficult to solve with traditional techniques, such as automation, controllability, high strength, etc., and can be applied to different application scenarios [20,21].

The resistance welding method studied in this paper has the characteristics of being simple and flexible, a short process, and having no surface treatment. It is an economical and efficient welding method and has great potential in the field of TPC connections. The resistance welding process takes about a few minutes. The resistance element (RE) in the welding layer is energized to generate heat, thereby increasing the temperature of the joint. The resistive elements can be carbon fiber, brass mesh, stainless steel (SS) mesh, or conductive nanocomposites [22,23]. The welding layer can also be innovatively mixed with carbon nanotubes, which enhances the welding interface [24]. Marti et al. [25] investigated the availability of different sandwich-type heating components for enhanced resistance welding. Most thermoplastic resins were easy to crystallize, and the cooling rate during resistance welding had a significant impact on the crystallinity and morphology [26–28]. Liu et al. [29] studied the relationship between geometric size, current density, and temperature response in the self-resistance electric (SRE) heating method of composite materials; determined the relationship between temperature rise rate and current density; and explored the deconsolidation behavior of SRE after heating. The final effect of resistance welding of thermoplastic composites also depended on the regulation of various process parameters, including welding current, clamping pressure, heating time, etc. [30]. Xiong et al. [31] used carbon fiber felt (CFF) composite film instead of pure resin film as a fusible component of electric resistance welding. The addition of CFF improved the lap shear strength (LSS) of welded joints and shortened the welding time (tw). LSS refers to the shear force that the unit welded surface can withstand when the welded surface is damaged, and its unit is expressed in megapascals (MPa). Barbosa et al. [32] used means of fracture analysis to study the resistance-welded joints of composite laminates. They believed that the identification of fracture morphology provides information about failure modes and contributes to the quality of the welding process. Under the same welding time and electrode pressure, as the welding current increases, the failure mode of resistance element welding (REW) joints changes from interface mode to partial button fracture [33].

With the continuous development of computer science, the welding process can be simulated and optimized with the help of computers and software [23]. Lionetto et al. [34] accurately modeled the temperature distribution of laminates in continuous induction welding of thermoplastic matrix composites. Machine learning can also be used for multi-objective optimization of complex welding processes to achieve an optimal solution [35].

Box–Behnken design (BBD) is a design method of response surface experiment that is commonly used to study the influence of multiple factors on a response variable [36–38]. Using Design Expert 13 software, we can determine the nonlinear relationships between factors through a small number of experiments and establish corresponding mathematical models. Vinayagamoorthy R optimized the drilling parameters of composite materials using the Box–Behnken method, as well as each output factor, and finally obtained the best processing conditions [39].

Polyphenylene sulfide (PPS) is a high-performance engineering plastic with excellent mechanical properties, heat resistance, chemical stability, and electrical insulation. However, due to the high crystallinity and low surface energy of PPS resin, there are some limitations when using traditional methods for connection. Its unidirectional carbon fiber-reinforced polyphenylene sulfide composite (UCF/PPS) is one of the most important thermoplastic composites. Therefore, it is of representative significance to study the resistance welding process of UCF/PPS. Generally, there are many factors that affect the final welding effect of UCF/PPS resistance welding. Therefore, in order to achieve efficient and stable welding effects, resistance welding technology needs to be systematically explored and improved. In this study, the effects of resistance element mesh size, processing methods, pressure holding time, welding temperature, welding pressure, and power density on welding strength were evaluated. This paper proposes the use of the Box–Behnken design response surface method (BBD-RSM) to optimize welding parameters. The response surface curve was drawn to evaluate the influence of three main process factors on welding quality, and the interaction between the factors was studied. The corresponding quadratic regression model was established to optimize the welding conditions and summarize the best process parameter range. Finally, the accuracy of the quadratic regression model prediction was verified by practice.

## 2. Materials and Methods

### 2.1. Materials

The materials used for the resistant welding experiments in this research were UCF/PPS composite materials (Nanjing Advanced Thermoplastic Composite Co., Ltd., Nanjing, Jiangsu, China). The UCF/PPS was a unidirectional carbon fiber prepreg with a nominal fiber volume content of 68%, a thickness of 0.3 mm, and a width of 90 mm.

The UCF/PPS prepreg was pressed into a laminate with a thickness of 2 mm, a width of 100 mm, and a length of 110 mm, as shown in Figure 1a. The stacking direction of the laminates was unidirectional, with a total of nine layers. Specimens with a length of 100 mm and a width of 20 mm were cut from the laminates, as shown in Figure 1b.
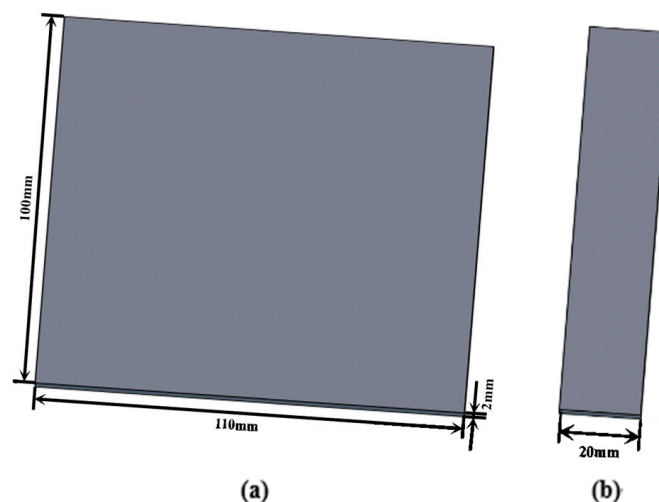


**Figure 1.** (**a**) Schematic diagram of UCF/PPS laminate and (**b**) schematic diagram of UCF/ PPS specimen.

PPS film was made of PPS resin pellets (Xinjiang Zhongtai Chemical Co., Ltd., Urumqi, Xingjiang, China). Its melting and initial decomposition temperatures were 283 °C and 430 °C, respectively. PPS resin was pressed into films with a thickness of 0.1 mm using a hot press at 300 °C. After cooling, the slices were cut into a length of 25 mm and a weight of 20 mm for use.

In this study, a 40-, 100-, and 200-mesh brass mesh was selected as the resistance element (RE). The brass (international standard name: CuZn35) plain weave meshes were provided by Anping County Mujie Wire Mesh Products Co., Ltd., Anping, Hebei, China.

## 2.2. Preparation of the Resistance Element

Resistance welding of thermoplastic composite materials uses the Joule heating effect to heat and melt the resin to join two specimens together. The power density per unit area in the welded joint is adjusted to control the heat and temperature distribution during welding. The power density can be calculated using the following formula [40]:

$$P = IU/LW \tag{1}$$

In the formula, $P$ is the power density in kW/m$^2$, $I$ is the current in A, $U$ is the voltage in V, $L$ is the welding length in mm, and $W$ is the welding width in mm.

In this research, brass resistance elements were cut to the same dimensions. The resistance elements were cleaned using ethanol and deionized water, and then they were dried for future use, as shown in Figure 2a. For high-quality welded joints, oxidation treatment and the addition of resin layers were used in this study to optimize the untreated resistance elements (UT-RE). When exploring different parameters, the high strength of the joint can make the difference more obvious. The resistance element was oxidized (Ox-RE) by placing it in a muffle furnace at 350 °C for 30 min, as shown in Figure 2b. The welding area of the resistance element was sandwiched between two PPS resin films and placed on a constant-temperature heating platform at 320 °C. PPS resin composite resistance element (Ox-RE/PPS) was prepared using the hot pressing method, and the thickness of the resin layer was controlled to 0.3 ± 0.02 mm, as shown in Figure 2c.



**Figure 2.** Resistance elements: (**a**) UT-RE, (**b**) Ox-RE, and (**c**) Ox-RE/PPS.

## 2.3. Experimental Methods

### 2.3.1. Resistance Welding Experiment

(1)    The single-lap resistance welding experiment

As shown in Figure 3a, the single-lap resistance welding experimental device consisted of a direct-current (DC) power supply, temperature monitoring system, pressure system, and resistance welding platform. The DC power supply (DP5060, Mestek Tools Co., Ltd., Shenzhen, China) was connected to the resistance element via copper electrodes, providing a maximum output power of 3000 W. The temperature monitoring system (YET-640X, Suma Electric Instrument Co., Ltd., Xinghua, China) adopted a hyperfine K-type thermocouple with a diameter of 0.1 mm. The thermocouple probe was wrapped with insulating tape to monitor and record the temperature inside the welding layer in real time. A universal testing machine (model E45, MTS Industrial Systems, Shenzhen, China) and a custom epoxy pressure block were used for constant displacement pressurization during welding.
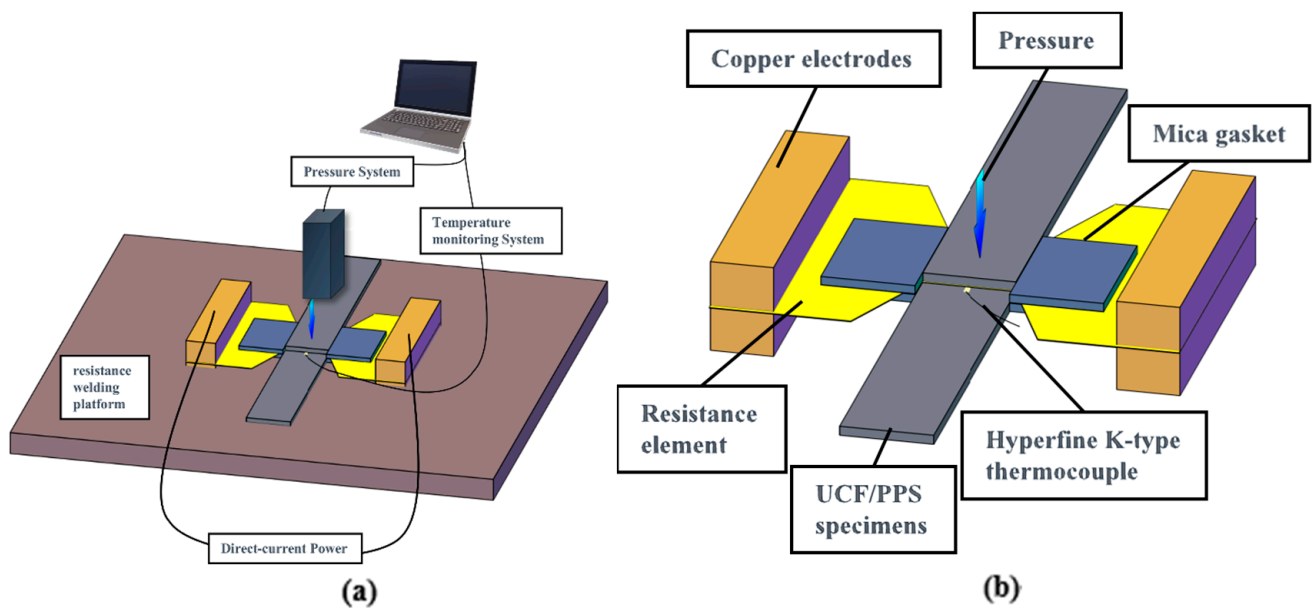
**Figure 3.** (**a**) Single-lap resistance welding experimental device and (**b**) schematic diagram of PPS/UCF single-lap resistance welding.

The specimens, resistance element, and hyperfine K-type thermocouple were placed on the welding platform and fixed with a horizontal fixture, as shown in Figure 3b. The temperature measurement point was located at the center of the welding layer, and the thermocouple was removed when heated to the target temperature. Mica gaskets were placed on both sides of the sample joint to control the thickness and limit the deformation of the sample during welding. The mica gasket also played a role in preventing excessive loss of the molten resin under pressure, thus reducing the production of defects.

(2)    The operation procedure for resistance welding

The operation procedure for resistance welding is described as follows. Before the experiment, the welding surface was polished with 320-mesh sandpaper, cleaned with absolute alcohol, and dried in the oven. The universal testing machine was controlled to press the welding part to avoid heat loss. The power was turned on, and the welding layer temperature began to rise. When the temperature of the welding layer reached 150 °C, the pressure was adjusted to the experimental value to ensure that the initial pressure was consistent for each test. Heating was continued to the target temperature, and then the power was turned off. Before taking out the sample, the pressure was maintained for a period of time.

### 2.3.2. Single-Factor Experimental Design

Prior to the formal resistance welding experiments, the resistance welding conditions of UCF/PPS composite specimens were initially explored to determine the approximate range of the studied parameters. The mesh size and treatment method of the resistance element used in the welding experiment directly affect the strength of the welded joint. In addition, PPS resin undergoes the process of melting and reconsolidation during welding, and the degree of infiltration, melting, and crystallinity of the resin are affected by the pressure holding time, welding temperature, welding pressure, and power density [30]. The welding temperature affects the fluidity of the resin. When the welding power density is constant, the welding temperature increases with the increase in welding time. Therefore, the welding temperature, welding time, and total power density are regarded as equivalent process parameters in this study [41].

The above six single factors are studied to determine the best process range of each factor and the main process parameters of response surface design. The mesh sizes of

the resistance elements are 40, 100, and 200 mesh, respectively. The RE process methods include untreated, oxidation treatment, and adding PPS resin. The welding process is divided into a pressure holding time of 0–180 s, a welding temperature of 300–330 °C, a welding pressure of 0.55–1.45 MPa, and a power density of 100–160 kW/m$^2$.

### 2.3.3. Optimization of the Resistance Welding Process Using Response Surface Methodology

Under the premise of the best other secondary factors, Box–Behnken design (BBD) with response surface methodology (RSM) was used to optimize the resistance welding process using Design-Expert 13 software. Ox-RE/PPS was selected for BBD experiments. Three main process parameters (A: welding temperature, B: welding pressure, and C: power density) were optimized and adjusted by the response surface method to obtain the best joint strength. The range of values of the three main parameters in BBD is shown in Table 1.

**Table 1.** The range of values of the three main parameters in BBD.

| Level | Factor | | |
|---|---|---|---|
| | A: T (°C) | B: F (MPa) | C: P (kW/m$^2$) |
| −1 | 300 | 0.85 | 100 |
| 0 | 310 | 1.15 | 120 |
| 1 | 320 | 1.45 | 140 |

Through the experimental results, the influence factors (i.e., welding temperature, welding pressure, and power density) and their interaction on the lap shear strength (LSS) can be determined. Analysis of variance (ANOVA) was used to determine the degree of influence, significance, and adequacy of the quadratic regression model. Design-Expert 13 software and Origin 2022 software were used to draw 2D array diagrams and 3D response surface diagrams, which intuitively reflected the main influence and interactive influence of influencing factors on the LSS. Finally, based on the response surface model, the joint strength after process optimization was predicted and verified.

### 2.4. Characterization

The test instrument was the universal testing machine (Model E45, MTS Industrial System, Shanghai, China), and the welding quality was evaluated by testing the lap shear strength (LSS) of UCF/PPS welding samples. The lap shear strength refers to the shear force that the unit welded surface can withstand when the welded surface is damaged, and its unit is expressed in megapascals (MPa). The test standard for LSS refers to ASTM D1002 [42], using a 100 kN force transducer without an extensiometer. The dimensions of the weld surface were 20 × 25 mm, the clamping area was 20 × 40 mm, the sample spacing was 75 mm, and the loading rate was 2 mm/min. Five samples were tested in each group.

The failed welding surface was cut into 5 × 5 mm, sprayed with gold, and observed using a scanning electron microscope (SEM, Quanta 250, FEI Corporation, Hillsboro, OR, USA). In the standard test environment, the damage morphology and cross-section of the welding surface were observed using an accelerating voltage of 5.00 kV, an SE imaging mode, and a working distance of 5.6 mm. The failure mechanism of the joints was analyzed based on the macroscopic and microscopic morphology of the fracture.

## 3. Results and Discussion

### 3.1. Effect of Resistance Elements on Welded Joints

#### 3.1.1. Mesh Size

The resistance element is made of brass mesh with different mesh sizes, which has good electrical conductivity and ductility. The results of the resistance welding experiment are shown in Figure 4. Under the same process conditions, the highest LSS (10.76 ± 0.36 MPa)

was obtained by using 100-mesh brass mesh. LSS was significantly lower than in other situations when 40-mesh brass mesh was used. The increase in the mesh number will increase the contact area with the resin, which is conducive to improving the joint strength [43]. However, the mesh pore size will decrease as the number of grids increases. PPS resin is difficult to infiltrate the welding layer, and the strength of the welded joint of the 200-mesh resistance unit is slightly lower than that of the 100-mesh resistance unit.
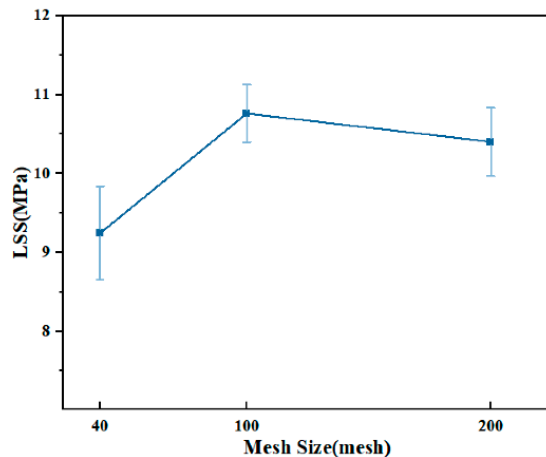


**Figure 4.** LSS of joints at different mesh sizes.

During the resistance welding of the UCF/PPS composite, a constant current was applied to the resistive element. The resistance element is energized to produce Joule heating, and the joint starts to heat from the inner layer to the outer layer. The heating curve at the center of the welding layer is shown in Figure 5. Different mesh sizes will directly affect the heat generated during welding [40]. When the number of meshes is small, the heat is concentrated near the wires, and the thermal influence range of each wire is limited. However, the larger the mesh number, the more metal wires in the unit area, and the smaller the total resistance, resulting in less heat being produced. The resistance and thermal influence range of the 100-mesh resistance element is between 40 and 200 mesh, so the test shows that its thermal efficiency is the highest.
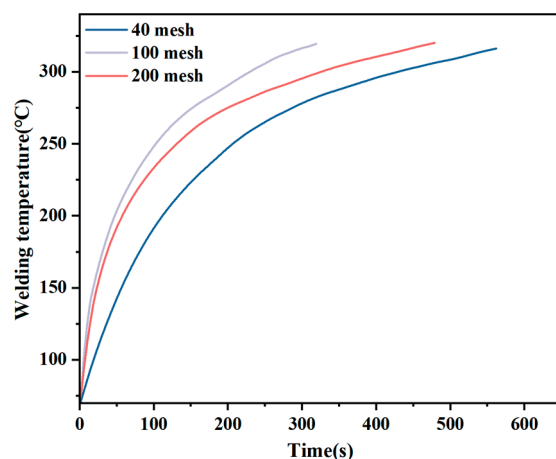


**Figure 5.** Heating curve: (**a**) brass mesh 40 mesh, (**b**) brass mesh 100 mesh, and (**c**) brass mesh 200 mesh.

The macroscopic morphology of the failure surface of welded joints with different mesh sizes is shown in Figure 6. After applying a load to destroy these welded joints, it can be seen that the failure occurs at the resin and metal mesh. Among them, due to the poor infiltration of the 40-mesh metal mesh by resin, a large loss of resin in the mesh can

be observed. However, the combination degree of 100-mesh and 200-mesh metal mesh with resin is improved. When the joint is damaged, the metal mesh is torn irregularly, which plays the role of the reinforcing phase. In conclusion, 100-mesh brass mesh is the best choice as a resistance element.
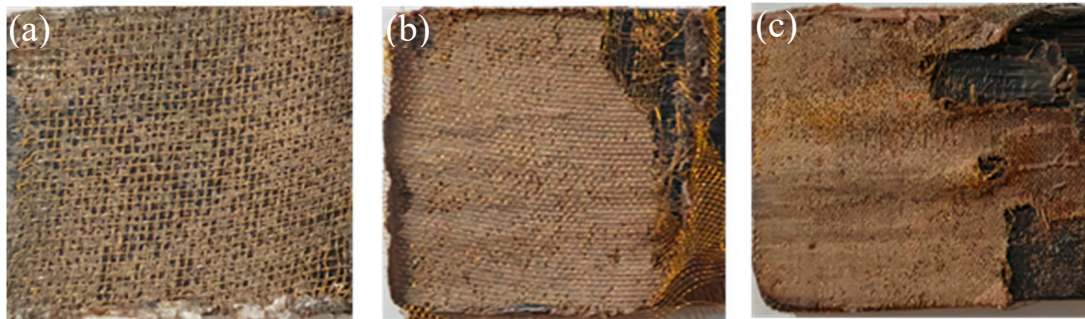


**Figure 6.** Macroscopic morphology of the failure surface: (**a**) brass mesh 40 mesh, (**b**) brass mesh 100 mesh, and (**c**) brass mesh 200 mesh.

### 3.1.2. RE Process Method

Three types of resistance element, namely, UT-RE, Ox-RE, and Ox-RE/PPS, were used for resistance welding, respectively, and the joint quality was evaluated through the LSS test. The results are shown in Figure 7. The average LSS of the welded joints of UT-RE is 10.73 MPa, and the strength increased to 11.85 MPa after oxidation.
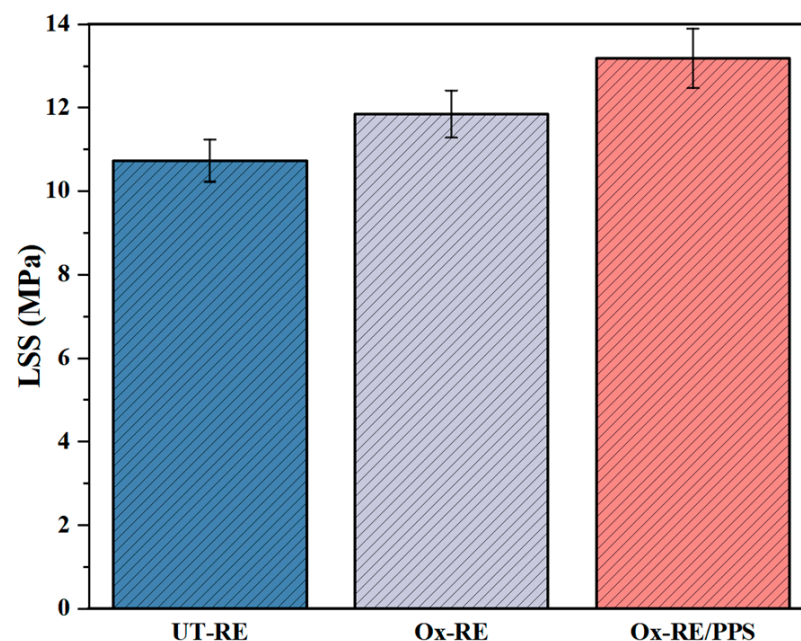


**Figure 7.** LSS of joints at different RE process methods.

The PPS resin can be fully infiltrated onto the surface of the metal mesh by hot pressing. During the welding process, the resin layer also plays a role in reducing the heat loss in the heating area and making the heat transfer more uniform. The joint strength of Ox-RE/PPS reached 13.18 MPa, which was 11.22% higher than that of Ox-RE. Therefore, more reliable welded joints can be obtained with Ox-RE/PPS compared to UT-RE.

The macroscopic morphology of the failure surface of the welded joint with different RE process methods is shown in Figure 8. Due to the low surface energy of the PPS resin, the adhesion to the brass surface is poor. After high-temperature oxidation of brass, the oxide forms a rough oxide layer on the surface, which helps to improve the surface energy.

The PPS resin film and the resistance element were combined by hot pressing. After adding the resin, it can be seen that a small amount of fiber fracture occurs on the failure surface of the joint. It indicates that the resin in the welding layer is immersed in the fibers on the surface of the laminate, so the strength of the welded joint is improved.
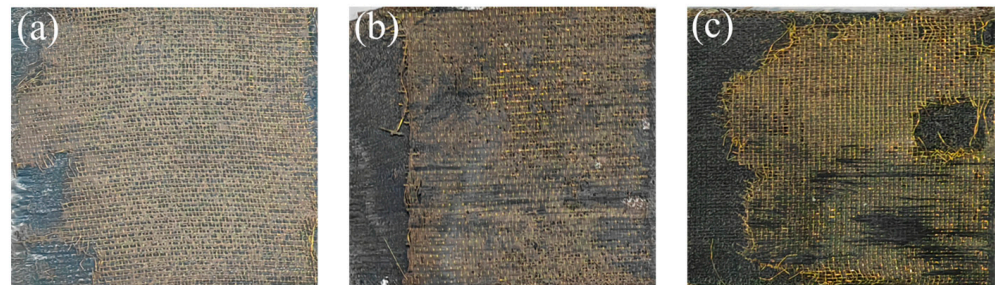


**Figure 8.** Macroscopic morphology of the failure surface: (**a**) UT-RE, (**b**) Ox-RE, and (**c**) Ox-RE/PPS.

The SEM in Figure 9a shows that the adhesion between the surface of the untreated brass wire and the resin is poor, and the surface of the wire is smooth with only a small amount of resin remaining. Failure occurs at the brass wire/resin interface failure and resin/matrix debonding. The microscopic morphology of the Ox-RE welded joint is shown in Figure 9b. After the joint was damaged, more resin remained on the surface of the wire, showing a tearing state. The microscopic morphology of the Ox-RE/PPS welded joint is shown in Figure 9c. Interlayer failures include fiber breakage and resin failure. After the damage, the brass mesh was still largely coated with resin.
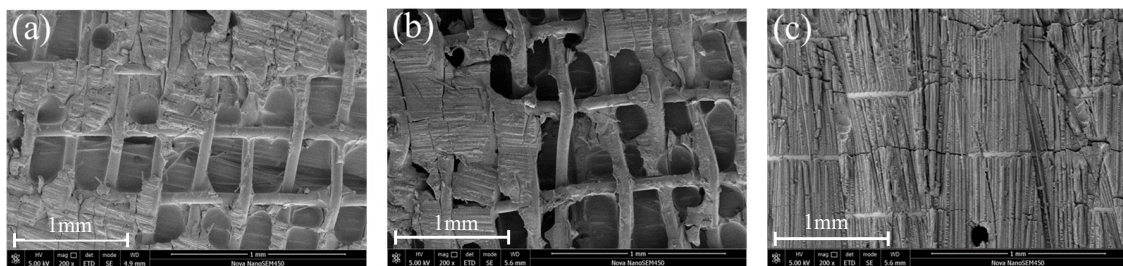


**Figure 9.** Microscopic morphology of the failure surface: (**a**) UT-RE, (**b**) Ox-RE, and (**c**) Ox-RE/PPS.

SEM was used to observe the microscopic morphology of the cross-sections of the welded specimens (Figure 10a,b). Without the addition of PPS resin, the resin of the UCF/PPS matrix was insufficient to fill the welding layer. In the SEM image, it can be observed that there are obvious pores in the cross-section of the welded joint, which is the weak point inside the joint. After welding using Ox-RE/PPS, all parts of the welded joint were tightly bonded, with good resin infiltration and no obvious defects.
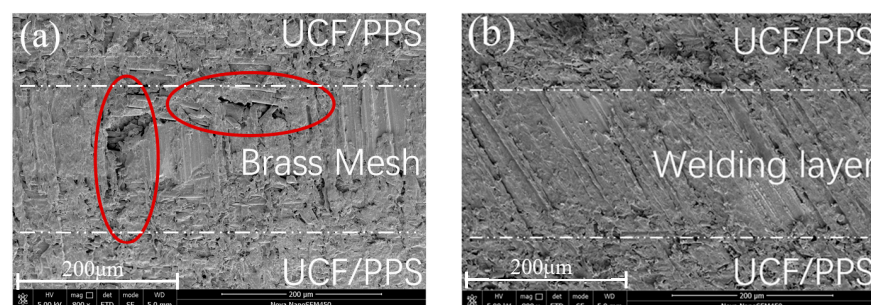


**Figure 10.** Microscopic morphology of the section: (**a**) Ox-RE and (**b**) Ox-RE/PPS.

### 3.2. Effect of the Welding Process on the Welded Joint

3.2.1. Pressure Holding Time

After the power is turned off, the pressure holding can reduce the cooling rate of the joint, maintain the stability of the joint shape, and reduce the residual stress. PPS resin is easy to crystallize during cooling [26]. Appropriate cooling rates contribute to the formation of an ordered molecular chain structure and improve the mechanical properties, heat resistance, and dimensional stability of the joint. According to Figure 11, the LSS of the joint increases with the extension of the holding time and reaches its maximum at 60 s. The crystallinity of PPS resin is higher when the holding time is more than 60 s, which leads to an increase in joint brittleness. The pressure holding time continues to extend, and the quality of the joint tends to be constant.
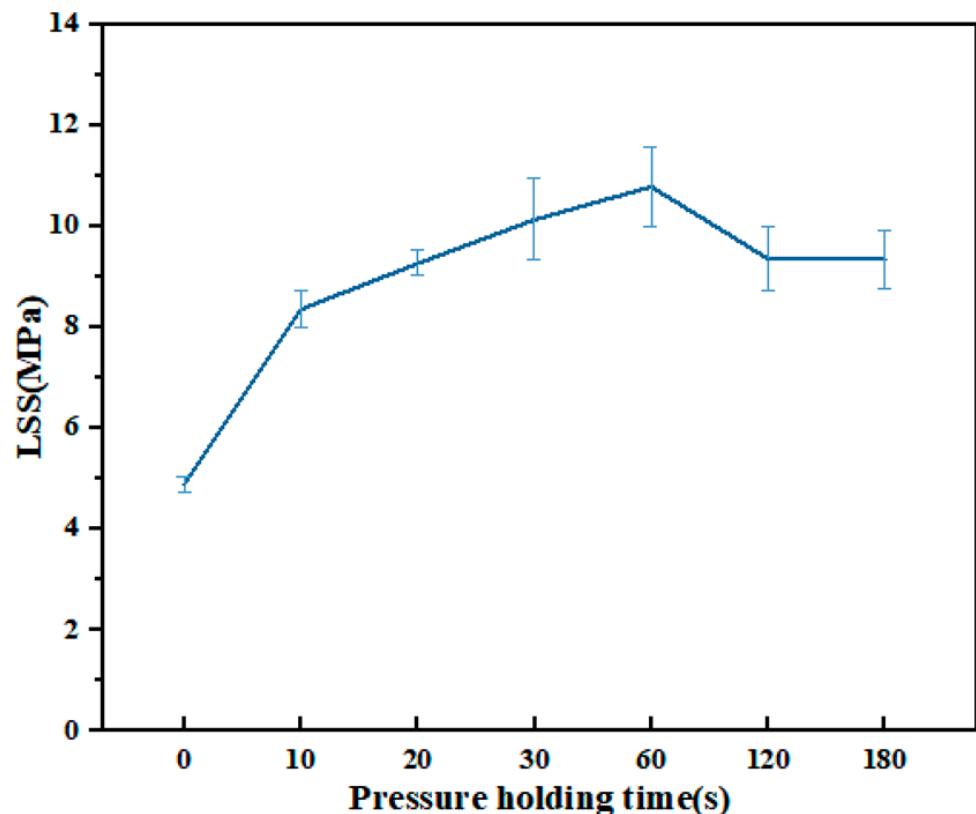


**Figure 11.** LSS of joints at different pressure holding times.

3.2.2. Welding Temperature

During welding, the metal wire makes the welding layer resin and the matrix resin melt, and the molecular chain moves to form a whole structure. As shown in Figure 12, with the increase in the highest temperature, the LSS curve shows a trend of first increasing and then decreasing, reaching its maximum value at 310 °C. The edge effect of the resistive element [44] can cause the heating rate at both ends of the welded joint to be higher than that in the middle. Setting a low welding target temperature will result in too little welding time. The resin did not melt sufficiently to form an unstable joint, so the joint strength was not high. In the appropriate temperature range, the higher the welding temperature, the deeper the thermal influence depth of the resistance element in the vertical direction. A too-high welding temperature can significantly improve the mobility of PPS, and the resin is more likely to extrude at the edge of the joint, leading to a decrease in the joint strength. The LSS curve has obvious fluctuations, which can prove that temperature is the main influencing factor during resistance welding. Thermal degradation of PPS resin would be inevitable if the temperature continued to increase [45].
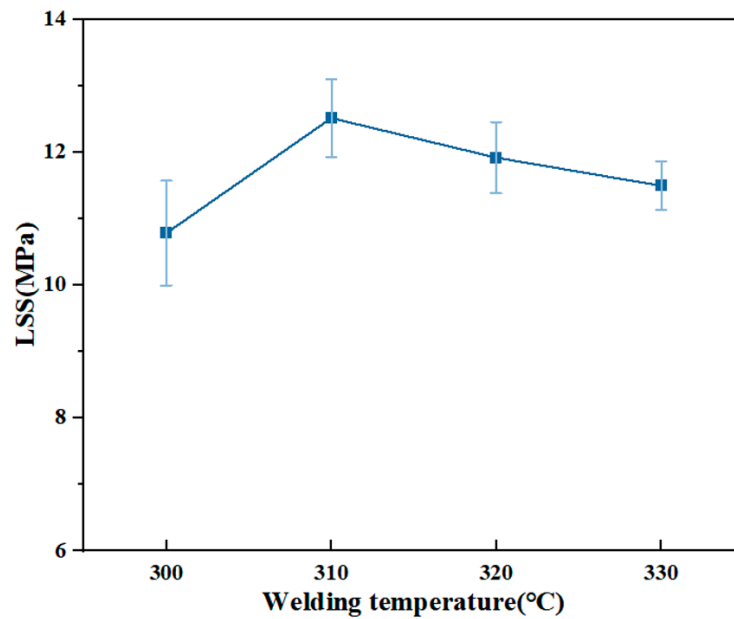
**Figure 12.** LSS of joints at different welding temperatures.

3.2.3. Welding Pressure

The corresponding welding strength under different welding pressures is shown in Figure 13. Welding pressure is an important factor in resistance welding, which must be applied appropriately to ensure that the spline welding surface is tightly bonded to the welding layer after melting [46]. As the pressure increases, the welding strength first slightly decreases and then increases. At low pressure, the layers of the welded joint are separated and cannot form a good contact. Because of the presence of an air layer, heat cannot be efficiently transferred to the matrix, and the time to complete welding becomes longer during the experiment. Insufficient pressure causes insufficient resin flow in the welding layer and poor joint performance. The optimum welding pressure for the joint is about 1.15 MPa. When the welding pressure increased to 1.45 MPa, the resin at the welding interface was lost under the pressure, and the strength decreased significantly.
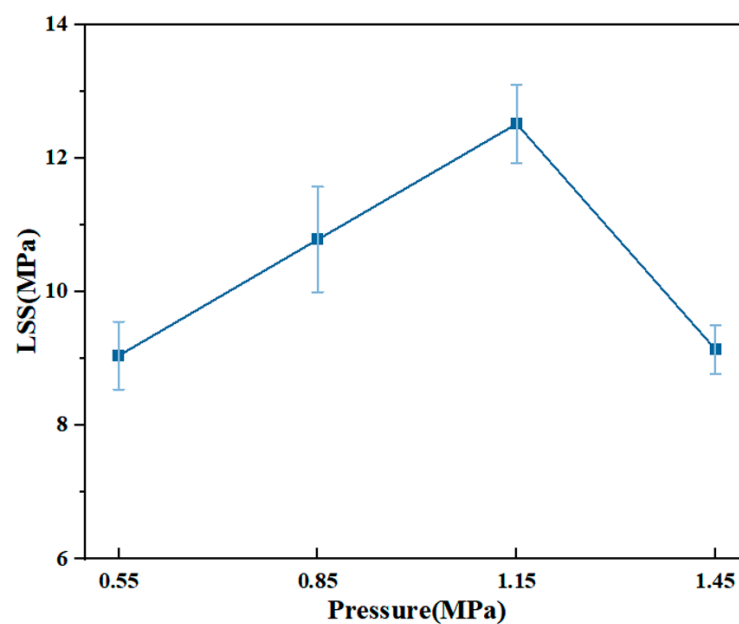


**Figure 13.** LSS of joints at different welding pressures.

### 3.2.4. Power Density

Preliminary experiments show that a too-low power density cannot form an effective joint. The heating rate increases with increasing power [29]. As shown in Figure 14, the LSS curve shows a trend of first increasing and then decreasing, and the joint strength is the highest at 120 kW/m². At 100 kW/m², the heat generated per unit time is limited, and the fusion of each part of the welding joint is poor, which affects the consistency of the welded joint. The long welding processing time will also increase the economic cost, which is not conducive to the actual processing. High power density can lead to heat accumulation in the joint, which leads to matrix deformation and high-temperature fracture of PPS resin molecular chains, thus reducing the joint strength.
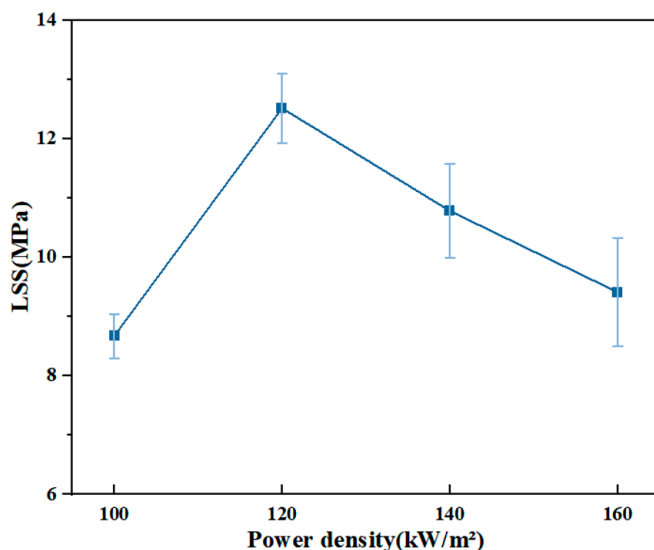


**Figure 14.** LSS of joints at different power densities.

### 3.3. *Optimization of the Resistance Welding Process Using RSM*

### 3.3.1. Quadratic Regression Model

Table 2 shows the experimental design based on the Box–Behnken method and its experimental results, which include 17 sets of experiments combined by three independent factors.

**Table 2.** Box–Behnken experimental design and results.

| No. | A: T (°C) | B: F (MPa) | C: P (kW/m²) | LSS (MPa) |
|-----|-----------|------------|--------------|-----------|
| 1   | 310       | 1.45       | 100          | 9.85      |
| 2   | 300       | 1.15       | 140          | 10.04     |
| 3   | 320       | 1.15       | 100          | 9.6       |
| 4   | 310       | 1.15       | 120          | 13.44     |
| 5   | 310       | 1.15       | 120          | 13.56     |
| 6   | 310       | 0.85       | 100          | 9.88      |
| 7   | 310       | 1.15       | 120          | 13.61     |
| 8   | 300       | 1.45       | 120          | 10.92     |
| 9   | 310       | 1.15       | 120          | 13.31     |
| 10  | 300       | 0.85       | 120          | 11.91     |
| 11  | 320       | 0.85       | 120          | 12.85     |
| 12  | 310       | 1.45       | 140          | 11.91     |
| 13  | 320       | 1.45       | 120          | 12.46     |
| 14  | 320       | 1.15       | 140          | 12.22     |
| 15  | 300       | 1.15       | 100          | 9.57      |
| 16  | 310       | 1.15       | 120          | 13.7      |
| 17  | 310       | 0.85       | 140          | 12.24     |

The quadratic regression model of welding strength using the Box–Behnken experiment design was based on the uncoded levels of the three independent variables. In this study, the regression equation for resistance welding joints is as follows:

$$Y = -985.75109 + 6.19328 \times A - 3.52528 \times B + 0.497637 \times C + 0.05 \times A \times B + 0.002688 \times A \times C$$
$$- 0.0125 \times B \times C - 0.010508 \times A^2 - 4.86944 \times B^2 - 0.005289 \times C^2 \tag{2}$$

In the formula, $Y$ represents the LSS in MPa, $A$ represents the welding temperature in °C, $B$ represents the welding pressure in MPa, and $C$ represents the power density in $kW/m^2$.

The ANOVA results of the quadratic regression model are summarized in Table 3. The statistical significance and adequacy of the model were verified by variance analysis. The F statistic is the ratio of the regression variance to the error variance and is used to test whether the fit of the regression model is significant. A higher F-value indicates a better fit of the regression model. The *p*-value is the probability of the F statistic and is used to determine whether the F statistic is significant. When the *p* value is less than 0.05, it indicates that the regression model has a significant fit (**). In contrast, when the *p*-value is greater than 1, the fitting degree of the model term is not significant. The coefficient of determination ($R^2$) reflects the proportion of the regression model that explains the degree of variation in the dependent variable, with values ranging from 0 to 1. The closer the model is to 1, the better the model fits the observed data.

**Table 3.** The ANOVA results of the quadratic regression model.

| Source | Sum of Squares | Degrees of freedom | Mean Square | F-Value | *p*-Value | Significance |
|---|---|---|---|---|---|---|
| Model | 37.59 | 9 | 4.18 | 64.58 | <0.0001 | ** |
| A | 2.75 | 1 | 2.75 | 42.51 | 0.0003 | ** |
| B | 0.3785 | 1 | 0.3785 | 5.85 | 0.0462 | ** |
| C | 7.05 | 1 | 7.05 | 108.99 | <0.0001 | ** |
| AB | 0.09 | 1 | 0.09 | 1.39 | 0.2767 | |
| AC | 1.16 | 1 | 1.16 | 17.87 | 0.0039 | ** |
| BC | 0.0225 | 1 | 0.0225 | 0.3478 | 0.5739 | |
| $A^2$ | 4.65 | 1 | 4.65 | 71.87 | <0.0001 | ** |
| $B^2$ | 0.8087 | 1 | 0.8087 | 12.5 | 0.0095 | ** |
| $C^2$ | 18.85 | 1 | 18.85 | 291.38 | <0.0001 | ** |
| Residual | 0.4528 | 7 | 0.0647 | | | |
| Lack of fit | 0.3603 | 3 | 0.1201 | 5.19 | 0.0727 | |
| Pure error | 0.0925 | 4 | 0.0231 | | | |
| $R^2$ | 0.9881 | | Adjusted $R^2$ | | 0.9728 | |
| Mean | 11.83 | | Predicted $R^2$ | | 0.8447 | |
| C.V. % [a] | 2.15 | | Adeq Precision | | 21.2956 | |

[a] Coefficient of variation.

The F-value of the quadratic regression model is 64.58, and the *p*-value is less than 0.0001, indicating that the model can significantly predict the welding strength. The good fit of the quadratic regression model is contradicted by the fact that the model lacks fit [36]. The F-value of lack of fit in the table is 5.19, and the *p*-value is greater than 0.05, which is not significant, indicating that the model does not lack fit. The coefficient of determination $R^2$ is 0.9881, which indicates that 98.881% of the variability in welding strength is explained by this model. This shows that the predicted welding strength is close to the BBD experimental value [37], which confirms the reliability of the model.

Adeq Precision is the ratio of effective signal to noise, and greater than 4 is reasonable [37]. The precision of this experiment is 21.2956, which indicates that the model has high accuracy in the design space [38]. The experimental and predicted values of welding strength are shown in Figure 15. The difference between the actual value and the predicted value is less than 0.2, indicating that the model has reasonable consistency. In addition, the coefficient of variation (C.V.) was low (2.15%), indicating that the experimental data are accurate and reliable [47].
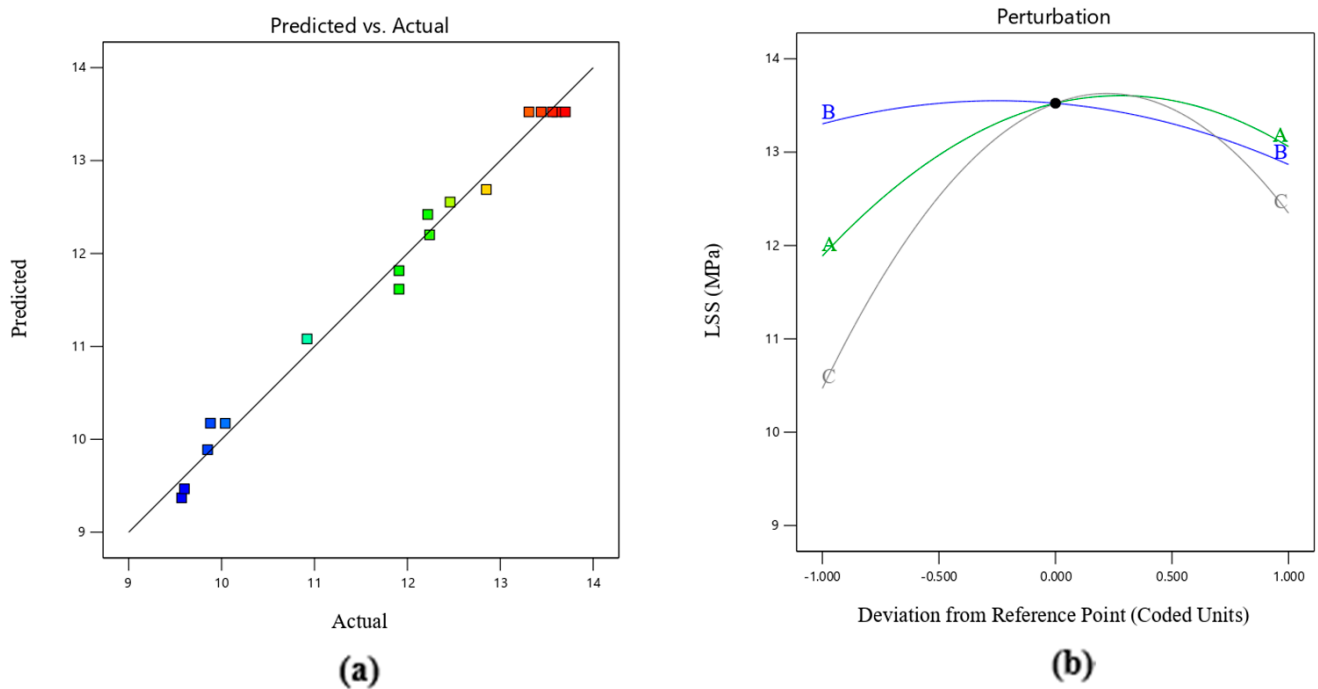
**Figure 15.** (**a**) Experimental and predicted values of welding strength and (**b**) perturbation plot of welding strength. The color square in Figure 15a correspond to the LSS experiment results in Table 2.

The *p*-value is used to test the significance level of model items. If $p < 0.05$, it means that there is a statistically significant difference in the item; otherwise, there is no significance [48]. As shown in Table 3, in the established model, A, B, C, AC, $A^2$, $B^2$, and $C^2$ have significant impacts on the model, while other terms have no significant impacts. A perturbation plot of welding strength is shown in Figure 15b. The curvature of the perturbation diagram can reflect the sensitivity of each parameter to the welding strength, and the steeper the slope, the more significant the influence. It can be seen from the figure that the order of influence of the three parameters on LSS is C > A > B, that is, power density > welding temperature > welding pressure.

### 3.3.2. Effect of Process Parameters on Welding Strength

Drawing a three-dimensional surface diagram of the interaction of parameters can more intuitively reflect the influence of parameters on LSS and the interaction between various process parameters (Figure 16). The interaction of T and F was studied by fixing P at 1.15 MPa. Figure 16a shows the synergistic effect of T and F on the welding strength. The TF surface plot is closest to a sphere, proving that the interaction is weak. The analysis shows that the LSS curve fluctuates obviously with the increase in welding temperature under a certain welding pressure, which proves that the temperature is the main influencing factor in the process of resistance welding. During welding, heat is transferred from the inside to the outside. As the temperature of the inner layer increases, the sandwich structure (substrate/resistance element/substrate) is gradually welded together. Excessive temperature can increase the fluidity of PPS and cause deformation of the joint, leading to a decrease in welding strength. When the pressure changes at the same target temperature, the LSS profile curve is relatively straight. This means that at any temperature, pressure plays a role. Low temperatures have a greater impact on pressure than high temperatures.
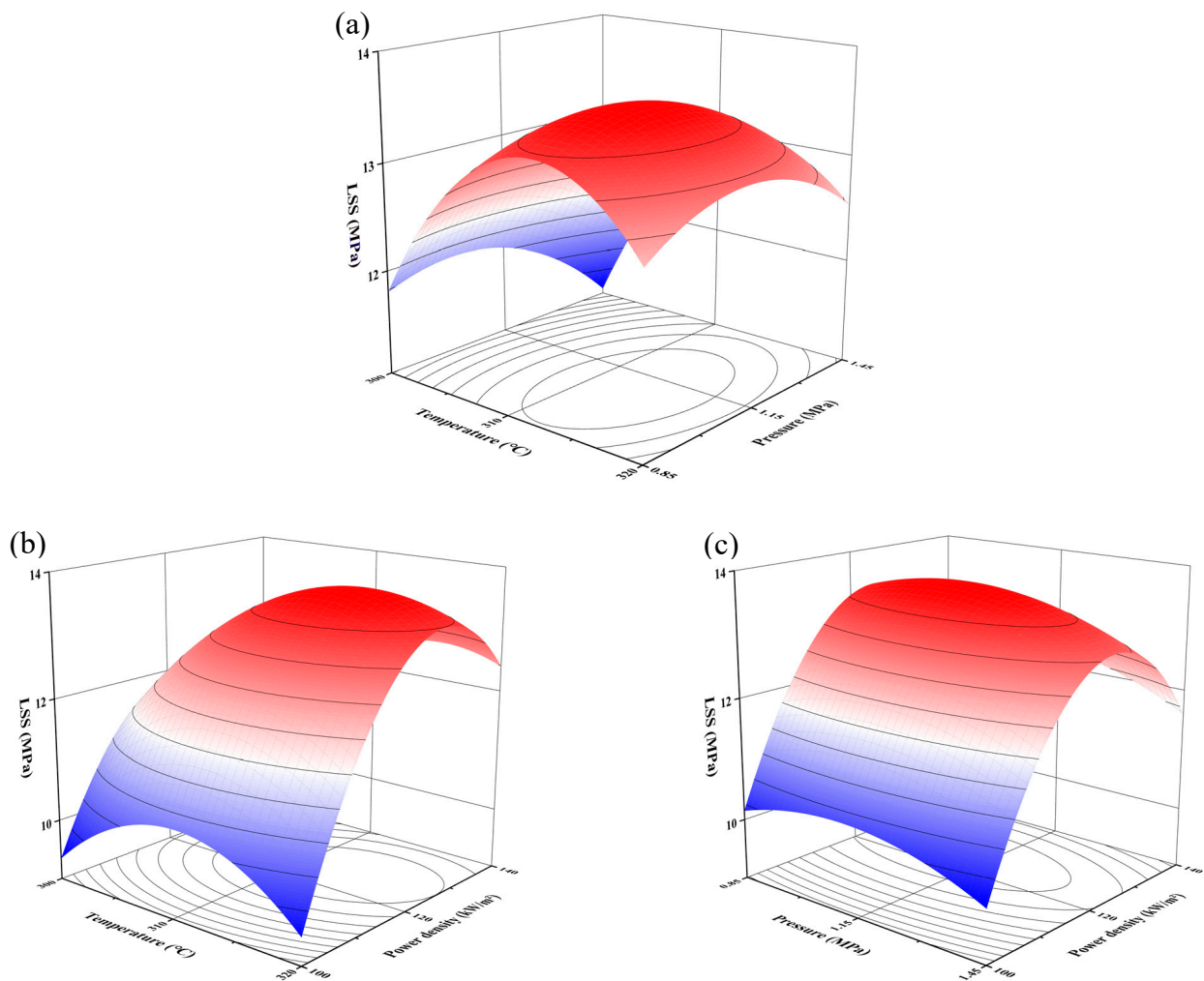
**Figure 16.** 3D surface diagram of interaction: (**a**) T and F, (**b**) T and P, and (**c**) F and P. The welding strength from low to high corresponds to the color in figure form blur to red.

Figure 16b shows the 3D surface diagram of the influence of a welding temperature of 300–320 °C and a power density of 100–140 kW/m$^2$ on welding strength. The power density determines the heating rate during welding, and the target temperature determines the welding time. The TP surface plot is closest to an ellipse, proving that it has the most perfect interaction. Thus, the AC term had a significant effect, and there was a clear interaction. It can be observed that at the same temperature, the slope of the medium and low power density is larger, which has an extremely significant effect on the welding strength. At the same power, the contour of the surface fluctuates obviously, so the power also has an obvious influence on the temperature.

Figure 16c shows the 3D surface plot of the influence of F and P on the welding strength, where the welding pressure is 0.85–1.45 MPa and the power density is 100–140 kW/m$^2$. It can be seen from the figure that the curvature of the pressure curve is small for a certain power density. It can be concluded that the influence of welding strength is limited, and the overall curve profile shows a downward trend. When the pressure is the same, the welding strength changes greatly with the increase in pressure. This phenomenon matches the conclusion of the order of influence in the perturbation map.

The variation trend of the 3D surface plot contour showed that the interaction between T and P was the most significant, and the effect of temperature and power on LSS was greater than that of pressure, which was consistent with the results of the ANOVA.

*3.4. Optimization and Verification of the Model*

Design Expert 13 was used to optimize and calculate the optimal process parameter range of the response surface model to achieve the desired LSS level. The top five best solutions are shown in Table 4. Within the scope of the plan, it is predicted that welded joints with an LSS of 13.73 ± 0.02 MPa can be obtained. The actual verification result is 13.58 ± 0.2 MPa, which is highly correlated with the numerical optimization solution, proving that BBD-RSM can effectively optimize for the actual welding situation. The optimized joint strength can reach 87.61% of the hot-pressing connection method (15.5 MPa). The strength of the hot pressing connection method is shown in Figure A1.

**Table 4.** The best solutions.

| No. | A: T (°C) | B: F (MPa) | C: P (kW/m$^2$) | LSS (MPa) |
|-----|-----------|------------|-----------------|-----------|
| 1 | 313.272 | 1.199 | 124.981 | 13.707 |
| 2 | 314.205 | 1.133 | 127.969 | 13.722 |
| 3 | 313.125 | 1.059 | 122.983 | 13.737 |
| 4 | 314.107 | 1.089 | 125.004 | 13.763 |
| 5 | 314.064 | 1.038 | 124.350 | 13.744 |

## 4. Conclusions

Among the various connection methods for thermoplastic composite materials, resistance welding has the characteristics of short processing time, simple surface treatment, high mechanical properties, simple equipment, and flexible operation. In an emergency, welding can be completed quickly using only resistive elements, a controlled power supply, and a clamping device. In the production process, the size of the welding area can be adjusted freely, and the heating efficiency of the resistance element can be flexibly controlled. Therefore, resistance welding is considered to be a very promising welding technique.

In this study, BBD-RSM was used to deeply explore the internal relationship between UCF/PPS welding strength and process factors. This method has the advantages of fewer tests, shorter calculation time, higher model accuracy, and accurate prediction results. It is hoped that it can be extended to other thermoplastic composite connection research.

Based on the analysis and discussion of the experimental results, the following conclusions are summarized:

(1) When the brass mesh size is 100 mesh, it has the best resin infiltration effect and the highest heating efficiency on the welding surface. After the 100-mesh brass mesh was oxidized, the surface roughness of the brass mesh was improved, and the interface bonding strength of the PPS resin was improved. This proves that a simple surface treatment can significantly improve welding strength. Finally, using Ox-RE/PPS for welding, the defects within the welding layer were reduced, and the welding strength reached 13.18 MPa. The failure mode changed from resin failure and implant tear to plate interlayer failure and carbon fiber fracture.

(2) The LSS of the joint first increased and then decreased with the extension of the holding time, and then tended to be stable, reaching a maximum value at 60 s. The single-factor experiment determined that the maximum welding strength was obtained at 310 °C, 1.15 MPa, and 120 kW/m$^2$ for welding temperature, pressure, and power density, respectively. These three process factors were the main process factors in resistance welding.

(3) The parameters of the three main process factors were substituted into the BBD-RSM to construct a quadratic regression model with high fit and prediction ability. From the 3D surface diagram analysis, the influence of power density is the largest, and the interaction between welding temperature and power density is the most significant. Combined with the analysis of Design Expert 13 software, the optimal process parameters were obtained as follows: welding temperature: 313–314 °C, welding pressure: 1.04–1.2 MPa, power density: 124–128 kW/m$^2$. After multiple

factor optimization, the LSS of the welded joint prepared in the optimal parameter range reached 13.58 MPa, and the welding strength increased by 26.56% compared with the UT-RE without process optimization.

(4) Combined with the above conclusions, it can be concluded that BBD-RSM can effectively analyze and optimize the process parameters of resistance welding. Moreover, an efficient and systematic resistance welding process can obtain high-quality welded joints. However, due to the limited properties of the material itself, if we want to improve the resistance welding performance, we need to take other measures, such as resin layer reinforcement and interface bonding strength. For example, on the basis of resistance welding combined with other connection methods to achieve higher strength, surface modifiers (silane coupling agents, surfactants, etc.) are used to further enhance the interface properties between RE and resin, and fillers (short fiber materials, nanomaterials, etc.) are added to enhance the mechanical properties of the resin and then improve the joint properties.

**Author Contributions:** D.-W.Y. mainly completed this study, including writing, experiments, and representation tests. J.Y., X.-J.W. and J.-C.Y. participated in the conception and writing of the study. X.-T.Q. and H.-Y.L. participated in the representation test and data analysis. All authors have read and agreed to the published version of the manuscript.

**Institutional Review Board Statement:** Not applicable.

**Informed Consent Statement:** Not applicable.

**Data Availability Statement:** Data are contained within the article.

**Conflicts of Interest:** The authors declare no conflict of interest.

## Appendix A
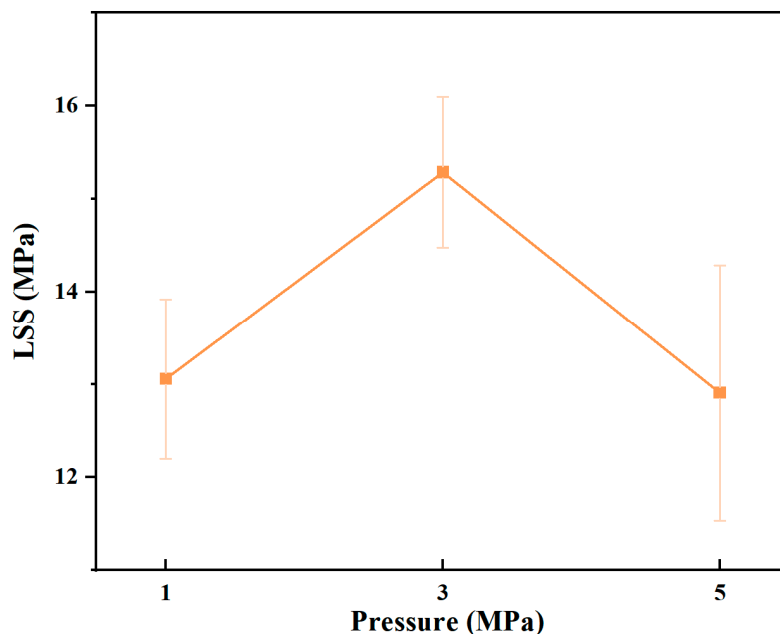


**Figure A1.** Strength of the hot pressing connection method.
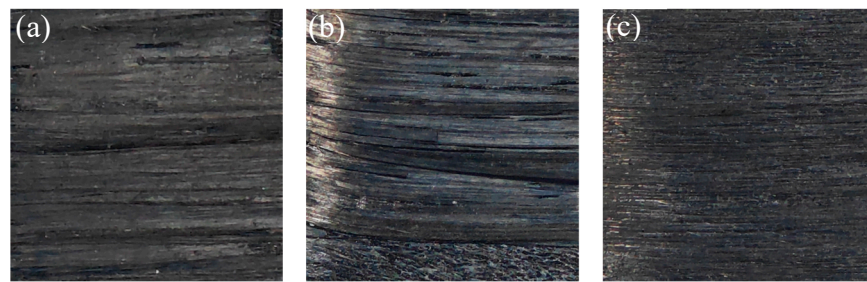
**Figure A2.** Macroscopic morphology of the failure surface: (**a**) 1 MPa, (**b**) 3 MPa, and (**c**) 5 MPa.
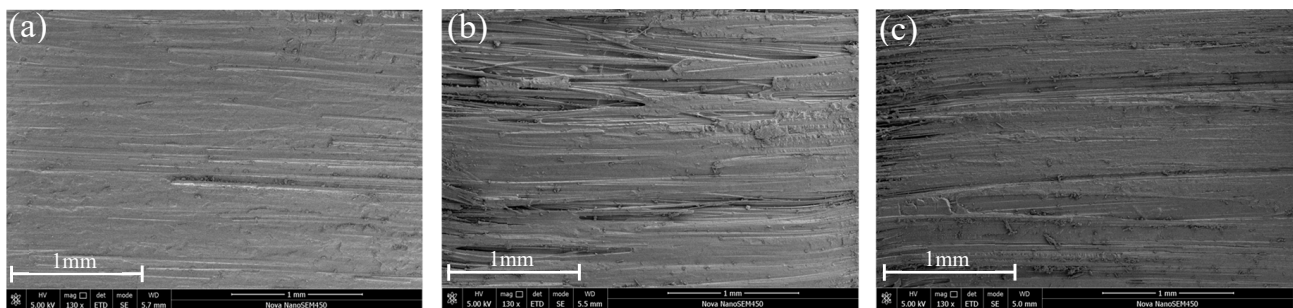


**Figure A3.** Microscopic morphology of the failure surface: (**a**) 1 MPa, (**b**) 3 MPa, and (**c**) 5 MPa.

The hot pressing connection method is the most basic one in hot-melting connection technology. In this section, the UCF/PPS splines were lapped together using the hot pressing process, and the resistance welding strength was evaluated based on the highest measured hot pressing connection strength. This experiment discusses the influence of different pressures on the hot-pressing connection effect when the hot-pressing die temperature is set near the processing temperature of PPS resin and there is sufficient melting and cooling time. The LSS test results of the hot-pressed connection method under different pressures are shown in Figure A1. The average strength of the joint formed at 3 MPa was 15.5 MPa. The maximum average LSS of hot-pressed specimens was used as a reference for evaluating the resistance welding strength. Figures A2 and A3 show macroscopic and microscopic images of the failure surface.

## References

1. Jia, G.; Catalanotti, G.; Falzon, B.G.; Higgins, C.; McClory, C.; Thiebot, J.A.; Zhang, L.; He, M.M.; Jin, Y.; Sun, D. Process Characteristics, Damage Mechanisms and Challenges in Machining of Fibre Reinforced Thermoplastic Polymer (FRTP) Composites: A Review. *Compos. Part B Eng.* **2024**, *273*, 111247.
2. Zhao, L.; Huang, Z.P.; Xiong, S.W.; Peng, J.S.; Sun, J.X.; Yin, X.Z.; Guo, N.N.; Xiong, B.; Song, X.Y.; Huang, L.P.; et al. Polyphenylene Sulfide Composite Laminate from Flexible Nonwovens and Carbon Fiber Fabrics Prepared by Thermal Lamination and Thermal Treatment. *Polym. Bull.* **2019**, *76*, 5633–5648. [CrossRef]
3. Reis, J.P.; de Moura, M.; Samborski, S. Thermoplastic Composites and Their Promising Applications in Joining and Repair Composites Structures: A Review. *Materials* **2020**, *13*, 5832. [CrossRef] [PubMed]
4. Pramanik, A.L.; Basak, A.K.; Dong, Y.; Sarker, P.K.; Uddin, M.S.; Littlefair, G.; Dixit, A.R.; Chattopadhyaya, S. Joining of Carbon Fibre Reinforced Polymer (CFRP) Composites and Aluminium Alloys—A Review. *Compos. Part A Appl. Sci. Manuf.* **2017**, *101*, 1–29. [CrossRef]
5. Osti de Moraes, D.V.; de Melo Morgado, G.F.; Magnabosco, R.; Rezende, M.C. Study of the Influence of PPS, PAEK, and PEEK Thermoplastic Matrices on the Static Mechanical Behavior of Carbon Fiber-Reinforced Composites. *Polym. Compos.* **2024**, *45*, 1726–1736. [CrossRef]
6. Ma, C.-c.M.; Hsia, H.-c.; Liu, W.-l.; Hu, J.-t. Thermal and Rheological Properties of Poly(Phenylene Sulfide) and Poly(Ether Etherketone) Resins and Composites. *Polym. Compos.* **1987**, *8*, 256–264. [CrossRef]
7. Ahn, S.; Park, C.; Choi, J.-H.; Kim, Y.S.; Yoo, Y. A Concise Review of High Performance PPS Composites using Various Fillers. *Elastomers Compos.* **2022**, *57*, 81–91.
8. Chen, G.W.; Mohanty, A.K.; Misra, M. Progress in Research and Applications of Polyphenylene Sulfide Blends and Composites with Carbons. *Compos. Part B Eng.* **2021**, *209*, 108553. [CrossRef]

9. Brauner, C.; Nakouzi, S.; Zweifel, L.; Tresch, J. Co-Curing Behaviour of Thermoset Composites with a Thermoplastic Boundary Layer for Welding Purposes. *Adv. Compos. Lett.* **2020**, *29*, 387–402. [CrossRef]

10. Yang, Z.; Jiang, R.S.; Zuo, Y.J. Riveting Damage Behavior and Mechanical Performance Assessments of CFRP/CFRP Single-Lap Gasket-Riveted Joints. *Eng. Fail. Anal.* **2023**, *149*, 107253. [CrossRef]

11. Wei, Y.; Jin, X.H.; Luo, Q.T.; Li, Q.; Sun, G.Y. Adhesively Bonded Joints—A Review on Design, Manufacturing, Experiments, Modeling and Challenges. *Compos. Part B Eng.* **2024**, *276*, 111225. [CrossRef]

12. Xiong, X.H.; Wang, D.S.; Wei, J.; Zhao, P.; Ren, R.; Dong, J.P.; Cui, X. Resistance Welding Technology of Fiber Reinforced Polymer Composites: A Review. *J. Adhes. Sci. Technol.* **2021**, *35*, 1593–1619. [CrossRef]

13. Xie, L.; Liu, H.B.; Wu, W.Q.; Abliz, D.; Duan, Y.G.; Li, D.C. Fusion Bonding of Thermosets Composite Structures with Thermoplastic Binder Co-Cure and Prepreg Interlayer in Electrical Resistance Welding. *Mater. Des.* **2016**, *98*, 143–149. [CrossRef]

14. Bruijn, T.D.; van Hattum, F. Rotorcraft Access Panel from Recycled Carbon PPS—The World's First Flying Fully Recycled Thermoplastic Composite Application in Aerospace. *Reinf. Plast.* **2021**, *65*, 148–150. [CrossRef]

15. Calabrese, L.; Cicala, G.; Di Bella, G.; Proverbio, E.; Tosto, C.; Saitta, L. Optimisation of Ultrasonic Welding Process of Carbon/Epoxy Composites using Nylon-Based or PES Thermoplastic Interlayers. *Compos. Part B Eng.* **2024**, *275*, 11131810. [CrossRef]

16. Pappadà, S.; Salomi, A.; Montanaro, J.; Passaro, A.; Caruso, A.; Maffezzoli, A. Fabrication of a Thermoplastic Matrix Composite Stiffened Panel by Induction Welding. *Aerosp. Sci. Technol.* **2015**, *43*, 314–320. [CrossRef]

17. Li, W.C.; Palardy, G. Investigation of Welding Repair Methods for Thermoplastic Composite Joints. *Compos. Part B Eng.* **2023**, *264*, 110924. [CrossRef]

18. Bonmatin, M.; Chabert, F.; Bernhart, G.; Cutard, T.; Djilali, T. Ultrasonic Welding of CF/PEEK Composites: Influence of Welding Parameters on Interfacial Temperature Profiles and Mechanical Properties. *Compos. Part A Appl. Sci. Manuf.* **2022**, *162*, 107074. [CrossRef]

19. de Souza, S.D.B.; Abrahão, A.B.R.M.; Costa, M.L.; Marlet, J.M.F.; Hein, L.R.O.; Botelho, E.C. Experimental Investigation of Processing Welding Parameters for PPS/Carbon Fiber Laminates for Aeronautical Applications. *Adv. Mater. Res.* **2016**, *1135*, 62–74. [CrossRef]

20. Pereira da Costa, A.; Cocchieri Botelho, E.; Leali Costa, M.; Eiji Narita, N.; Tarpani, J.R. A Review of Welding Technologies for Thermoplastic Composites in Aerospace Applications. *J. Aerosp. Technol. Manag.* **2012**, *4*, 255–265. [CrossRef]

21. Barroeta Robles, J.; Dubé, M.; Hubert, P.; Yousefpour, A. Repair of Thermoplastic Composites: An Overview. *Adv. Manuf. Polym. Compos. Sci.* **2022**, *8*, 68–96. [CrossRef]

22. Rohart, V.; Lebel, L.L.; Dubé, M. Improved Adhesion Between Stainless Steel Heating Element and PPS Polymer in Resistance Welding of Thermoplastic Composites. *Compos. Part B Eng.* **2020**, *188*, 107876. [CrossRef]

23. Brassard, D.; Dubé, M.; Tavares, J.R. Modelling Resistance Welding of Thermoplastic Composites with a Nanocomposite Heating Element. *J. Compos. Mater.* **2021**, *55*, 625–639. [CrossRef]

24. Zhao, P.; Zhang, Z.B.; Li, Y.L.; Tian, L.; Wang, C.; Xiong, X.H. Resistance Welding of Thermoplastic Composites via a Novel Carbon Nanofilm Implant. *Mater. Lett.* **2022**, *328*, 133216. [CrossRef]

25. Marti, I.B.; Kaynak, C. Effects of Interlayer Forms on the Resistance Welding Performance of PAEK/CF Thermoplastic Composite Laminates. *J. Thermoplast. Compos. Mater.* **2023**, *36*, 4945–4976. [CrossRef]

26. Li, X.K.; Zhang, T.Y.; Li, S.; Liu, H.S.; Zhao, Y.; Wang, K. The Effect of Cooling Rate on Resistance-Welded CF/PEEK Joints. *J. Mater. Res. Technol.* **2021**, *12*, 53–62. [CrossRef]

27. Yan, P.; Peng, W.X.; Yang, F.; Cao, Y.; Xiang, M.; Wu, T.; Fu, Q. Investigation on Thermal Degradation Mechanism of Poly(Phenylene Sulfide). *Polym. Degrad. Stab.* **2022**, *197*, 109863. [CrossRef]

28. Oshima, S.; Higuchi, R.; Kato, M.; Minakuchi, S.; Yokozeki, T.; Aoki, T. Cooling Rate-Dependent Mechanical Properties of Polyphenylene Sulfide (PPS) and Carbon Fiber Reinforced PPS (CF/PPS). *Compos. Part A Appl. Sci. Manuf.* **2023**, *164*, 107250. [CrossRef]

29. Liu, Y.H.; Tang, H.P.; Wang, X.Y.; Zhai, Z.Y. Characterization of Joule Heating and Deconsolidation Behavior of Continuous Carbon Fiber Reinforced Polyamide 6 Composites under Self-Resistance Electric Heating. *Polym. Compos.* **2021**, *42*, 6417–6429. [CrossRef]

30. Totla, H.S.; Gupta, A.; Mishra, S.; Sharma, S.; Selvaraj, S.K. Resistance Welding Analysis of Thermoplastic Composite Structures in Aeronautical Applications. *Int. J. Interact. Des. Manuf.* **2023**. [CrossRef]

31. Xiong, X.H.; Zhao, P.; Ren, R.; Zhang, Z.B.; Ji, S.D. Resistance Welded Composite Joints Strengthened by Carbon Fiber Felt: Mechanical Properties, Failure Modes and Mechanism. *Mater. Res. Express* **2019**, *6*, 085323. [CrossRef]

32. Miranda Barbosa, L.C.; Brejão de Souza, S.D.; Botelho, E.C.; Cândido, G.M.; Rezende, M.C. Fractographic Evaluation of Welded Joints of PPS/Glass Fiber Thermoplastic Composites. *Eng. Fail. Anal.* **2019**, *102*, 60–68. [CrossRef]

33. Zhang, Y.X.; Yang, Y.; Hu, J.M.; Luo, Z.; Bi, J.; Li, Y.; Su, J. Microstructure and Joining Mechanism of Al/CFRTP Resistance Element Welded Joints. *J. Manuf. Process.* **2022**, *84*, 251–259. [CrossRef]

34. Lionetto, F.; Pappadà, S.; Buccoliero, G.; Maffezzoli, A. Finite element modeling of continuous induction welding of thermoplastic matrix composites. *Mater. Des.* **2017**, *120*, 212–221. [CrossRef]

35. Mongan, P.G.; Modi, V.; McLaughlin, J.W.; Hinchy, E.P.; O'Higgins, R.M.; O'Dowd, N.P.; McCarthy, C.T. Multi-Objective Optimisation of Ultrasonically Welded Dissimilar Joints Through Machine Learning. *J. Intell. Manuf.* **2022**, *33*, 1125–1138. [CrossRef] [PubMed]

36. Dharma, S.; Masjuki, H.H.; Ong, H.C.; Sebayang, A.H.; Silitonga, A.S.; Kusumo, F.; Mahlia, T.M.I. Optimization of Biodiesel Production Process for Mixed Jatropha Curcas-Ceiba Pentandra Biodiesel using Response Surface Methodology. *Energy Convers. Manag.* **2016**, *115*, 178–190. [CrossRef]

37. Milano, J.; Ong, H.C.; Masjuki, H.H.; Silitonga, A.S.; Chen, W.H.; Kusumo, F.; Dharma, S.; Sebayang, A.H. Optimization of Biodiesel Production by Microwave Irradiation-Assisted TranseSterification for Waste Cooking Oil- Calophyllum Inophyllum Oil via Response Surface Methodology. *Energy Convers. Manag.* **2018**, *158*, 400–415. [CrossRef]

38. Adamu, M.; Haruna, S.I.; Ibrahim, Y.E.; Alanazi, H. Evaluation of the Mechanical Performance of Concrete Containing Calcium Carbide Residue and Nano Silica using Response Surface Methodology. *Environ. Sci. Pollut. Res.* **2022**, *29*, 67076–67102. [CrossRef] [PubMed]

39. Vinayagamoorthy, R. Parametric Optimization Studies on Drilling of Sandwich Composites using the Box-Behnken Design. *Mater. Manuf. Process.* **2017**, *32*, 645–653. [CrossRef]

40. Wei, D.L.; Gu, Y.Z.; Zhu, H.R.; Li, M.; Wang, S.K. Influence of Electrical Heating Metal Mesh and Power Density on Resistance Welding of Carbon Fiber/PEEK Composite. *Polymers* **2022**, *14*, 2563. [CrossRef]

41. Okayasu, M.; Kubota, T. An Electrical Resistance Joining Technology for Carbon Fiber-Reinforced Polyphenylene Sulfide Composites. *J. Mater. Eng. Perform.* **2020**, *29*, 2134–2143. [CrossRef]

42. Available online: https://www.astm.org/d1002-10r19.html (accessed on 24 April 2024).

43. Requena, I.G.; Lobera, A.S.; Fernandez, L.M.V. Characterizing of meshes for resistance welding of high temperature reinforced laminate thermoplastic (RLT). *Procedia Eng.* **2013**, *63*, 556–563. [CrossRef]

44. Eveno, E.C.; Gillespie, J.W. Resistance Welding of Graphite Polyetheretherketone Composites: An Experimental Investigation. *J. Thermoplast. Compos. Mater.* **1988**, *1*, 322–338. [CrossRef]

45. Xiong, X.H.; Tian, L.; Zhao, P.; Zhang, L.; Zhang, Z.B.; Wang, C. Ultra-rapid resistance welding of polypropylene within 1 s by monofilament implant assistance. *Mater. Lett.* **2022**, *317*, 132112. [CrossRef]

46. Du, B.; Chen, L.M.; Liu, H.C.; He, Q.H.; Qin, W.M.; Li, W.G. Resistance welding of glass fiber reinforced thermoplastic composite: Experimental investigation and process parameter optimization. *Chin. J. Aeronaut.* **2020**, *33*, 3469–3478. [CrossRef]

47. Prakash Maran, J.; Manikandan, S.; Thirugnanasambandham, K.; Vigna Nivetha, C.; Dinesh, R. Box–Behnken Design Based Statistical Modeling for Ultrasound-Assisted Extraction of Corn Silk Polysaccharide. *Carbohydr. Polym.* **2013**, *92*, 604–611. [CrossRef]

48. Adamu, M.; Ibrahim, Y.E.; Alanazi, H. Evaluating the Influence of Elevated Temperature on Compressive Strength of Date-Palm-Fiber-Reinforced Concrete using Response Surface Methodology. *Materials* **2022**, *15*, 8129. [CrossRef]

# Innovative CF/PVC Foam Applicated for Automotive Synthetic Leather with High-Performance and Reduced VOC Emissions

Hongfu Li * 🔟, Ying Wu 🔟, Lingyan Wu, Changwei Cui and Kangmin Niu *

School of Materials Science and Engineering, University of Science and Technology Beijing, Beijing 100083, China; wuying@ustb.edu.cn (Y.W.)
* Correspondence: lihongfu@ustb.edu.cn (H.L.); niukm@ustb.edu.cn (K.N.)

**Abstract:** Polyvinyl chloride (PVC) foam, valued for its mechanical and thermal properties along with cost-effectiveness, is extensively utilized across diverse industries. However, its high volatile organic compound (VOC) emissions hinder its adoption in eco-friendly synthetic leather. This study proposes a solution by optimizing the formulation design and foaming processes and achieving mechanical property enhancement via carbon-fiber-reinforced PVC composite foam (CF/PVC). The aim is to reduce PVC usage via enhancing its intrinsic properties. Systematic investigations were carried out on the impact of foaming raw materials, foaming processes, fiber content, and fiber length on the foaming performance, mechanical properties, and VOC emissions. The material formulation and process parameters were successfully optimized. Further assessment of various indicators such as the density, mechanical properties, and tear resistance of synthetic leather samples confirmed that the innovative CF/PVC foam developed in this study meets the requirements for automotive interior applications. Notably, the tensile strength and tear resistance of CF/PVC composite synthetic leather increased by 50% and 29%, respectively, compared to pure PVC, while VOC emissions decreased by 28%. It is anticipated that a more pronounced reduction in VOC emissions will be achieved in practical automotive interior leather applications when further considering the reinforcing effect of fibers, which leads to a reduction in PVC usage. The findings present a technical reference for innovative applications, aiming to enhance PVC foam performance and minimize emissions.

**Keywords:** PVC foam; automotive synthetic leather; carbon fiber; mechanical properties; VOC emission

## 1. Introduction

Thermoplastic polyvinyl chloride (PVC) foam exhibits favorable mechanical properties, thermal insulation, wear resistance, chemical durability, and cost-effectiveness [1,2], contributing to its extensive applications in diverse sectors, including automotive interiors, fashion, home furnishings, etc. [3,4]. Particularly, in the domain of synthetic leather, the characteristics of rich color options, customizable patterns, and animal-friendly make PVC foam a preferred choice and an indispensable material in our daily life [5–9]. However, with the advancement of socioeconomic development and increased consumer awareness of health, as well as a growing emphasis on energy efficiency and environmental sustainability, the inherent high potential volatile organic compound (VOC) emissions associated with PVC, stemming from its chlorine-containing chemical structure and high content of additives, limit its potential applications in environments like automotive interiors, where VOC emissions could directly affect human health. For example, vinyl chloride ($C_2H_3Cl$) is used in the synthesis of PVC. The liver is mainly affected by exposure to air containing vapors of vinyl chloride, resulting in liver damage or impaired liver function [10]. Furthermore, it is highly likely to be carcinogenic for the people residing close to factories that produce vinyl chloride or within heavy VOCs [10–13]. Based on the evaluation of Wang's work [14], it is recommended that PVC products should be stored in a well-ventilated place for at least 28 days before indoor use. Therefore, in the context of meeting basic performance

requirements, reducing PVC usage while simultaneously lowering inherent VOC emission levels holds practical significance for green and health-oriented applications of PVC.

Addressing this challenge, optimizing material formulation and foaming processes is the most direct and efficient means to reduce PVC foam VOC emissions [15]. Furthermore, borrowing from the concept of fiber-reinforced composites in the aerospace industry, where high material-specific strength design can effectively achieve structural weight reduction, achieving high mechanical performance in PVC foam represents a potential and feasible approach to directly reducing PVC usage. Specifically, regarding material formulation and foaming processes, optimization can be achieved through the use of plasticizers, heat stabilizers, and related process parameters. For instance, Demir et al. [16] studied the effects of Ca/Zn stearate and organotin heat stabilizers and zeolite, $CaCO_3$, cellulose, and luffa flours fillers and their concentrations on PVC foam morphology, foam density, compressive mechanical properties, and water uptake capacities. The morphology of the sample without any filler showed that the employment of Ca stearate and Zn stearate heat stabilizers instead of organotin stabilizers increases foam formation and decreases pore sizes and regularity in pore size distribution. Foams with organotin stabilizer were more resistant to heat than the ones with Ca/Zn stearate for long heating periods. Foams, including organotin-based heat stabilizers, have a compact structure. Samples containing zeolite, $CaCO_3$, cellulose, or luffa flour had lower pore volume but higher Young's modulus and stress values compared to unfilled samples. Shi et al. [17] investigated the effect of different plasticizers on PVC properties. The thermal stability, migration resistance, and transparency of PVC with tributyl citrate (TBC) were better than PVC with dioctyl phthalate (DOP) due to the good compatibility between TBC and $Zn(Arg)_2$. The best properties were further achieved when a mixture of dioctyl terephthalate (DOTP) and TBC in a 1:1 ratio was used as a plasticizer for $Zn(Arg)_2$-stabilized PVC. Additionally, the longer the carbon chain in citric acid esters, the better the thermal stability and transparency of PVC sample due to the hydroxyl group in citric acid esters. Santos et al. [18] introduced paraffin phase change materials to improve the thermal regulation performance of PVC foam synthetic leather. This addition increased the response time of synthetic leather to changes in environmental temperature, achieving a warming effect in winter and a cooling effect in summer, thereby enhancing comfort. It can be inferred that by selecting appropriate formulations of PVC additives and optimizing process parameters it is possible to achieve low VOC emissions by enhancing the stability of PVC.

For the modification of PVC to achieve high mechanical performance, the application of fiber-reinforced polymers and foaming materials to achieve high specific strength and realize PVC usage reduction is a burgeoning trend and research focus in the field [19,20]. Fiber-reinforced PVC foams can significantly enhance the compressive strength, stress relaxation damping, deformation, and thermal deformation temperature of the original foam matrix. For instance, Huo et al. [21] carried out injection molding studies to investigate the impact of molding pressure, temperature, and the amount of glass fiber on the properties of PVC materials. Higher pressure resulted in improved molding effectiveness, leading to increased tensile and shear strength. An optimal mold temperature around 100 °C was recommended, as lower temperatures resulted in material looseness and an uneven surface, while excessively high temperatures led to PVC resin degradation and increased ductility. The recommended glass fiber addition was 15 wt.%. Hassan et al. [22] studied the influence of the orientation angle of glass fibers in PVC substrates on material impact resistance. The highest impact compressive strength was observed when the load direction was perpendicular to the glass fibers, whereas the resistance to impact was minimal when the load direction was parallel to the fibers. Fu et al. [23] utilized extrusion and injection molding to investigate the effects of different fiber addition amounts and lengths on product performance. The study indicated that an increase in fiber content significantly reduced the residual fiber length, resulting in a sudden drop in material strength and modulus, making it prone to breakage. Zhao et al. [24] explored the processing of fiber-reinforced PVC composite materials using glass fiber cloth, short glass fibers, and PVC resin as base

materials, leading to a substantial improvement in PVC tensile strength, wear resistance, and service life. Kabir et al. [25] proposed the concept of a critical fiber length in their study of fiber-reinforced polymer materials. When fibers are too long their dispersion is poor, leading to aggregation and bending, causing stress concentration, and preventing the achievement of the desired reinforcement effect. Therefore, in practical studies of enhanced modification, it is crucial to optimize fiber content and length parameters.

However, as evident from the aforementioned, the PVC foam modification primarily focused on glass fiber reinforcement. Few research studied involving carbon-fiber-reinforced PVC composite foam (CF/PVC) were reported. Meanwhile, studies have been conducted on the modification of other thermoplastic resins and foams using carbon fiber reinforcement, owing to its significant impact on high specific strength. For instance, Yunus et al. and Li et al. [26,27] investigated the mechanical properties of short-carbon-fiber-reinforced polypropylene composite materials (CF/PP). The optimal tensile strength and bending performance were achieved when the carbon fiber content was 10%, concurrently exhibiting some improvement in wear resistance. Rezaei et al. [28] explored the impact of different carbon fiber lengths on the properties of CF/PP composites. Results indicated that, when the fiber content was constant, composites reinforced with longer fibers exhibited more pronounced improvements in temperature resistance and mechanical properties. Wang et al. [29,30] investigated the influence of $CO_2$ saturation pressure and carbon fiber weight percentage on the cell morphology of CF/PP composite foams. At low weight percentages of carbon fiber, a significant portion of the composites remained unfoamed with non-uniform cell size distribution. However, well-defined closed cell structures were observed in the foamed areas. The most uniform cell distribution and morphology were noted with 25 wt.% carbon fiber. Sebaey et al. [31,32] investigated the energy absorption behavior of polyurethane (PU) foam-filled, carbon-fiber-reinforced polymer composite tubes under impact, demonstrating that PU foam is suitable for designing advanced energy absorbers.

This study, targeting the green solution of PVC foam synthetic leather materials for automotive interiors, systematically manipulated the foam formulation, component quantities, and the temperature and time process parameters to investigate their impact on foaming and mechanical properties. The influences of short carbon fibers on the foaming and mechanical properties of PVC foam were further investigated. Ultimately, high-performance CF/PVC composite foam synthetic leather was achieved, characterized by surface density, mechanical properties, and environmental performance that meet the requirements for automotive interior applications, displaying both high performance and low VOC emissions.

## 2. Materials and Methods

### 2.1. Materials

Three types of PVC paste produced via emulsification methods were used for raw matrix resin comparison. The PVC base material of PR-450 (K-value 65) was supplied by Taiwan Plastics Corporation (Ningbo) Limited (Ningbo, China), while 75HV (K-value 73) and 75SK (K-value 72) were provided by Guangzhou Denghua Chemical Co., Ltd. (Guangzhou, China). The plasticizer of diisononyl phthalate (DPHP) was supplied by Xiong County Jinquan Chemical Co., Ltd. (Baoding, China). The foaming agent of azodicarbonamide (ADC) was sourced from Hengshui Jindu Rubber & Chemical Co., Ltd. (Hengshui, China). The zinc oxide foaming promoter, denoted as 311AC, was supplied by Zibo Huaxing Plastic Additives Co., Ltd. (Zibo, China). The acrylic ester processing aid, PA-40, was purchased from Shanghai Kynol Chemical Co., Ltd. (Shanghai, China). The powder calciumzinc stabilizer, known as Stab5, was provided by Guangdong Gaokeda Technology Industry Co., Ltd. (Shantou, China). Short-cut carbon fibers were obtained from Shanghai Lishuo Composite Material Technology Co., Ltd. (Shanghai, China).

## 2.2. Preparation of PVC Foam

A predetermined ratio of PVC base material, plasticizer DPHP (60–80 phr), foaming agent ADC (10–30 phr), processing aid PA-40 (1–4 phr), and heat stabilizer Stab5 (1 phr) were thoroughly mixed and plasticized using a stirring machine (SFJ-400, Huapai Chemical Equipment Co., Ltd., Hefei, China). Subsequently, a vacuum was applied using a vacuum stirrer (ME0089, Getai Machinery Co., Ltd., Dongguan, China) to eliminate air bubbles. The mixed resin paste was poured onto a release paper, and a uniform layer of resin film with a thickness of 0.3 mm was applied using a scraper on the release paper. Foam expansion was carried out on a preheated foaming machine (Jolly, Zhengda Machinery Co., Ltd., Ruian, China) at temperatures ranging from 190 to 215 °C for a foaming duration of 40–90 s. The control of various components of PVC foam and foaming parameters (such as foaming temperature and foaming time) was achieved, and the preparation process of PVC foam was optimized by examining the foam thickness and pore size distribution. The mass ratios of different materials involved in the study were based on the mass of the PVC base material, set as 100 phr.

## 2.3. Preparation of CF/PVC Composite Foam

The short carbon fiber reinforced PVC foam composite materials were prepared using a compression molding method. Optimized material compositions, along with a specific quantity (0–25 phr) of short carbon fibers (0–8 mm), were manually mixed through hand stirring. The pre-mixed materials were then poured into a preheated internal mixer (XH-406BE-50-400, Xihua Testing Instrument Co., Ltd., Dongguan, China) maintained at 150 °C. The front roller speed of the mixer was set at 15 r/min, while the rear paddle speed was set at 10 r/min, and the mixing process continued for 15 min. The resulting block-shaped material was placed into a mold lined with release paper, with a thickness of 0.3 mm. Using a flat vulcanization press (XH-406BE-50-400, Dongguan Xihua Machinery Technology Co., Ltd., Dongguan, China), the material was hot-pressed at 160 °C for 1 min, followed by a cold press for 2 min. Subsequently, the block-shaped material was placed in a preheated coating machine at 195 °C and foamed for 60 s. After the foaming process, the material was removed and cooled to room temperature for 24 h. The simplified preparation process for CF/PVC composite foam is illustrated in Figure 1.
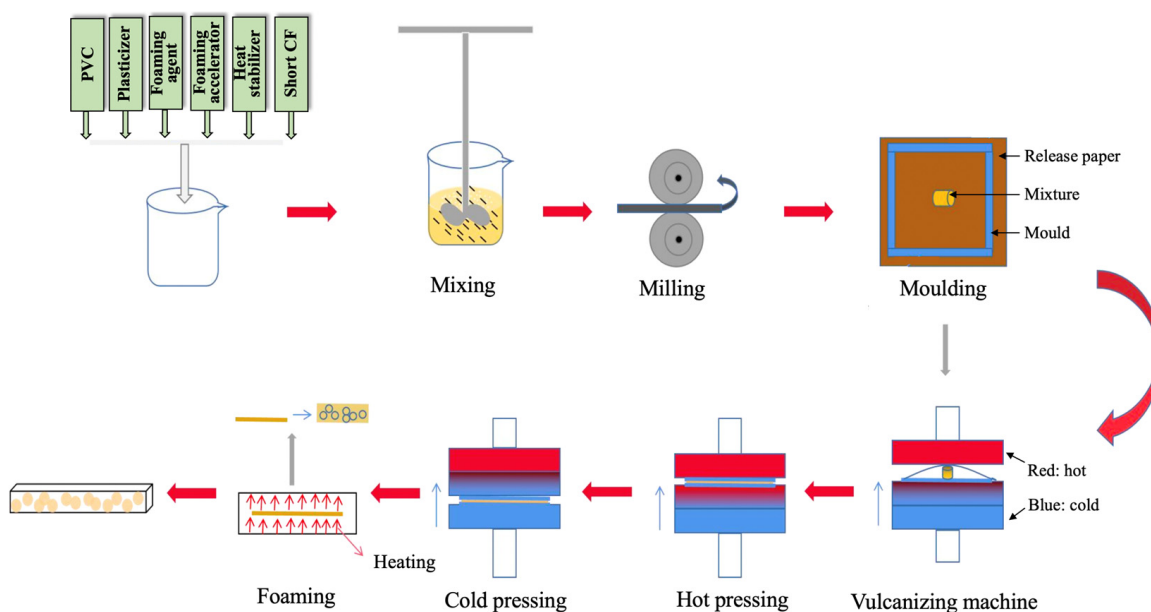


**Figure 1.** Schematic illustrations of the fabrication process of CF/PVC composite foam using the calendering method.

## 2.4. Preparation of PVC Foam Synthetic Leather

The preparation process of PVC foam synthetic leather, including CF/PVC composite foam synthetic leather, is depicted in Figure 2.
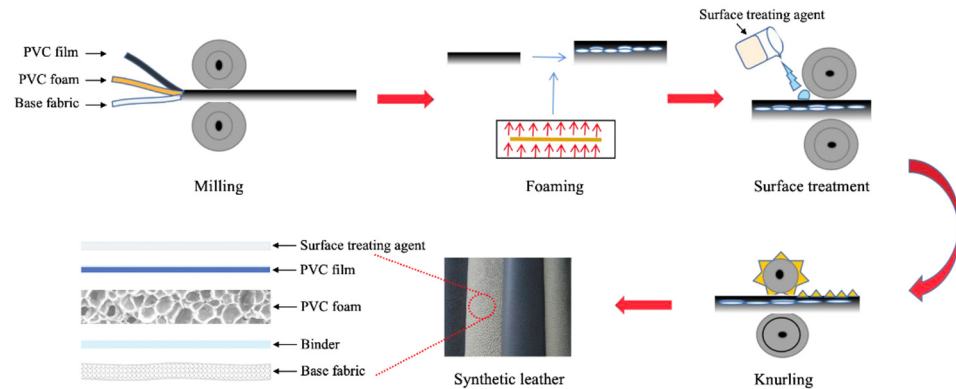


**Figure 2.** Schematic fabrication process and the layered structure of PVC foam artificial leather.

Blending and pre-plasticization were first performed according to the formulation of PVC foaming material. Subsequently, the mixture was pressed through the hot and cold pressing processes described in Section 2.3 to form a 0.3 mm thick composite material sheet. After a layer of surface PVC film was coated on the sheet in the coating machine, they were heated to 195 °C and maintained for 60 s to shape the surface layer and foam the PVC foaming layer. Then, a surface treating agent of 0.1 mm thick tax was coated on the surface of the foamed layer, and the base fabric was placed flat on the adhesive, put into the coating machine, and heated and dried. Finally, the surface pattern treatment was carried out using water-based polyurethane on a knurling machine after the coating and drying process.

## 2.5. Characterizations and Tests

The apparent density of the foam material was measured using an automatic electronic density meter (BYES-600C, Youzhi Automation Equipment Co., Ltd., Huizhou, China) based on the Archimedes principle buoyancy method according to GMW3182. Foam thickness was measured using a digital thickness gauge (0–10 mm/0.01, Huizhou Xinhui Instrument Equipment Co., Ltd., Huizhou, China), and the foam morphology was observed using a handheld digital microscope (DGX1-AM413, Beijing Haifuda Technology Co., Ltd., Beijing, China). Microscopic morphology was examined using scanning electron microscopy (SEM, Quanta 650, FEI Company, Hillsboro, OR, USA). Image J software (v1.54) was utilized for data collection and analysis of foam pore size distribution, importing microscopic images of the pores into the software for automatic analysis of pore size distribution.

The tensile properties were tested according to the General Motors test standard GMW 3010N [33], using dumbbell-shaped specimens. Tear resistance performance was evaluated according to the ISO 13937-2 standard [34], employing trouser tear specimens for testing. Tensile and tear properties were analyzed using a high–low temperature tensile testing machine (CM2500D, Dawei Xing Technology Co., Ltd., Shenzhen, China) with a test speed set at 100 mm/min, and each sample was tested 3–5 times.

The headspace method, a common test in the automotive industry for benzene-type volatile organic compounds, was used to evaluate the VOC emission from PVC foam synthetic leather according to GMW3205. Specifically, 2 g of PVC foam synthetic leather was placed in a 20 mL headspace bottle and kept at 120 °C for 60 min. A certain amount of gas was then withdrawn from the headspace bottle using a syringe, and the withdrawn gas was analyzed using a gas chromatograph (7890A GC, Agilent, Santa Clara, CA, USA) to assess VOC emissions.

## 3. Results and Discussion

### 3.1. Properties of PVC Foam

#### 3.1.1. The Influence of PVC Raw Materials on Foaming

As depicted in Figure 3a, the sequence of foaming thickness and apparent density for three different PVC types is 75HV > PR-450 > 75SK.
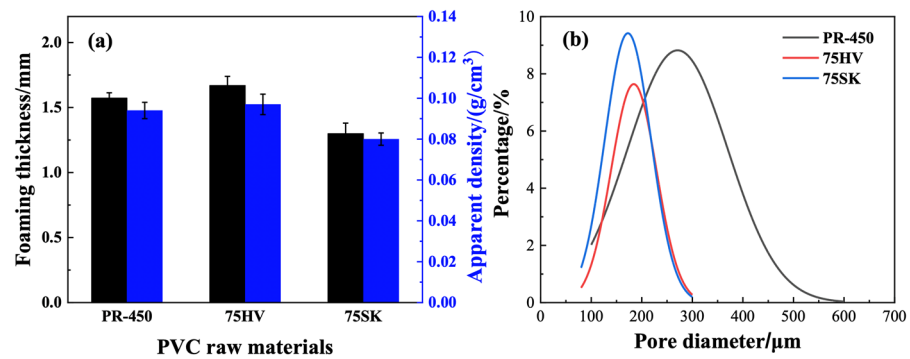


**Figure 3.** Foaming properties of different PVCs: (**a**) Foaming thickness and apparent density; (**b**) Pore size distribution.

Generally, larger foaming thickness should result in smaller apparent density of the foam. However, in this study, as the foaming thickness of PVC increases its apparent density also increases. This is attributed to the positive correlation between the density of PVC, serving as the base material for foaming, and the density of the foamed material. The density of PVC powders follows the order of 75HV > PR-450 > 75SK, consequently influencing the apparent density sequence of the foamed materials, which is also 75HV > PR-450 > 75SK. The SEM images (Figure 4) of the pore structure after foaming for the three PVC types were imported into the Image J software v1.54, and the results of the pore size distribution are shown in Figure 3b.
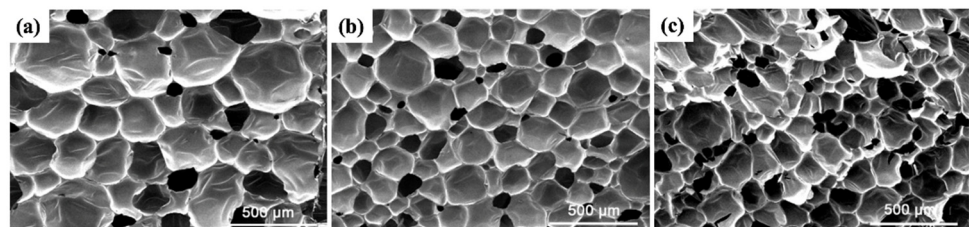


**Figure 4.** SEM images of different PVC foams: (**a**) PR-450; (**b**) 75HV; (**c**) 75SK.

The study indicates that the pore size distribution for PR-450 foaming is between 100 and 600 μm, mainly concentrated in the range of 200–400 μm. For 75HV and 75SK foaming, the pore size distribution is within 100–300 μm, predominantly centered around 100–250 μm. Due to the higher viscosity of 75HV resin paste compared to 75SK resin paste, it inhibits pore overflow. Consequently, 75HV foaming material has more pores internally than 75SK, contributing to the larger foaming thickness of 75HV. Considering both foaming thickness and pore size distribution, 75HV is selected as the preferred PVC raw material for subsequent research.

#### 3.1.2. The Influence of Functional Additives on PVC Foaming

The PVC foaming process involves three main steps: bubble nucleus formation, growth, and stabilization. During foaming, the system undergoes rapid depressurization or heating, causing an increase in viscosity and expansion of the melt, leading to the generation of numerous gas nuclei under these unstable conditions. The type and amount of foaming agent are crucial factors influencing the foaming performance of PVC foam

materials. Therefore, selecting appropriate foaming agents and their concentrations can produce materials with increased foaming thickness and reduced weight. Investigating the effect of foaming agent concentration on PVC foaming, different amounts of foaming agents were introduced. The results indicate that the chemical foaming agent ADC performs better than physical foaming agents, as shown in Figure 5a.
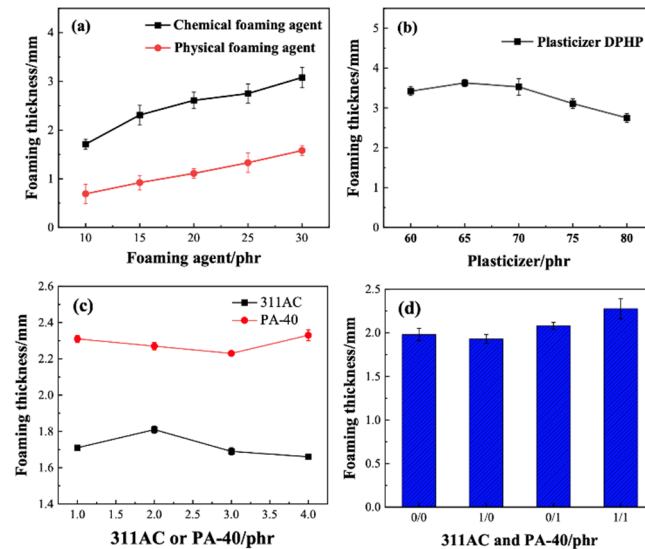


**Figure 5.** Influence of the material and content of the foaming agent (**a**), plasticizer (**b**), accelerator 311AC and processing agent PA-40 (**c**), and 311AC/PA-40 content on the foaming thickness of PVC foams (**d**).

An increase in foaming agent concentration leads to an increase in the number of pores, accompanied by the phenomenon of pore fusion and enlargement. In other words, the quantity of large pores and foaming thickness increases. Too little foaming agent results in insufficient foaming thickness, while excessive amounts lead to undesirable coalescence and stringing between pores, causing material damage.

To investigate the influence of plasticizer dosage on PVC foaming characteristics, different amounts of plasticizer were added to PVC foam materials. As shown in Figure 5b, with the increase in plasticizer content, the foaming thickness initially increases and then decreases. The presence of the plasticizer reduces the viscosity of the PVC melt, promoting the growth of pores and making them expand more easily after pressure removal, thereby increasing the foaming thickness and volume [5]. However, when the dosage of DPHP is relatively high there is a noticeable decrease in foaming thickness. Excessive addition of plasticizer can result in excessively low viscosity of the PVC melt, reducing the hindrance to pore growth. This may lead to phenomena such as pore adhesion, coalescence, and increased collapse between pores [35]. Through experiments, it was determined that adding 65 phr of DPHP plasticizer could produce PVC foam materials with better foaming effects, achieving a foaming thickness of up to 3.63 mm.

ADC is a commonly used foaming agent, but its dissolution temperature is relatively high. For low decomposition temperature materials like PVC, this can lead to issues such as temperature mismatch and uneven pore distribution. To address these problems, foaming additives can be added to optimize the performance of ADC. As shown in Figure 5c, the research results indicate that adding an appropriate amount of foaming additive (331AC) can enhance the foaming performance of PVC. However, with the increase in processing aid (PA-40) content, the foaming thickness of PVC initially decreases and then increases. This is because the increased content of processing aid leads to frictional heat generation, resulting in higher temperature and shorter resin melting time, which reduces foaming thickness. However, when the addition amount is 4 phr, the increased temperature and rapid resin melting lead to larger pores and increased foaming thickness. Under different

311AC/PA-40 ratios (Figure 5d), when 311AC/PA-40 is 1/1 PVC exhibits the best foaming performance, achieving a foaming thickness of 2.31 mm, better than the cases without additives or with only one type of additive. Through comprehensive analysis, the optimal solution is to add 1 phr of foaming additive and 1 phr of processing aid.

Based on the above exploration, the preferred formulation for PVC foaming materials is presented in Table 1.

**Table 1.** Optimized compounds of foaming PVC.

| Material | Role | Weight Ratio (phr) |
|----------|------|--------------------|
| PVC | Resin | 100 |
| DPHP | Plasticizer | 65 |
| ADC | Foaming agent | 25 |
| 311AC | Foaming accelerator | 1 |
| PA-40 | Processing agent | 1 |
| Stab5 | Heat stabilizer | 1 |

3.1.3. The Influence of Foaming Process on PVC Foaming

Foaming temperature and time are the two crucial parameters affecting PVC foam pore parameters. This is attributed to the fact that the process of foaming agent decomposition does not occur instantaneously and requires heating and a certain amount of time.

In order to investigate the effect of PVC foaming temperature on the foaming thickness, experiments were conducted using PVC resin paste with different foaming temperatures but the same foaming time. In the actual production of products, a low heating temperature may result in the foaming ratio of the product not meeting the requirements, with fewer formed pores, and the product's elasticity being relatively poor. Conversely, a high heating temperature may cause the premature decomposition of the foaming agent, leading to the foaming thickness of the foamed material not reaching the expected level [36]. As shown in Figure 6a, foaming was carried out on the PVC resin paste at temperatures ranging from 190 °C to 215 °C, and the foaming thickness was tested.
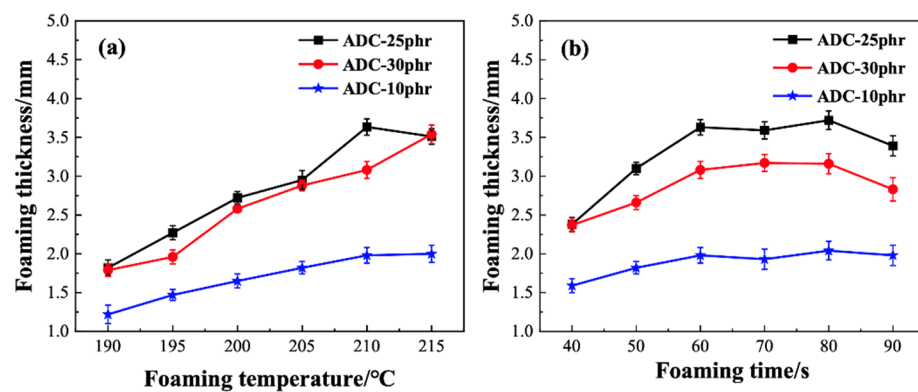


**Figure 6.** Influence of foaming temperature (**a**) and foaming time on the foaming thickness (**b**) of PVC foams.

The results indicate that with the increase in foaming temperature the foaming thickness also increases. When the foaming agent ADC content is 25 phr and the foaming temperature is 210 °C the foaming thickness reaches its maximum value. This is because, with the increase in temperature, the decomposition rate of the foaming agent accelerates, leading to a faster generation of gas, thereby increasing the foaming thickness.

Utilizing a constant foaming temperature of 210 °C, we investigated the influence of foaming time on the foaming performance of PVC. As shown in Figure 6b, with an increase in foaming time from 40 s to 90 s, the foaming thickness exhibited a gradually increasing trend. Specifically, from 40 s to 60 s the foaming thickness of PVC increased rapidly, while

after 60 s the increase became less pronounced; in some cases, a decrease in foaming thickness was observed. This phenomenon is attributed to the gradual decomposition of the ADC foaming agent at 210 °C, releasing gas that forms within the matrix, achieving the foaming effect. As the foaming heating time increases, the decomposition rate of the foaming agent accelerates, and the speed of gas generation also increases. Due to the sharp increase in the number of bubbles, the foaming expansion rate rapidly increases, leading to an increase in foaming thickness. However, when the decomposition of the generated gas ceases upon further heating, the already-formed PVC pores may stick together due to the influence of heat, resulting in phenomena such as coalescence and collapse of the foam structure, leading to a reduction in foaming thickness. Therefore, we recommend selecting the optimal foaming temperature and time as 210 °C and 60 s, respectively.

### 3.2. Properties of CF/PVC Composite Foam

#### 3.2.1. The Influence of Carbon Fibers on PVC Foaming

We employed four different lengths of carbon fibers (2 mm, 4 mm, 6 mm, and 8 mm) to reinforce PVC foamed materials and examined their foaming quality and apparent density. As depicted in Figure 7a with 8 phr carbon fibers, the increase in carbon fiber length has an impact on the foaming quality of PVC foamed materials.
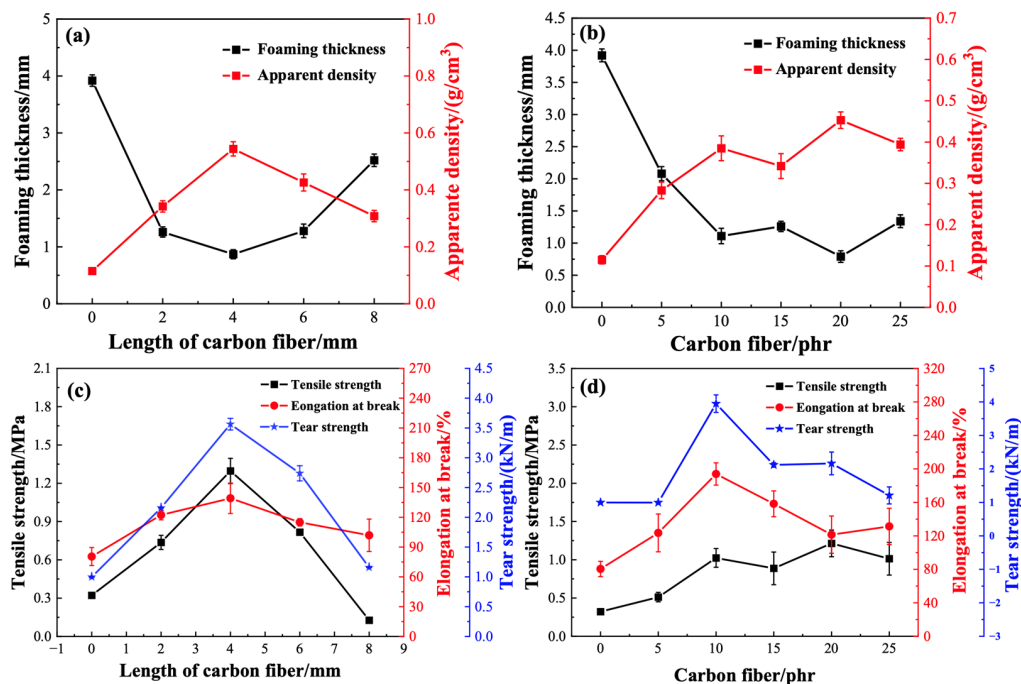


**Figure 7.** Influence of length and content of short carbon fibers on the foaming thickness and apparent density (**a**,**b**) and mechanical properties (**c**,**d**) of PVC foams.

Specifically, with the elongation of carbon fiber length, the foaming thickness of PVC foamed materials initially decreases and then increases, while the density exhibits an initial increase followed by a decrease. This phenomenon arises due to the introduction of short carbon fibers, which facilitates the formation of numerous gas nuclei alongside the carbon fibers. During the growth of gas nuclei, hindered by the presence of carbon fibers, the bubbles are less likely to expand, ultimately resulting in smaller pore diameters and reduced material foaming thickness. When adding carbon fibers with lengths greater than 4 mm, the foaming extent of PVC foamed materials increases with the elongation of the carbon fiber length. This is because longer added carbon fiber lengths result in the formation of more gas nuclei, which reach saturation earlier and are prone to overflow and expansion. Figure 7b illustrates the impact of using different short carbon fibers on the foaming thickness and density of PVC foamed materials. The foaming thickness exhibits

a fluctuating decreasing trend with the increase in short carbon fiber content, while the apparent density demonstrates an opposite trend with an increase in fiber content.

### 3.2.2. The Influence of Carbon Fibers on the Mechanical Properties of PVC Foam

To investigate the impact of adding short-cut fibers on the mechanical properties of PVC foam materials, various lengths and quantities of short-cut carbon fibers were incorporated into PVC foaming materials, and their changes in mechanical properties were recorded. As depicted in Figure 7c, with the increase in carbon fiber length the strength of PVC foaming materials initially increases and then decreases. Specifically, when the added carbon fiber length is 4 mm, the tensile strength, fracture elongation, and tear strength are 1.30 MPa, 139%, and 3.56 kN/m, respectively. For carbon fiber lengths less than 4 mm, the increase in fiber length results in a greater enhancement of the mechanical strength of PVC foam. This is because, with a moderate increase in carbon fiber length, the contact area between short-cut carbon fibers and PVC increases, reinforcing the interface interaction and requiring greater tension upon fracture, thereby leading to increased mechanical strength. However, when carbon fiber lengths exceed 4 mm, a significant decrease in material strength is observed. This is attributed to the entanglement and agglomeration of excessively long carbon fibers, causing uneven distribution within the resin matrix. Consequently, areas with entangled carbon fibers are more prone to fracture under external forces, resulting in a decline in material strength.

Continuing the exploration using short-cut carbon fibers with a length of 4 mm, we examined the influence of fiber content on the properties of PVC foam materials. Figure 7d illustrates the relationship between tensile strength, tear strength, fracture elongation, and the added amount of short-cut carbon fibers. Tensile strength shows a gradual increase with the rise in short-cut carbon fiber content. However, tear strength and fracture elongation exhibit an initial increase followed by a decrease with the increase in short-cut carbon fiber content, reaching maximum values of 3.95 kN/m and 194%, respectively, at a fiber addition of 10 phr.

To explore the reasons behind the enhancement in mechanical properties with fiber addition, we conducted SEM observations of the PVC foam after mechanical property testing, as shown in Figure 8.
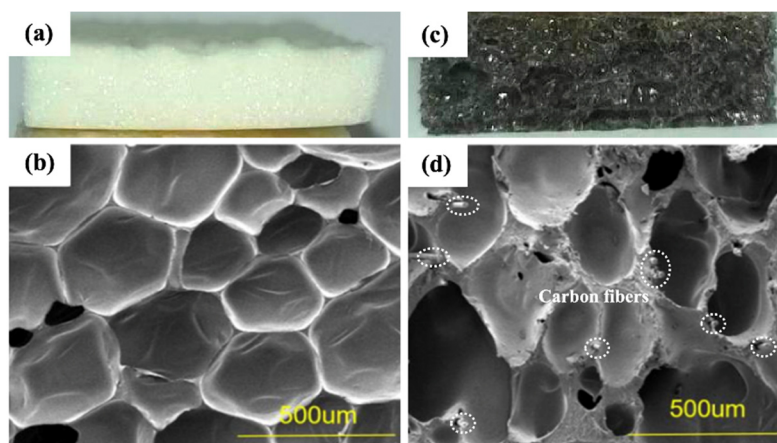


**Figure 8.** Digital and SEM images: (**a**,**b**) PVC foam; (**c**,**d**) CF/PVC composite foam.

After adding short-cut carbon fibers, the morphology of PVC foam materials remained similar to that before addition, characterized by nearly circular closed cells and a small number of open cells. Short-cut carbon fibers were mainly distributed on the cell wall, reinforcing the cell wall strength. Under the internal stress of pure foam, once a foam column ruptures, adjacent foam walls also rupture, and cracks rapidly propagate to nearby foam. In fiber reinforced foam, when cracks widen to the fibers, the presence of fibers causes

crack termination and deviation, reducing the internal stress of cracks and enhancing the overall mechanical properties of PVC foam materials.

### 3.3. CF/PVC Composite Foam Synthetic Leather

3.3.1. Areal Density and Mechanical Properties

Table 2 provides a comparison of the areal density, tensile properties, and tear resistance of synthetic leathers produced from different PVC foam materials with automotive standard values.

**Table 2.** Areal density and tensile property of artificial leather fabricated using different PVC foams.

|  | PVC Foam | CF/PVC Foam | Requirements |
|---|---|---|---|
| Areal density (g/m$^2$) | 765 | 773 | 800 $\pm$ 80 [37] |
| Tensile strength (MPa) | 32.6 | 48.9 | >35 [33] |
| Elongation at break (%) | 214 | 185 | 180–215 [33] |
| Tear strength (kN/m) | 11.4 | 14.7 | >10 [34] |

- Areal density: The areal density of automotive PVC foam synthetic leather should be below 800 $\pm$ 80 g/m$^2$ [37]. In this study, the average areal densities of the PVC foam synthetic leather and CF/PVC composite foam synthetic leather prepared were 765 g/m$^2$ and 773 g/m$^2$, respectively, meeting the requirements.

- Tensile properties: The tensile strength of synthetic leather made from PVC foam material is 32.6 MPa. In contrast, the tensile strength of synthetic leather prepared from CF/PVC composite foam increased to 48.9 MPa, a 50% improvement. This is attributed to the increased tensile strength of the foamed layer, and the addition of short fibers results in a rougher sample surface, enhancing the bonding between the PVC foam layer and other layers of PVC synthetic leather, thereby improving the overall tensile strength. However, the break elongation of synthetic leather prepared using CF/PVC foam material is reduced. Specifically, the elongation at break for synthetic leather prepared from PVC foam material is 214%, while for CF/PVC composite foam it decreases to 185%. The addition of carbon fibers reduces the mobility of PVC molecular chains during deformation, resulting in decreased plasticity, ultimately leading to a reduction in the elongation at break of PVC synthetic leather and a slight decrease in flexibility. Nevertheless, automotive-grade PVC foam synthetic leather requires a tensile strength greater than 35 MPa and a break elongation of 180–215% [33]. The tensile strength and break elongation of CF/PVC composite synthetic leather in this study still comply with the specified criteria.

- Tear resistance: The tear strength of synthetic leather prepared from neat PVC foam material is 11.4 kN/m, whereas synthetic leather prepared from CF/PVC composite foam material shows an increased tear strength of 14.7 kN/m. This improvement is attributed to the addition of fibers, which hinder the expansion of cracks, requiring greater tearing force to rupture PVC foam synthetic leather and, thus, enhancing tear resistance. Automotive-grade PVC foam synthetic leather requires tear strength greater than 10 kN/m [34], and the tear strength of CF/PVC foam synthetic leather in this study also meets the requirements.

3.3.2. VOC Emissions Evaluation

We carried out tests for "three aldehydes and five benzenes" and the overall VOC volatilization situation. Table 3 presents the VOC emission characteristics of two types of PVC foam synthetic leather.

The VOC tests for synthetic leather produced using PVC foam and CF/PVC composite foam both met the requirements [38]. Although the addition of carbon fibers resulted in a slight increase in the release of aldehydes and benzene VOCs in CF/PVC composite foam synthetic leather, the total VOC volatilization decreased from 5.505 mg/m$^3$ for pure PVC foam to 3.975 mg/m$^3$. This may be attributed to the fact that adding fibers helps

promote bubble nucleation, increasing micropores in the foam, which is conducive to the volatilization and emission of VOCs. However, at the same time, the inclusion of carbon fibers to some extent restricts the movement of PVC molecular chains, enhances the thermal stability of the foaming material, and delays aging and thermal decomposition under high-temperature conditions, thereby reducing the total VOC emissions. Similar results were also observed in hemp-fiber-reinforced polypropylene composites, where the VOC emissions reduction was attributed to the thermal stability enhancement through fiber reinforcement, as evidenced by the differential thermal analysis (DTA) and thermogravimetric analysis (TGA) [39]. Gu et al. [40] clearly showed that PU composite foam had improved cell size and higher glass transition temperature ($T_g$) due to the presence of wood fiber characterized by thermal gravimetric analysis (TGA) and differential scanning calorimetry (DSC) results. Furthermore, the carbon fiber inducing polymer thermal stability enhancement can be widely found in traditional fiber-reinforced thermoplastic composites such as CF/PP, CF/Nylon, etc. [19,41]. Therefore, in this paper, the addition of CF not only enhances the mechanical properties of PVC foam as expected, which can reduce VOC emissions due to the PVC usage reduction attributed to the high specific strength of CF/PVC itself, but also directly enhances the thermal stability of PVC foam, which further lowers the level of VOC emissions during its applications. In conclusion, the addition of carbon fibers plays a dual role in positively reducing VOC emissions from PVC foam when applied in synthetic leather.

**Table 3.** VOC emissions of PVC and CF/PVC foam synthetic leather (Units: mg/m$^3$).

| PVC Foam Materials | Methanal | Acrolein | Acetaldehyde | Benzene | Methylbenzene | Styrene | Xylene | Ethylbenzene | Total VOC [1] |
|---|---|---|---|---|---|---|---|---|---|
| PVC foam | 0.005 | 0.000 | 0.022 | 0.002 | 0.019 | 0.000 | 0.000 | 0.000 | 5.505 |
| CF/PVC foam | 0.009 | 0.000 | 0.030 | 0.005 | 0.025 | 0.000 | 0.029 | 0.000 | 3.975 |
| Requirements [38] | ≤0.10 | ≤0.05 | ≤0.05 | ≤0.11 | ≤1.10 | ≤0.26 | ≤1.50 | ≤1.50 | |

[1] The "Total VOC" not only includes aldehydes and benzene but also encompasses plasticizers, substances generated from PVC aging itself, various stabilizers, materials produced by the thermal decomposition of ADC foaming agent, and the cumulative sum of some chlorine-containing small molecules.

## 4. Conclusions

This study aimed to enhance the performance of PVC foam materials and reduce VOC emissions. The optimization of the PVC foam material formulation and foaming process, coupled with the incorporation of short carbon fiber reinforcement technology, was undertaken to produce PVC foam and CF/PVC composite foam synthetic leather with comprehensive and application-compliant properties. The key conclusions are as follows:

1. The types and ratios of PVC raw materials, plasticizers, foaming agents, and processing aids significantly impact the foaming performance of PVC foam materials. The optimal foaming formulation for PVC was determined as follows: using 75HV as the base material, adding 65 phr plasticizer, 25 phr foaming agent, 1 phr foaming assistant, 1 phr processing aid, and 1 phr thermal stabilizer.

2. The tensile strength and tear strength of CF/PVC composite foam synthetic leather were improved compared to PVC foam synthetic leather, increasing from 32.6 MPa to 48.9 MPa and from 11.4 kN/m to 14.7 kN/m, respectively. Although the elongation at break decreased from 214% to 185%, it still met the requirements for automotive interior applications. High performance implies reduced PVC usage and lower VOC emissions.

3. Due to the hindering effect of carbon fiber on PVC molecular chain movement, the aging of PVC foam was inhibited, resulting in a reduction in total VOC emissions from 5.505 mg/m$^3$ for PVC foam synthetic leather to 3.975 mg/m$^3$ for CF/PVC composite foam synthetic leather.

4. The CF/PVC composite foam synthetic leather production process presented in this study demonstrates excellent scalability. Future endeavors could focus on optimizing

cost implications to enhance its market competitiveness, for instance, by incorporating recycled carbon fibers.

## References

1. Tang, Y.; Zhang, W.; Jiang, X.; Zhao, J.; Xie, W.; Chen, T. Experimental investigations on phenomenological constitutive model of closed-cell PVC foam considering the effects of density, strain rate and anisotropy. *Compos. Part. B-Eng.* **2022**, *238*, 109885. [CrossRef]
2. You, J.; Xing, H.; Xue, J.; Jiang, Z.; Tang, T. Preparation of rigid cross-linked PVC foam with excellent thermal insulation through adding high-reflectivity IR opacifier. *Compos. Sci. Technol.* **2021**, *203*, 108566. [CrossRef]
3. Balıkoğlu, F.; Demircioğlu, T. Flexural behaviour of the composite sandwich beams with grid-scored foam: Experimental and theoretical approach. *Thin-Walled Struct.* **2022**, *171*, 108691. [CrossRef]
4. Luong, D.D.; Pinisetty, D.; Gupta, N. Compressive properties of closed-cell polyvinyl chloride foams at low and high strain rates: Experimental investigation and critical review of state of the art. *Compos. Part. B-Eng.* **2013**, *44*, 403–416. [CrossRef]
5. Zattini, G.; Ballardini, S.; Benelli, T.; Mazzocchetti, L.; Giorgini, L. Safer plasticized polyvinyl chloride synthetic leathers for the automotive industry: Evaluation of alternatives to antimony compounds as flame retardants. *Polym. Eng. Sci.* **2019**, *59*, 2488–2497. [CrossRef]
6. Altindag, I.A.; Akdogan, Y. Spectrophotometric characterization of plasticizer migration in poly (vinyl chloride)-based artificial leather. *Mater. Chem. Phys.* **2021**, *258*, 123954. [CrossRef]
7. Zhang, J.P.; Zhang, C.C.; Zhang, F.-S. A novel process for waste polyvinyl chloride recycling: Plant growth substrate development. *J. Environ. Chem. Eng.* **2021**, *9*, 105475. [CrossRef]
8. Defonseka, C. *Polymeric Coating Systems for Artificial Leather: Standard and Latest Technologies*; Walter de Gruyter GmbH & Co KG: Berlin, Germany, 2022.
9. Xu, M.; Cao, C.; Hu, H.; Ren, Y.; Guo, G.; Gong, L.; Zhang, J.; Zhang, T.; Yao, H. Perspective on the disposal of PVC artificial leather via pyrolysis: Thermodynamics, kinetics, synergistic effects and reaction mechanism. *Fuel* **2022**, *327*, 125082. [CrossRef]
10. David, E.; Niculescu, V.C. Volatile organic compounds (VOCs) as environmental pollutants: Occurrence and mitigation using nanomaterials. *Int. J. Environ. Res. Public Health* **2021**, *18*, 13147. [CrossRef]
11. Hahladakis, J.N.; Velis, C.A.; Weber, R.; Iacovidou, E.; Purnell, P. An overview of chemical additives present in plastics: Migration, release, fate and environmental impact during their use, disposal and recycling. *J. Hazard. Mater.* **2018**, *344*, 179–199. [CrossRef]
12. Health Care Without Harm Europe. *The Polyvinyl Chloride Debate: Why PVC Remains a Problematic Material*; Health Care Without Harm Europe: Bruxelles, Belgium, 2021.
13. Xue, J.; Cai, H.; Li, W.; Pei, Y.; Guan, H.; Guo, Z.; Wu, C.; Qu, C.; Li, W.; Liu, J. Emissions of VOCs and SVOCs from polyvinyl chloride building materials: Contribution to indoor odor and inhalation health risks. *Build. Environ.* **2023**, *229*, 109958. [CrossRef]
14. Wang, Q.; Shen, J.; Cao, T.; Du, J.; Dong, H.; Shen, X. Emission characteristics and health risks of volatile organic compounds and odor from PVC-overlaid particleboard. *BioResources* **2019**, *14*, 4385–4402. [CrossRef]
15. Khalil, H.A.; Tehrani, M.; Davoudpour, Y.; Bhat, A.; Jawaid, M.; Hassan, A. Natural fiber reinforced poly(vinyl chloride) composites: A review. *J. Reinf. Plast. Compos.* **2013**, *32*, 330–356. [CrossRef]
16. Demir, H.; Sipahioğlu, M.; Balköse, D.; Ülkü, S. Effect of additives on flexible PVC foam formation. *J. Mater. Proc. Technol.* **2008**, *195*, 144–153. [CrossRef]
17. Shi, Y.; Yao, Y.; Lu, S.; Chen, L.; Chen, S.; He, H.; Ma, M.; Wang, X. Synergistic effect of two plasticizers on thermal stability, transparency, and migration resistance of zinc arginine stabilized PVC. *Polymers* **2022**, *14*, 4560. [CrossRef] [PubMed]

18. Maia, I.; Santos, J.; Abreu, M.J.; Miranda, T.; Carneiro, N.; Soares, G. PVC-based synthetic leather to provide more comfortable and sustainable vehicles. In *IOP Conference Series: Materials Science and Engineering*; IOP Publishing: Bristol, UK, 2017; Volume 254, p. 122006.

19. Alshammari, B.A.; Alsuhybani, M.S.; Almushaikeh, A.M.; Alotaibi, B.M.; Alenad, A.M.; Alqahtani, N.B.; Alharbi, A.G. Comprehensive review of the properties and modifications of carbon fiber-reinforced thermoplastic composites. *Polymers* **2021**, *13*, 2474. [CrossRef] [PubMed]

20. Yao, S.-S.; Jin, F.L.; Rhee, K.Y.; Hui, D.; Park, S.J. Recent advances in carbon-fiber-reinforced thermoplastic composites: A review. *Compos. Part. B-Eng.* **2018**, *142*, 241–250. [CrossRef]

21. Ho, X.; Yu, Y.; Wang, N. Preparation and properties of glass fiber/polyvinyl chloride composites. *Chin. Adhes.* **2016**, *25*, 43–46.

22. Hassan, A.; Akbari, A.; Hing, N.K.; Ratnam, C.T. Mechanical and thermal properties of ABS/PVC composites: Effect of particles size and surface treatment of ground calcium carbonate. *Polym.-Plast. Technol. Eng.* **2012**, *51*, 473–479. [CrossRef]

23. Fu, S.; Lauke, B.; Mäder, E.; Yue, C.; Hu, X. Tensile properties of short-glass-fiber-and short-carbon-fiber-reinforced polypropylene composites. *Compos. Part A Appl. Sci. Manuf.* **2000**, *31*, 1117–1125. [CrossRef]

24. Zhao, H.; Jiang, S. Study on properties of PVC based materials reinforced by glass fiber. *Guangzhou Chem.* **2012**, *40*, 57–59.

25. Kabir, S.F.; Mathur, K.; Seyam, A.F.M. A critical review on 3D printed continuous fiber-reinforced composites: History, mechanism, materials and properties. *Compos. Struct.* **2020**, *232*, 111476. [CrossRef]

26. Li, J.; Cai, C.L. Friction and wear properties of carbon fiber reinforced polypropylene composites. *Adv. Mater. Res.* **2011**, *284*, 2380–2383. [CrossRef]

27. Yunus, R.B.; Zahari, N.; Salleh, M.; Ibrahim, N.A. Mechanical properties of carbon fiber-reinforced polypropylene composites. *Key Eng. Mater.* **2011**, *471*, 652–657. [CrossRef]

28. Rezaei, F.; Yunus, R.; Ibrahim, N. Effect of fiber length on thermomechanical properties of short carbon fiber reinforced polypropylene composites. *Mater. Des.* **2009**, *30*, 260–263. [CrossRef]

29. Gogoi, R.; Maurya, A.K.; Manik, G. A review on recent development in carbon fiber reinforced polyolefin composites. *Compos. Part C Open Access* **2022**, *8*, 100279. [CrossRef]

30. Wang, C.; Ying, S.; Xiao, Z. Preparation of short carbon fiber/polypropylene fine-celled foams in supercritical $CO_2$. *J. Cell. Plast.* **2013**, *49*, 65–82. [CrossRef]

31. Abedi, M.M.; Nedoushan, R.J.; Yu, W.R. Enhanced compressive and energy absorption properties of braided lattice and polyurethane foam hybrid composites. *Int. J. Mech. Sci.* **2021**, *207*, 106627. [CrossRef]

32. Sebaey, T.A.; Rajak, D.K.; Mehboob, H. Internally stiffened foam-filled carbon fiber reinforced composite tubes under impact loading for energy absorption applications. *Compos. Struct.* **2021**, *255*, 112910. [CrossRef]

33. *GMW3010-2019*; General Motors Company Worldwide Engineering Standards: Determination of Tensile and Elongation Properties. General Motors Company: Detroit, MI, USA, 2019.

34. *ISO 13937*; Tear Properties of Fabrics. ISO: Geneva, Switzerland, 2000.

35. Degefu, D.M.; Liao, Z.; Berardi, U.; Doan, H. Salient parameters affecting the performance of foamed geopolymers as sustainable insulating materials. *Constr. Build. Mater.* **2021**, *313*, 125400. [CrossRef]

36. Verdu, J.; Zoller, A.; Marcilla, A. Plastisol foaming process. Decomposition of the foaming agent, polymer behavior in the corresponding temperature range and resulting foam properties. *Polym. Eng. Sci.* **2013**, *53*, 1712–1718. [CrossRef]

37. *GMW3182-2022*; General Motors Company Worldwide Engineering Standards: Determination of Mass per Area. General Motors Company: Detroit, MI, USA, 2022.

38. *GMW3205-2023*; General Motors Company Worldwide Engineering Standards: Determining the Resistance to Odor Propagation of Interior Materials. General Motors Company: Detroit, MI, USA, 2023.

39. Li, Z.; Wei, X.; Liu, J.; Han, H.; Jia, H.; Song, J. Mechanical properties and VOC emission of hemp fibre reinforced polypropylene composites: Natural freezing-mechanical treatment and interface modification. *Fibers Polym.* **2021**, *22*, 1050–1062. [CrossRef]

40. Gu, R.; Sain, M.M.; Konar, S.K. A feasibility study of polyurethane composite foam with added hardwood pulp. *Ind. Crops Prod.* **2013**, *42*, 273–279. [CrossRef]

41. Kada, D.; Koubaa, A.; Tabak, G.; Migneault, S.; Garnier, B.; Boudenne, A. Tensile properties, thermal conductivity, and thermal stability of short carbon fiber reinforced polypropylene composites. *Polym. Compos.* **2018**, *39*, E664–E670. [CrossRef]

# The Influence of Thermal Parameters on the Self-Nucleation Behavior of Polyphenylene Sulfide (PPS) during Secondary Thermoforming

Yi Ren [1,2], Zhouyang Li [1], Xinguo Li [1,2], Jiayu Su [1,2], Yue Li [3], Yu Gao [1,2], Jianfeng Zhou [1], Chengchang Ji [1,2], Shu Zhu [1,2,*] and Muhuo Yu [1,2,*]

1   State Key Laboratory for Modification of Chemical Fibers and Polymer Materials, Shanghai Collaborative Innovation Center of High-Performance Fibers and Composites (Province-Ministry Joint), Key Laboratory of High-Performance Fibers & Products, Ministry of Education, Center for Civil Aviation Composites, Donghua University, Shanghai 201620, China; renyidhu@163.com (Y.R.); 211100211@mail.dhu.edu.cn (Z.L.); lxg_0814@163.com (X.L.); 2210343@mail.dhu.edu.cn (J.S.); 11825055@zju.edu.cn (Y.G.); zjf@dhu.edu.cn (J.Z.); jicc@dhu.edu.cn (C.J.)
2   Key Laboratory of Shanghai City for Lightweight Composites, College of Materials Science and Engineering, Donghua University, Shanghai 201620, China
3   School of Chemistry and Chemical Engineering, Frontiers Science Center for Transformative Molecules, Shanghai Jiao Tong University, Shanghai 201306, China; liyue0411@sjtu.edu.cn
*   Correspondence: zhushu@dhu.edu.cn (S.Z.); yumuhuo@dhu.edu.cn (M.Y.)

**Highlights:**

1.  The influence of temperature parameters in two thermal cycles on the self-nucleation (SN) behavior was revealed.
2.  The heating rate and processing melt temperature during the first thermal cycle exhibited a synergistic effect on the SN behavior.
3.  Under appropriate conditions, both the first and second thermal cycles can generate SN behavior, but the mechanisms were different.

**Abstract:** During the secondary thermoforming of carbon fiber-reinforced polyphenylene sulfide (CF/PPS) composites, a vital material for the aerospace field, varied thermal parameters profoundly influence the crystallization behavior of the PPS matrix. Notably, PPS exhibits a distinctive self-nucleation (SN) behavior during repeated thermal cycles. This behavior not only affects its crystallization but also impacts the processing and mechanical properties of PPS and CF/PPS composites. In this article, the effects of various parameters on the SN and non-isothermal crystallization behavior of PPS during two thermal cycles were systematically investigated by differential scanning calorimetry. It was found that the SN behavior was not affected by the cooling rate in the second thermal cycle. Furthermore, the lamellar annealing resulting from the heating process in both thermal cycles affected the temperature range for forming the special SN domain, because of the refined lamellar structure, and expelled various defects. Finally, this study indicated that to control the strong melt memory effect in the first thermal cycle, both the heating rate and processing melt temperature need to be controlled simultaneously. This work reveals that through collaborative control of these parameters, the crystalline morphology, crystallization temperature and crystallization rate in two thermal cycles are controlled. Furthermore, it presents a new perspective for controlling the crystallization behavior of the thermoplastic composite matrix during the secondary thermoforming process.

**Keywords:** polyphenylene sulfide; self-nucleation; non-isothermal crystallization; secondary thermoforming

## 1. Introduction

Advanced thermoplastic composites have garnered extensive attention due to their noteworthy attributes including lightweight, high strength, excellent toughness, elevated damage tolerance, and recyclability [1,2]. Carbon fiber-reinforced polyphenylene sulfide (CF/PPS) composites, as a vital material for the aerospace field, exhibit a compelling cost-performance ratio, especially when compared to poly(ether-ether ketone) (CF/PEEK) composites, despite marginal disparities in mechanical performance. Utilizing the characteristics of PPS that can be melted and cooled repeatedly, innovative manufacturing approaches such as stamping forming [3–5], in situ consolidation [6–8], and induction welding [9–11] have been devised. These secondary thermoforming methods enable rapid fabrication of CF/PPS composites, consequently reducing production cycles and minimizing manufacturing costs.

The thermal history of CF/PPS composites in the secondary thermoforming is complicated, involving multiple melting and cooling processes. PPS, as the matrix of thermoplastic composites, is a semi-crystalline polymer. The crystallization behavior of PPS is significantly influenced by these processes. Although the crystallization and melting behaviors [12–15] of PPS have been extensively investigated, most of studies only focused on a single melt-cooling cycle for PPS [16–20], ignoring the potential influence of multiple thermal cycles on the crystallization behavior of PPS. Self-nucleation (SN) is a distinctive nucleation mechanism observed in semi-crystalline polymers under specific conditions of repeated thermal cycling. The generation of SN is due to the residual crystalline fragments or locally ordered region in the melt [21]. The SN behavior in crystallization process manifests as promoted polymer crystallization behavior without the addition of external heterogeneous surfaces, such as nucleating agents [22], resulting in an increase in crystallization temperature during non-isothermal crystallization processes [23,24]. Therefore, it is important to pay attention to the effect of multiple thermal cycles on PPS crystallization.

It is noteworthy that PPS exhibits a strong melt memory effect [16,25,26]. Even when melted at 40 °C above its melting point, the crystallization process still shows SN behavior. Furthermore, within the processing melt temperature range of 292–323 °C, the SN behavior of PPS remains unchanged with temperature variations [26]. A similar melt memory effect is observed in many copolymers [27–32] and some homopolymers [33–38]. They all demonstrate SN behaviors a few to several tens of degrees above their melting point. This pronounced melt memory effect could be attributed to either a unique molecular chain topology [29,39,40] or potent intermolecular interactions [41].

PPS has a distinct structure, with alternating phenyl rings and sulfur atoms, leading to numerous sulfur bonds in its molecular chain. Consequently, PPS displays considerable instability at elevated temperatures. Potential thermal degradation actions, like chain scission [42,43], branching [44] and crosslinking [45,46], can change the molecular chain structure and conformation in the PPS melt, leading to its pronounced melt memory effect and unique SN behavior. Therefore, it is crucial to understanding the effects of thermal parameters in multiple thermal cycle on the SN behavior of PPS, and discern how to influence the molecular chain conformation to control the SN behavior. Such insights can guide the selection of thermal protocols in specific manufacturing processes.

In this study, the crystallization and remelting behaviors of PPS across two thermal cycles were systematically investigated. Employing the DSC technique, the relationship between the various thermal parameters in two thermal cycles and the SN behaviors of PPS were explored. Notably, through a comprehensive analysis involving crystallization temperature, processing melt temperature and crystalline morphology, the significant impact of lamellae annealing on the SN behavior of PPS was illuminated. The synergistic relationship between heating rates and processing melt temperature in affecting the crystallization behavior of PPS was highlighted. Overall, this work will not only provide new insights into the SN behavior of PPS, but also provide a theoretical basis for the controllable processing of PPS and CF/PPS composites.

## 2. Materials and Methods

### 2.1. Materials

The material studied in this work is a commercial PPS film obtained from Zhejiang NHU Co., Ltd. (Shaoxing, China). It has a weight-average molecular weight ($M_w$) of 48,200 g/mol, and a polydispersity index (PDI) of 4.03. The specified glass transition temperature is 87 °C and the melting point is 284.6 °C.

### 2.2. Characterizations

#### 2.2.1. Differential Scanning Calorimetry

The melting and crystallization behaviors were performed using a TA Instruments Q20 (TA instrument, New Castle, DE, USA) under a nitrogen atmosphere (50 mL/min). The instrument was calibrated before each set of scans with high-purity indium or tin. Samples (6.0 ± 0.5 mg) were sealed in aluminum pans.

The primary objective of this study is to investigate the influence of various thermal cycle parameters on the SN behavior and the crystallization behavior of PPS during two thermal cycles. These parameters include the heating rate ($H_{r1}$) and processing melt temperature ($T_{s1}$) during the first thermal cycle, as well as the heating rate ($H_{r2}$), melting temperature ($T_s$), and cooling rate ($C_{r1}$) during the second thermal cycle. This section provides a brief overview of the thermal protocol corresponding to PPS undergoing melt-cooling. The detailed thermal protocols examining the impact of individual variables on crystallization behavior are presented in the Section 3.

The thermal protocol comprises two thermal cycles, and a reheating step for analyzing the PPS crystal structure, as shown in Figure 1.
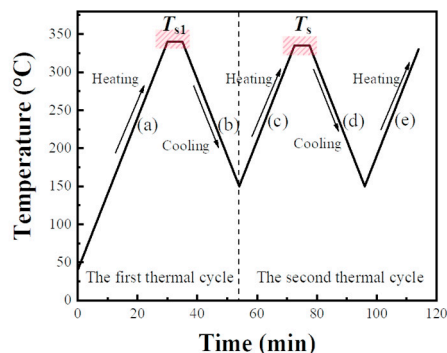


**Figure 1.** The thermal protocol used in DSC experiments. (a)–(e) respectively represent the heating and cooling stages during the thermal cycles.

For the first thermal cycle:

(a) Due to the broad melting range of PPS, the melting peak occurs between 250 °C and 290 °C. To ensure melting completely and eliminated any thermal history effects during the first melting process, the sample was heated to the initial processing melt temperature ($T_{s1}$) at a specified heating rate ($H_{r1}$), and held for 5 min. Incomplete melting due to a too-low $T_{s1}$ would impact the consistency of the PPS melt during the first thermal cycle, ultimately affecting the investigation of PPS crystallization behavior.

(b) The sample was then cooled to 150 °C at a designated cooling rate, completing its initial crystallization.

For the second thermal cycle:

(c) The crystallized sample was subsequently reheated to the processing melt temperature ($T_s$) at a specified heating rate ($H_{r2}$), and held for 5 min. Different $T_s$ led to distinct molecular chain conformations in PPS, subsequently resulting in varied SN behaviors and crystallization behaviors.

(d)   The sample was cooled again to 150 °C at a specified cooling rate ($C_{r2}$) for its second crystallization.

(e)   Finally, the twice-crystallized sample was heated from 150 °C to 330 °C at a rate of 10 °C/min to analyze the crystalline structure forming in the second crystallization.

2.2.2. Polarized Optical Microscopy

The crystalline morphology of PPS during crystallization was observed by Olympus BX-53 optical microscopes (Olympus Corporation, Shinjuku-ku, Japan) operating in reflection mode equipped with a Linkam THMS 600 hot stage (Linkam Scientific Instruments Ltd., Tadworth, UK). Images were taken with a Motic CCD camera, and for analysis of crystallization on cooling, NIH ImageJ software (Version 1.46 r) was used.

## 3. Results and Discussion

### 3.1. Effect of the Cooling Rate in the Second Thermal Cycle on the SN Behavior of PPS

During the secondary thermoforming of PPS, the molecular chain conformation in the melt exhibits variations based on the processing melt temperature. Specifically, with an elevation in processing melt temperature, the conformation transitions sequentially through stages: from residual crystalline fragments to locally ordered regions of molecular chains, followed by relaxation, interdiffusion, re-entanglement, and eventually reverts to a fully disordered random coil conformation [26]. It is worth noting that, due to differences in entropy, these various conformations of molecular chains showcase different crystallization temperature upon cooling. Additionally, the cooling rate is a significant factor affecting the non-isothermal crystallization behavior of semi-crystalline polymers, profoundly influencing the nucleation and subsequent crystal growth behaviors [47–52]. Therefore, it is imperative to focus on the influence of varying cooling rates on crystallization temperature of PPS when PPS exhibits SN behaviors. The thermal protocol applied to PPS was illustrated in Figure 2a.

The SN behavior of PPS is greatly influenced by the secondary processing melt temperature. In our previous studies [26], we observed distinct SN behaviors of PPS at different secondary processing melt temperatures, which we divided into six domains, as shown in Figure 2b. Each domain represented by a different colored line on the PPS melting enthalpy curve. Domain $II_b$ represents PPS melting within a specific temperature range, where residual crystalline fragments remain in the melt. These fragments act as self-seeds and promote the nucleation process during cooling. Domain $II_a$ indicates PPS melting within a temperature range where crystalline fragments are absent and are replaced by locally ordered molecular chains. This configuration can promote the nucleation process in PPS. Notably, PPS has a unique region called Domain II'. Within this domain, the crystallization temperature remains constant despite the increase in processing melt temperature, and maintaining a high nucleation density. This domain forms because the molecular chains in PPS cannot interdiffuse within this temperature range due to the complex molecular chain topology of the PPS amorphous region and the strong interaction between molecular chains. PPS is in Domain $II_a'$ when the melting temperature is sufficient for interdiffusion of PPS molecular chains through thermal motion. In this domain, as the melting temperature continues to increase, the self-nucleation behavior of PPS gradually disappears. Based on prior research, five typical secondary processing melt temperatures ($T_s$) were selected for applying two thermal cycles to PPS. Each of these temperatures falls within specific ranges that can induce various SN behaviors in PPS. These temperatures are marked with red dots in Figure 2. A temperature of 285 °C corresponds to Domain $II_b$. For Domain II', two temperatures were selected: 295 °C corresponds to the lower temperature of this domain, while 315 °C represents the higher temperature. A temperature of 326 °C corresponds to Domain $II_a'$, and 335 °C corresponds to the temperature region where the SN effect almost disappears. After melting at these varied temperatures, three different cooling rates were used to finish non-isothermal crystallization during the PPS cooling process.
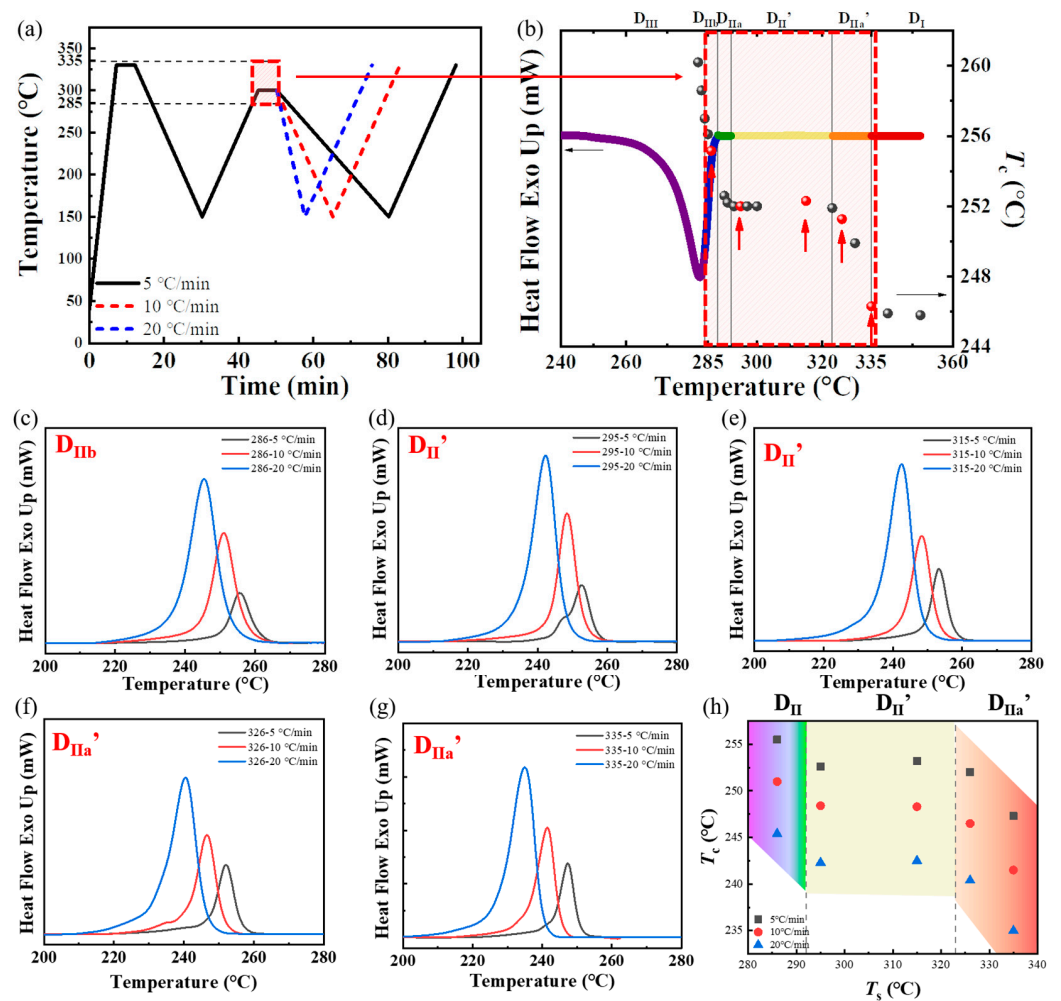
**Figure 2.** (**a**) The thermal protocol used by DSC, in which the cooling rates of the second thermal cycle is different. (**b**) The reference for the division of PPS Domain [26]. DSC cooling scans at different cooling rates when the secondary processing melt temperature ($T_s$) is (**c**) 285 °C, (**d**) 295 °C, (**e**) 315 °C, (**f**) 325 °C, and (**g**) 335 °C. The corresponding SN domain was marked in the upper left corner, and the legend showed the corresponding cooling rate at the $T_s$. (**h**) Peak crystallization temperature ($T_c$) as a function of the $T_s$ with different cooling rates. The colors of the shadows correspond to the temperature ranges associated with the different domains of PPS SN behavior.

As shown in Figure 2c–g, it is evident that with a constant $T_s$, the crystallization peak shifted to a lower temperature with an increase in cooling rate. Figure 2h illustrates a declining trend in the peak crystallization temperature ($T_c$) of PPS within Domain II$_b$ as the $T_s$ increased. When the $T_s$ was in Domain II′, the $T_c$ of PPS remained unaltered with variations in $T_s$, even if the cooling rate was different. As the $T_s$ continued to increase, the $T_c$ of PPS decreased again. This could be attributed to the diminishing melting memory effect, caused by the PPS molecular chains gradually reverting to a random coil conformation. Notably, although a higher cooling rate resulted in an overall decrease in crystallization temperature, the exhibited trend—a decline, followed by stabilization, and a subsequent decline—with respect to $T_s$ variations remains consistent across different crystallization rates.

The consistency in the trend of $T_c$ and $T_s$ shown between different cooling rate groups in Figure 2h indicated that the molecular chain conformations associated with different SN behaviors of PPS were highly stable in the melt. This signifies that, while the cooling rate can alter the crystallization temperature, the nucleation mechanism during the crystallization process is not affected by the cooling rate. Furthermore, the constant $T_c$ maintained in Domain II′ across different cooling rates suggested that the molecular chain conformation of

PPS is consistent within this temperature range. Even if melt temperature differed by 20 °C, the molecular chains in the melt all maintain this particular metastable state. Consequently, theses conformation exhibited the same efficacy in fostering nucleation and facilitating the growth of spherulites, resulting in the same crystallization temperature within Domain II'.

### 3.2. Effect of the Heating Rate in the Second Thermal Cycle on the SN Behavior of PPS

As the crystals are heated, they undergo a process known as annealing. This process could further promote lamellae growth, leading to a more perfect internal crystalline structure [53–55]. For CF/PPS composites during secondary thermoforming, there exists a significant difference in heating rates due to diverse processing method. Such variation in heating rate might result in different annealing processes for the PPS spherulites. This can potentially lead to varying degrees of perfection in the PPS crystalline structure, ultimately influencing the SN behavior of PPS. As depicted in Figure 3, heating rates of 10 °C/min, 20 °C/min, and 40 °C/min were chosen to examine the impact of different heating rates in the second thermal cycle on the SN behavior of PPS.
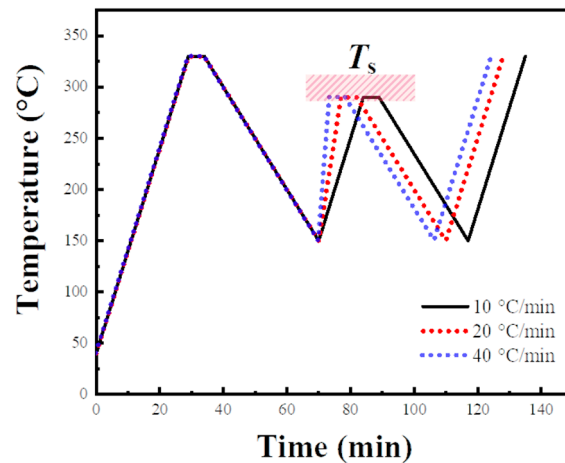


**Figure 3.** Thermal protocol used in experiment of investigating the relationship between the crystallization behavior and heating rate in the second thermal cycle. The range of the secondary processing melt temperature ($T_s$) was from 283 °C to 350 °C, and the stay period at $T_s$ was 5 min.

From Figure 4a–a″, it can be observed that the trend in crystallization temperature ($T_c$) changes with $T_s$ remained largely consistent across different secondary heating rates. Initially, as $T_s$ increased, the crystallization peak shifted to a lower temperature. This trend sustained until a specific temperature was reached, after which the $T_c$ plateaued, maintaining this equilibrium until approximately 320 °C. Beyond this $T_s$, the $T_c$ of PPS declined once more, which then remained constant at a higher temperature. The Using a heating rate of 20 °C/min for illustration: At $T_s$ of 283 °C, the $T_c$ descended from 256.1 °C to 253.2 °C with increasing $T_s$. Subsequently, once $T_s$ surpassed 288 °C, the $T_c$ remained steady at 253.2 °C, persisting until 325 °C. When $T_s$ exceeded 325 °C, the crystallization peak once again trended towards a lower temperature, ultimately stabilizing beyond 340 °C. From Figure 4b–b″, it can be noted that when $T_s$ was 283 °C, samples with different heating rates exhibited double peaks in the remelting curves after second crystallization. This is the typical characteristic representation of Domain III. It means that at this temperature, the PPS spherulites were only partially melted, and the unmelted part was annealed.
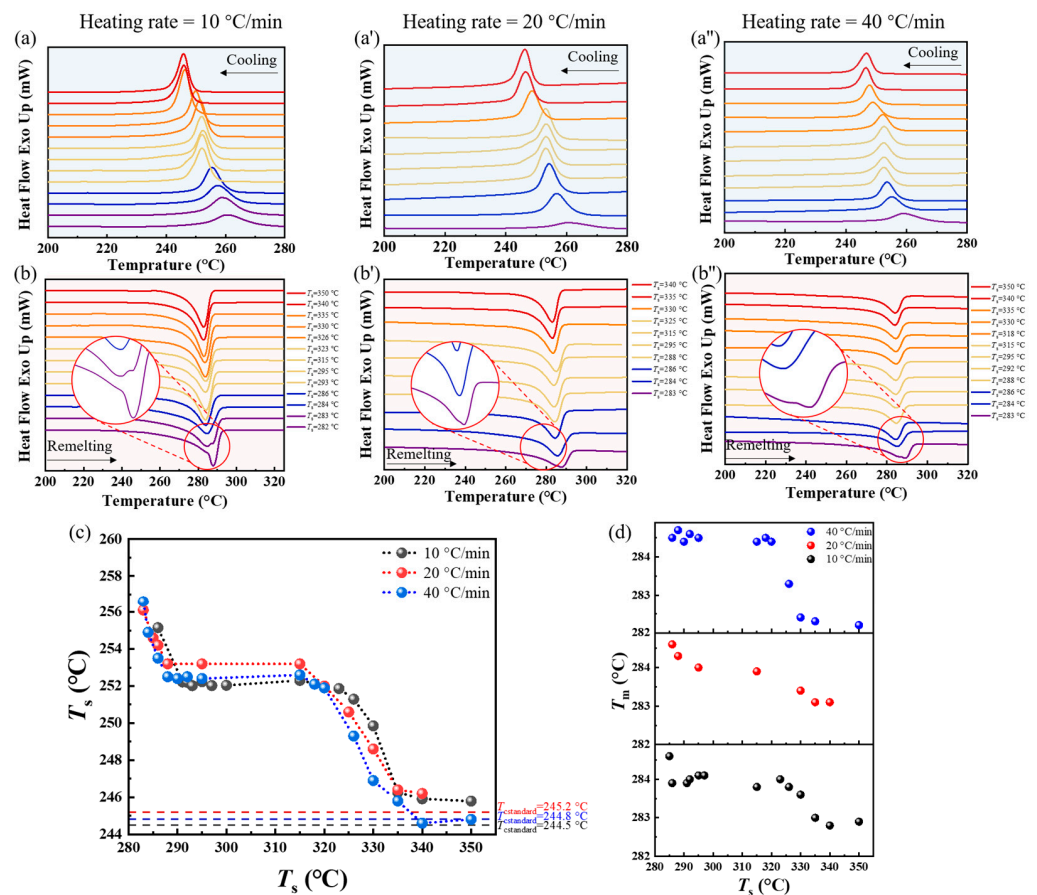
**Figure 4.** DSC cooling scans from the indicated $T_s$ during the second thermal cycle, when the secondary heating rate was set to (**a**) 10 °C/min, (**a′**) 20 °C/min, and (**a″**) 40 °C/min. Different line colors represented different domains where PPS was located. Subsequent DSC heating scans which correspond to the third heating segments. The secondary heating rate was set to (**b**) 10 °C/min, (**b′**) 20 °C/min, and (**b″**) 40 °C/min. (**c**) Peak crystallization temperature ($T_c$) as a function of $T_s$ for different heating rates during the second thermal cycle. The dashed line represents the standard crystallization temperature of PPS. (**d**) Peak remelting temperature ($T_m$) after crystallization in the second thermal cycle as a function of $T_s$.

To clearly analyze the influence of the heating rate on the SN behavior, the relationship between the $T_c$ and the $T_s$ under different heating rates was compiled into Figure 4c. It can be observed that the heating rate did not significantly affect the relationship between $T_s$ and corresponding $T_c$. Furthermore, regardless of the heating rate, the special region (Domain II′) consistently emerged between 292 °C and 318 °C. Within this region, the $T_c$ did not change with an increase in the $T_s$. This phenomenon further validated the stable existence of this region. However, it should be noted that an increase in the heating rate caused Domain II′ to shift overall to lower temperature. When the heating rate was 10 °C/min, the $T_s$ range of domain II′ is defined between 292 °C and 323 °C, which was based on the relationship between the $T_s$ and $T_c$. However, when the heating rate was 20 °C/min and 40 °C/min, respectively, this domain began at 288 °C, and the $T_c$ no longer changed with the increase in $T_s$. Only when the $T_s$ exceed 320 °C/min, the $T_c$ decreased again with the increasing $T_s$.

The change in the temperature region of Domain II′ suggests that the SN behavior of PPS is indeed influenced by different heating rates in the second thermal cycle. Analyzing the $T_c$ between groups with different heating rates reveals that despite the heating rates varied, the $T_c$ within Domain II′ remained almost consistent. This indicates that the molecular chain conformation in the melt prior to crystallization is essentially the same, and therefore the promotion effect on post-melting crystallization is nearly identical. When PPS

spherulites undergo a secondary heating process, annealing occurs and the lamellae thicken. Additionally, during the annealing process, various defects contained within the PPS crystalline regions are gradually expelled such as branched chains, impurities, and various dislocations [56]. This makes the topological structure of the amorphous molecular chains between the crystalline regions even more complex. When the heating rate is slow, the lamellar have sufficient time to anneal and become thicker. Therefore, a higher temperature is required to destroy the more perfect residual crystalline fragments and locally ordered regions. It also requires a higher temperature to break the metastable state where the molecular chains are relaxed but do not interdiffuse. Conversely, faster rates suppress the annealing process and the lamellar thickening behavior, such as 20 °C/min. This allows PPS molecular chains to reach a metastable state at a lower processing melt temperature, ultimately destroying the metastable state at a lower temperature. Furthermore, it can be inferred from Figure 4d that the SN behavior of PPS leads to a discernible rise in the peak remelting temperature of the crystals. As this SN behavior gradually diminished with increasing $T_s$, there was a corresponding gradual reduction in the peak remelting temperature, which eventually kept stable.

### 3.3. Effect of the Heating Rate in the First Thermal Cycle on the SN Behavior of PPS

The premise of SN behavior in semi-crystalline polymers is that the polymer needs to be sufficiently crystallized before the secondary melting. In the actual secondary thermo-forming process of CF/PPS composites, the raw material may either be amorphous or in a fully crystallized state, potentially leading to inconsistencies in the initial crystallization behavior of PPS. In this study, the PPS film is amorphous, and cold crystallization will occur during its first heating process. Then, the lamellae thicken and become perfect due to annealing during the heating process. Compared with the melt crystallization, the crystals of PPS with imperfect structure resulting from cold crystallization are more significantly affected by annealing. Hence, the amorphous PPS raw material might be strongly influenced by the heating rate in the first thermal cycle. Figure 4 have found that there were subtle differences in the memory effect of PPS melt under different heating rates in the second thermal cycle. Therefore, it is of interest to see if applying different heating rates in the first thermal cycle to the amorphous PPS film will affect its initial crystallization behavior, and finally change the SN behavior during the second crystallization of PPS.

The PPS was subjected to a heating rate of 10 °C/min and maintained at 330 °C for 5 min in the first thermal cycle. After cooling process, the temperature was increased again to observe the changes in the relationship between crystallization temperature ($T_{c2}$) and the processing melt temperature ($T_s$) in the second thermal cycle. As shown in Figure 5a, it was found that when $T_s$ below 295 °C, the $T_{c2}$ of PPS consistently decreased with the rise of $T_s$. This is consistent with the SN behavior exhibited by PPS in previous experiments. As the $T_s$ increased, diminishing residual crystalline fragments in the melt weakened the promotion effect of the self-seeds on PPS crystallization. However, for $T_s$ exceeding 295 °C, the $T_{c2}$ dropped to around the initial crystallization temperature ($T_{c1}$). This phenomenon is quite unique. According to the previous experimental results of the SN behavior of PPS, $T_s$ should be within the temperature range that could form PPS's special SN domain (Domain II'). In this range, while the $T_{c2}$ of PPS does not change with the increasing $T_s$, the $T_{c2}$ of PPS at this range should be higher than the $T_{c1}$. This is because although PPS might lack residual crystalline fragments or ordered structural regions, its intricate amorphous chain topology restricts the interdiffuse of molecular chains. This particular conformation, with its inherent low entropy, promote the nucleation behavior of PPS. The phenomenon depicted in Figure 5b, as suggested by other literature reports, indicates that the memory effect of the polymer melt has disappeared and the SN behavior no longer occurs. At this temperature, the PPS melt was homogeneous, and nucleation was trigger on the foreign pre-existing surface provided by high-temperature-resistant heterogeneities [56].
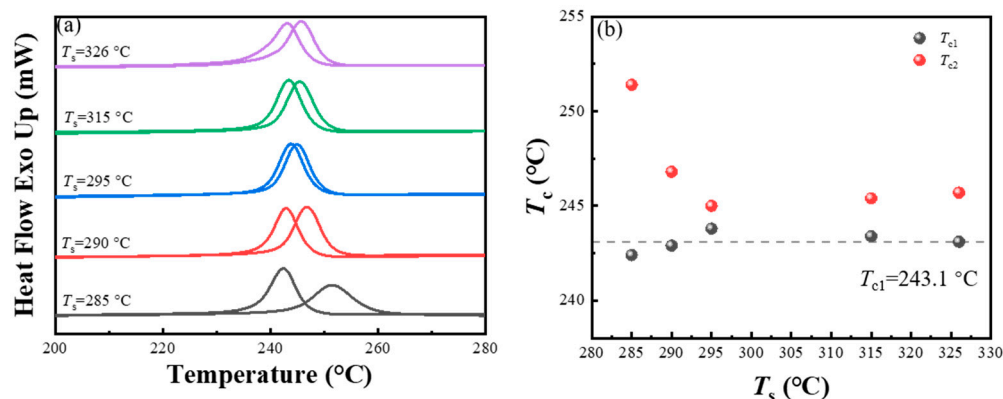
**Figure 5.** (**a**) DSC cooling scans during the first and second thermal cycles. The corresponding secondary processing melt temperature ($T_s$) is marked on the left side of the curve. (**b**) Peak crystallization temperature as a function of the $T_s$, which corresponds to the first ($T_{c1}$) and second ($T_{c2}$) cooling segments, respectively. The heating rate in the first thermal cycle was set to 10 °C/min, and the initial processing melt temperature was set to 330 °C.

Interestingly, as depicted in Figure 5b, with a heating rate of 10 °C/min in the first thermal cycle, the $T_{c1}$ of PPS was 243.1 °C. However, when the first heating rate was escalated to 40 °C/min, under the same processing melt temperature and cooling rate, the $T_{c1}$ of PPS was 240.5 °C. The slower first heating rate resulted in a higher $T_{c1}$ for PPS during the initial crystallization. This suggests that the first heating rate had an impact on the $T_{c1}$. Could this result explain the phenomenon that $T_{c2}$ approached $T_{c1}$ is not due to the disappearance of the SN effect, but rather because the $T_{c1}$ increased due to the slow first heating rate? To further analyze the impact of the initial heating rate on both primary crystallization behavior and behavior after secondary melting, experiments were conducted while maintaining the same first processing melt temperature as before, which is 330 °C. The heating rates were set to 5 °C/min, 10 °C/min, 15 °C/min, 20 °C/min, and 40 °C/min. The thermal protocols were shown in Figure 6. With the processing melt temperature in the second thermal cycle selected as 295 °C, the thermal flow changes in the sample during thermal cycling at different heating rates were recorded.
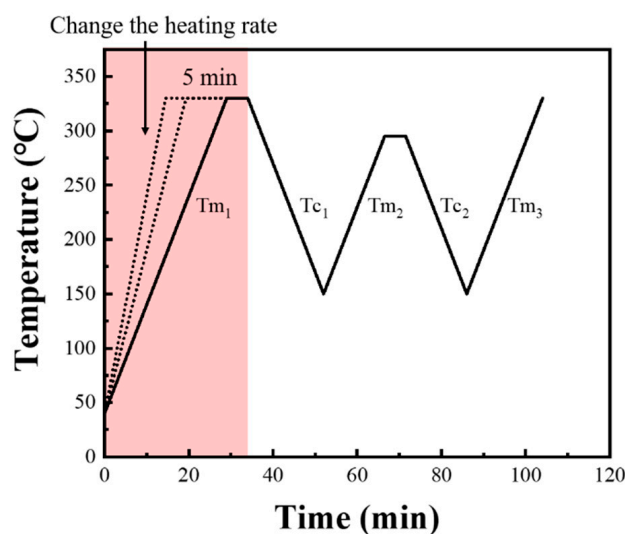


**Figure 6.** Thermal treatment process used in experiment of investigating the relationship between the crystallization behavior and the first heating rate.

As seen in Figure 7a, the varying first heating rates profoundly influenced both initial crystallization behavior and the second crystallization behavior. Notably, when the

initial heating rate was 5 °C/min, the cooling curve of the initial cooling process almost coincides with that of the secondary cooling process. However, as the initial heating rate accelerated, the curves corresponding to the first and second crystallization process gradually separated. The first crystallization peak shifted towards a lower temperature, while the second crystallization peak shifted towards a higher temperature. Eventually, when the heating rate exceeded 20 °C/min, the relative positions of the two curves attained stability. The relationship between the crystallization temperature of the two stages and the initial heating rate was summarized in Figure 7b. It can be seen that when the first heating rate was 5 °C/min, the crystallization temperatures of the two stages were almost the same. As the heating rate increased, the $T_{c1}$ gradually decreased, from 245.8 °C to 241.1 °C. In contrast, the $T_{c2}$ gradually increased, from 246.2 °C to 248.0 °C. This resulted in an increasing temperature difference between the crystallization temperature of the two stages. When the heating rate was 40 °C/min, compared with the sample at a heating rate of 20 °C/min, the variances of crystallization temperature in both crystallization process were minimal, maintaining a steady temperature gap. It is crucial to highlight that although the initial processing melt temperature is the same, a slower heating rate resulted in a higher crystallization temperature (~4 °C). This suggests that there were some ordered structures in the melt that promoted the crystallization process of PPS, and these structures were formed at the slower heating rate.
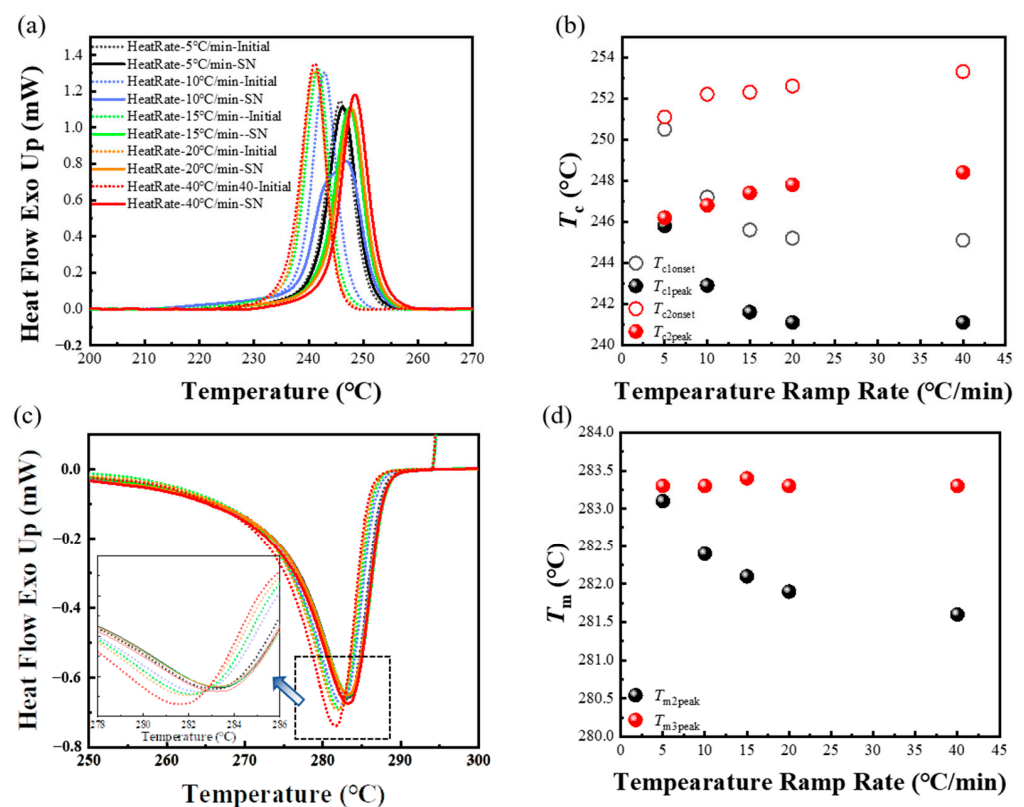


**Figure 7.** (**a**) DSC cooling scans and (**b**) onset crystallization temperature ($T_{conset}$) and peak crystallization temperature ($T_{cpeak}$) as a function of the temperature ramp rate, which corresponds to the first and secondary cooling segments, respectively. The selected secondary processing melt temperature was 295 °C. (**c**) The original DSC heating scans and (**d**) onset remelting temperature ($T_{monset}$) and peak remelting temperature ($T_{mpeak}$) as a function of heating rate in the first thermal cycle, which corresponds to the remelting process of spherulites forming in the initial and second crystallization, respectively.

Beyond the evident shifts in crystallization temperature, the impact of the initial heating rate on PPS crystallization behavior can also observe from the change in the remelting

behavior of spherulites forming in the prior and subsequent cycles, as shown in Figure 7c,d. With the increases in the first heating rate, the peak remelting temperature of the spherulites forming in initial crystallization gradually decreased, dropping from 283.1 °C to 282.2 °C. In contrast, the peak remelting temperature of the spherulites forming in second crystallization remained relatively unchanged. It is noteworthy that the trend of the peak remelting temperature of the initial crystallization with the initial heating rate was almost the same as the trend of the peak melting temperature exhibited by the different SN behavior of PPS. The peak melting temperature could reflect the structural information of lamellae. According to Gibbs–Thomson equation [57], a higher peak remelting temperature corresponds to a more perfect lamellar structure. As can be seen from Figure 4d, if PPS displays SN behaviors during the cooling process after secondary melting, the peak remelting temperature of the formed crystals would be higher than that of regular spherulites. This is because PPS melt, which can generate SN behavior, can start to crystallize at a higher temperature during non-isothermal crystallization. The molecular chains move and arrange thoroughly at high temperature, leading the lamellae to become more orderly and perfected. As a result, it requires a higher temperature to melt these perfect lamellae. Thus, the static peak remelting temperature of spherulites forming in the subsequent crystallization, as depicted in Figure 7d, indicated that the crystalline structure of the second crystallization was not affected by the heating rate in the first thermal cycle.

It is worth noting that since there was SN behavior during the second crystallization process when the first heating rate was 40 °C/min. It could be speculated that SN behavior also occurred during the second crystallization when the first heating rate was 5 °C/min, due to the same $T_{m3peak}$. Moreover, a consistent initial and second crystallization temperature at this heating rate suggested the same crystallization behaviors. Thus, based on the nearly identical crystallization temperature and peak remelting temperature in the two thermal cycles at a slower initial heating rate, it could be deduced that PPS exhibited SN behavior during the first crystallization.

To verify that under different heating rates in the first thermal cycle, PPS exhibits various crystallization behavior during the first crystallization due to the influence of cold crystallization and annealing. The same thermal protocol as DSC was applied to PPS films using a hot stage. The crystalline morphology was observed in real time by microscopy. Figure 8a shows that when the heating rate was 40 °C/min, the crystalline morphology of the initial crystallization manifested as standard spherulites. When the sample underwent a secondary melting and cooling, the SN behavior occurred, and the crystalline morphology was transformed into tiny crystals. However, at a heating rate of 5 °C/min, the initial crystalline morphology already presented as very tiny crystals, as shown in Figure 8b. This is the typical crystalline morphology following the SN behavior of PPS, where the volume of the spherulite dropped to a level that is difficult to discern with the naked eye. When this sample underwent the secondary melting and crystallization, the crystalline morphology is similar to that of the initial crystallization.

This result directly confirms that at a slower heating rate, PPS exhibits SN behavior during the initial crystallization process, leading to a significant increase in the crystallization temperature of PPS and a drastic reduction in crystalline size. This is due to the cold crystallization of the amorphous PPS film when it was heated in the first thermal cycle, and the crystals formed in the cold crystallization process underwent annealing during the slow heating process. This annealing process thickened the lamellae, perfected their structure, and expelled the various defects, thus forming a complex molecular chain topology between the lamellae. When the initial processing melt temperature was 330 °C, while the temperature can melt the annealed crystals, the complex molecular chain topology between the crystalline regions prevented the locally ordered relaxation molecular chains, originated from crystalline region, from reverting to the random coil conformation. Consequently, due to the advantage of entropy, the nucleation process of PPS is promoted by ordered molecular chains, manifesting as an increase in crystallization temperature and a sharp decrease in spherulitic size. However, when the heating rate surpasses 20 °C/min,

the annealing process is suppressed, and the crystalline structure is not fully perfected. Thus, 330 °C could disrupt the metastable structure where molecular chains can relax but cannot interdiffuse. Ultimately, due to the absence of melt memory effect, PPS forms standard spherulites during cooling process. Additionally, the imaging results indicated that in situations where crystalline morphology cannot be obtained, the correlation between crystallization temperature and post-crystallization peak remelting temperatures could qualitatively predict crystalline morphology of PPS under given thermal conditions.
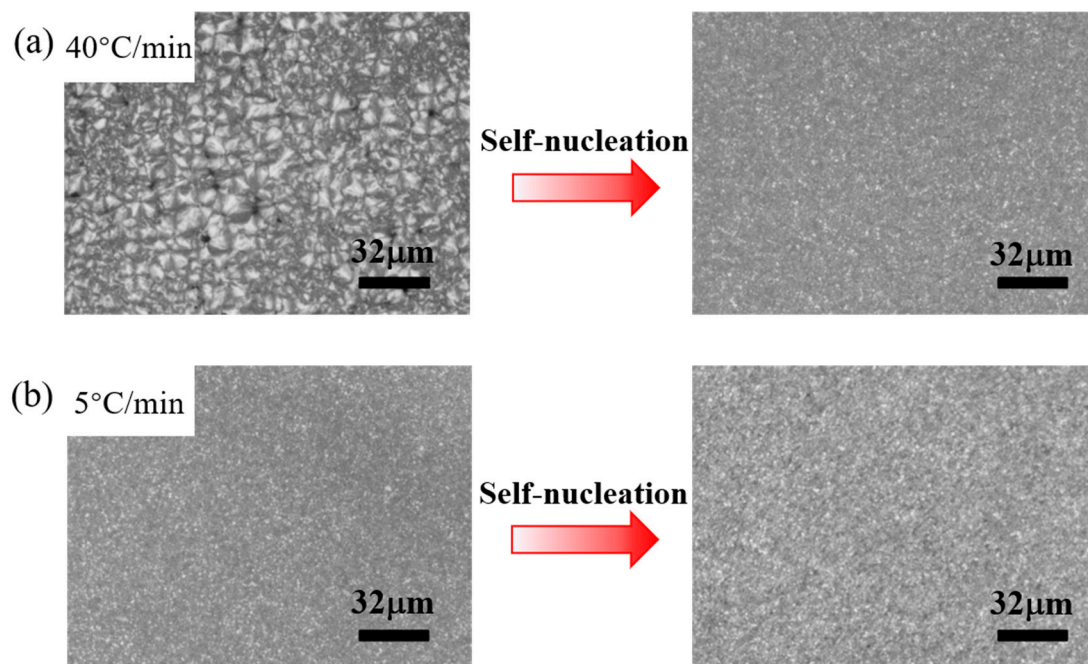


**Figure 8.** The change in PPS crystalline morphology in the first thermal cycle and the second thermal cycle. (**a**) The initial heating rate is 40 °C/min. (**b**) The initial heating rate is 5 °C/min.

*3.4. Effect of the Processing Melt Temperature in the First Thermal Cycle on the SN Behavior of PPS*

The slow heating rate induces the annealing and thickening of lamellae in the PPS, which consequently elevates the processing melt temperature required for the polymer chains to return to the random coil conformation. This phenomenon's implications for PPS processing are often understated in practical applications, which might lead to heightened crystallization temperature and increased viscosity during cooling process. To avoid the SN behavior occurring in the first thermal cycle, a higher processing melt temperature was used to eliminate the strong melt memory effect in PPS. By heating PPS at rate of 10 °C/min, annealing and thickening of the lamellae occurred after cold crystallization of PPS. The first processing melt temperature was then set to 340 °C. It can be seen from Figure 9a that when the processing melt temperature of second thermal cycle ($T_s$) was set to 330 °C, the crystallization peak is separated from the crystallization peak of the first thermal cycle. As $T_s$ increased, the crystallization peak began to shift toward low temperature. Finally, the crystallization peaks of the first and second thermal cycles were coincided when $T_s$ increased to 340 °C. Figure 9b shows that after PPS melting at 340 °C in the first thermal cycle, the $T_{c1}$ dropped to 239.5 °C, a reduction of 3.6 °C compared to the $T_{c1}$ when the initial processing melt temperature was 330 °C. Importantly, the cooling rate for both sets were the same. Furthermore, it is noteworthy that a reemergence of the discrepancy between $T_{c1}$ and $T_{c2}$ was observed during the second thermal cycle of PPS. The $T_{c2}$ was approximately 8 °C higher than the $T_{c1}$, which is a typical manifestation of the SN behavior. As the processing melt temperature in the second thermal cycle ($T_s$) increased, the $T_{c2}$ gradually decreased due to the diminishing melt memory effect.
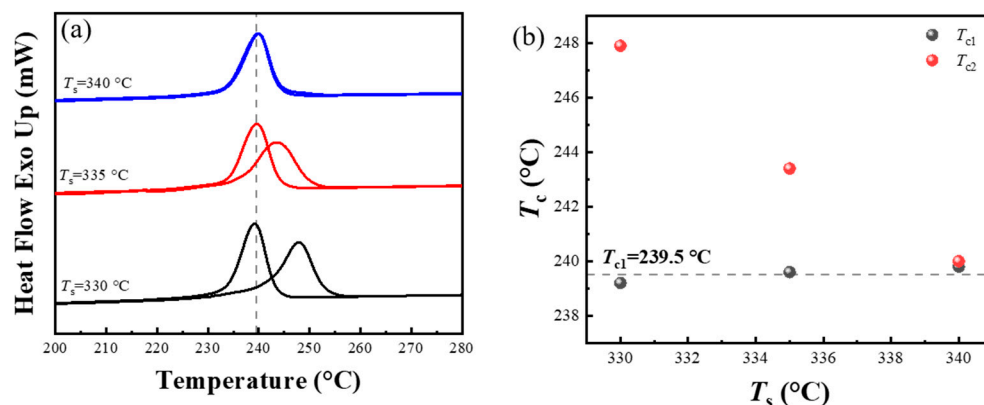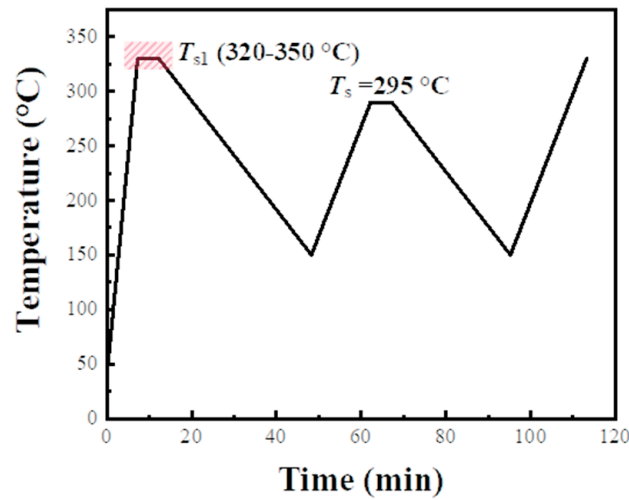
**Figure 9.** (**a**) DSC cooling scans during the first and second thermal cycles. The corresponding secondary processing melt temperature ($T_s$) is marked on the left side of the curve. (**b**) Peak crystallization temperature as a function of the $T_s$, which corresponds to the cooling segments in the first ($T_{c1}$) and second thermal cycle ($T_{c2}$), respectively. The first heating rate was set to 10 °C/min, and the initial melting rate was set to 340 °C.

The experiment with an initial processing melt temperature of 340 °C also demonstrated the synergistic effects of the first heating rate and the initial processing melt temperature. A slower heating rate could induce a strong melt memory effect, which could be counteracted by elevating the initial processing melt temperature. To clearly reveal the impact of the single factor of initial processing melt temperature on the SN behavior in the second crystallization process, the heating should be set above 20 °C/min. This helps to reduce the influence of annealing and thickening during the initial heating process on the melt memory effect. Although the literature has widely reported the impact of the initial processing melt temperature on the crystallization temperature [58–60], it is important to focus on that whether it affects the crystallization behavior in the second thermal cycle.

The thermal protocol that was used to study the relationship between crystallization behaviors and initial processing melt temperature is shown in Figure 10. It can be seen from Figure 11a that when the initial processing melt temperature of PPS was below 330 °C, the initial crystallization temperature decreased from 252.4 °C to 244.4 °C with an elevation in the initial processing melt temperature. This is due to the melt memory effect caused by the PPS spherulites formed during cold crystallization, and the insufficient initial processing melt temperature cannot dimmish the melt memory effect. Although the annealing and thickening after cold crystallization is suppressed by fast heating rates, a suitably high processing melt temperature is essential to diminish the melt memory effect. In the thermal protocol corresponding to Figure 10, this proper initial processing melt temperature ($T_{s1}$) was 330 °C, which corresponding to the lowest initial crystallization temperature ($T_{c1}$). Beyond this processing melt temperature, the $T_{c1}$ of PPS slightly increased with the increase in $T_{s1}$, potentially due to minor crosslinking of molecular chains occurring within PPS.

Interestingly, when PPS underwent the second thermal cycle to induce the SN behavior, the $T_{c2}$ was consistently around 252.4 °C. Figure 11b reveals that although PPS underwent melting at different temperature in the first thermal cycle, the heat flow curves during the secondary cooling process were almost identical, with no significant changes in peak shapes or positions. This consistency suggests minimal influence from the first processing melt temperature on second crystallization behavior with the SN effect. Furthermore, Figure 11c demonstrates that as the initial processing melt temperature gradually increased, the peak remelting temperature of the spherulites forming in the initial crystallization exhibited the same variation trend as the crystallization temperature. Notably, when the initial processing melt temperature was 320 °C, the crystallization and peak remelting temperature from both the prior and subsequent cycles were nearly the same, as shown in Figure 11d. Correspondingly, the heat flow curves during the cooling process and the

heating process for spherulites remelting almost overlapped, indicating the occurrence of the SN behavior in both thermal cycles.



**Figure 10.** Thermal treatment process used in experiment of investigating the relationship between the crystallization behavior and initial processing melt temperature in the first thermal cycle.
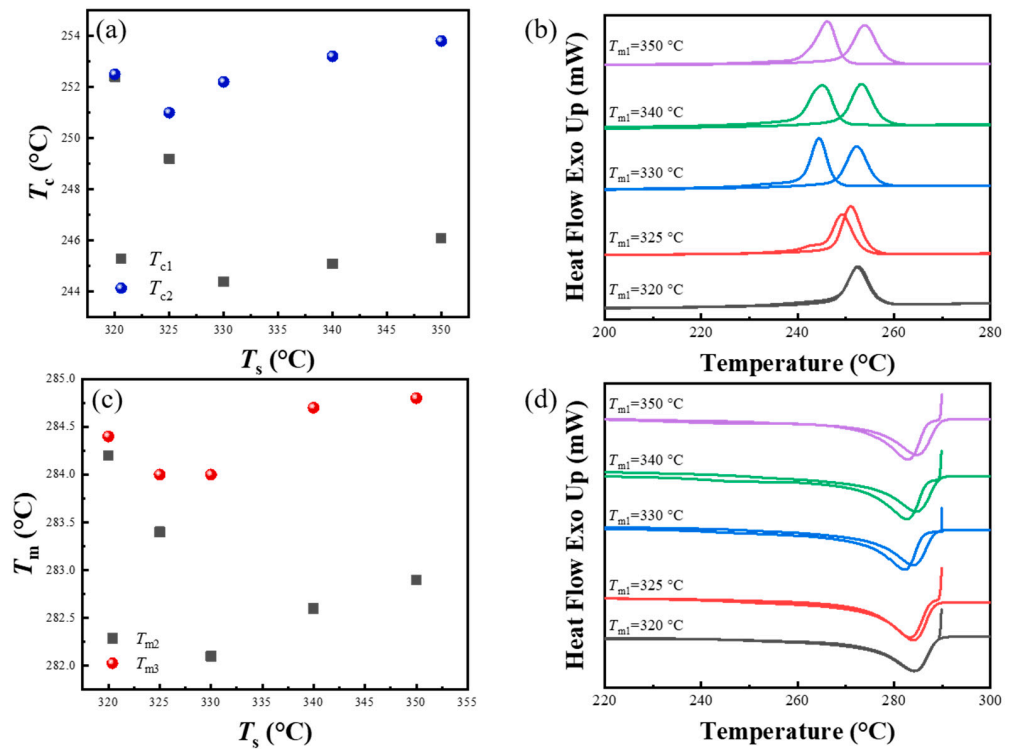


**Figure 11.** (**a**) Peak crystallization temperature as a function of the selected initial processing melt temperature ($T_{s1}$), which corresponds to the cooling segments in the first ($T_{c1}$) and second thermal cycle ($T_{c2}$), respectively. (**b**) The original DSC cooling scans corresponding to the cooling process in two thermal cycle. The corresponding $T_{s1}$ is marked on the left side of the curve. The secondary processing melt temperature was set to 295 °C. (**c**) Peak remelting temperature as a function of the $T_{s1}$, which corresponds to the remelting process of spherulites forming in the initial ($T_{m2}$) and second crystallization ($T_{m3}$), respectively. (**d**) The original DSC heating scans.

## 4. Conclusions

This study systematically investigated the crystallization and remelting behaviors of PPS during two thermal cycles. The effects of various conditions in the thermal cycles on the SN and crystallization behaviors of PPS were established.

(1) While the cooling rate in the second thermal cycle changed the crystallization temperature of PPS, it did not influence the SN behavior of PPS, which was manifested as the same temperature range of the special SN domain, as well as the consistent change trend between the processing melt temperature and crystallization temperature in the second thermal cycle across different crystallization rates.

(2) The heating rate of the second thermal cycle has a marginal influence on the perfection of the crystal. During the heating process of spherulites to melting, a slower heating rate led to significant annealing and thickening of lamellae, such as a rate less than 10 °C/min. As a result, the overall temperature range required for the formation of the specific Domain II' in PPS was lower by approximately 4 °C.

(3) When PPS undergoes the first thermal cycle, there is a synergistic effect between the heating rate and the processing melt temperature. At a slower heating rate or a lower processing melt temperature, such as a rate less than 10 °C/min or a first-cycle processing melt temperature below 330 °C, PPS displays SN behavior. The SN behavior observed in the first thermal cycle originates from crystals formed during the cold crystallization of PPS. These crystals are annealed, and the lamella thickening at a lower heating rate. Additionally, the defect excluded from the lamella might heighten the existing entanglement of the molecular chains. This results in PPS requiring a higher temperature to revert to the random coil conformation. In addition, even with a faster heating rate like 40 °C/min, if the processing melt temperature is too low and insufficient to disrupt the locally ordered regions of the PPS molecular chains, it will also lead to a strong melt memory effect. Therefore, controlling the SN behavior of PPS requires simultaneous control of these two factors.

In summary, this study revealed the temperature parameters necessary for the initiation or inhibition of SN behavior in PPS during two thermal cycles. Furthermore, it elucidated the impact of each temperature parameter on PPS SN behavior, providing novel insights to control the crystallization temperature and morphology of PPS during secondary thermoforming processes.

**Institutional Review Board Statement:** Not applicable.

**Informed Consent Statement:** Not applicable.

**Data Availability Statement:** Data are contained within this article.

**Conflicts of Interest:** The authors declare that they have no known competing financial interests or personal relationships that could have appeared to influence the work reported in this paper.

## References

1. Jagadeesh, P.; Rangappa, S.M.; Siengchin, S.; Puttegowda, M.; Thiagamani, S.M.K.; Rajeshkumar, G.; Kumar, M.H.; Oladijo, O.P.; Fiore, V.; Cuadrado, M.M.M. Sustainable recycling technologies for thermoplastic polymers and their composites: A review of the state of the art. *Polym. Compos.* **2022**, *43*, 5831–5862. [CrossRef]
2. Stoeffler, K.; Andjelic, S.; Legros, N.; Roberge, J.; Schougaard, S.B. Polyphenylene sulfide (PPS) composites reinforced with recycled carbon fiber. *Compos. Sci. Technol.* **2013**, *84*, 65–71. [CrossRef]
3. Wang, H.Y.; Liu, H.B.; Ding, Z.R.; Li, N. Experimental and constitutive modelling studies of semicrystalline thermoplastics under solid-state stamp forming conditions. *Polymer* **2021**, *228*, 123939. [CrossRef]
4. Özdemir, A.O.; Karatas, C.; Kocak, H.; Demiral, M. Investigation of earing defect and thickness distribution in stamp forming of continuous glass fiber reinforced polypropylene composite laminates. *J. Thermoplast. Compos. Mater.* **2023**, *36*, 2154–2168. [CrossRef]
5. Sitohang, R.D.R.; Grouve, W.J.B.; Warnet, L.L.; Akkerman, R. Effect of in-plane fiber waviness defects on the compressive properties of quasi-isotropic thermoplastic composites. *Compos. Struct.* **2021**, *272*, 114166. [CrossRef]
6. Chen, J.P.; Fu, K.K.; Li, Y. Understanding processing parameter effects for carbon fibre reinforced thermoplastic composites manufactured by laser-assisted automated fibre placement (AFP). *Compos. Part A Appl.* **2021**, *140*, 106160. [CrossRef]
7. Boon, Y.D.; Joshi, S.C.; Bhudolia, S.K. Filament Winding and Automated Fiber Placement with In Situ Consolidation for Fiber Reinforced Thermoplastic Polymer Composites. *Polymers* **2021**, *13*, 1951. [CrossRef]
8. Donough, M.J.; Shafaq; St John, N.A.; Philips, A.W.; Prusty, B.G. Process modelling of In-situ consolidated thermoplastic composite by automated fibre placement—A review. *Compos. Part A Appl.* **2022**, *163*, 107179. [CrossRef]
9. O'Shaughnessey, P.G.; Dube, M.; Villegas, I.F. Modeling and experimental investigation of induction welding of thermoplastic composites and comparison with other welding processes. *J. Compos. Mater.* **2016**, *50*, 2895–2910. [CrossRef]
10. Pappada, S.; Salomi, A.; Montanaro, J.; Passaro, A.; Caruso, A.; Maffezzoli, A. Fabrication of a thermoplastic matrix composite stiffened panel by induction welding. *Aerosp. Sci. Technol.* **2015**, *43*, 314–320. [CrossRef]
11. Farahani, R.D.; Dube, M. Novel Heating Elements for Induction Welding of Carbon Fiber/Polyphenylene Sulfide Thermoplastic Composites. *Adv. Eng. Mater.* **2017**, *19*, 1700294. [CrossRef]
12. Mai, K.C.; Zhang, M.Q.; Zeng, H.M.; Qi, S.C. Double melting phenomena of polyphenylene sulfide and its blends. *J. Appl. Polym. Sci.* **1994**, *51*, 57–62. [CrossRef]
13. Ghanbari, L.N.; Crater, E.R.; Enos, N.R.; McNair, O.D.; Moore, R.B.; Wiggins, J.S. Polyphenylene sulfide for high-rate composite manufacturing: Impacts of processing parameters on chain architecture, rheology, and crystallinity. *Polym. Degrad. Stab.* **2023**, *218*, 110580. [CrossRef]
14. Um, C.; Jung, D.; Yu, S.Y.; Lee, S.S.; Lee, H.W.; Lee, P.C.; Ko, Y.K.; Jeoung, S.K.; Ha, J.U. Study on Physical Properties of Polyphenylene Sulfide Composites with Variothermal Mold Temperatures. *Polym. Korea* **2020**, *44*, 798–803. [CrossRef]
15. Zuo, P.Y.; Tcharkhtchi, A.; Shirinbayan, M.; Fitoussi, J.; Bakir, F. Effect of thermal aging on crystallization behaviors and dynamic mechanical properties of glass fiber reinforced polyphenylene sulfide (PPS/GF) composites. *J. Polym. Res.* **2020**, *27*, 77. [CrossRef]
16. Hu, S.H.; Yang, F.; Xiang, M.; Cao, Y.; Wu, T.; Fu, Q. Competition of memory effect and thermal degradation on the crystallization behavior of polyphenylene sulfide. *Polymer* **2022**, *262*, 125427. [CrossRef]
17. Ferrara, J.A.; Seferis, J.C.; Sheppard, C.H. Dual-mechanism kinetics of polyphenylene sulfide (PPS) melt-crystallization. *J. Therm. Anal. Calorim.* **1994**, *42*, 467–484. [CrossRef]
18. Jog, J.P.; Bulakh, N.; Nadkarni, V.M. Crystallization of polyphenylene sulfide. *B Mater. Sci.* **1994**, *17*, 1079–1089. [CrossRef]
19. Furushima, Y.; Nakada, M.; Yoshida, Y.; Okada, K. Crystallization/Melting Kinetics and Morphological Analysis of Polyphenylene Sulfide. *Macromol. Chem. Phys.* **2018**, *219*, 1700481. [CrossRef]
20. Oshima, S.; Higuchi, R.; Kato, M.; Minakuchi, S.; Yokozeki, T.; Aoki, T. Cooling rate-dependent mechanical properties of polyphenylene sulfide (PPS) and carbon fiber reinforced PPS (CF/PPS). *Compos. Part A Appl.* **2023**, *164*, 107250. [CrossRef]
21. Sangroniz, L.; Cavallo, D.; Müller, A.J. Self-Nucleation Effects on Polymer Crystallization. *Macromolecules* **2020**, *53*, 4581–4604. [CrossRef]
22. Candau, N.; Fernandes, J.P.C.; Vasmer, E.; Maspoch, M.L. Cellulose nanocrystals as nucleating agents for the strain induced crystallization in natural rubber. *Soft Matter* **2022**, *18*, 8663–8674. [CrossRef]
23. Yang, J.H.; Xu, T.; Lu, A.; Zhang, Q.; Tan, H.; Fu, Q. Preparation and properties of poly (p-phenylene sulfide)/multiwall carbon nanotube composites obtained by melt compounding. *Compos. Sci. Technol.* **2009**, *69*, 147–153. [CrossRef]
24. Diez-Pascual, A.M.; Naffakh, M. Tuning the properties of carbon fiber-reinforced poly(phenylene sulphide) laminates via incorporation of inorganic nanoparticles. *Polymer* **2012**, *53*, 2369–2378. [CrossRef]
25. Yan, P.; Yang, F.; Xiang, M.; Wu, T.; Fu, Q. New insights into the memory effect on the crystallization behavior of poly(phenylene sulfide). *Polymer* **2020**, *195*, 122439. [CrossRef]
26. Ren, Y.; Lu, Y.G.; Zhang, B.; Su, J.Y.; Liu, W.P.; Zhou, J.F.; Yu, M.H.; Zhu, S. Control of the crystalline morphology of polyphenylene sulfide in secondary thermoforming by the strong memory effect of crystallization. *Polymer* **2023**, *281*, 126067. [CrossRef]
27. Chen, X.; Mamun, A.; Alamo, R.G. Effect of Level of Crystallinity on Melt Memory Above the Equilibrium Melting Temperature in a Random Ethylene 1-Butene Copolymer. *Macromol. Chem. Phys.* **2015**, *216*, 1220–1226. [CrossRef]
28. Gao, H.; Vadlamudi, M.; Alamo, R.G.; Hu, W. Monte Carlo Simulations of Strong Memory Effect of Crystallization in Random Copolymers. *Macromolecules* **2013**, *46*, 6498–6506. [CrossRef]

29. Reid, B.O.; Vadlamudi, M.; Mamun, A.; Janani, H.; Gao, H.; Hu, W.; Alamo, R.G. Strong Memory Effect of Crystallization above the Equilibrium Melting Point of Random Copolymers. *Macromolecules* **2013**, *46*, 6485–6497. [CrossRef]

30. De Stefano, F.; Cicolella, A.; Barreca, A.; Scoti, M.; De Rosa, C. Melt memory in propene-pentene isotactic copolymers: The case of defects hosted in the crystals. *Polym. Chem.* **2023**, *14*, 5260–5273. [CrossRef]

31. Liao, Y.L.; Pan, L.; Ma, Z.; Cavallo, D.; Liu, G.M.; Wang, D.J.; Müller, A.J. How 4-(7-Octen-1-yl)-N,N-diphenylaniline co-units induce strong melt memory effects in isotactic polypropylene random copolymers. *Polymer* **2023**, *282*, 126184. [CrossRef]

32. Sangroniz, L.; Safari, M.; de Ilarduya, A.M.; Sardon, H.; Cavallo, D.; Müller, A.J. Disappearance of Melt Memory Effect with Comonomer Incorporation in Isodimorphic Random Copolyesters. *Macromolecules* **2023**, *56*, 7879–7888. [CrossRef]

33. Jariyavidyanont, K.; Janke, A.; Androsch, R. Crystal self-nucleation in polyamide 11 of different semicrystalline morphology. *Polymer* **2019**, *184*, 121864. [CrossRef]

34. Joijode, A.S.; Hawkins, K.; Tonelli, A.E. Improving Poly(ethylene terephthalate) Through Self-nucleation. *Macromol. Mater. Eng.* **2013**, *298*, 1190–1200. [CrossRef]

35. Shen, J.F.; Zhou, Y.F.; Lu, Y.G.; Wang, B.H.; Shen, C.Y.; Chen, J.B.; Zhang, B. Later Stage Melting of Isotactic Polypropylene. *Macromolecules* **2020**, *53*, 2136–2144. [CrossRef]

36. Balzano, L.; Rastogi, S.; Peters, G. Self-Nucleation of Polymers with Flow: The Case of Bimodal Polyethylene. *Macromolecules* **2011**, *44*, 2926–2933. [CrossRef]

37. Vassiliadou, O.; Chrysostomou, V.; Pispas, S.; Klonos, P.A.; Kyritsis, A. Molecular dynamics and crystallization in polymers based on ethylene glycol methacrylates (EGMAs) with melt memory characteristics: From linear oligomers to comb-like polymers. *Soft Matter* **2021**, *17*, 1284–1298. [CrossRef]

38. Sangroniz, L.; Ocando, C.; Cavallo, D.; Müller, A.J. Melt Memory Effects in Poly(butylene succinate) Studied by Differential Fast Scanning Calorimetry. *Polymers* **2020**, *12*, 2796. [CrossRef] [PubMed]

39. Liu, X.; Yu, W. Role of Chain Dynamics in the Melt Memory Effect of Crystallization. *Macromolecules* **2020**, *53*, 7887–7898. [CrossRef]

40. Arandia, I.; Mugica, A.; Zubitur, M.; Arbe, A.; Liu, G.; Wang, D.; Mincheva, R.; Dubois, P.; Muller, A.J. How Composition Determines the Properties of Isodimorphic Poly(butylene succinate-ran-butylene azelate) Random Biobased Copolymers: From Single to Double Crystalline Random Copolymers. *Macromolecules* **2015**, *48*, 43–57. [CrossRef]

41. Liu, X.R.; Wang, Y.; Wang, Z.F.; Cavallo, D.; Muller, A.J.; Zhu, P.; Zhao, Y.; Dong, X.; Wang, D.J. The origin of memory effects in the crystallization of polyamides: Role of hydrogen bonding. *Polymer* **2020**, *188*, 122117. [CrossRef]

42. Peters, O.A.; Still, R.H. The thermal degradation of poly (phenylene sulphide)—Part 1. *Polym. Degrad. Stab.* **1993**, *42*, 41–48. [CrossRef]

43. Reents, W.D., Jr.; Kaplan, M.L. Mass spectral analysis of poly (p-phenylene sulphide). *Polymer* **1982**, *23*, 310–313. [CrossRef]

44. Yan, P.; Peng, W.X.; Yang, F.; Cao, Y.; Xiang, M.; Wu, T.; Fu, Q. Investigation on thermal degradation mechanism of poly(phenylene sulfide). *Polym. Degrad. Stab.* **2022**, *197*, 109863. [CrossRef]

45. Lian, D.; Zhang, R.; Lu, J.; Dai, J. Performances and structure changes of neat PPS fiber and nano Ti-SiO$_2$-modified PPS fiber after over-temperature oxidation. *High Perform. Polym.* **2018**, *30*, 328–338. [CrossRef]

46. Hawkins, R.T. Chemistry of the cure of poly (p-phenylene sulfide). *Macromolecules* **1976**, *9*, 189–194. [CrossRef]

47. Hu, Y.Y.; Liao, Y.; Zheng, Y.N.; Ikeda, K.; Okabe, R.; Wu, R.F.; Ozaki, R.; Xu, J.; Xu, Q.Y. Influence of Cooling Rate on Crystallization Behavior of Semi-Crystalline Polypropylene: Experiments and Mathematical Modeling. *Polymers* **2022**, *14*, 3646. [CrossRef] [PubMed]

48. Boelle, S.; Alms, J.; Weihermueller, M.; Robisch, M.; Wipperfuerth, J.; Hopmann, C.; Dahlmann, R. Modelling of the melting point shift in semi-crystalline thermoplastics dependent on prior cooling rate and heating rate. *Polymer* **2022**, *254*, 125100. [CrossRef]

49. Heidrich, D.; Gehde, M. Calorimetric analysis of the crystallization of PBT considering the dynamic cooling condition of real processing. *Polym. Test.* **2020**, *85*, 106459. [CrossRef]

50. Moghadam, A.S.N.; Rafizadeh, M.; Taromi, F.A. Non-isothermal crystallization kinetics of polyethylene terephthalate: A study based on Tobin, Hay and Nakamura models. *Iran. Polym. J.* **2023**, *32*, 125–137. [CrossRef]

51. Speranza, V.; Salomone, R.; Pantani, R. Effects of Pressure and Cooling Rates on Crystallization Behavior and Morphology of Isotactic Polypropylene. *Crystals* **2023**, *13*, 922. [CrossRef]

52. Volpe, V.; Speranza, V.; Schrank, T.; Berer, M.; Pantani, R. An investigation of crystallization kinetics of polyoxymethylene in processing conditions. *Polym. Adv. Technol.* **2022**, *34*, 634–645. [CrossRef]

53. Ren, J.Y.; Ouyang, Q.F.; Ma, G.Q.; Li, Y.; Lei, J.; Huang, H.D.; Jia, L.C.; Lin, H.; Zhong, G.J.; Li, Z.M. Enhanced dielectric and ferroelectric properties of poly (vinylidene fluoride) through annealing oriented crystallites under high pressure. *Macromolecules* **2022**, *55*, 2014–2027. [CrossRef]

54. Bair, H.E.; Salovey, R.; Huseby, T.W. Melting and annealing of polyethylene single crystals. *Polymer* **1967**, *8*, 9–20. [CrossRef]

55. Schick, C.; Androsch, R. The Origin of Annealing Peaks in Semicrystalline Polymers: Enthalpy Recovery or Melting? *Macromolecules* **2020**, *53*, 8751–8756. [CrossRef]

56. Hu, W.B. *Principles of Polymer Crystallization*; Chemical Industry Press: Beijing, China, 2013.

57. Hoffman, J.D.; Davis, G.T.; Lauritzen, J.I., Jr. The rate of crystallization of linear polymers with chain folding. In *Treatise on Solid State Chemistry: Volume 3 Crystalline and Noncrystalline Solids*; Springer: Berlin/Heidelberg, Germany, 1976; pp. 497–614.

58. Yin, Y.G.; Song, Y.; Xiong, Z.J.; Zhang, X.Q.; de Vos, S.; Wang, R.Y.; Joziasse, C.A.P.; Liu, G.M.; Wang, D.J. Effect of the melting temperature on the crystallization behavior of a poly(L-lactide)/poly(D-lactide) equimolar mixture. *J. Appl. Polym. Sci.* **2016**, *133*, 43015. [CrossRef]

59. Supaphol, P.; Lin, J.S. Crystalline memory effect in isothermal crystallization of syndiotactic polypropylenes: Effect of fusion temperature on crystallization and melting behavior. *Polymer* **2001**, *42*, 9617–9626. [CrossRef]

60. Kong, W.L.; Zhu, B.; Su, F.M.; Wang, Z.; Shao, C.G.; Wang, Y.M.; Liu, C.T.; Shen, C.Y. Melting temperature, concentration and cooling rate-dependent nucleating ability of a self-assembly aryl amide nucleator on poly(lactic acid) crystallization. *Polymer* **2019**, *168*, 77–85. [CrossRef]

MDPI

*Article*

# Interfacial Enhancement and Composite Manufacturing of Continuous Carbon-Fiber-Reinforced PA6T Composites via PrePA6T Ultrafine Powder

**Jiahong Yao [1], Zhao Wang [1], Jiacao Yang [2,\*], Xiaojun Wang [2,\*] and Jie Yang [2,3]**

1   College of Polymer Science and Engineering, Sichuan University, Chengdu 610064, China;
    yaojiahong@stu.scu.edu.cn (J.Y.); wangzhao2019@outlook.com (Z.W.)
2   Analytical and Testing Center, Sichuan University, Chengdu 610064, China; ppsf@scu.edu.cn
3   State Key Laboratory of Polymer Materials Engineering, Sichuan University, Chengdu 610065, China
\*   Correspondence: jiacaoyang@outlook.com (J.Y.); wangxj@scu.edu.cn (X.W.)

**Abstract:** Semi-aromatic poly (hexamethylene terephthalamide) (PA6T) oligomer (prePA6T) ultrafine powder, with a diameter of <5 μm, was prepared as an emulsion sizing agent to improve the impregnation performance of CF/PA6T composites. The prePA6T hyperfine powder was acquired via the dissolution and precipitation "phase conversion" method, and the prePA6T emulsion sizing agent was acquired to continuously coat the CF bundle. The sized CF unidirectional tape was knitted into a fabric using the plain weave method, while the CF/PA6T laminated composites were obtained by laminating the plain weave fabrics with PA6T films. The interfacial shear strength (IFSS), tensile strength (TS), and interlaminar shear strength (ILSS) of prePA6T-modified CF/PA6T composites improved by 54.9%, 125.3%, and 120.9%, respectively. Compared with the commercial polyamide sizing agent product PA845H, the prePA6T sizing agent showed better interfacial properties at elevated temperatures, especially no TS loss at 75 °C. The SEM observations also indicated that the prePA6T emulsion has an excellent impregnation effect on CF, and the fracture mechanism shifted from adhesive failure mode to cohesive failure mode. In summary, a facile, heat-resistant, undamaged-to-fiber environmental coating process is proposed to continuously manufacture high-performance thermoplastic composites, which is quite promising in mass production.

**Keywords:** carbon fiber; PA6T; sizing agent; thermoplastic composites; ultrafine powder

## 1. Introduction

Carbon-fiber-reinforced thermoplastic composites (CFRTPs) have the advantages of good impact toughness, high damage tolerance, repairability, recyclability, and a short molding period compared with carbon-fiber-reinforced thermosetting composites (CFRTSs). Particularly, high-performance CFRTPs based on polyphenylene sulfide (PPS), polyether ether ketone (PEEK), polyetherimide (PEI), semi-aromatic poly (hexamethylene terephthalamide) (PA6T), etc., have great superiority in terms of heat resistance, mechanical properties, chemical stability, etc., which are widely applied in the aerospace, automotive, and military industries [1–3]. Semi-aromatic polyamide 6T (PA6T), the polycondensation product of terephthalic acid and hexanediamine, consists of rigid aromatic rings and flexible aliphatic chains, which integrate the excellent heat resistance and corrosion resistance of aromatic polyamides and the processibility and flowability of aliphatic ones. By virtue of its comprehensive properties, PA6T has extensive application prospects in the field of precision electronic and automobile parts.

CFRTPs have drawn great attention from researchers in both academia and industry due to their excellent comprehensive properties. The interface of fiber and resin is crucial in determining stress transfer. However, it is difficult to acquire a good interaction between fiber and resin due to the chemical inertia of CF. Accordingly, quite a few methods have been

devised to promote interfacial interaction between resin matrix and CF by both physical and chemical means. Methods such as plasma treatment [4], oxidation treatment [5–7], high-energy radiation treatment [8,9], etc., are widely employed to introduce functional groups to activate the CF, although such CF modification methods require redundant treating procedures and would damage the CF's intrinsic properties [4,10–14].

Among those existing fiber modification methods, sizing is a common, efficient, and low-cost way to treat carbon fiber, in which an even polymer coating is formed to improve the wettability, reactivity, adhesion, and abrasive resistance without damaging the CF chemical structure. However, the commercial sizing agents that are widely utilized now are mostly intended for CFRTSs [15,16], showing poor adhesion and stability [17] when it comes to thermoplastic composites, especially high-performance ones. Consequently, developing sizing agents specifically for high-performance CFRTPs with good compatibility and thermal resistance is of vital significance for special engineering thermoplastics. In addition, continuously processing and manufacturing continuous carbon-fiber-reinforced thermoplastic composites is indispensable in commercial mass production as continuous fibers in the matrix provide much stronger mechanical properties [18]. Hence, the sizing process must be facile and continuously operable. In our previous work [19], a PA6T oligomer was synthesized and deposited on a CF surface with the assistance of ultrasound, and the PA6T interfacial layer was coated on the CF surface via in situ polymerization, which significantly improved its interfacial properties. However, such ultrasound-assisted coating technology is not suitable for the continuous treatment of CF. On this basis, this paper aims to explore a facile and efficient technology to prepare continuous carbon-fiber-reinforced PA6T composites.

The high melt viscosity and weak interaction between resin and the fiber bundle [20–23] are the main points restricting the processing and overall performance of special engineering plastic composites. To solve such problems, a series of processing techniques were exploited, such as solution impregnation [21,22], pultrusion [24,25], powder impregnation [26,27], film lamination [28], fiber blending [29,30], etc. In fact, the insolubility of PA6T makes solution processing hard to implement. In addition, pultrusion requires sufficient dwell time in the customized die head for PA6T, which is at risk of thermal oxygen degradation or crosslinking [31–34]. Moreover, it is hard for film lamination processes to obtain a good impregnation state, which may result in many internal defects [28]. As for powder impregnation, the resin particles are dispersed in the fiber bundle and then melt to the molding, which evades the impregnation difficulty for high-viscosity melting. In modern powder impregnation processes, the size of the resin particles is usually over 50 μm, whereas the diameter of CF is around 5–7 μm. Research [26] has shown that the driving force for resin particles to penetrate the fiber bundle will rise much higher as the resin particle size increases. Moreover, it is hard to process polymers with high molecular weights into powders without damaging their intrinsic structures. Therefore, using resin particles with tiny sizes would be conducive to CF impregnation. Interfacial performance enhancement can be achieved via the in-situ polymerization of prePA6T.

Here, the dissolution and precipitation "phase conversion" method was put forward to acquire prePA6T hyperfine powder (diameter < 5 μm). The prePA6T powder was prepared into an oligomer emulsion sizing agent and continuously impregnated on a CF bundle using self-made spreading–impregnating equipment without an additional driving force, followed by lamination and hot-pressing with resin films after in situ polymerization to prepare continuous carbon-fiber-reinforced PA6T composites. On that basis, the effects of the solid content and polymerization degree on the micro- and macro-properties were discussed, and the discrepancy in the modification effect between the prePA6T emulsion sizing agent and the commercial product PA845H was compared. In summary, this article aims to explore an efficient, continuous, heat-resistant, undamaged-to-fiber coating technology for the preparation of high-performance thermoplastic composites with excellent interfacial performance and comprehensive properties.

## 2. Experimental Section

### 2.1. Materials

A PA6T (PA6T/6 = 50:50, random copolymer) oligomer with a degree of polymerization of around 4 was synthesized by a novel solution–solid phase one-pot polycondensation method according to our previous work [17,28]. The specific method is presented in the Supporting Information. PA6T (PA6T/6 = 50:50, random copolymer) resin was provided by Sanli Benzo New Materials Co., Ltd. (Qingdao, China). Carbon fiber (TC35-12K) (diameter: 7 μm) was purchased from Formosa Plastics Group (Taiwan, China). The PA6T oligomer (terephthalate-hexamethylamine salt) was synthesized in our laboratory. Concentrated sulfuric acid (98 wt%), N-methylpyrrolidone (NMP, AR, 99%), terephthalic acid (polymer grade), hexamethylenediamine (AR), caprolactam (CPL), and sodium dodecyl benzene sulfonate (SDBS, AR, 90%) were all acquired from Kelong Chemical Co., Ltd. (Chengdu, China) and used as received. Michelman Hydrosize TMPA845 fiber sizing agent (PA845H), a polyamide aqueous dispersion (solid content 22–24%), was supplied by Michelmen Chemical Trading Co., Ltd. (Shanghai, China), and polyethylene oxide (PEO, PFZ blue) was purchased from Sumitomo (Kyoto, Japan).

### 2.2. Sample Preparation for Micro-Bond Test

As shown in Figure 1, the carbon fibers were immersed in the prePA6T/NMP solution at different concentrations (5 wt%, 10 wt%, 20 wt%, and 25 wt%) for 10 min. After filtering from the solution, the CFs were quickly placed in deionized water, so that the prePA6T precipitated on the CF surface and a uniform coating formed. Subsequently, the coated CFs were dried in an oven, followed by heating at 320 °C for 2, 5, 10, and 14 min to acquire PA6T sized CFs with different solution concentrations and reaction degrees. For comparison, CF was immersed in the commercial sizing agent PA845H for 10 min with the same post-treatments applied and was labeled as CF-PA845H. The microdroplets were prepared via the knotting method to characterize the micro-interfacial performance. After that, the PA6T fiber was knotted on the sized CF, and the microdroplet was acquired after being melted. The IFSS test was carried out on the microdroplet, and detailed experiment information can be seen in the Supplementary Materials.
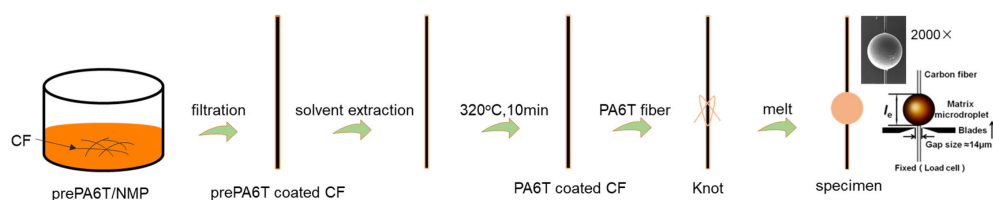


**Figure 1.** Schematic of single carbon fiber coating process.

For convenience of expression, the prePA6T-treated carbon fibers are named as CF-x-y min, where x and y denote the solution concentration and polymerization time, respectively.

### 2.3. Preparation of prePA6T Hyperfine Powder and Emulsion

PrePA6T with a degree of polymerization of around 4 was synthesized according to our previous work [19] and was then dissolved in NMP at 140 °C. The prePA6T hyperfine powder was acquired by the dissolution and precipitation "phase conversion" method, in which three techniques were applied to acquire prePA6T particles: rapid cooling precipitation in NMP, non-solvent precipitation in deionized water, and non-solvent precipitation in ethanol. For comparison, the prePA6T/NMP solution was sonicated to acquire oligomer powder. After washing and filtration, the powders were dispersed in deionized water to determinate the particle size and distribution so as to screen the technology with the smallest particle size and narrowest distribution.

To acquire a stable and uniform dispersion state, the prePA6T hyperfine powder was dispersed in deionized water with 1 wt‰ of SDBS and PEO added in. A series of

dispersions with different solid concentrations were prepared (1 wt%, 2 wt%, 5 wt%, and 10 wt%).

## 2.4. Preparation of CF/PA6T Composites

As shown in Figure 2, a continuous preparation route of CF/PA6T composites was exploited to acquire tensile and ILSS test specimens. The CF unidirectional tape was prepared by impregnating the continuous CF bundles with the prePA6T emulsion sizing agent and the commercial product PA845H. PA6T film was prepared by hot-pressing the PA6T resin at 320 °C with an applied pressure of 2.5 MPa. Meanwhile, the unidirectional tape was knitted into fabric by plain weave method.
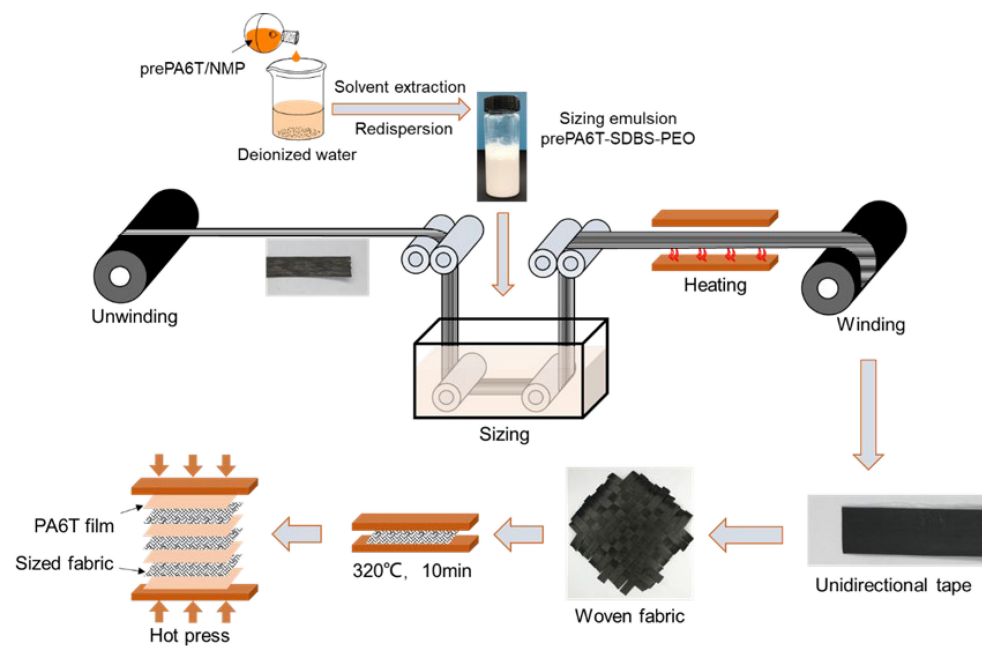


**Figure 2.** Schematic of continuous carbon fiber coating and CF/PA6T composite preparation.

Next, the plain weave fabric was hot-pressed at 320 °C for 2 min, 5 min, 10 min, and 14 min to explore the effect of polymerization degree on the composite performance. PA6T-laminated composites were prepared by laminating the PA6T resin films and sized fabrics. Based on the polymerization time, the unidirectional tape with a coating concentration of 10 wt% was named as CF-10′-z min, where 10′ represents the coating concentration and z represents the polymerization time.

## 2.5. Characterization

The intrinsic viscosity, particle size and distribution, surface morphology, heat resistance, and macro- and micro-mechanical properties were characterized. The experimental details can be seen in the Supplementary Materials.

## 3. Results and Discussion

### 3.1. The Morphology and IFSS of Sized Single CF

The surface morphology of the sized CFs was inspected by the SEM test. As shown in Figure 3, few resins could be found on the fiber surface at 5 wt% concentration. As the coating concentration increased, the coated resin layer thickened. At 25 wt% concentration, a complete coat formed on the CF surface and grooves, where in situ polymerization occurred to enhance the stress transfer efficiency. For comparison, the modification effect of the commercial aliphatic PA sizing agent PA845H was also discussed. As we can see, the polyamide nanoparticles aggregated on the surface of the PA845H-treated fiber with the assistance of the film-forming agent, and a compact coating formed so as to bridge the

resin matrix and CF. However, additives in PA845H such as a film-forming agent would worsen the heat resistance and overall performance of composites.
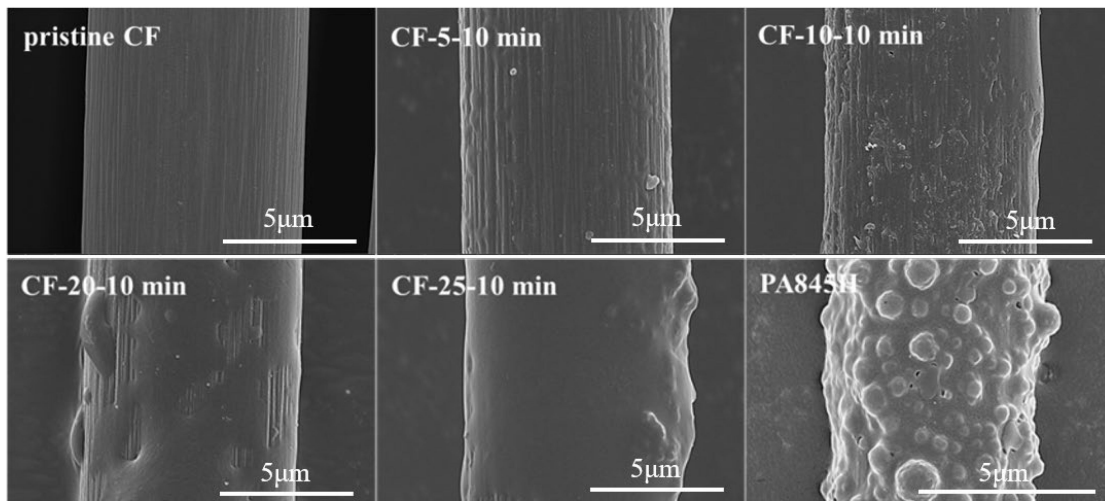


**Figure 3.** Fiber morphology with different concentrations of PA6T oligomer solution coated.

As we can see in Figure 4a, the intrinsic viscosity increased as the polymerization time lengthened due to the growing molecular weight. Interestingly, the viscosity rose rapidly in the early polymerization stage as more active terminal groups existed. After 10 min of polymerization, the [η] rose to 0.87 dL/g, which closely resembled the matrix resin's value of 0.89 dL/g. Figure 4b shows that the resin turned yellow as the polymerization time increased, indicating that the resin underwent slight thermal and oxygen degradation. When the reaction time increased to 14 min, the resin color deepened and the intrinsic viscosity increased rapidly to 1.09 dL/g, indicating the forming of a cross-linked structure.
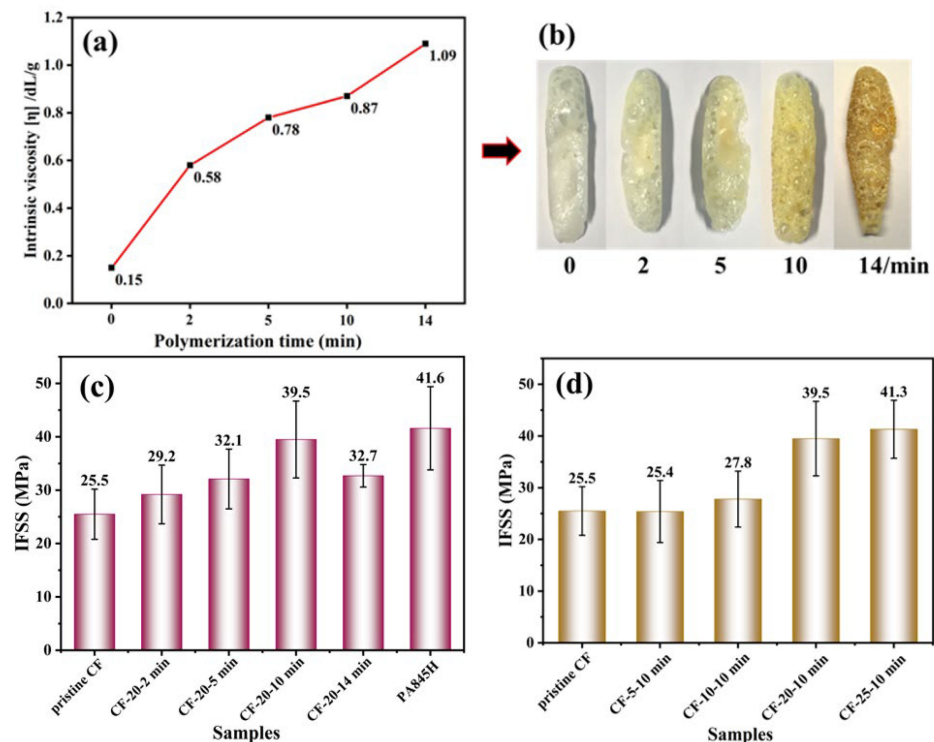


**Figure 4.** The intrinsic viscosity (**a**) and surface morphology (**b**) of PA6T coating with different polymerization times, and the IFSS of CF/PA6T composites with different polymerization times (**c**) and different concentrations of PA6T oligomer coating (**d**).

Some research has been conducted on the effect of sizing agent molecular weight on the interfacial performance of thermosetting plastic composites [35–38]. It was demonstrated that a thermosetting sizing agent with a high molecular weight would make the molecular chain move hard, resulting in a weak interface with the bulk resin matrix. Conversely, low-molecular-weight ones have more active groups, markedly enhancing the wettability of the fiber surface and rendering a stronger interaction. However, there are few reports on thermoplastic sizing agents. It can be seen in Figure 4c that the IFSS gradually increased as the polymerization degree increased when the polymerization time was less than 14 min. It could be explained that the linear molecular structure of prePA6T allowed for better mobility, despite having a higher molecular weight. In addition, the long molecular chains were more likely to tangle with the matrix resins, and more amide bonds provided stronger hydrogen bonding, so the IFSS performance enhanced as the polymerization time increased. Nevertheless, a long polymerization time at high temperatures would intensify the thermal oxygen degradation of the coating layer [39,40], thus bringing about a decrease in IFSS value at 14 min polymerization time. In conclusion, the IFSS of CF-20-10 min increased from 25.5 MPa initially to 39.5 MPa with an increase rate of 55%. This improvement is comparable to that of PA845H, which saw an increase of 63% to 41.6 MPa.

The micro IFSS value did not fluctuate much at low coating concentrations, which indicated that the polymer particles were too dispersed and diluted at a low content to form a complete coating over the fiber. Therefore, the enhancement effect on the interfacial performance was not notable enough, which was consistent with the SEM images of the surface morphology in Figure 3. At 20 wt% concentration, a stable and interconnected coating formed, which gave rise to a remarkable improvement of 54.9% in the IFSS. After that, the IFSS did not increase much at 25 wt% concentration as a complete coating had formed.

The adhesiveness between a resin and a fiber can be determined by the fiber morphology after debonding. As shown in Figure 5, the surface of the debonded pristine CF was smooth and no residual resin existed in the grooves, indicating a poor interaction between the resin matrix and pristine CF. By contrast, residual resin could be observed on the surface and grooves of sized CFs after debonding, which verified that the low-viscosity oligomer had better impregnation on the CF. After in situ polymerization, a stable and uniform polymer coating formed on the CF surface, effectively bridging the fiber and resin matrix and improving the IFSS of the composites.
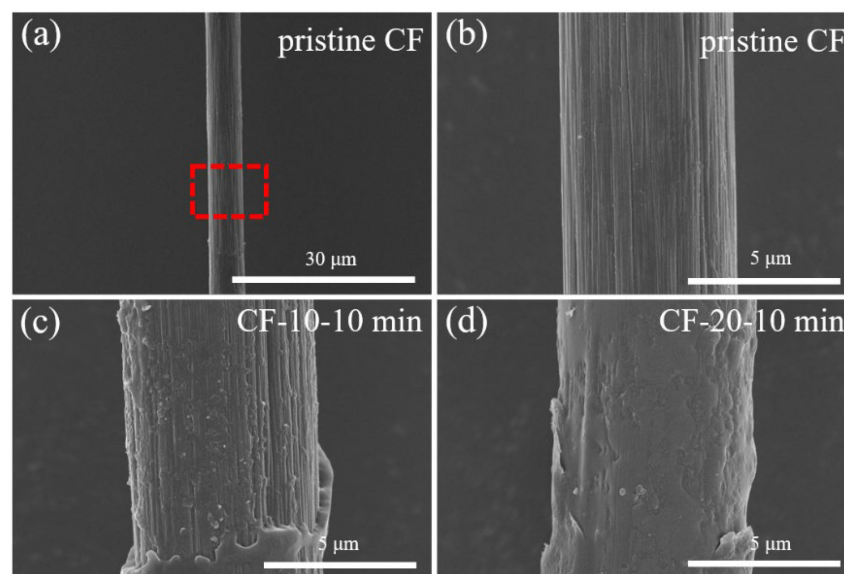


**Figure 5.** Fiber morphology after debonding with different concentrations of PA6T oligomer coated: (**a**) pristine CF; (**b**) magnification of highlighted part of (**a**) pristine CF; (**c**) CF-10-10 min; (**d**) CF-20-10 min.

### 3.2. Interfacial Properties at Elevated Temperatures

High-performance CFRTPs are usually utilized in harsh service environments such as high temperatures, so heat resistance is vital for composites. Therefore, TGA and the micro-bond test under elevated temperatures were employed. The TGA curves in Figure 6 show that the thermal decomposition temperatures of the prePA6T-modified CF were over 400 °C, whereas the PA845H-modified CF had a lower thermal decomposition temperature and char yield. There are two stages of losing weight for PA845H. The first stage is at around 350 °C, which is attributed to the decomposition of dispersing agent and film-forming agent. The second stage is at over 400 °C, which results from the decomposition of the aliphatic polyamide backbone. There were two main reasons for this discrepancy in thermal stability. Firstly, the rigid benzene rings in the PA6T backbone enhanced the thermal tolerance, while the aliphatic polyamide in PA845H with more flexibility reduced the heat resistance. Secondly, the heat-labile additives in PA845H contributed to the approximately 15% weight loss at around 350 °C.
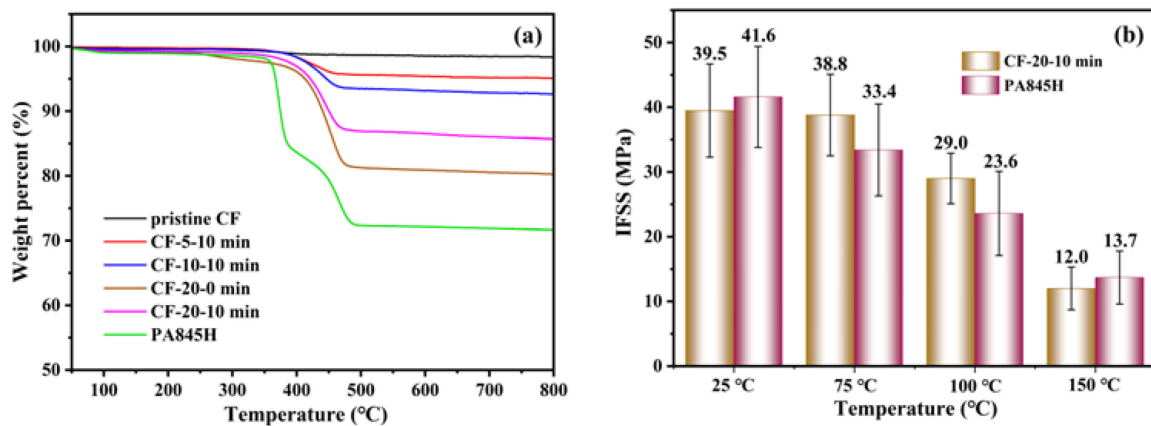


**Figure 6.** The TGA curves of PA6T oligomer solution-coated CF (**a**); the IFSS comparison between PA6T oligomer- and PA845H-coated CF/PA6T composites under elevated testing temperatures (**b**).

Comparing the IFSS of CF-20-10 min and CF-PA845H at elevated temperatures, the IFSS decreased steadily as the temperature increased. It is believed that the grasping force of the resin microdroplet on CF weakened due to the discrepancy in thermal expansion coefficient between the resin and CF. Additionally, the shrinking static friction force, originating from the resin grasping force on fiber in the radial direction, accounted for the major loss in IFSS [41]. As shown in Figure 6, the IFSS of CF-20-10 min at 75 °C decreased by merely 0.7 MPa compared to 25 °C, while the IFSS of CF-PA845H dropped by 19.7%, which resulted from the heat resistance discrepancy of the two sizing agents. As discussed before, there are plenty of additives with poor heat resistance in PA845H, and the primary component of PA845H is aliphatic polyamide, whose $T_g$ is 50–55 °C [42]. As the temperature was elevated at 75 °C (above the $T_g$ of aliphatic polyamide), the grasping force weakened notably due to the remarkably increasing thermal expansion coefficient discrepancy between the fiber and resin. However, the semi-aromatic polyamide PA6T has a $T_g$ of 85 °C, which shows a lower thermal expansion coefficient at 75 °C. Thus, the in situ polymerization-modified PA6T coating has a better interfacial modification effect at elevated temperatures than PA845H.

### 3.3. PrePA6T Particle Size Distribution and Emulsion Preparation

Considering the complex post-treatment techniques and large solvent consumption in the solution coating process, it is challenging to implement the coating of continuous fiber, so it was necessary to prepare prePA6T powder as a stable emulsion slurry. The dissolution and precipitation "phase conversion" method was exploited to prepare polymer micro-particles [43]. In this method, the solutes are precipitated from the solvent by rapidly

cooling or adding non-solvent to acquire particles with micron or nanoscale size, which is a common way to prepare inorganic nanomaterials. In this study, the best precipitation condition was explored, and the oligomer particle size and distribution are shown in Figure 7. The results showed that deionized water is the best candidate for the precipitant. According to the Flory–Huggins theory, the capacity for a polymer solution to precipitate depends on the interaction parameter between non-solvent and solvent. It was found that the interaction between $H_2O$ and NMP is stronger than that between ethanol and NMP. When the oligomer/NMP solution was poured into the water, the intense interaction broke the thermodynamic equilibrium, and the nucleation sites were too numerous to adhere to each other, contributing to the tiny particle size.
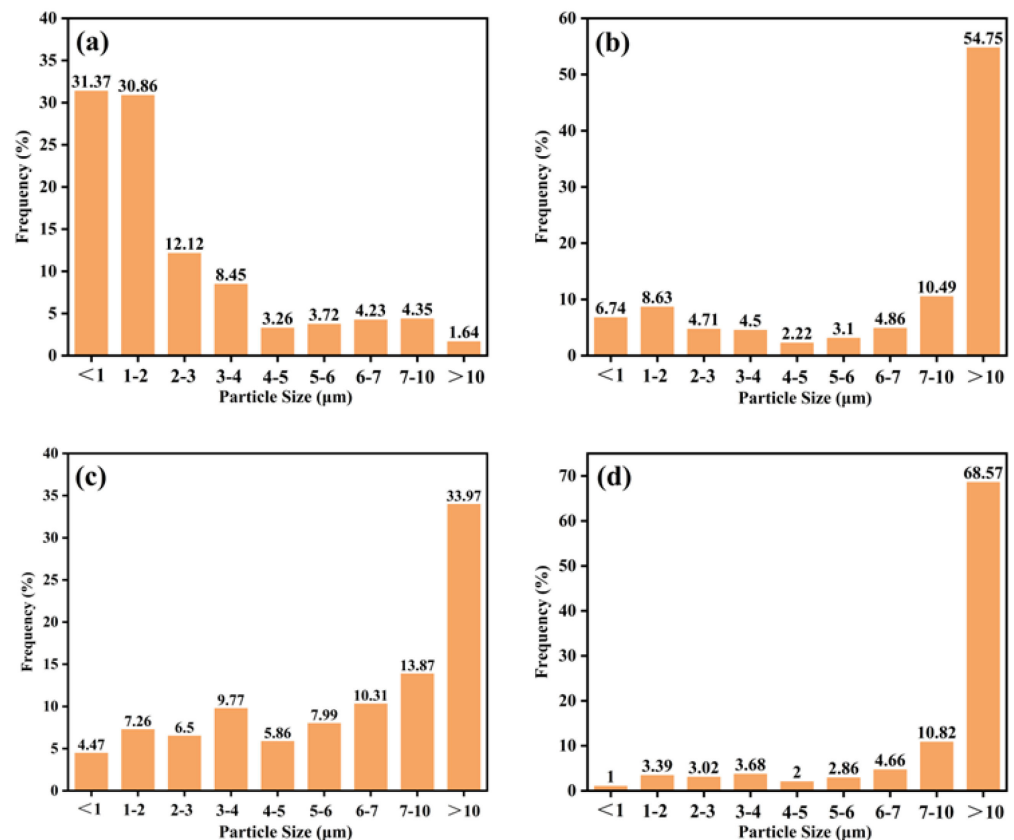


**Figure 7.** The oligomer particle size and distribution obtained via phase separation of PA6T oligomer solution by (**a**) non–solvent precipitation in deionized water (**b**) and non–solvent precipitation in ethanol; (**c**) rapid cooling precipitation in NMP; (**d**) sonication in NMP.

Based on this, the surfactant SDBS and the thickener PEO were added to keep the emulsion stable. It was shown that the emulsion has stability as good as commercial PA845H, and no apparent sediment was observed after one month.

*3.4. Morphologies of Emulsion-Coated CF Unidirectional Tapes*

The morphologies of the coated CF unidirectional tapes are shown in Figure 8. Similar with Figure 3, little resin could be found on the surface of CF-1′-10 min and CF-2′-10 min. At 10 wt% concentration, the CF was entirely wrapped by resin, and the interspaces between CFs were adequately filled. Comparatively, it was hard to distinguish the single filament for CF unidirectional tape coated by PA845H with a higher solid content, suggesting that PA845H had an excellent coating and film-forming performance.
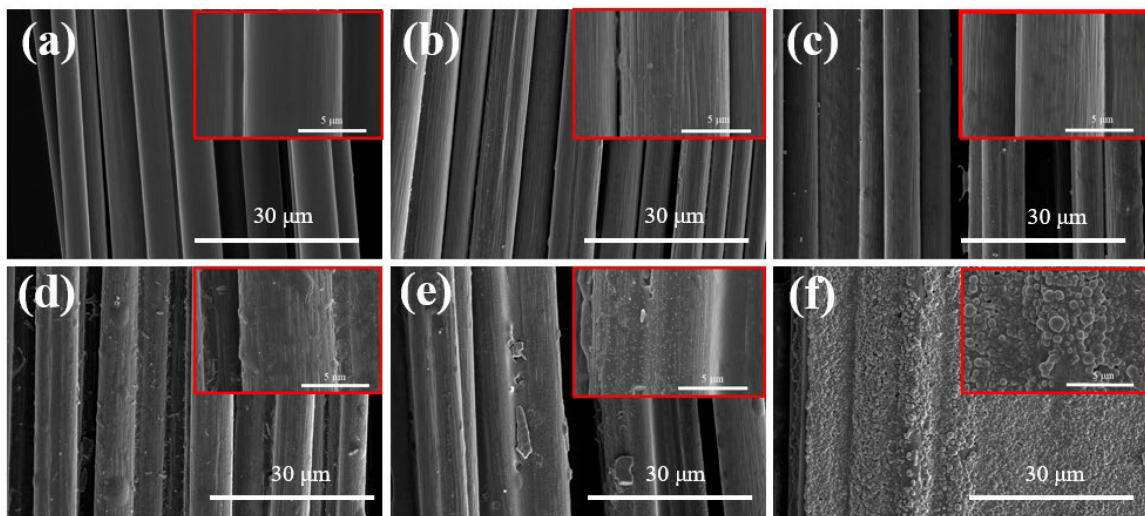
**Figure 8.** The CF bundle morphology with different concentrations of PA6T oligomer coated: (**a**) pristine CF; (**b**) CF-1′-10 min; (**c**) CF-2′-10 min; (**d**) CF-5′-10 min; (**e**) CF-10′-10 min; (**f**) PA845H (higher magnification images were marked with red box).

### 3.5. Mechanical Properties of Fabric PA6T/CF Composites

Tensile performance is an important indicator to evaluate the macro-mechanical property of fabric CF/PA6T composites, and the results are displayed in Figure 9 and Tables S1 and S2. The pristine CF reinforced composites exhibited a tensile strength of 225.4 MPa, which indicated a poor interaction between the CF and resin matrix, in accordance with the IFSS and SEM results. The higher coating concentration enhanced the tensile strength distinctly, which is attributed to a better impregnation state without internal defects, thus improving the stress transfer effect. According to the fracture morphology of the CF/PA6T composites presented in Figure 10, as the coating concentration increased, the pull-out CFs displayed a rougher surface, and residual resin could be found on the surface. As shown in Figure 9b, the variation trend of tensile performance was not completely positively related with the polymerization time. As elaborated before, when the polymerization time exceeded 10 min, the mechanical performance deteriorated due to thermal oxygen degradation. It is worth nothing that although PA845H-coated CF had the best IFSS, the tensile performance was not optimal, which is attributed to the additives in the coating layer resulting in more defects at the interface.
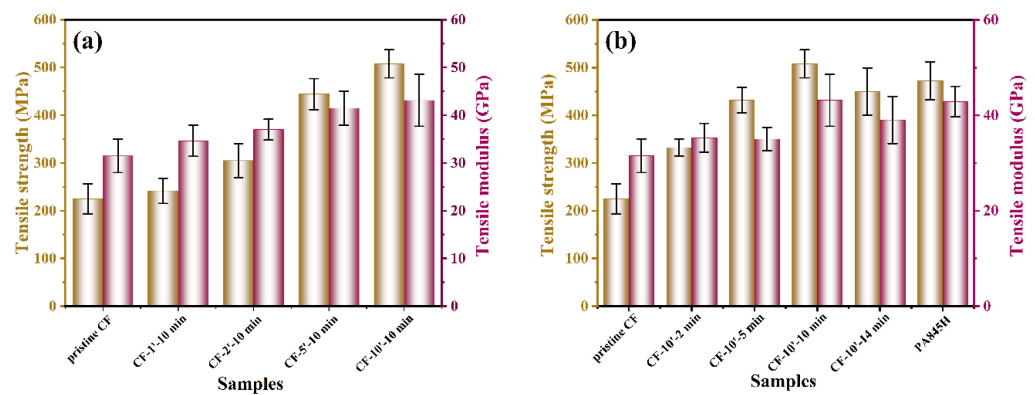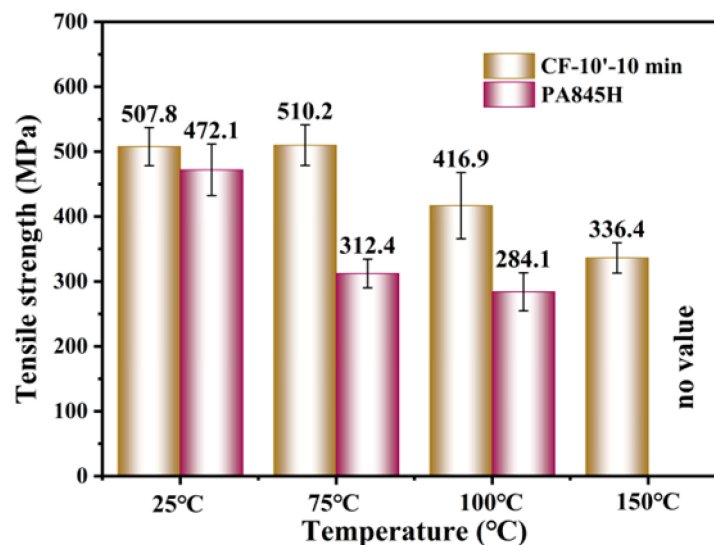


**Figure 9.** (**a**) The tensile strength of CF/PA6T composites with different concentrations of PA6T oligomer modification; (**b**) the tensile strength of CF/PA6T composites with different polymerization times of PA6T oligomer coating.
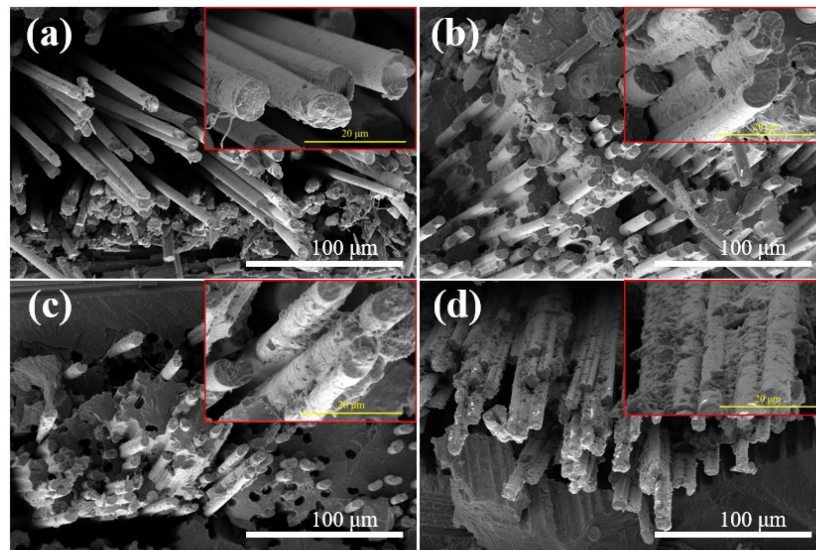
**Figure 10.** The fracture morphology of CF/PA6T composites: (**a**) pristine CF; (**b**) CF-5′-10 min; (**c**) CF-10′-10 min; (**d**) PA845H (higher magnification images were marked with red box).

To verify the high-temperature mechanical performance, a series of tensile tests of composites were carried out under elevated temperatures. The results in Figure 11 are in line with the IFSS results, as CF-10′-10 min had almost no decline when the temperature was elevated at 75 °C, while the PA845H-modified composite showed a sharper decline. Consistent with the IFSS results at elevated temperatures, it was verified again that the prePA6T-modified composites have good high-temperature mechanical properties, and there was no loss of strength under $T_g$ (85 °C), which is superior to the composites modified by PA845H. For CF-PA845H, tensile strength could not be acquired at 150 °C due to the softening of PA845H. In brief, it is shown, thus, that the prePA6T emulsion has not only an equivalent interfacial modification performance but also better mechanical properties at elevated temperature, which is more adaptable to complicated and rigorous application scenarios.



**Figure 11.** The tensile strength of CF/PA6T composites under elevated testing temperatures.

The tensile properties of the carbon fiber fabric-reinforced polyamide composites prepared by different processing methods are listed in Table 1. Compared with the direct forming of fiber fabric, a novel process of hot-pressing film with in situ polymerized

prePA6T ultrafine powder impregnating the fiber bundle is innovated in this research system. In our work, better tensile properties could be achieved with a lower fiber content, which was mainly due to to the better infiltration and penetration of the low-viscosity prePA6T hyperfine powder and the stronger bonding force with CF after in situ polymerization. Moreover, the 3D printed CF/PA12 composite had higher tensile strength for the higher fiber orientation in the unidirectional composite system.

**Table 1.** The tensile strength of CF/PA composites obtained via different preparation techniques.

| Samples | CF/PA6 [44] | CF(40 vol%)/PA66 [45] | CF(31.9vol%)/PA12 [46] | CF(36.2% vol%)/PA6T this Work |
|---|---|---|---|---|
| Processing method | T-RTM (fabric) | Interfacial polymerization (fabric) | 3D printing (UD) | Powder + compression molding (fabric) |
| Tensile strength (MPa) | 431.2 | 408 | 530.1 | 507.8 |
| Tensile modulus (GPa) | 34.7 | 35.4 | 54.8 | 43.1 |

*3.6. ILSS of Fabric Laminated Composites*

Interlaminar failure is the primary failure form of laminated composites, so ILSS (Interlaminar Shear Strength) is the most critical performance criterion for evaluating this, as well as the most direct performance parameter that reflects the macro fiber–resin interfacial properties of composite materials [47]. According to the IFSS results, the micro IFSS value rose with the polymerization degree increasing, which aligned with the macro ILSS variation tendency shown in Figure 12. Moreover, the ILSS of CF-10′-10 min was elevated from 25.8 MPa in the pristine state to 57.0 MPa, an increase of 120.9%. The result verifies that the higher molecular weight of the interfacial layer brings high mechanical strength, strong hydrogen bonding, and more molecular chain entanglement, which effectively prompts the improved interfacial performance. The SEM images in Figure 13 also indicate that the interlaminar fracture morphology changed from finely divided resin particles (CF-10′-2 min) to tearing films (CF-10′-10 min). However, with the weakening of the thermal oxygen aging reaction on the interfacial layer, the ILSS of CF-10′-14 min deteriorated.
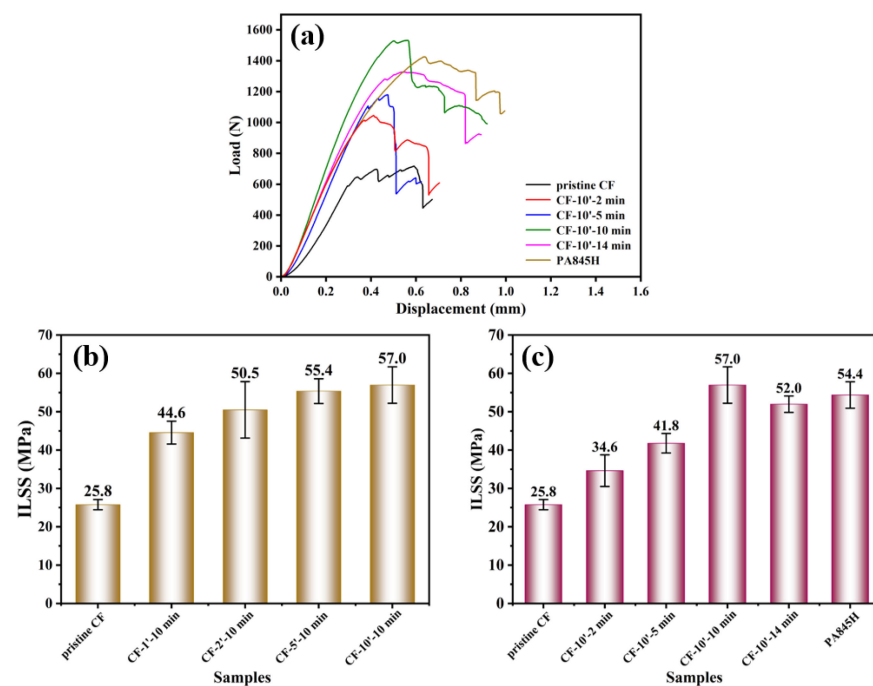


**Figure 12.** The interlaminar shear property of CF/PA6T composites: (**a**) force–displacement curve; the ILSS of composites with different (**b**) coating concentrations and (**c**) polymerization times.
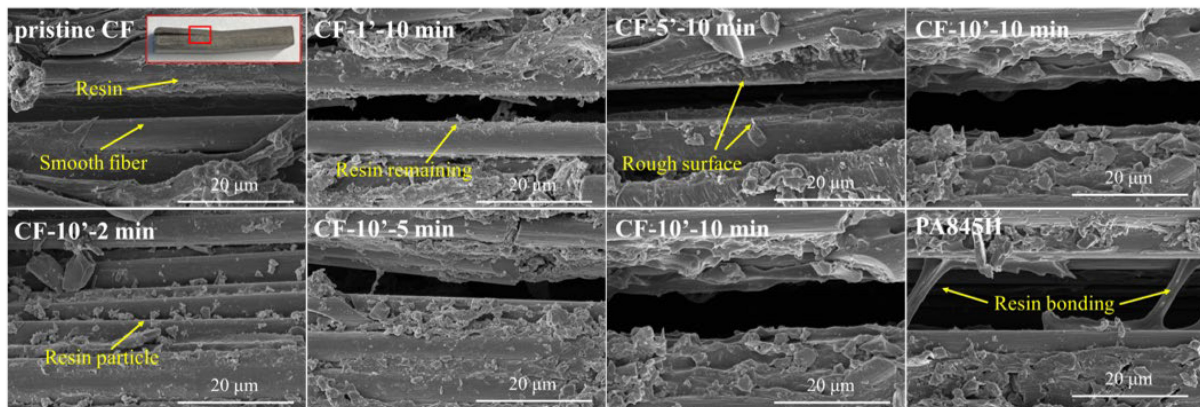
**Figure 13.** The interlaminar fracture (crack propagation) morphology of composites (the observation spot was marked with red box).

In addition, although the PA845H-modified CF/PA6T composite had the highest micro IFSS, its macro ILSS was still lower than that of CF-10′-10 min, probably resulting from other components in the slurry having introduced plentiful interfaces and defects, destroying the uniformity and integrality of the matrix.

Figure 13 presents the cracks in the delaminated composites to evaluate the interlayer reaction. In Figure 13, the pristine CF shows a smooth surface, indicating poor interaction between the CF and resin matrix. On increasing the concentration of prePA6T emulsion and the polymerization time, more remaining resin could be observed on the CF, showing the enhanced interaction. Interestingly, the resin bonding phenomenon could only be found in the interlaminar fracture of the PA845H-modified composite, indicating that other components in the PA845H slurry may play a role in improving the interlayer toughness. The resin bonding slows down the crack propagation speed and enhances the interlayer crack toughness, which can also be confirmed by the load–displacement curve in Figure 12.

## 4. Conclusions

In this paper, prePA6T hyperfine powder with a diameter of less than 5 μm and narrow size distribution was prepared via the dissolution and precipitation "phase conversion" method, and a stable prePA6T sizing agent was acquired. Remarkably, the prePA6T sizing agent has excellent heat resistance and interfacial performance under elevated temperatures. The effects of polymerization time and emulsion concentration on fiber surface morphologies, IFSS, ILSS, and tensile performance were also discussed.

At a low coating concentration, the IFSS did not vary much. At 20 wt% concentration, the IFSS increased rapidly by 55% as a uniform coating formed and the entanglement and hydrogen bonding enhanced. The higher concentration than this did not improve the IFSS much. Further, a long polymerization time (320 °C, 14 min) would lead to thermal oxidation aging and degrade the IFSS. Compared with PA845H, the PA6T coating exhibited better mechanical performance at an elevated temperature. Concretely, PA6T showed no IFSS loss under 75 °C.

The prePA6T ultrafine powder prepared by the "phase conversion" method had a tiny and narrow particle size distribution. The emulsion sizing agent prepared using the prePA6T oligomer had good penetration and impregnation effects on CF bundles. As the emulsion concentration increased to 10 wt%, the tensile strength of the fabric laminated composite rose to 507.8 MPa, achieving a higher tensile strength than the aliphatic PA composites prepared by injection molding at a low fiber fraction. Moreover, increasing the polymerization degree enhanced the interfacial interaction, thus improving the tensile strength. Notably, the prePA6T-modified composites had no tensile strength loss at 75 °C, and the tensile strength at 100 °C remained over 80%. However, CF-PA845H had

a poor mechanical performance at elevated temperatures due to poor heat resistance and additional components.

The ILSS was improved with increasing the emulsion concentration and polymerization. A higher emulsion concentration (10 wt%) and proper polymerization degree (320 °C-10 min) endowed better interaction between CF and resin. CF-10′-10 min had the best TS and ILSS, having improved by 125.3% and 120.9%, while the CF-PA845H improved by 109.4% and 120.9%. Further, the additional component in PA845H led to the existence of resin bonding, enhancing the interlayer crack toughness.

In summary, a facile, continuous, heat-resistant, undamaged-to-fiber, and environmental coating technology was exploited to manufacture continuous fiber-reinforced PA6T composites. The CF/PA6T interfacial performance was efficiently improved, and high-performance thermoplastic composites with exceptional properties were prepared successfully.

**Supplementary Materials:** The following supporting information can be downloaded at: https://www.mdpi.com/article/10.3390/ma17071557/s1, Figure S1: Synthesis of PA6T, (PA6T/6 = 50:50, random copolymer; Figure S2: The tensile specimen of continuous CF/PA6T composite; Figure S3: Interlaminar shear test of continuous CF/PA6T composite; Table S1: The tensile strength of CF/PA6T composite with different emulsion concentration coated; Table S2: The tensile strength of CF/PA6T composite with different polymerization time.

# References

1. Soutis, C. Fibre Reinforced Composites in Aircraft Construction. *Prog. Aerosp. Sci.* **2005**, *41*, 143–151. [CrossRef]
2. Zhang, H.; Wu, Y.; Wang, K.; Peng, Y.; Wang, D.; Yao, S.; Wang, J. Materials Selection of 3D-Printed Continuous Carbon Fiber Reinforced Composites Considering Multiple Criteria. *Mater. Des.* **2020**, *196*, 109140. [CrossRef]
3. Yao, S.-S.; Jin, F.-L.; Rhee, K.Y.; Hui, D.; Park, S.-J. Recent Advances in Carbon-Fiber-Reinforced Thermoplastic Composites: A Review. *Compos. Part B Eng.* **2018**, *142*, 241–250. [CrossRef]
4. Li, R.; Ye, L.; Mai, Y.-W. Application of Plasma Technologies in Fibre-Reinforced Polymer Composites: A Review of Recent Developments. *Compos. Part A Appl. Sci. Manuf.* **1997**, *28*, 73–86. [CrossRef]
5. Shim, J.-W.; Park, S.-J.; Ryu, S.-K. Effect of Modification with HNO3 and NaOH on Metal Adsorption by Pitch-Based Activated Carbon Fibers. *Carbon* **2001**, *39*, 1635–1642. [CrossRef]
6. Pittman, C.U.; He, G.-R.; Wu, B.; Gardner, S.D. Chemical Modification of Carbon Fiber Surfaces by Nitric Acid Oxidation Followed by Reaction with Tetraethylenepentamine. *Carbon* **1997**, *35*, 317–331. [CrossRef]
7. Xu, B.; Wang, X.; Lu, Y. Surface Modification of Polyacrylonitrile-Based Carbon Fiber and Its Interaction with Imide. *Appl. Surf. Sci.* **2006**, *253*, 2695–2701. [CrossRef]
8. Li, J.; Huang, Y.; Xu, Z.; Wang, Z. High-Energy Radiation Technique Treat on the Surface of Carbon Fiber. *Mater. Chem. Phys.* **2005**, *94*, 315–321. [CrossRef]

9.  Clough, R.L. High-Energy Radiation and Polymers: A Review of Commercial Processes and Emerging Applications. *Nucl. Instrum. Methods Phys. Res. Sect. B Beam Interact. Mater. At.* **2001**, *185*, 8–33. [CrossRef]

10. Zhang, T.; Wang, Z.; Zhang, G.; Liu, S.; Long, S.; Yang, J.; Yang, J.; Wang, X. Improvement of Interfacial Interaction between Poly(Arylene Sulfide Sulfone) and Carbon Fiber via Molecular Chain Grafting. *Compos. Sci. Technol.* **2022**, *224*, 109463. [CrossRef]

11. Sharma, M.; Gao, S.; Mäder, E.; Sharma, H.; Wei, L.Y.; Bijwe, J. Carbon Fiber Surfaces and Composite Interphases. *Compos. Sci. Technol.* **2014**, *102*, 35–50. [CrossRef]

12. Pamula, E.; Rouxhet, P.G. Bulk and Surface Chemical Functionalities of Type III PAN-Based Carbon Fibres. *Carbon* **2003**, *41*, 1905–1915. [CrossRef]

13. Jiang, D.; Liu, L.; Long, J.; Xing, L.; Huang, Y.; Wu, Z.; Yan, X.; Guo, Z. Reinforced Unsaturated Polyester Composites by Chemically Grafting Amino-POSS onto Carbon Fibers with Active Double Spiral Structural Spiralphosphodicholor. *Compos. Sci. Technol.* **2014**, *100*, 158–165. [CrossRef]

14. Shin, H.K.; Park, M.; Kim, H.-Y.; Park, S.-J. An Overview of New Oxidation Methods for Polyacrylonitrile-Based Carbon Fibers. *Carbon Lett.* **2015**, *16*, 11–18. [CrossRef]

15. Fernandez, B.; Arbelaiz, A.; Valea, A.; Mujika, F.; Mondragon, I. A Comparative Study on the Influence of Epoxy Sizings on the Mechanical Performance of Woven Carbon Fiber-epoxy Composites. *Polym. Compos.* **2004**, *25*, 319–330. [CrossRef]

16. Dai, Z.; Shi, F.; Zhang, B.; Li, M.; Zhang, Z. Effect of Sizing on Carbon Fiber Surface Properties and Fibers/Epoxy Interfacial Adhesion. *Appl. Surf. Sci.* **2011**, *257*, 6980–6985. [CrossRef]

17. Bowman, S.; Jiang, Q.; Memon, H.; Qiu, Y.; Liu, W.; Wei, Y. Effects of Styrene-Acrylic Sizing on the Mechanical Properties of Carbon Fiber Thermoplastic Towpregs and Their Composites. *Molecules* **2018**, *23*, 547. [CrossRef] [PubMed]

18. Kabir, S.M.F.; Mathur, K.; Seyam, A.-F.M. A Critical Review on 3D Printed Continuous Fiber-Reinforced Composites: History, Mechanism, Materials and Properties. *Compos. Struct.* **2020**, *232*, 111476. [CrossRef]

19. Wang, Z.; Dong, Y.; Yang, J.; Wang, X.; Zhang, M.; Zhang, G.; Long, S.; Liu, S.; Yang, J. Improved Interfacial Shear Strength in Carbon Fiber Enhanced Semi-Aromatic Polyamide 6T Composite via in-Situ Polymerization on Fiber Surface. *Compos. Sci. Technol.* **2022**, *223*, 109401. [CrossRef]

20. Gabrion, X.; Placet, V.; Trivaudey, F.; Boubakar, L. About the Thermomechanical Behaviour of a Carbon Fibre Reinforced High-Temperature Thermoplastic Composite. *Compos. Part B Eng.* **2016**, *95*, 386–394. [CrossRef]

21. Giraud, I.; Franceschi-Messant, S.; Perez, E.; Lacabanne, C.; Dantras, E. Preparation of Aqueous Dispersion of Thermoplastic Sizing Agent for Carbon Fiber by Emulsion/Solvent Evaporation. *Appl. Surf. Sci.* **2013**, *266*, 94–99. [CrossRef]

22. Wu, G.M.; Schultz, J.M. Processing and Properties of Solution Impregnated Carbon Fiber Reinforced Polyethersulfone Composites. *Polym. Compos.* **2000**, *21*, 223–230. [CrossRef]

23. Duchoslav, J.; Unterweger, C.; Steinberger, R.; Fürst, C.; Stifter, D. Investigation on the Thermo-Oxidative Stability of Carbon Fiber Sizings for Application in Thermoplastic Composites. *Polym. Degrad. Stab.* **2016**, *125*, 33–42. [CrossRef]

24. Barkanov, E.; Akishin, P.; Namsone-Sile, E. Effectiveness and Productivity Improvement of Conventional Pultrusion Processes. *Polymers* **2022**, *14*, 841. [CrossRef] [PubMed]

25. Minchenkov, K.; Vedernikov, A.; Safonov, A.; Akhatov, I. Thermoplastic Pultrusion: A Review. *Polymers* **2021**, *13*, 180. [CrossRef]

26. Padaki, S.; Drzal, L.T. A Simulation Study on the Effects of Particle Size on the Consolidation of Polymer Powder Impregnated Tapes. *Compos. Part A Appl. Sci. Manuf.* **1999**, *30*, 325–337. [CrossRef]

27. Vaidya, U.K.; Chawla, K.K. Processing of Fibre Reinforced Thermoplastic Composites. *Int. Mater. Rev.* **2013**, *53*, 185–218. [CrossRef]

28. Cho, B.-G.; Ram Joshi, S.; Hun Han, J.; Kim, G.-H.; Park, Y.-B. Interphase Strengthening of Carbon Fiber/Polyamide 6 Composites through Mixture of Sizing Agent and Reduced Graphene Oxide Coating. *Compos. Part A Appl. Sci. Manuf.* **2021**, *149*, 106521. [CrossRef]

29. Bernet, N.; Michaud, V.; Bourban, P.E.; Manson, J.A.E. An Impregnation Model for the Consolidation of Thermoplastic Composites Made from Commingled Yarns. *J. Compos. Mater.* **1999**, *33*, 751–772. [CrossRef]

30. Schäfer, J.; Stolyarov, O.; Ali, R.; Greb, C.; Seide, G.; Gries, T. Process–Structure Relationship of Carbon/Polyphenylene Sulfide Commingled Hybrid Yarns Used for Thermoplastic Composites. *J. Ind. Txtiles* **2016**, *45*, 1661–1673. [CrossRef]

31. Song, H.; Zhou, D.; Guo, J. Thermal-Oxidative Aging Effects on the Properties of Long Glass Fiber Reinforced Polyamide 10T Composites. *Polym. Compos.* **2018**, *39*, 2117–2125. [CrossRef]

32. Shi, K.; Ye, L.; Li, G. Thermal Oxidative Aging Behavior and Stabilizing Mechanism of Highly Oriented Polyamide 6. *J. Therm. Anal. Calorim.* **2016**, *126*, 795–805. [CrossRef]

33. Yang, K.; Liu, Y.; Zheng, Z.; Lu, G.; Tang, Z.; Chen, X. Synthesis and Thermal Degradation Mechanism of a Semi-Aromatic Copolyamide from Renewable Sources. *Polym. Degrad. Stab.* **2022**, *203*, 110089. [CrossRef]

34. Zuo, X.; Zhang, K.; Lei, Y.; Qin, S.; Hao, Z.; Guo, J. Influence of Thermooxidative Aging on the Static and Dynamic Mechanical Properties of Long-Glass-Fiber-Reinforced Polyamide 6 Composites. *J. Appl. Polym. Sci.* **2014**, *131*, 39594. [CrossRef]

35. Zhang, R.L.; Huang, Y.D.; Su, D.; Liu, L.; Tang, Y.R. Influence of Sizing Molecular Weight on the Properties of Carbon Fibers and Its Composites. *Mater. Des.* **2012**, *34*, 649–654. [CrossRef]

36. Wu, Z.; Cui, H.; Chen, L.; Jiang, D.; Weng, L.; Ma, Y.; Li, X.; Zhang, X.; Liu, H.; Wang, N.; et al. Interfacially Reinforced Unsaturated Polyester Carbon Fiber Composites with a Vinyl Ester-Carbon Nanotubes Sizing Agent. *Compos. Sci. Technol.* **2018**, *164*, 195–203. [CrossRef]

37. Cheng, T.H.; Zhang, J.; Yumitori, S.; Jones, F.R.; Anderson, C.W. Sizing Resin Structure and Interphase Formation in Carbon Fibre Composites. *Composites* **1994**, *25*, 661–670. [CrossRef]

38. Zhang, R.L.; Huang, Y.D.; Liu, L.; Tang, Y.R.; Su, D.; Xu, L.W. Effect of the Molecular Weight of Sizing Agent on the Surface of Carbon Fibres and Interface of Its Composites. *Appl. Surf. Sci.* **2011**, *257*, 1840–1844. [CrossRef]

39. Cui, X.; Ma, L.; Wu, G. Mussel-Inspired Co-Deposition of Polydopamine/Silica Nanoparticles onto Carbon Fiber for Improved Interfacial Strength and Hydrothermal Aging Resistance of Composites. *Polymers* **2020**, *12*, 712. [CrossRef]

40. Li, N.; Wu, Z.; Yang, X.; Wang, C.; Zong, L.; Pan, Y.; Wang, J.; Jian, X. One-Pot Strategy for Covalent Construction of POSS-Modified Silane Layer on Carbon Fiber to Enhance Interfacial Properties and Anti-Hydrothermal Aging Behaviors of PPBES Composites. *J. Mater. Sci.* **2018**, *53*, 16303–16317. [CrossRef]

41. Thomason, J.L.; Yang, L. Temperature Dependence of the Interfacial Shear Strength in Glass–Fibre Polypropylene Composites. *Compos. Sci. Technol.* **2011**, *71*, 1600–1605. [CrossRef]

42. Krause, B.; Kroschwald, L.; Pötschke, P. The Influence of the Blend Ratio in PA6/PA66/MWCNT Blend Composites on the Electrical and Thermal Properties. *Polymers* **2019**, *11*, 122. [CrossRef] [PubMed]

43. Dechet, M.A.; Baumeister, I.; Schmidt, J. Development of Polyoxymethylene Particles via the Solution-Dissolution Process and Application to the Powder Bed Fusion of Polymers. *Materials* **2020**, *13*, 1535. [CrossRef]

44. Kim, B.-J.; Cha, S.-H.; Kong, K.; Ji, W.; Park, H.W.; Park, Y.-B. Synergistic Interfacial Reinforcement of Carbon Fiber/Polyamide 6 Composites Using Carbon-Nanotube-Modified Silane Coating on ZnO-Nanorod-Grown Carbon Fiber. *Compos. Sci. Technol.* **2018**, *165*, 362–372. [CrossRef]

45. Botelho, E.C.; Figiel, Ł.; Rezende, M.C.; Lauke, B. Mechanical Behavior of Carbon Fiber Reinforced Polyamide Composites. *Compos. Sci. Technol.* **2003**, *63*, 1843–1855. [CrossRef]

46. Liu, T.; Tian, X.; Zhang, Y.; Cao, Y.; Li, D. High-Pressure Interfacial Impregnation by Micro-Screw in-Situ Extrusion for 3D Printed Continuous Carbon Fiber Reinforced Nylon Composites. *Compos. Part A Appl. Sci. Manuf.* **2020**, *130*, 105770. [CrossRef]

47. Zhang, C.; Zhang, G.; Shi, X.; Wang, X. Effects of Carbon Nanotubes on the Interlaminar Shear Strength and Fracture Toughness of Carbon Fiber Composite Laminates: A Review. *J. Mater. Sci.* **2022**, *57*, 2388–2410. [CrossRef]

*Article*

# Effect of Process Parameters on Joint Performance in Hot Pressure Welding of 6061 Aluminum Alloy to CF/PA66

Haipeng Zhou [1,2], Yang Li [1,2,3,*], Weidong Liu [4,*], Yan Luo [4], Sansan Ao [1,2] and Zhen Luo [1,2]

1 School of Materials Science and Engineering, Tianjin University, Tianjin 300354, China; tjuzhp3868@163.com (H.Z.); ao33@tju.edu.cn (S.A.); lz_tju@163.com (Z.L.)
2 State Key Laboratory of Advanced Welding and Joining, Harbin Institute of Technology, Harbin 150001, China
3 International Institute for Innovative Design and Intelligent Manufacturing of Tianjin University in Zhejiang, Shaoxing 312000, China
4 College of Aeronautical Engineering, Civil Aviation University of China, Tianjin 300300, China; 2022012177@cauc.edu.cn
* Correspondence: liyang86@tju.edu.cn (Y.L.); wdliu@cauc.edu.cn (W.L.)

**Abstract:** Polymer–metal hybrid structures combine the merits of polymer and metal materials, making them widely applicable in fields such as aerospace and automotive industries. However, the main challenge lies in achieving efficient and strong connections between the metal and polymer components. This paper uses the jet electrochemical machining (Jet-ECM) method to customize the surface morphologies on 6061 aluminum alloy (AA6061) sheets. The connection between AA6061 and carbon fiber-reinforced PA66 (CF/PA66) is then achieved through hot pressure welding (HPW). The effects of aluminum alloy surface morphology, welding force, and welding time on the mechanical properties and microstructure of the joint are investigated. The optimal process parameters are determined by the design of the experiment. The results show that the aluminum alloy surface morphology has the greatest impact on the mechanical property of the welded joint. The optimal process parameters are surface morphology with wider, shallower, and sparsely distributed grooves on the aluminum alloy surface, the welding force is 720 N, the welding time is 12 s, the welding temperature is 360 °C, the cooling time is 16 s, and the optimal peak load of the joint is 6690 N. Under the optimal parameters, the fracture morphology in the AA6061 side is almost entirely covered with CF/PA66. The joint experiences cohesive failure in most areas and fiber-matrix debonding in a small area.

**Keywords:** hot-pressure welding; carbon fiber-reinforced thermoplastic composite; aluminum alloy; process optimization

## 1. Introduction

Optimized lightweight designs often require the use of multi-materials, often with different physical properties, such as different metals [1–3] or polymer composites and metals [3,4]. Among different multi-material structures, the metal–carbon fiber-reinforced polymer (CFRP) hybrid structure takes the advantages of both metal and CFRP and has been proven to be superior in terms of fatigue performance, impact properties, and vibration resistance [5]. In recent years, the metal/CFRP hybrid structure has been widely used in the automobile and aerospace industries. For example, the BMW 7 series applied metal/CFRP hybrid components to its various important structures such as the roof beam, B pillar, C pillar, threshold beam, and central channel [6]. Lee et al. [7] demonstrated that a steel/CFRP B-pillar exhibited 10% higher crashworthiness and was 44% lighter compared with the tailor-welded steel B-pillar. Al/CFRP and Ti/CFRP hybrid structures are generally used in wing panels, helicopter blades, fairings, fixed trailing edges, space optical benches, ship hulls, and engine cowlings [8].

Since the wide application of metal/CFRP structure, the demand for the joining between metal and CFRP is increasing. However, due to the huge difference in the physical and chemical properties between metal and CFRP, obtaining high-strength metal/CFRP dissimilar joints has become a technical bottleneck. According to the polymer matrix, CFRP can be divided into carbon fiber-reinforced thermoset composite (CFRTS) and carbon fiber-reinforced thermoplastic composite (CFRTP). CFRTS can only be cured one time; therefore, adhesive bonding and mechanical fastening are the main joining methods for it [9,10]. In comparison with CFRTS, CFRTP has weldability, and welding is considered a promising method for joining CFRTP and metal. The general principle of metal and CFRTP welding is using a certain heat source to heat the metal workpiece to a temperature that is above the melting point of the CFRTP. Heat is transferred to the metal/CFRTP interface through heat conduction of the metal, and the CFRTP melts and moistens the metal surface. After the welding is completed, the joint cools to room temperature, and a metal/CFRTP joint forms. Figure 1 shows the general process of metal/CFRTP welding.
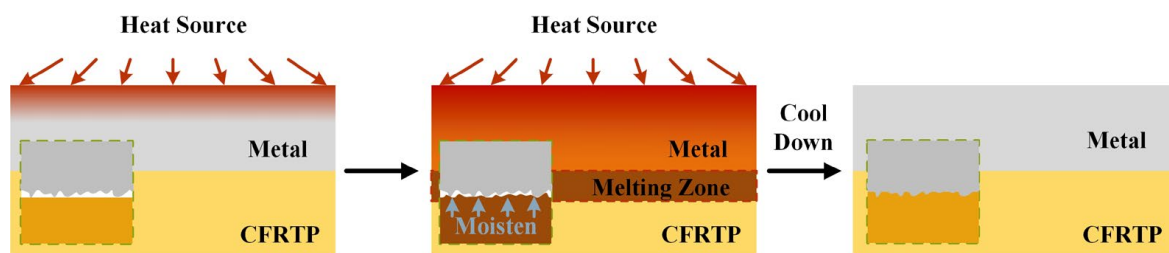


**Figure 1.** General principle of metal/CFRTP welding.

The main welding methods of metal/CFRTP include laser welding [11–18], friction welding [19–27], ultrasonic welding [28–34], hot pressure welding [35–41], and so on. Among them, hot pressure welding (HPW) has the characteristics of simple equipment structure, environmental friendliness, ease of automation, etc., and has a broad development space and application prospect. A number of scholars have conducted studies on the HPW of metal to CFRTP. Barrak et al. [35] prefabricated two holes on the aluminum alloy sample and used HPW to connect the hybrid structure of aluminum alloy and polyamide. The maximum tensile–shear strength of the joint was 2.5 MPa. Zou et al. [36] used hydrofluoric acid (HF) to etch Ti-6Al-4V alloy (TC4) to obtain low roughness surface and used HPW to connect TC4 and poly(ethylene terephthalate) (PET). This study showed that roughness is not a factor in determining joint strength. The factor that can improve the interfacial bonding of metals and polymers is the synergistic effect of surface particle anchoring and chemical bonding. Du et al. [37] used an anodizing method to prepare microporous structures on the surface of aluminum alloy and used ultrasonic-assisted hot pressing technology to weld polypropylene/aluminum alloy dissimilar materials. Liu et al. [38] investigated the effect of laser texturing on the joint performance in HPW of TC4 titanium alloy and CFRTP. The results showed that the textured TC4 surface improved the wettability of molten CFRTP to TC4, thereby enhancing the tensile–shear force of the joint. Saborowski et al. [39] used an Nd/YVO$_4$ nanosecond laser system to create a pin structure with scalable height through single-pulse drilling on 6082 aluminum alloy and connected it to polyamide 6 using HPW. The experimental results showed that pulse drilling pin structures show excellent wetting behavior.

At present, the commonly used method to improve the strength of metal/CFRTP hot-pressure welded joints is to increase the macro- or micro-mechanical interlocking between both. The macro-mechanical interlocking is mainly conducted by prefabricating holes [35], raised structures [38,39], or combined use [40] on the metal surface. During the HPW process, the molten CFRTP matrix will flow into the holes, or the raised structures will be inserted into the CFRTP matrix and form an interlocking structure after cooling. The micro-mechanical interlocking is fulfilled by creating microporous structures [37] or groove structures [41] on the metal surface. One difference between the two structures is that the

microporous structure is highly random, while the groove structure can be customized and, therefore, has better controllability. For example, Liu et al. [38] investigated the influence of textured grid width on the tensile–shear force of the TC4/CFRP joint made by HPW. The experimental results indicated that laser texturing obviously improved the TC4 surface roughness and wettability of molten CFRP, which increased the interfacial joining area and thus enhanced the shear force of the joint. Zhang et al. [41] investigated the effect of a laser-textured surface on the HPW of 6061 aluminum alloy to glass fiber-reinforced thermoplastic (GFRTP). The results showed that the higher the surface roughness of aluminum alloy, the better the wettability of molten GFRTP and the stronger the joint mechanical properties. Liu et al. [42] studied the effect of groove width and groove depth on the joint strength of Al/CFRTP. The results show that the tensile–shear strength of CFRTP/Al joints first increases and then decreases with the increase in groove width and groove depth. Rodríguez-Vidal et al. [43] investigated the effect of textured groove structure density, structure depth, and cavity angle on the laser-welded steel/PA6-GF30 joints. They found that the textured groove structure density was the primary influencing factor for the joint strength, while the structure depth and cavity angle had little effect. Liang et al. [44] investigated the effect of texturing direction (0°, 45°, 90°) on the Ti/GFRTP laser welded joint strength. The tensile–shear strength could reach the maximum when the texturing direction was perpendicular to the tensile direction (0° texturing). However, these studies did not control the total surface areas of the textures to be equivalent, so it is difficult to compare which structure is better.

This study takes 6061 aluminum alloy and carbon fiber reinforced nylon 66 composite material (CF/PA66) as the research materials. Jet electrochemical machining (JET-ECM) was used to customize the groove size and quantity on the aluminum alloy surface. To better compare the effect of groove size on joint performance, this paper created four surface morphologies under the premise that the textured surface areas are equivalent. Based on a customized HPW machine, the effects of metal surface morphology, welding temperature, welding time, and welding force on the joint performance were investigated.

## 2. Experimental Procedure

The experimental materials, methods, and equipment will be introduced in the following part.

### 2.1. Experimental Material

In this study, 6061 aluminum alloy (AA6061) and CF/PA66 were used as the experimental materials. The dimensions of the aluminum alloy and CF/PA66 sheets were 100 mm × 40 mm × 1.5 mm$^3$ and 100 mm × 40 mm × 3 mm$^3$, respectively. Table 1 gives the chemical composition of 6061 aluminum alloy. The CF/PA66 sheets were injection molded by pellets provided by EMS (Grivory®GCL-4H, Suzhou, China). The physical properties of the CF/PA66 are listed in Table 2. Since the CF/PA66 material is hygroscopic, the CF/PA66 sheets were dried at 80 °C for 4 h before welding.

**Table 1.** Chemical composition of 6061 aluminum alloy (wt%).

| Element | Al | Fe | Cu | Mn | Mg | Si | Zn | Ti | Al |
|---|---|---|---|---|---|---|---|---|---|
| AA6061 | 96 | 0.7 | 0.25 | 0.15 | 1.0 | 0.6 | 0.25 | 0.15 | Bal. |

**Table 2.** Properties of AA6061 and CF/PA66 sheets.

| Material | Melting Point (°C) | Elastic Modulus (GPa) | Tensile Strength (MPa) | Elongation (%) |
|---|---|---|---|---|
| AA6061 | 650 | 68.7 | 311 | 12.5 |
| CF/PA66 | 260 | 29.5 | 335 | 1.4 |

The microstructure of the cross-section (perpendicular to the injection direction) and longitudinal section (parallel to the injection direction) of the CF/PA66 (taken by an optical microscope, Zeiss Axio VerT.A1 produced by Carl Zeiss Suzhou Co., Ltd., Suzhou, China) is shown in Figure 2. The gray part is the polymer matrix, and the white part is the carbon fiber. It can be seen that most of the fibers are round in the cross-section and oval in the longitudinal. This is because the fibers will flow along the injection direction.
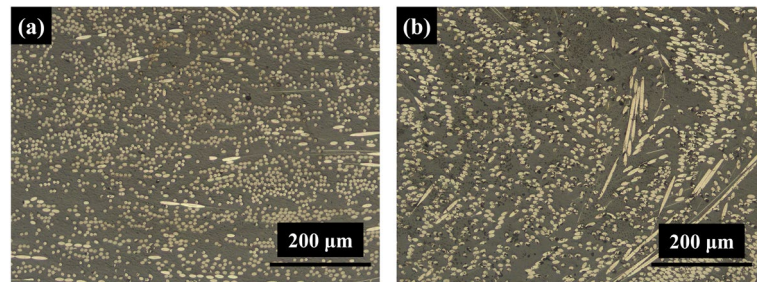


**Figure 2.** Microscopic morphologies of CF/PA66 sheet: (**a**) cross-section; (**b**) longitudinal section.

## 2.2. Experimental Methods

### 2.2.1. Aluminum Alloy Surface Treatment

The aluminum alloy surface was textured using jet electrochemical machining (Jet-ECM) technology (Civil Aviation University of China, Tianjin, China), which removes material using the principle of anodic oxidation dissolution by spraying electrolyte from a cathode nozzle onto the anode workpiece. The schematic diagram of the processing process is shown in Figure 3. The workpiece and tool were fixed on a self-developed machining platform, and the electrolyte was passed through a rectangle nozzle. After the groove processing in one direction was completed, the workpiece was rotated 90° and then processed the grooves in the other direction. The designed dimensions of the grooves are given in Table 3. The design principle of the four surface morphologies is to keep the total surface area of grooves approximately equal. According to the designed dimensions of the grooves, a trial-and-error method was used to determine the Jet-ECM processing parameters, as shown in Table 4. Figure 4 (taken by a mobile phone camera) shows the macroscopic view of the four surface morphologies of the processed aluminum alloy workpieces. Among them, the No. 1 surface morphology has the narrowest, deepest grooves and the largest quantity of grooves, and the No. 4 surface morphology has the widest, shallowest, and lowest quantity of grooves.
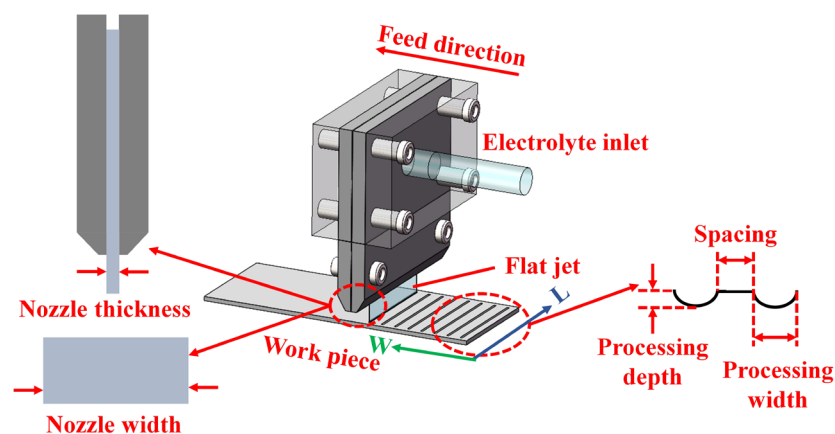


**Figure 3.** Schematic diagram of the Jet-ECM process.

**Table 3.** Designed groove dimensions of the four surface morphologies of aluminum alloy sheet.

|  | No. 1 | No. 2 | No. 3 | No. 4 |
|---|---|---|---|---|
| Processing width (mm) | 0.372 | 0.551 | 0.711 | 0.881 |
| Processing depth (mm) | 0.073 | 0.054 | 0.044 | 0.035 |
| Spacing (mm) | 0.372 | 0.551 | 0.711 | 0.881 |
| Groove quantity in width (W) direction | 46 | 32 | 25 | 20 |
| Groove quantity in length (L) direction | 19 | 14 | 11 | 9 |
| Total surface area of grooves (mm$^2$) | 26.065 | 25.944 | 25.812 | 25.665 |

**Table 4.** Processing parameters for the four surface morphologies.

| Surface Morphology | Nozzle Thickness (mm) | Electrolyte | Flow Rate (m/s) | Processing Time (s) | Processing Current (A) |
|---|---|---|---|---|---|
| No. 1 | 0.1 | 20%NaCl | 4.28 | 10 | 1.8 |
| No. 2 | 0.2 | 20%NaCl | 4.28 | 10 | 1.8 |
| No. 3 | 0.3 | 20%NaCl | 4.28 | 10 | 1.8 |
| No. 4 | 0.4 | 20%NaCl | 4.28 | 10 | 1.8 |
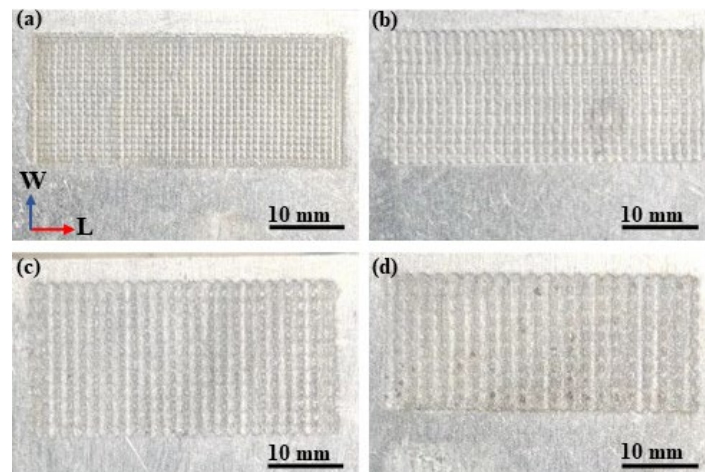


**Figure 4.** Macroscopic view of the four surface morphologies of aluminum alloy sheet: (**a**) No. 1; (**b**) No. 2; (**c**) No. 3; (**d**) No. 4.

2.2.2. Hot Pressure Welding

Figure 5 shows the schematic of the HPW setup. Two workpieces were placed in a lap-shear configuration, where a 6061 aluminum alloy sheet was placed on top of a CF/PA66 sheet. The size of the lap area was 20 mm × 40 mm. A copper block with size of 20 mm × 40 mm was used to heat up the aluminum sheet and apply welding force to the materials system. Two air-blowing pipes were distributed on both sides of the copper block. After the welding is completed, air is blown to the welding position to cool the weldment rapidly. After the air blowing was completed, the copper block was raised, and the welding was completed.

Based on the preliminary tests, a four-level orthogonal array test with five factors was designed, as shown in Table 5. Five samples were welded for each parameter, where four samples were used for tensile–shear test, and one sample was used for cross-sectional microscopy. After getting the tensile–shear test results, an online software, SPSS26.0 (Statistical Product and Service Software), was used to analyze the tensile–shear data.
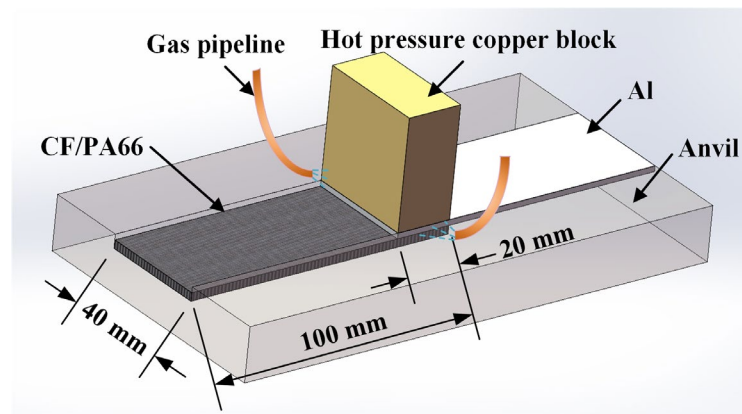
**Figure 5.** Schematic of the welding setup.

**Table 5.** Five four-level factors orthogonal array test.

| | Temperature (°C) | Welding Time (s) | Welding Force (N) | Cooling Time (s) | Surface Morphology |
|---|---|---|---|---|---|
| Level 1 | 320 | 6 | 460 | 10 | No. 1 |
| Level 2 | 340 | 8 | 720 | 12 | No. 2 |
| Level 3 | 360 | 10 | 980 | 14 | No. 3 |
| Level 4 | 380 | 12 | 1240 | 16 | No. 4 |

The welding forces of 460, 720, 980, and 1240 N correspond to 0.2, 0.3, 0.4, and 0.5 MPa in the welding machine settings, respectively.

According to the orthogonal array test results, the three parameters (surface morphology, welding force, welding time) that have the greatest influence on the tensile shear property were determined, and univariate tests were carried out. The experimental parameters are shown in Table 6.

**Table 6.** Univariate experiments.

| | Temperature (°C) | Welding Time (s) | Welding Force (N) | Cooling Time (s) | Surface Morphology |
|---|---|---|---|---|---|
| Group 1 | 360 | 12 | 720 | 16 | Nos. 1, 2, 3, 4 |
| Group 2 | 360 | 12 | 460, 720, 980, 1260 | 16 | No. 4 |
| Group 3 | 360 | 6, 8, 10, 12 | 720 | 16 | No. 4 |

Tensile–shear tests were conducted on a microcomputer-controlled electronic universal testing machine with 100 kN capacity (produced by Shenzhen Wance Testing Machine Co., Ltd., Shenzhen, China). The cross-head speed was 2 mm/min. During the test, two pads with the same thickness as the workpieces were added to both ends of the workpieces to ensure that the workpiece is subject to upward tensile force along the same straight line, as shown in Figure 6.

Standard metallography specimen preparation method was used to reveal the cross-section morphology of the joint. The surface of the metallographic specimens was polished with sandpaper of different grits from 200# to 2000#. A PG-1A metallographic polishing machine was used for polishing. The polished specimens were cleaned with alcohol. The cross-section of the joints was observed by an optical microscope (Zeiss Axio VerT.A1 produced by Carl Zeiss Suzhou Co., Ltd., Suzhou, China). Energy spectrum analysis (EDS) was used to analyze the chemical elements on the metal/CFRTP interface. The joints' fracture morphologies after tensile–shear test were observed by a tungsten filament scanning electron microscope SU1510 (Hitachi High-Technologies Corporation, Tokyo, Japan). Due to the poor electrical conductivity of the CF/PA66, a low vacuum coating instrument (Leica EM ACE200, Leica Microsystems Limited, Hong Kong, China) was used

to spray gold on the composite surface before conducting SEM observation, and the gold spraying time was set to 50 s.
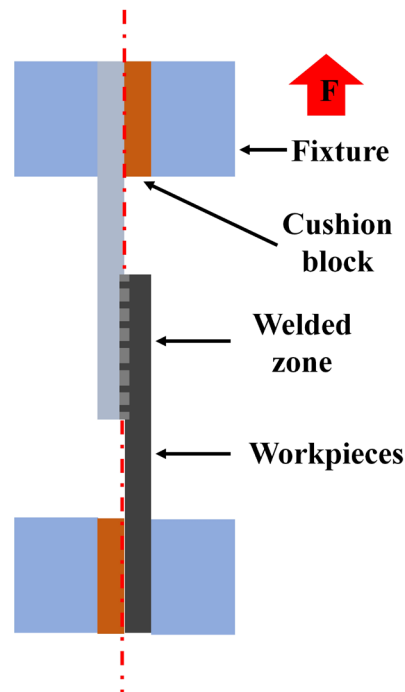


**Figure 6.** Schematic diagram of tensile–shear test.

## 3. Results and Discussion

### 3.1. Orthogonal Experimental Results

Table 7 shows the tensile–shear test results of the orthogonal array test. To explore the degree of effect of each factor on the joint tensile–shear property and determine the optimal level and combination of the process parameters, the orthogonal array test is analyzed by range analyses. The range analysis has the advantages of easy calculation, simple analysis, and intuitionistic data, which are always used in the theoretical analysis of experimental results.

**Table 7.** Tensile–shear test results of the orthogonal array test.

| No. | Temperature (°C) | Welding Time (s) | Welding Force (N) | Cooling Time (s) | Surface Morphology | Peak Load (N) | | | |
|---|---|---|---|---|---|---|---|---|---|
| | | | | | | 1 | 2 | 3 | 4 |
| 1 | 320 | 6 | 460 | 10 | No. 1 | 4446.5 | 3555.8 | 3068.3 | 3681.5 |
| 2 | 320 | 8 | 720 | 12 | No. 2 | 5415.1 | 4839.5 | 3718.7 | 5372.2 |
| 3 | 320 | 10 | 980 | 14 | No. 3 | 5190.7 | 5668.5 | 4342.4 | 4025.5 |
| 4 | 320 | 12 | 1240 | 16 | No. 4 | 5363.9 | 5963.8 | 4499.7 | 4732.3 |
| 5 | 340 | 6 | 720 | 14 | No. 4 | 5541.1 | 5349.1 | 4281.3 | 5305.8 |
| 6 | 340 | 8 | 460 | 16 | No. 3 | 4996.9 | 4890.1 | 5477.3 | 4363.1 |
| 7 | 340 | 10 | 1240 | 10 | No. 2 | 3969.9 | 4253.9 | 4901.4 | 4152.9 |
| 8 | 340 | 12 | 980 | 12 | No. 1 | 4455.7 | 4394.7 | 1508.8 | 4983.3 |
| 9 | 360 | 6 | 980 | 16 | No. 2 | 5376.6 | 4052.1 | 3821.8 | 5417.5 |
| 10 | 360 | 8 | 1240 | 14 | No. 1 | 4083.1 | 4118.8 | 3862.3 | 3963.6 |
| 11 | 360 | 10 | 460 | 12 | No. 4 | 5381.3 | 5328.1 | 5131.8 | 4872.3 |
| 12 | 360 | 12 | 720 | 10 | No. 3 | 6663.9 | 6343.9 | 5322.2 | 4899.1 |
| 13 | 380 | 6 | 1240 | 12 | No. 3 | 3550.1 | 3860.2 | 5558.6 | 4058.8 |
| 14 | 380 | 8 | 980 | 10 | No. 4 | 4726.9 | 4563.6 | 5198.6 | 4412.5 |
| 15 | 380 | 10 | 720 | 16 | No. 1 | 4618.7 | 4819.9 | 3788.1 | 4546.9 |
| 16 | 380 | 12 | 460 | 14 | No. 2 | 6088.5 | 6379.1 | 4176.9 | 3542.8 |

Table 8 shows the range analysis of the orthogonal array test, where $K_i$ is the sum of all peak loads at level $i$ of each factor. For example, $K_1$ represents the sum of all peak loads of experiments with a temperature of 320 °C. According to $K_i$, the optimal level and combination can be obtained. R is the range $(\max(K_1, K_2, K_3, K_4) - \min(K_1, K_2, K_3, K_4))$ that reflects the degree of effect of each factor and level on the tensile–shear force. The larger the R value, the greater the degree of effect of this factor on the peak load. It shows that the surface morphology has the greatest influence on the joint strength, followed by welding force, welding time, welding temperature, and cooling time. The optimal parameters were No. 4 surface morphology, welding force of 720 N, welding time of 12 s, welding temperature of 360 °C, and cooling time of 16 s.

**Table 8.** Range analysis of the orthogonal array test.

| $K_i$ | Temperature | Welding Time | Welding Force | Cooling Time | Surface Morphology |
|---|---|---|---|---|---|
| $K_1$ | 18,470.8 N | 17,730.8 N | 18,844.8 N | 18,540.4 N | 16,074.0 N |
| $K_2$ | 18,306.0 N | 18,500.4 N | 20,206.4 N | 18,207.2 N | 18,869.6 N |
| $K_3$ | 19,656.4 N | 18,748.0 N | 18,134.8 N | 18,980.0 N | 19,803.2 N |
| $K_4$ | 18,472.4 N | 19,929.6 N | 17,723.2 N | 19,182.4 N | 20,163.2 N |
| R | 1350.4 N | 2198.8 N | 2483.2 N | 642.0 N | 4089.2 N |
| Degree of effect | surface morphology > welding force > welding time > welding temperature > cooling time | | | | |
| Optimal level | 360 °C | 12 s | 720 N | 16 s | No. 4 |
| Optimal process parameters | No. 4 surface morphology, welding force 720 N, welding time 12 s, welding temperature 360 °C and cooling time 16 s | | | | |

A more intuitive display of the effect of each factor is shown in Figure 7. The most important three factors (surface morphology, welding force, and welding time) will be discussed in Section 3.2. The cooling time has a limited influence on the peak load, indicating that 10 s was enough for the joint to cool down. It is noted that temperature also has limited influence in this study. A possible reason is that the welding temperature in this study refers to the temperature of the heated copper block, not the temperature of the welding interface. Therefore, no matter what welding temperature was used, the connection started when the interface temperature reached the melting point of the CF/PA66. Our next work will use more accurate test methods to study the impact of the welding interface temperature on joint performance.
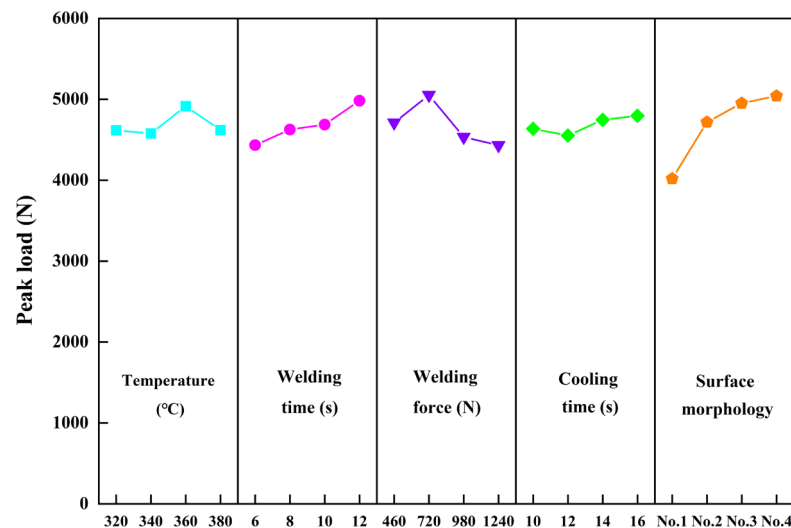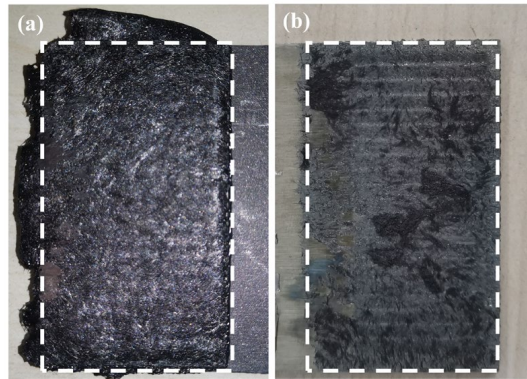


**Figure 7.** The main effect plot of process parameters on the peak load in tensile–shear test.

Figure 8 shows the fracture morphologies under the optimal parameters. It can be seen that the surface of AA6061 was entirely covered by the CF/PA66. More details about the fracture behavior will be discussed in Section 3.2.4.



**Figure 8.** Fracture morphologies: (**a**) CF/PA66; (**b**) AA6061.

Figure 9 shows the SEM cross-sectional morphology of a joint made by the optimal parameters. A tight bonding between the AA6061 and CF/PA66 can be observed at the interface. Some mechanical interlocking between the CF/PA66 and AA6061 can be seen in the magnified view, as shown in Figure 9c. Note that some tiny pores can be observed in the interior of the CF/PA66. These pores do not appear at the interface, so it is speculated that these pores originally exist within the polymer matrix.
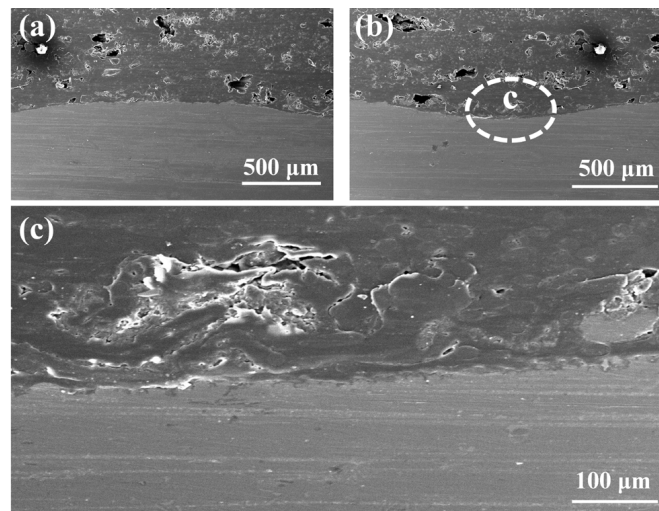


**Figure 9.** Cross-sectional morphologies of a joint made with the optimal parameters: (**a**) the convex part of the cross-section; (**b**) the concave part of the cross-section; (**c**) the magnification of the area c in (**b**).

## 3.2. The Influence of Process Parameters on the Joint Strength

### 3.2.1. The Influence of Surface Morphology

Figure 10 shows the macroscopic morphologies of joints made with different surface morphologies. No obvious difference can be observed among the four joints.

Figure 11 shows the peak load of joints made with different aluminum alloy morphologies. With a comparable total surface area of grooves, the aluminum surface had a wider, shallower, and smaller quantity of grooves, resulting in stronger joints. From the cross-section of the joint, the surface with a narrow, deeper, and larger quantity of grooves will result in an unfilled or unbonded area, as shown in Figure 12a–c. One possible reason is that when two surfaces with comparable surface areas are subjected to the same force, the

surface with more densely arranged grooves will disperse the force applied to the grooves, reducing the force that promotes the flow of molten CFPA66 into the grooves.
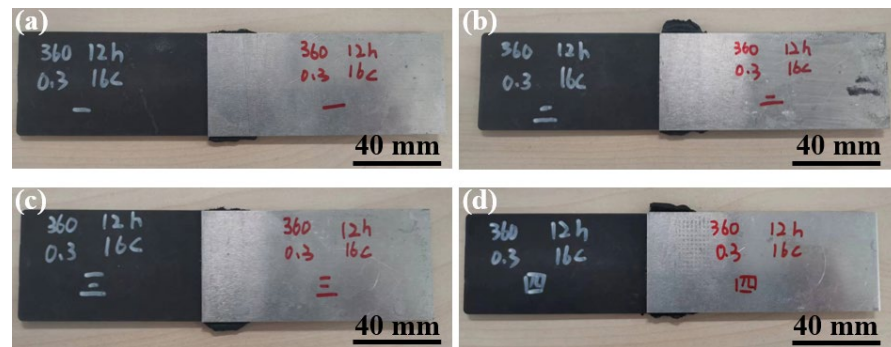


**Figure 10.** Macroscopic morphologies of Al/CFRTP joints: (**a**) No. 1; (**b**) No. 2; (**c**) No. 3; (**d**) No. 4.
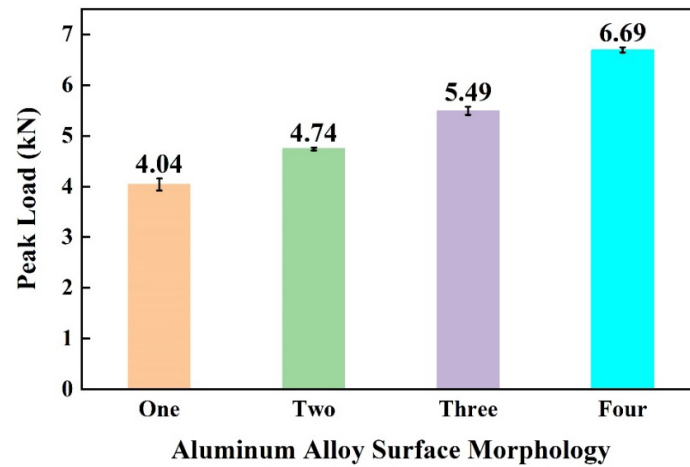


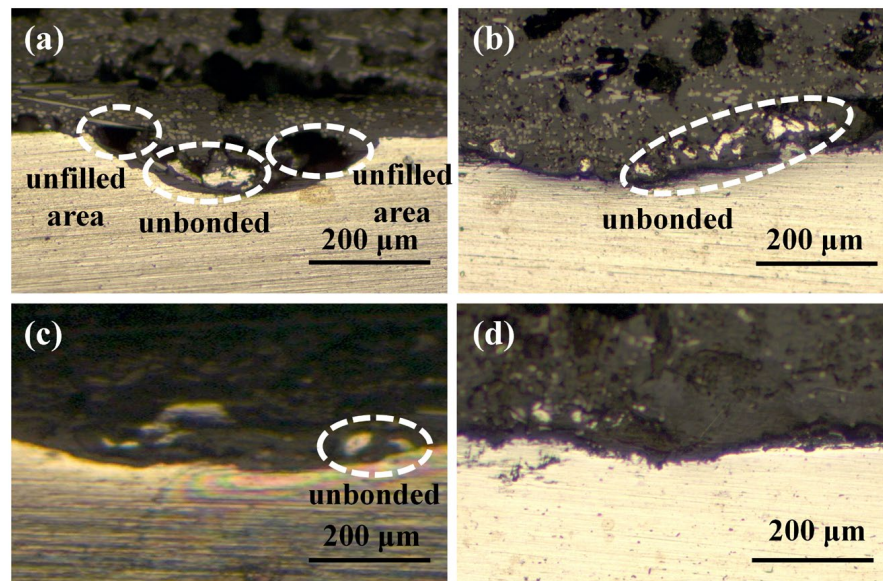**Figure 11.** Effect of aluminum alloy surface morphology on the peak load of joints.



**Figure 12.** Cross-sectional morphologies of joints made with different aluminum alloy surface morphologies: (**a**) No. 1; (**b**) No. 2; (**c**) No. 3; (**d**) No. 4.
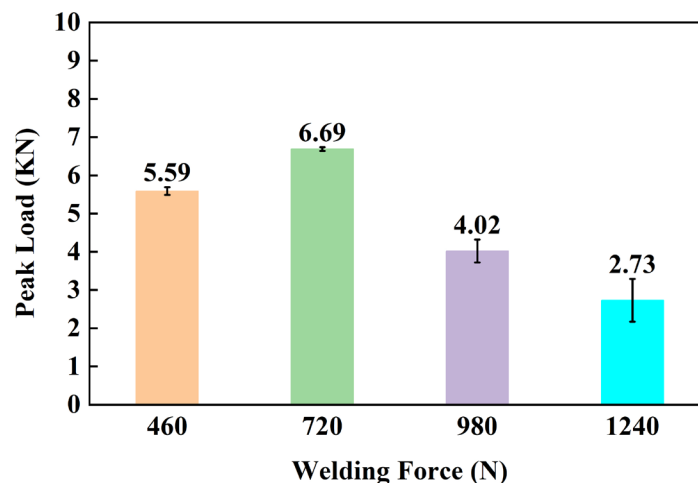
3.2.2. Effect of Welding Force

Figure 13 shows the joints made with different surface morphologies welding forces. As the welding force increased, the extrusion amount of CF/PA66 at the edge showed an increasing trend.

Figure 14 shows the effect of welding force on the peak load of joints. The peak load of joints increased first and then decreased with the increase in welding force. This can be explained by the cross-sectional microstructures of Al/CFRTP joints, as shown in Figure 15. When the welding force was relatively low, the grooves on the aluminum alloy surface could not be filled completely, as shown in Figure 15a. This is because molten PA66 has a large viscosity and requires sufficient welding force to cause it to flow. When the welding force was optimal, no obvious defect could be seen in the joint (Figure 15b). When the welding force is too high, as shown in Figure 15c,d, there will be a large area of unfilled and unbonded metal surface in the joint because of the extrusion of molten CF/PA66. In addition, the extrusion of CF/PA66 also led to the thinning of the CF/PA66 sheet, resulting in a significant decrease in the peak load of the joint.
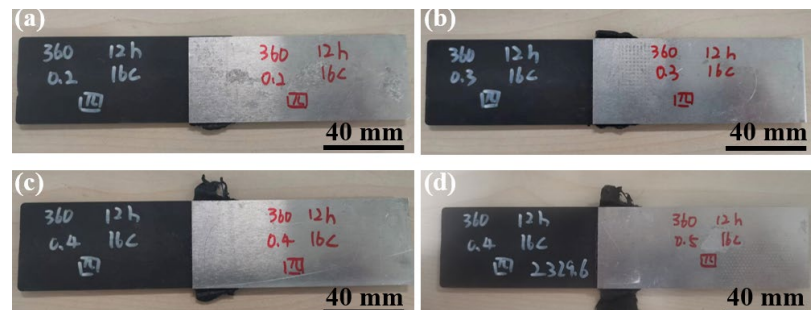


**Figure 13.** Macroscopic morphologies of Al/CFRTP joints under four welding forces: (**a**) 460 N; (**b**) 720 N; (**c**) 720 N; (**d**) 1240 N.



**Figure 14.** Effect of welding force on the peak load of joints.

3.2.3. Effect of Welding Time

Figure 16 shows the macroscopic morphologies of joints made with different welding times. No obvious difference can be observed among the four joints.

Figure 17 shows the effect of welding time on the peak load of joints. It can be seen that the peak load increased as the welding time increased. This can be explained by the cross-sectional microstructures of Al/CFRTP joints, as shown in Figure 18. According to the cross-sections of the joints shown in Figure 18, some unbonded areas can be seen in the joints made with short welding time. This indicates that the wetting and bonding of CF/PA66 to the AA6061 requires sufficient time.
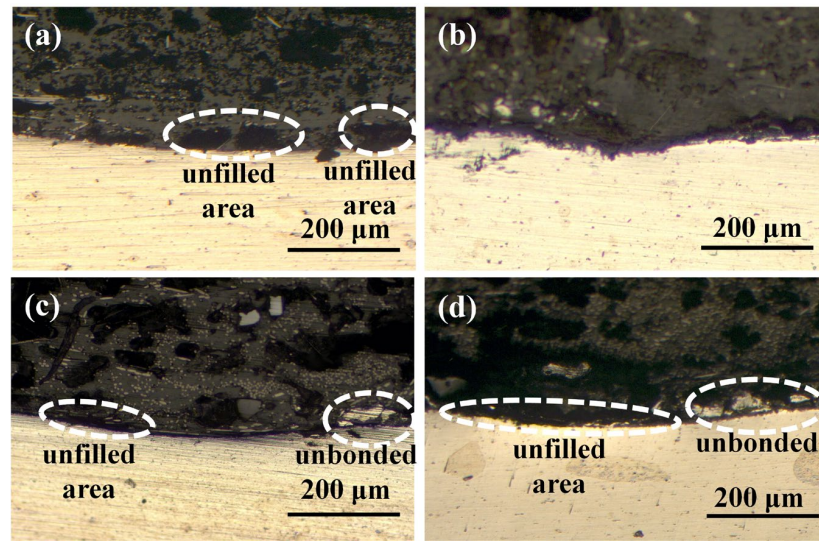
**Figure 15.** Cross-sectional morphologies of joints made with different welding forces: (**a**) 460 N; (**b**) 720 N; (**c**) 980 N; (**d**) 1260 N.
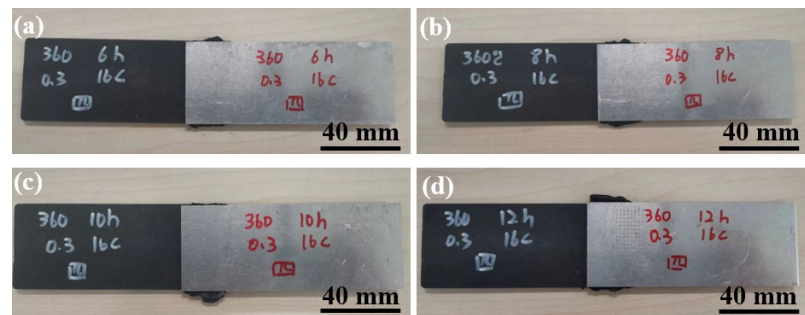


**Figure 16.** Macroscopic morphology of lap joints under four welding times: (**a**) 6 s; (**b**) 8 s; (**c**) 10 s; (**d**) 12 s.
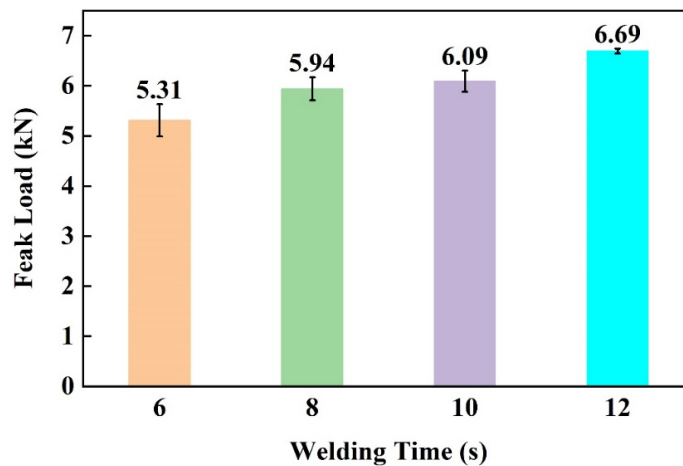


**Figure 17.** Effect of welding time on the peak load of joints.

3.2.4. Analysis of Fracture Morphology

When the joint is subjected to external loads, stress concentration will occur in the weak area at the interface, leading to the failure of the joint. Figure 19 shows the fracture surface morphology of a joint with a relatively low peak load (~4000 N) (welding time 6 s, temperature 320 °C, welding force 460 N, cooling time 10 s, No. 1 surface morphology). It can be seen that when the joint strength was low, the molten resin could not completely

cover the surface of the aluminum alloy, and the processed grooves can still be seen, as shown in Figure 19a. Figure 19d shows a bare aluminum alloy surface. Its corresponding fracture position on the CF/PA66 side is shown in Figure 19e. It can be seen that some fibers were completely coated inside the resin. These phenomena indicate that this location experienced adhesive failure, i.e., interfacial bond failure between the CF/PA66 and the AA6061. In some locations, resin and fibers can also be observed on the AA6061 side, as shown in Figure 19c. Its corresponding fracture position on the CF/PA66 side is shown in Figure 19f. This failure is a cohesive failure since both sides were covered with a polymer matrix. Generally, cohesive failure is considered the preferred failure mode in a tensile–shear test because it means the bonding strength between the polymer and metal is stronger than the shear strength of the polymer matrix. Since only a small area of the welded joint experienced cohesive failure, leading to a relatively low peak load.
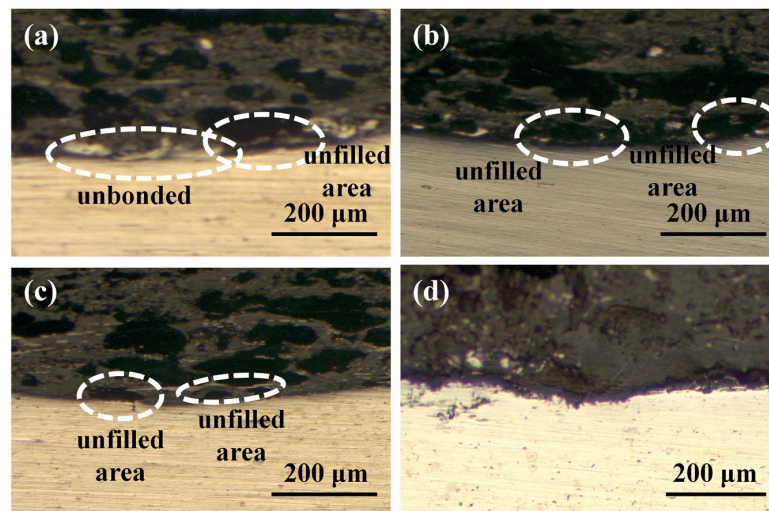


**Figure 18.** Cross-sectional morphologies of the joints made with different welding times: (**a**) 6 s; (**b**) 8 s; (**c**) 10 s; (**d**) 12 s.
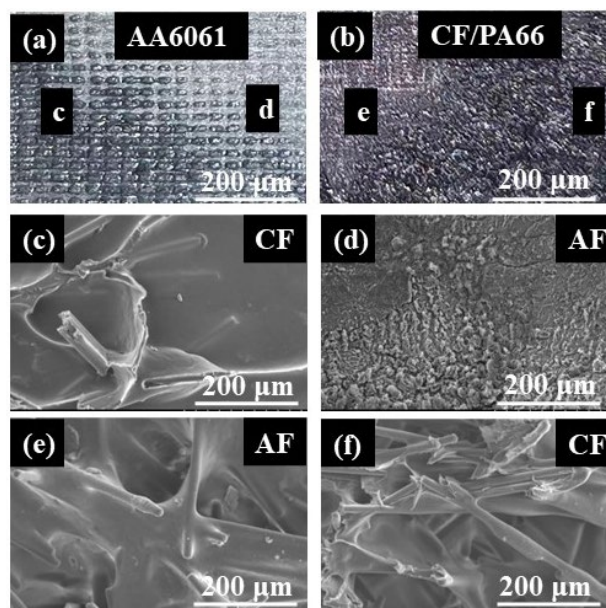


**Figure 19.** Fracture morphology of a joint with relatively low peak load: (**a**) fracture on the aluminum alloy side; (**b**) fracture on the CF/PA66 side; (**c**) area c on the aluminum alloy side; (**d**) area d on the aluminum alloy side; (**e**) area e on the CF/PA66 side; (**f**) area f on the CF/PA66 side (AF stands for adhesive failure; CF stands for cohesive failure).

The fracture morphology of a joint made with the optimal parameters is shown in Figure 20. It can be observed that the surface of the aluminum alloy was almost covered with CF/PA66. Only a small area of the joint experienced adhesive failure, as shown in Figure 20c. The aluminum alloy in most areas of the fracture (Figure 20d–g) was covered in resin, indicating cohesive failure had occurred. A small amount of bared fibers was observed in Figure 20h, indicating the occurrence of fiber-matrix debonding.
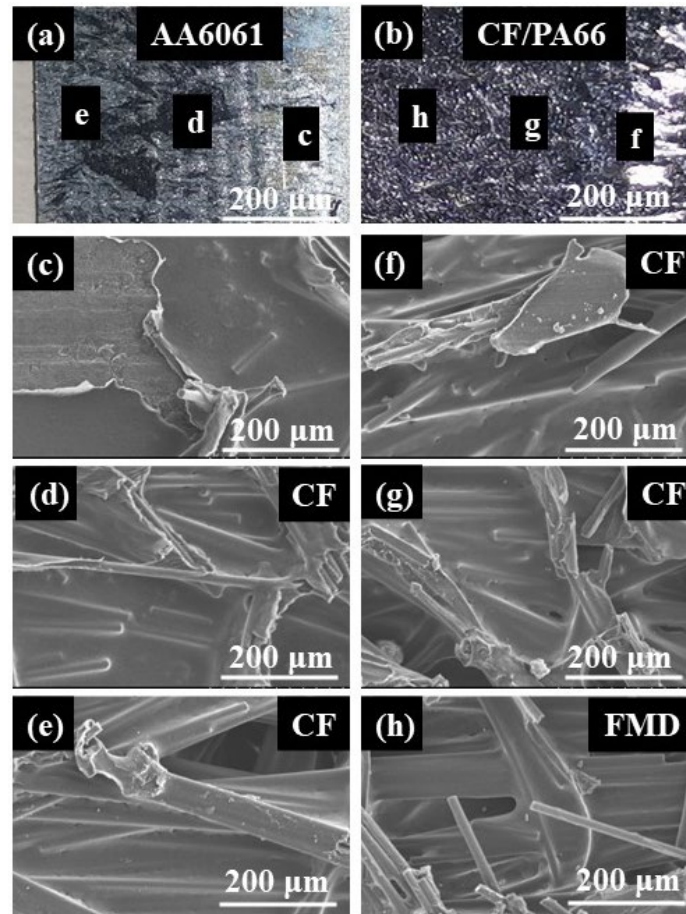


**Figure 20.** Fracture morphology of a joint with optimal peak load: (**a**) fracture on the aluminum alloy side; (**b**) fracture on the CF/PA66 side; (**c**) area c on the aluminum alloy side; (**d**) area d on the aluminum alloy side; (**e**) area e on the aluminum alloy side; (**f**) area f on the CF/PA66 side; (**g**) area g on the CF/PA66 side; (**h**) area h on the CF/PA66 side (CF stands for cohesive failure; FMD stands for fiber-matrix debonding).

## 4. Conclusions

This study employed HPW to join AA6061 and CF/PA66. Jet-ECM was used to make grooves on the aluminum alloy surface. The process parameters (welding temperature, welding time, welding force, cooling time, and surface morphology) were optimized through orthogonal experiments. The main conclusions are given as follows.

(1) Aluminum alloy surface morphology had the greatest impact on the joint performance, followed by welding force, welding time, welding temperature, and cooling time. With a comparable total surface area of grooves, the grooves with a wider width and shallower depth contributed to higher joint strength.

(2) There existed an optimal welding force that maximized the joint strength. A longer welding time facilitated the wetting and bonding of the molten resin to the aluminum alloy, resulting in a stronger joint. Welding temperature had limited influence on the joint performance.

(3) Under the optimal parameters, the fracture morphology in the AA6061 side was almost covered with CF/PA66. Most of the joints experienced cohesive failure, and there was fiber-matrix debonding in a small area.

One limitation of this study is that the welding temperature used in the experiment was the temperature of the heated copper block, not the temperature of the welding interface, which may cause some deviations. Our next work will use more accurate test methods to study the impact of the welding interface temperature on joint performance. In addition, we will attempt to further improve the joint strength, such as further optimizing the surface morphology or using silane coupling agents to improve the bonding ability between metal and polymer.

**Author Contributions:** Formal analysis, H.Z. and Y.L. (Yan Luo); Funding acquisition, Y.L. (Yang Li); Investigation, H.Z., Y.L. (Yang Li) and Y.L. (Yan Luo); Methodology, W.L. and S.A.; Supervision, Y.L. (Yang Li), W.L. and Z.L.; Visualization, H.Z.; Writing—original draft, H.Z.; Writing—review and editing, Y.L. (Yang Li), W.L., S.A. and Z.L. All authors have read and agreed to the published version of the manuscript.

**Institutional Review Board Statement:** Not applicable.

**Informed Consent Statement:** Not applicable.

**Data Availability Statement:** The data presented in this study are available upon request from the corresponding author.

**Conflicts of Interest:** The authors declare no conflicts of interest.

## References

1. Moritz, T.; Scheithauer, U.; Weingarten, S.; Abel, J.; Michaelis, A.; Hampel, S.; Cano, S.C. Hybridization of materials and processes by additive manufacturing. In Proceedings of the 3rd International Conference on Progress in Additive Manufacturing, Singapore, 14–17 May 2018; pp. 14–17.
2. Kalashnikov, K.; Kalashnikova, T.; Semenchuk, V.; Knyazhev, E.; Panfilov, A. Development of a Multimaterial Structure Based on $CuAl_9Mn_{10}$ Bronze and Inconel 625 Alloy by Double-Wire-Feed Additive Manufacturing. *Metals* **2022**, *12*, 2048. [CrossRef]
3. Czerwinski, F. Current Trends in Automotive Lightweighting Strategies and Materials. *Materials* **2021**, *14*, 6631. [CrossRef]
4. Lee, J.M.; Min, B.J.; Park, J.H.; Kim, D.H.; Kim, B.M.; Ko, D.C. Design of Lightweight CFRP Automotive Part as an Alternative for Steel Part by Thickness and Lay-Up Optimization. *Materials* **2019**, *12*, 2309. [CrossRef] [PubMed]
5. Kavitha, K.; Vijayan, R.; Sathishkumar, T. Fiber-metal laminates: A review of reinforcement and formability characteristics. *Mater. Today* **2020**, *22*, 601–605.
6. Nico, D. BMW 7 Series' Carbon Core More Important That You Might Think. BMWBLOG. Available online: https://www.bmwblog.com/2015/09/01/bmw-7-series-carbon-core-more-important-that-you-might-think/ (accessed on 1 September 2015).
7. Lee, M.S.; Seo, H.Y.; Kang, C.G. Comparison of collision test results for center-pillar reinforcements with TWB and CR420/CFRP hybrid composite materials using experimental and theoretical methods. *Compos. Struct.* **2017**, *168*, 698–709. [CrossRef]
8. Sandeep, R.; Natarajan, A. Advances in joining technologies for the innovation of 21st century lightweight aluminium-CFRP hybrid structures. *Proc. Inst. Mech. Eng. Part E J. Process Mech. Eng.* **2022**, *236*, 1239–1255. [CrossRef]
9. Arenas, J.M.; Alía, C.; Narbón, J.J.; Ocaña, R.; González, C. Considerations for the industrial application of structural adhesive joints in the aluminium–composite material bonding. *Compos. Part B Eng.* **2013**, *44*, 417–423. [CrossRef]
10. Lionetto, F.; Pappadà, S.; Buccoliero, G.; Maffezzoli, A. Finite element modeling of continuous induction welding of thermoplastic matrix composites. *Mater. Des.* **2017**, *120*, 212–221. [CrossRef]
11. Choi, I.; Roh, H.D.; Jeong, W.N.; Jeong, H.Y.; Suh, S.; Yi, J.; Um, M.; Oh, Y.; Lee, K. Laser-assisted joining of carbon fiber reinforced polyetherketoneketone thermoplastic composite laminates. *Compos. Part A Appl. Sci. Manuf.* **2022**, *163*, 107228. [CrossRef]
12. Katayama, S.; Kawahito, Y. Laser direct joining of metal and plastic. *Scr. Mater.* **2008**, *59*, 1247–1250. [CrossRef]
13. Schricker, K.; Samfaß, L.; Grätzel, M.; Ecke, G.; Bergmann, J.P. Bonding mechanisms in laser-assisted joining of metal-polymer composites. *J. Adv. Join. Process.* **2020**, *1*, 100008. [CrossRef]
14. Wang, F.Y.; Bu, H.C.; Luo, J.B.; Zhang, P.G.; Wang, L.L.; Zhan, X.H. Influence of different micro-pattern types on interface characteristic and mechanical property of CFRTP/aluminum alloy laser bonding joint. *Int. J. Adv. Manuf. Technol.* **2022**, *120*, 3543–3557. [CrossRef]

15. Lambiase, F.; Genna, S. Experimental analysis of Laser assisted joining of Al-Mg aluminium alloy with Polyetheretherketone (PEEK). *Int. J. Adhes. Adhes.* **2018**, *84*, 265–274. [CrossRef]

16. Jung, K.; Kawahito, Y.; Katayama, S. Laser direct joining of carbon fibre reinforced plastic to stainless steel. *Sci. Technol. Weld. Join.* **2011**, *16*, 676–680. [CrossRef]

17. Ye, Y.Y.; Zou, Q.; Xiao, Y.N.; Jiao, J.K.; Liu, Y.Z.; Sheng, L.Y. Effect of interface pretreatment of Al alloy on bonding strength of the laser joined Al/CFRTP butt joint. *Micromachines* **2021**, *12*, 179. [CrossRef] [PubMed]

18. Lambiase, F.; Genna, S. Laser assisted joining of AA5053 aluminum alloy with polyvinyl chloride (PVC). *Opt. Laser Technol.* **2018**, *107*, 80–88. [CrossRef]

19. Ota, E.; Matsuda, T.; Shoji, H.; Ogura, T.; Miyasaka, F.; Sano, T.; Ohata, M.; Hirose, A. Friction stir spot welding of aluminum and carbon fiber reinforced thermoplastic using hybrid surface treatment improving interfacial properties. *Mater. Des.* **2021**, *212*, 110221. [CrossRef]

20. Geng, P.H.; Ma, N.S.; Ma, H.; Ma, Y.W.; Murakami, K.; Liu, H.H.; Aoki, Y.; Fujii, H. Flat friction spot joining of aluminum alloy to carbon fiber reinforced polymer sheets: Experiment and simulation. *J. Mater. Sci. Technol.* **2022**, *107*, 266–289. [CrossRef]

21. Das, A.; Bang, H.; Bang, H. Numerical modelling in friction lap joining of aluminium alloy and carbon-fiber-reinforced-plastic sheets. *IOP Conf. Ser. Mater. Sci. Eng.* **2018**, *369*, 012032. [CrossRef]

22. Bang, H.S.; Das, A.; Lee, S. Friction stir lap joining of automotive aluminium alloy and carbon-fiber-reinforced plastic. *IOP Conf. Ser. Mater. Sci. Eng.* **2018**, *369*, 012033. [CrossRef]

23. Nagatsuka, K.; Yoshida, S.; Tsuchiya, A.; Nakata, K. Direct joining of carbon-fiber–reinforced plastic to an aluminum alloy using friction lap joining. *Compos. Part B Eng.* **2015**, *73*, 82–88. [CrossRef]

24. Goushegir, S.; dos Santos, J.; Amancio-Filho, S. Friction spot joining of aluminum AA2024/carbon-fiber reinforced poly (phenylene sulfide) composite single lap joints: Microstructure and mechanical performance. *Mater. Des.* **2014**, *54*, 196–206. [CrossRef]

25. Ogawa, Y.; Akebono, H.; Tanaka, K.; Sugeta, A. Effect of welding time on fatigue properties of friction stir spot welds of Al to carbon fibre-reinforced plastic. *Compos. Sci. Technol.* **2019**, *24*, 235–242. [CrossRef]

26. André, N.M.; Goushegir, S.M.; Dos Santos, J.F.; Canto, L.B.; Amancio-Filho, S.T. Friction spot joining of aluminum alloy 2024-T3 and carbon-fiber reinforced poly(phenylene sulfide) laminate with additional PPS film interlayer: Microstructure, mechanical strength and failure mechanisms. *Compos. Part B Eng.* **2016**, *94*, 197–208. [CrossRef]

27. Lambiase, F.; Paoletti, A. Friction Assisted Joining of titanium and polyetheretherketone (PEEK) sheets. *Thin-Walled Struct.* **2018**, *130*, 254–261. [CrossRef]

28. Lionetto, F.; Balle, F.; Maffezzoli, A. Hybrid ultrasonic spot welding of aluminum to carbon fiber reinforced epoxy composites. *J. Mater. Process. Technol.* **2017**, *247*, 289–295. [CrossRef]

29. Yu, W.; Zhang, T.; Wang, Y. Effect of anodizing on ultrasonic welding of 6063 aluminum alloy and PPS. *Rare Met. Mater. Eng.* **2022**, *51*, 241–248.

30. Lionetto, F.; Mele, C.; Leo, P.; D'Ostuni, S.; Balle, F.; Maffezzoli, A. Ultrasonic spot welding of carbon fiber reinforced epoxy composites to aluminum: Mechanical and electrochemical characterization. *Compos. Part B Eng.* **2018**, *144*, 134–142. [CrossRef]

31. Yeh, R.Y.; Hsu, R.Q. Development of ultrasonic direct joining of thermoplastic to laser structured metal. *Int. J. Adhes.* **2016**, *65*, 28–32. [CrossRef]

32. Staab, F.; Liesegang, M.; Balle, F. Local shear strength distribution of ultrasonically welded hybrid Aluminium to CFRP joints. *Compos. Struct.* **2020**, *248*, 112481. [CrossRef]

33. Conte, U.; Villegas, I.; Tachon, J. Ultrasonic plastic welding of CF/PA6 composites to aluminium: Process and mechanical performance of welded joints. *J. Compos. Mater.* **2019**, *53*, 2607–2621. [CrossRef]

34. Kumar, R.; Kumar, O. Investigation of ultrasonic welding of carbon fiber reinforced thermoplastic to an aluminum alloy using a interfacial coating. *Mater. Manuf. Process.* **2021**, *36*, 1323–1331. [CrossRef]

35. Barrak, O.S.; Saad, M.L.; Mezher, T.; Hussein, K.; Hamzah, M.M. Joining of double pre-holed aluminum alloy AA6061-T6 to polyamide PA using hot press technique. *IOP Conf. Ser. Mater. Sci. Eng.* **2020**, *881*, 012062. [CrossRef]

36. Zou, X.; Sariyev, B.; Chen, K.; Jiang, M.Y.; Wang, M.; Hua, X.M.; Zhang, L.T.; Shan, A. Enhanced interfacial bonding strength between metal and polymer via synergistic effects of particle anchoring and chemical bonding. *J. Manuf. Process.* **2021**, *68*, 558–568. [CrossRef]

37. Du, K.P.; Huang, J.; Chen, J.; Li, Y.B.; Yang, C.L.; Xia, X.C. Mechanical property and structure of polypropylene/aluminum alloy hybrid prepared via ultrasound-assisted hot-pressing technology. *Materials* **2020**, *13*, 236. [CrossRef] [PubMed]

38. Liu, Y.F.; Su, J.H.; Tan, C.W.; Feng, Z.W.; Zhang, H.; Wu, L.J.; Chen, B.; Song, X.G. Effect of laser texturing on mechanical strength and microstructural properties of hot-pressing joining of carbon fiber reinforced plastic to Ti6Al4V. *J. Manuf. Process.* **2021**, *65*, 30–41. [CrossRef]

39. Saborowski, E.; Steinert, P.; Lindner, T.; Schubert, A.; Lampke, T. Pin-Shaped Surface Structures Generated by Laser Single Pulse Drilling for High-Strength Interfaces in Thermally Joined Polymer–Metal Hybrids. *Materials* **2023**, *16*, 687. [CrossRef]

40. Xia, H.B.; Yang, B.Y.; Su, J.H.; Liu, Y.F.; Su, X.; Wang, C.; Qiang, X.; Wu, T.; Tan, C.W. Improvement of Laser Welded TC4/CFRTP Joint Strength by Combination of Surface Modification of MAO and Laser Texturing. *Thin. Wall. Struct.* **2024**, *196*, 111409. [CrossRef]

41. Zhang, X.Y.; Su, J.H.; Feng, Z.W.; Liu, H.R.; Tan, C.W.; Chen, B.; Song, X.G. Effect of laser textured patterns on the interfacial characteristics and mechanical properties of 6061Al/GFRTP joints via hot-pressing. *Thin. Wall. Struct.* **2023**, *189*, 110916. [CrossRef]
42. Liu, X.; Wang, J.F.; Bu, H.C.; Wang, F.Y.; Zhan, X.H. Effect of groove configuration on mechanical properties and fracture behavior of 6061 Al alloy and CFRTP laser joint. *Int. J. Adv. Manuf. Technol.* **2022**, *123*, 1913–1924. [CrossRef]
43. Rodríguez-Vidal, E.; Sanz, C.; Soriano, C.; Leunda, J.; Verhaeghe, G. Effect of metal micro-structuring on the mechanical behavior of polymer–metal laser T-joints. *J. Mater. Process. Technol.* **2016**, *229*, 668–677. [CrossRef]
44. Liang, S.M.; Su, J.H.; Zhang, H.; Liu, H.R.; Tan, C.W.; Chen, B.; Song, X.G. The effect of groove texturing direction on laser joining of titanium alloy to CFRTP. *Opt. Laser Technol.* **2024**, *171*, 110416. [CrossRef]

*Article*

# Study on the Overmolding Process of Carbon-Fiber-Reinforced Poly (Aryl Ether Ketone) (PAEK)/Poly (Ether Ether Ketone) (PEEK) Thermoplastic Composites

**Ziyue Zhao, Jindong Zhang** ![ORCID]**, Ran Bi, Chunhai Chen, Jianan Yao \* and Gang Liu \***

Center for Advanced Low-Dimension Materials, State Key Laboratory for Modification of Chemical Fibers and Polymer Materials, College of Materials Science and Engineering, Donghua University, Shanghai 201620, China
\* Correspondence: yjn@dhu.edu.cn (J.Y.); liugang@dhu.edu.cn (G.L.); Tel.: +86-21-67798670 (J.Y.)

**Abstract:** This paper used poly (aryl ether ketone) (PAEK) resin with a low melting temperature to prepare laminate via the compression-molding process for continuous-carbon-fiber-reinforced composites (CCF-PAEK). Then, poly (ether ether ketone) (PEEK), or a short-carbon-fiber-reinforced poly (ether ether ketone) (SCF-PEEK) with a high melting temperature, was injected to prepare the overmolding composites. The shear strength of short beams was used to characterize the interface bonding strength of composites. The results showed that the interface properties of the composite were affected by the interface temperature, which was adjusted by mold temperature. PAEK and PEEK formed a better interfacial bonding at higher interface temperatures. The shear strength of the SCF-PEEK/CCF-PAEK short beam was 77 MPa when the mold temperature was 220 °C and 85 MPa when the mold temperature was raised to 260 °C. The melting temperature did not significantly affect the shear strength of SCF-PEEK/CCF-PAEK short beams. For the melting temperature increasing from 380 °C to 420 °C, the shear strength of the SCF-PEEK/CCF-PAEK short beam ranged from 83 MPa to 87 MPa. The microstructure and failure morphology of the composite was observed using an optical microscope. A molecular dynamics model was established to simulate the adhesion of PAEK and PEEK at different mold temperatures. The interfacial bonding energy and diffusion coefficient agreed with the experimental results.

**Keywords:** poly (aryl ether ketone); poly (ether ether ketone); overmolding; interfacial properties; molecular dynamics simulation

## 1. Introduction

High-performance thermoplastic composites have advantages such as high toughness, impact resistance, low moisture absorption rate, and excellent environmental resistance. Its raw materials can be transported and stored at room temperature. Moreover, it shows a fast-forming and secondary-forming speed [1–3]. Good welding, recycling, and reprocessing are also among their characteristics, which is why it has been widely used in aerospace technologies [4,5]. High-performance thermoplastic composites have advantages in fabricating cabin doors, covers, and other parts vulnerable to impact damage and must be loaded and unloaded repeatedly. It can effectively compensate for the inherent problems of insufficient interlaminar toughness, poor impact damage resistance, and poor open-hole strength of thermosetting composites. Typical high-performance thermoplastic composites include poly (ether ether ketone) (PEEK) [6], poly (aryl ether ketone) (PAEK), poly (phenylene sulfide) (PPS), poly (ether imide) (PEI), and other resin-based composites [7–9]. Its primary forming process includes molding, autoclave forming, automatic laying forming, welding forming, and stamping forming processes [10]. Compared with the forming process of thermosetting composites, thermoplastic composites have a short and flexible forming cycle. For locally reinforced structures, such as stiffened siding, thermosetting composites are usually co-cured, glued, or riveted [11]. However, thermoplastic

composites are generally formed by hot pressing. Then the reinforced panel structure is manufactured by unique connection processes of thermoplastic composites, such as induction and resistance welding [12–14]. Although the molding cycle is shortened to a certain extent, the welding process needs special equipment, and the secondary molding will lead to higher manufacturing costs. Therefore, the automotive industry commonly uses the overmolding [15–18] process of thermoplastic composites. Studying the overmolding process of high-performance thermoplastic composites for aerospace applications is of great engineering significance.

The overmolding process refers to the combination of the bearing efficiency of the continuous-fiber-reinforced thermoplastic composite structure and the manufacturing flexibility of the injection molding process of the short-carbon-fiber-reinforced thermoplastic composite. This is carried out to realize the low-cost integrated manufacturing of thermoplastic composites. Many studies have shown that the interfacial bonding of bilayer structures mainly depends on mechanical locking and resin-fusion mechanisms, and the latter is the main influencing factor. Aurrekoetxea et al. [19] studied the influence of the processing conditions on the interfacial bonding strength when polypropylene (PP) was injected into PP laminate. The interfacial bonding strength was superior when the temperature exceeded the matrix resin melting point. Robert Boros et al. [20] studied the influence of plasma treatment on the interfacial bonding strength of overmolding. The results show that the bonding strength of ABS/PA6 can reach 12 MPa after plasma treatment, but there is no bonding when untreated. Koki Matsumo et al. [21] studied a new method to realize the nanoscale interconnection between different layers by inserting thin films between them. The results show that the interlaminar shear strength is improved by adding a thin film containing short carbon fibers and carbon nanotubes at the overmolding interface. The optimization of the dispersion and forming conditions of carbon nanotubes significantly improved the interlaminar shear strength. To sum up, the interface treatment is the critical factor affecting the interfacial bonding strength in the overmolding process. Controlling the mold and melting temperatures, surface treatment, and other methods can improve the interfacial bonding strength.

However, regarding thermoplastic composites, reaching the melting temperature at the resin interface above (close to 340 °C) in the overmolding process is complex. In addition, it will become more difficult to remove the mold of the composite materials at high temperatures. Therefore, this paper uses PAEK as the resin matrix of continuous-fiber-reinforced composite materials with a relatively low melting temperature. With a high melting temperature, PEEK was applied as the resin matrix of the composite materials used in injection molding to prepare the overmolding materials. The melting temperature of the injection resin is expected to increase the interface temperature between the two materials to promote the mutual diffusion and fusion of resins at the interface and improve the interfacial bonding strength. This paper systematically studied the influence of mold and melting temperatures on composite materials' interfacial bonding strength. The mechanical properties and morphology of the composites were characterized using short-beam shear and SEM, and the experimental results were verified with a molecular dynamics simulation.

## 2. Experimental Materials and Methods

### 2.1. Experimental Materials

This study prepared the continuous-fiber thermoplastic composite (CCF-PAEK) using a one-way prepreg (T700/PAEK, Yingchuang New Materials Co., Ltd., Heilongjiang, China). The fiber surface density was 146 g·m$^{-2}$, the fiber volume fraction was 63 vol%, the resin content was 30 wt.%, and the nominal thickness was 0.165 mm. The reinforced fiber was T700 carbon fiber produced by Tuozhan Carbon Fiber Co., Ltd., Weihai, China. The matrix resin was PAEK resin (PAEK-H, Hairuite Engineering Plastics Co., Ltd., Heilongjiang, China).

The injection molding materials were PEEK and short carbon-fiber-reinforced poly (ether ether ketone) (SCF-PEEK) (Heilongjiang Yingchuang New Materials Co., Ltd., Heilongjiang, China), with a short carbon fiber content of 30 vol%.

The thermal properties of PAEK and PEEK are shown in Table 1. The glass transition temperatures of PAEK and PEEK were 148 °C and 143 °C. The melting temperatures of PAEK and PEEK were 322 °C and 343 °C, respectively.

**Table 1.** Thermal properties of PAEK and PEEK.

| Resin | $T_g$/°C | Melting/°C | | |
|---|---|---|---|---|
| | | $T_{onset}$ | $T_{peak}$ | $T_{final}$ |
| PAEK | 148 | 309 | 322 | 330 |
| PEEK | 143 | 334 | 343 | 347 |

*2.2. Preparation of the Composite Materials for Overmolding*

Continuous-fiber-reinforced composite laminates were prepared through compression molding. First, the prepreg was cut according to the size of the mold cavity, and it was ultrasonically welded to prepare the prepreg (KH-2870Z, Kehai Automation Equipment Co, Weihai, China). Then, the preformed body was put into the mold cavity coated with a high-temperature release agent and put into the press (LSVI-50T, POTOP, Guangzhou, China) for molding. First, the mold was heated to 300 °C, the pressure was set to 0.5 MPa and maintained for 30 min. Then, the temperature was raised to 360 °C, the pressure was set at 2 MPa, and it was maintained for 60 min. Then, air cooling was applied, and the pressure was maintained until the temperature dropped below 140 °C. The molding process is shown in Figure 1. Because the research on continuous-carbon-fiber-reinforced composites is relatively mature, we chose a better method for preparing continuous-carbon-fiber-reinforced composites studied by other group members [22]. We only reviewed the injection molding process, which is more influential in overmolding. The lay-up modes of continuous-fiber-reinforced composites are as follows: the shear sample of the short beam is $(0°)_{16s}$. The final preparation of CCF-PAEK fiber volume fraction was about 63 vol%, calculated as shown in Equation (2).
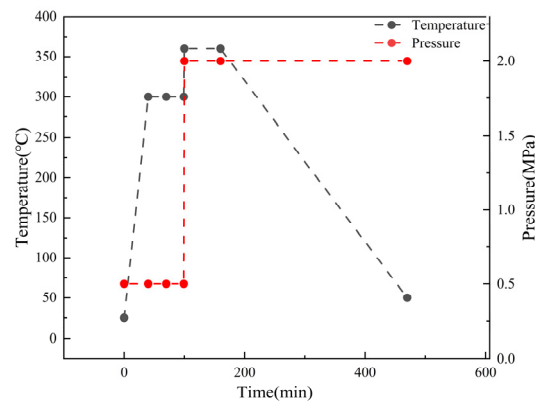


**Figure 1.** CCF-PAEK molding process.

For the continuous-fiber-reinforced composite laminates obtained by molding, inserts were prepared with a water cutting machine (Proto MAX, OMAX, Kent, WA, USA), as shown in Figure 2. The inserts were put into an ultrasonic cleaning machine containing acetone solution (JP-100, Jie Ming, Shenzhen, China) for 30 min to remove residual release agent on the surface. After cleaning, the inserts were put in the oven at 100 °C to dry for 30 min (DZF-6020, Jinghong, Shanghai, China). Then, the dried inserts were placed into the mold cavity of the injection molding machine for preheating. The preheating time was set to 3 min so that the prefabricated part can reach a temperature close to the mold (TY-600, TAYU, Hangzhou, China). Where the preheating time is set to 3 min, the relationship between the temperature of the prefabricated parts and time is indicated in Figure S2. PEEK or SCF/PEEK was injected into the surface of continuous-fiber-reinforced

composite laminates, and the pressure was maintained for 3 min. As shown in Table 2, single-factor experiments were designed to investigate the variation in shear strength of overmolding composites at different mold and melt temperatures, where A was used as the reference.

The technological parameters of overmolding are shown in Table 3. The higher melt temperature is conducive to transferring melt heat to the surface of the prefabricated parts prepared using PAEK at low melting temperatures so that the injection resin and the prefabricated parts form a good interface.

**Table 2.** Single-factor experimental design table.

| Num | $T_{mold}/^{\circ}C$ | $T_{inj}/^{\circ}C$ | Polymer Component |
|:---:|:---:|:---:|:---:|
| A | 260 | 400 | |
| 1 | 220 | 380 | |
| 2 | 240 | 390 | PEEK & SCF-PEEK |
| 3 | 280 | 410 | |
| 4 | / | 420 | |

**Table 3.** Overmolding process parameters.

| Num | $T_{mold}/^{\circ}C$ | $T_{inj}/^{\circ}C$ | Polymer Component |
|:---:|:---:|:---:|:---:|
| 1 | 220 | 400 | |
| 2 | 240 | 400 | |
| 3 | 260 | 400 | |
| 4 | 280 | 400 | PEEK & SCF-PEEK |
| 5 | 260 | 380 | |
| 6 | 260 | 390 | |
| 7 | 260 | 410 | |
| 8 | 260 | 420 | |
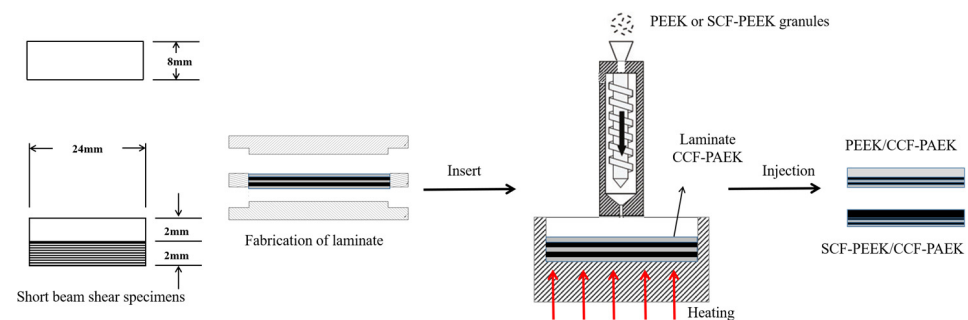


**Figure 2.** Sample size and overmolding process.

### 2.3. Test and Characterization

2.3.1. Mechanics Performance Test

According to ASTM D2344 [23], a short-beam shear-strength test was performed. The thickness:width:span:length ratio of the sample was 1:2:4:6, the overmolding sample size was 4 mm × 8 mm × 24 mm, and the span was 16 mm. Each group was averaged according to the 5 experimental data in the standard. Then, the shear strength of the short beam was calculated according to Equation (1):

$$F^{sbs} = 0.75 \times \frac{P_m}{b \times h} \tag{1}$$

where $F^{sbs}$ is the shear strength of the short beam; $P_m$ is the maximum load when the material is damaged; $b$ is the sample width; and $h$ is the sample thickness.

2.3.2. Morphology Analysis

A desktop scanning electron microscope (Regulus 8230, Hitachi, Tokyo, Japan) was used to characterize the micromorphology of the damaged section in the composite (the accelerating voltage was 5 kV). The surface of the damaged sample was pretreated with gold (spraying time of 60 s).

After using E54 epoxy resin and curing agent N,N-dimethylacetamide in a 10:1 mass ratio, the prepared resin solution was left for 30 min. The cut sample was fixed in a silicone mold (φ32 × h27 mm). The prepared resin was poured and cured in the electric blast-drying oven. Then, a gradient temperature rise was applied to the resin. After solidification, the metallographic sample was obtained and polished using sandpaper from small to large mesh numbers. Finally, nanopolishing liquid and a polishing cloth were selected for further polishing. Subsequently, a polarizing microscope (DM4-P, Leica, Germany) was used to observe the micromorphology of the samples.

2.3.3. Fiber Volume Fraction of Composite Materials

The fiber volume fraction in continuous-carbon-fiber-reinforced composites prepared by molding is calculated according to Equation (1).

$$(\rho_1/\rho_2) \times n/d = v \tag{2}$$

where $\rho_1$ is the surface density of the prepreg; $\rho_2$ is the bulk density of the fibers; n is the number of layups; d is the thickness of the prepreg layup; and v is the volume fraction of the continuous-carbon-fiber-reinforced composite.

2.3.4. Rheological Behavior Analysis

The viscosity curves of PAEK and PEEK resin under a shear flow field were measured with a capillary rheometer (RG25, Gautford, Germany).

2.3.5. Nanoindentation Test

The specimens were indented using a nanoindenter (G200X, KLA, Milpitas, CA, USA) to measure the microhardness and modulus at different locations. The advanced dynamic I and H methods were chosen for the tests, and the load was 25 mN.

2.3.6. Molecular Dynamics Simulation

Molecular dynamics simulations were performed to reveal the bonding mechanism of PEEK and PAEK during overmolding (Material Studio 2020), and diffusion coefficients and binding energies at different interface temperatures were calculated. The diffusion coefficient *D* is determined according to Einstein's relation [24,25] as follows:

$$MSD = t\langle|r_i(t) - r_i(0)|^2\rangle \tag{3}$$

$$D = \lim_{t \to \infty} \frac{1}{t}\langle|r_i(t) - r_i(0)|^2\rangle \tag{4}$$

where $r_i$ and *t* are the reference position and simulation time of each atom, and $r_i$ is the distance from the bit to the center of the mass of a single chain.

In the overmolding process, the formation of the interface depends not only on the mutual motion of the two-phase molecules but also on their self-motion. The radius of rotation ($R_g$) of polymer molecules was studied to investigate the mechanism of molecular self-motion further. The movement depends on the size of the polymer macromolecules and their center of mass, calculated as follows:

$$R_g = \sqrt{\frac{1}{M}\sum_i m_i(r_i - r_{cm})^2} \tag{5}$$

where $M$ and $r_{cm}$ are the total mass of the polymer chain in the system and the centroid position of the chain. It is assumed that multiple units are within the polymer chain. The mass of each element is mi, and $r_i$ is the distance from the atom to the centroid position of the individual chain. Usually, the rotation radius corresponds to the curl and contraction of the molecular chain. MSD and $R_g$ radius characterize the mobility of polymer molecules and chains.

The interface interaction energy between polymer layers mainly comprises van der Waals and electrostatic interaction energy. The interfacial bonding energy [26] is calculated as follows:

$$E_{joining} = E_{total} - (E_{PAEK} + E_{PEEK}) \tag{6}$$

where $E_{total}$, $E_{PAEK}$, and $E_{PEEK}$ are the total energy of the system, the energy of the PAEK resin layer, and the energy of the PEEK resin layer, respectively.

An atomic model of the PEEK/CCF-PAEK interface was established to study the effect of mold temperature on the adhesion behavior of the interface during PEEK/CCF-PAEK overmolding. Because the resin matrix is located in the outer layer of the interface, an atomic model was adopted at the PEEK/PAEK interface. It was assumed that the bonding occurred during injection, without considering subsequent pressure preservation and cooling processes. The atomic models of PEEK and PAEK layers were also constructed. Some modeling parameters, including polymerization, number of chains, initial density, and size, are given in Table 4.

**Table 4.** The main parameters of the atomic model of PEEK and PAEK.

| Material | Number of Chains | Degree of Polymerization | Total Amount of Atoms | Initial Density /g·cm³ | Box Size /nm³ |
|---|---|---|---|---|---|
| PEEK | 17 | 5 | 5542 | 1.3 | 4 × 6.2 × 2.4 |
| PAEK | 10 | 10 | 5886 | 1.3 | 4 × 6.2 × 2.4 |

All calculations in this paper were performed using molecular dynamics simulations via VASP. The condensed phase-optimized molecular-potential force field describes the atomic interactions in atomic simulation studies (universal—a purely diagonal harmonic force field). The bond stretching is described in harmonic terms. Three Fourier cosine expansions define angular bending. Cosine Fourier expansions describe the torsion. The van der Waals interaction is described by the Leonard–Jones potential. Electrostatic interactions were described with atomic monopole and shielding (distance-dependent) coulomb terms. The aim is to achieve high precision in predicting the properties of very complex mixtures. All simulations were performed in a constant temperature–constant volume canonical ensemble (NPT). The Verlet algorithm was used to integrate the equations of motion. The integration time step was 1 fs, and the Nosé–Hoover thermostat controlled the temperature. The simulation system balances 300 ps to stabilize the interaction. After this phase, the total intermolecular interaction energy of 300 ps was recorded at 5 ps intervals. Finally, the average values were calculated to eliminate fluctuations in the simulation.

## 3. Results and Discussions

### 3.1. Influence of Mold Temperature on the Interfacial Bonding Strength

The viscosity–temperature curves of PAEK and PEEK resin at the shear rate of 1000 s$^{-1}$ are shown in Figure 3. The viscosity of PAEK at 340 °C~400 °C is about 89~237 Pa·s, and for PEEK at 360 °C~420 °C is 203~330 Pa·s. Both resins have shear-thinning behavior, and the viscosity changes tend to be consistent with the increase in temperature (the viscosity decreases with the increase in temperature). The lower the viscosity of the melt, the better the diffusion because the mixing process requires the melt to spread as far as possible at the interface before cooling.
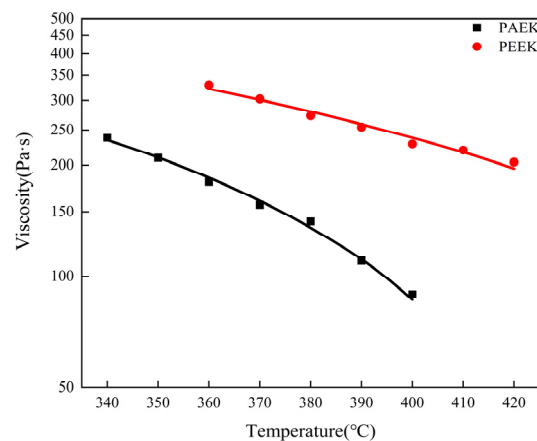
**Figure 3.** Temperature–viscosity curves of PAEK and PEEK resins.

The shear strengths of PEEK/CCF-PAEK and SCF-PEEK/CCF-PAEK at different mold temperatures are shown in Figure 4. In Figure 4a, the stress–strain curves of the two materials under different mold temperatures are shown. The strain of the sample increases slowly before it reaches the failure stress, and finally, shear failure occurs. The shear strength of the composite can be improved by adding short carbon fiber.
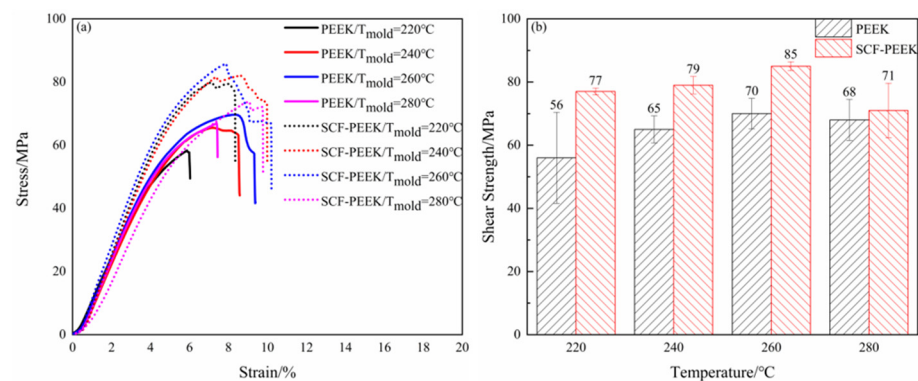


**Figure 4.** Influence of mold temperature on short-beam shear strength: (**a**) stress–strain curves of overmolding samples at different mold temperatures; (**b**) mold temperature and shear strength of the short beam.

Figure 4b shows the shear strength of PEEK/CCF-PAEK and SCF-PEEK/CCF-PAEK short beams at different die temperatures. The shear strength of PEEK/CCF-PAEK is 56 MPa, 65 MPa, 70 MPa, and 68 MPa, respectively, whereas the shear strength of SCF-PEEK/CCF-PAEK is 77 MPa, 79 MPa, 85 MPa, and 71 MPa, respectively. The results show that the shear strength of the short beam can be improved with the increase in mold temperature. Mold temperature affects the interfacial temperature holding time between injection melt and insert and the contact time before curing. Therefore, with the increase in mold temperature, the temperature of the interface layer is gradually increased to promote the melting and diffusion of PAEK resin at low melting temperature and improve the interface bonding strength.

Shear failure modes of short beams of overmolding composites at different mold temperatures are shown in Figures 5 and 6. Under shear force, cracks begin to occur on both sides of the sample and expand to the middle. The failure of PEEK/CCF-PAEK was mainly caused by the interface delamination when the mold temperatures were 220 °C and 240 °C. In this case, the interfacial bonding strength was weak. PEEK/CCF-PAEK failure was mainly caused by the interlayer fracture when the mold temperatures were increased to 260 °C and 280 °C (Figure 5c,d). In this case, a strong interfacial bonding was observed.
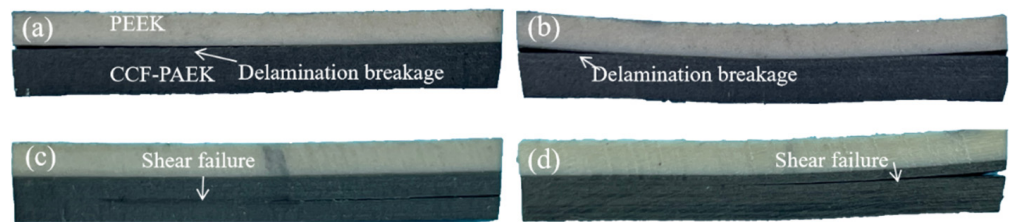
**Figure 5.** PEEK/CCF-PAEK, composite failure samples, prepared at different mold temperatures: (**a**) 220 °C; (**b**) 240 °C; (**c**) 260 °C; and (**d**) 280 °C.
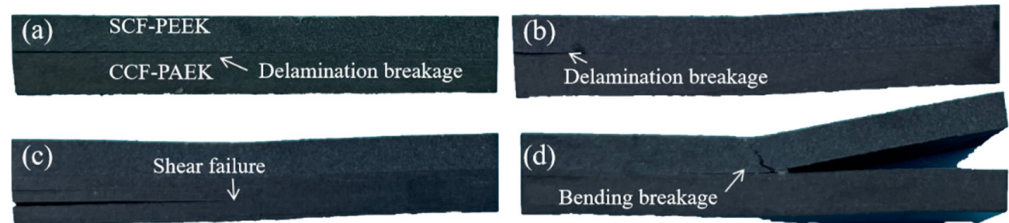


**Figure 6.** SCF-PEEK/CCF-PAEK, composite failure samples, prepared at different mold temperatures: (**a**) 220 °C; (**b**) 240 °C; (**c**) 260 °C; and (**d**) 280 °C.

Similarly, the failure of SCF-PEEK/CCF-PAEK was similar to that shown in Figure 6. The interfacial bonding failure was the main issue when the mold temperatures were 220 °C and 240 °C. In the latter case, the cracks at the interface gradually became smaller. When the mold temperatures increased to 260 °C and 280 °C; the failure of SCF-PEEK/CCF-PAEK was an interlaminar fracture of CCF-PAEK and bending failure of SCF-PEEK. Due to the flexural deformation and interlaminar shear deformation by overmolding, the lamination between PEEK, SCF-PEEK, and CCF-PAEK will occur when the interfacial bonding strength weakens. With the increase in interfacial bonding strength, the interfacial delamination of the composite decreases gradually, and the interlaminar fracture of the resin increases. Wang et al. [27] studied the effect of resin content in polyimide/bisphenol A diisocyanate laminates on the shear strength of short beams. They showed that a lower resin content would limit the full infiltration of the fibers and reduce the shear strength of short composite beams. In overmolding composites, the resin content of the PEEK or SCF-PEEK side is more than that of CCF-PAEK. It should be noted that PEEK resin has a higher toughness. Therefore, when the interfacial bonding strength of overmolding composite materials is higher, shear delamination failure no longer occurs at the interface but occurs inside the laminate.

We observed the specimen failure mode and the microscopic morphology of the resin surface after specimen destruction, where the direction of the destruction morphology observation is indicated in Figure S3. At a mold temperature of 220 °C, i.e., Figure 7a, the PEEK damage surface morphology is relatively smooth, and only the PEEK resin portion can be observed. When the mold temperature is raised to 240 °C, i.e., Figure 7b, the PEEK resin surface is adhered to the CCF-PAEK portion of the continuous carbon fiber and its resin, indicating that resin melting begins to occur at the PEEK/CCF-PAEK interface at this time [28]. However, at this time, the interfacial bond strength is relatively low, and shear damage still occurs at the interface, as shown in Figure 5b. Until the mold temperature is raised above 260 °C as shown in Figure 7c,d, only continuous fibers and their resin in CCF-PAEK can be observed in the damage morphology at this time, and combined with Figure 5c,d, it can be seen that shear damage occurs at the interlayer of CCF-PAEK at this time.
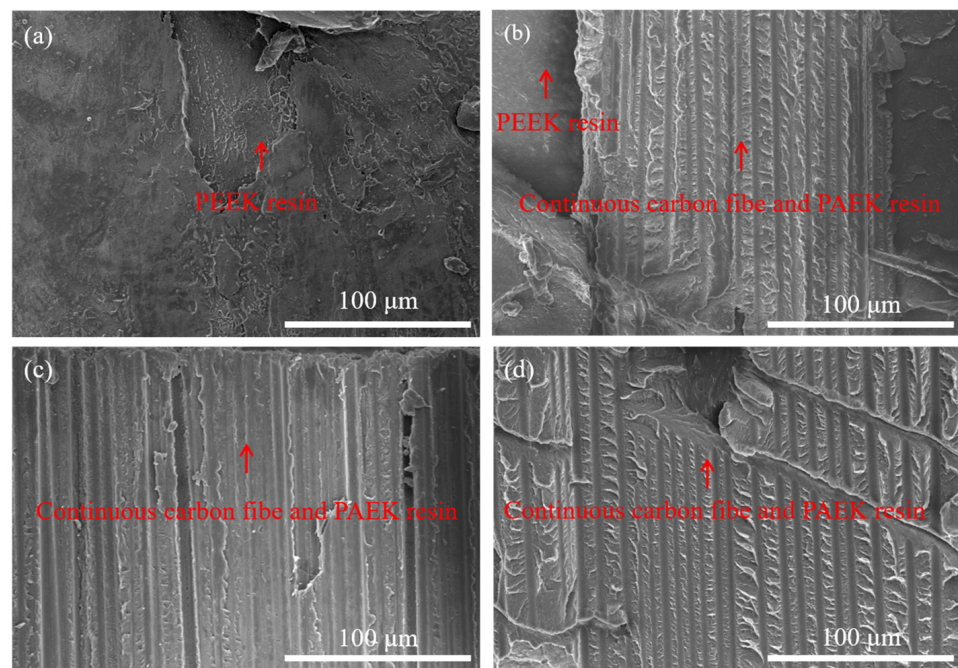
**Figure 7.** Failure morphology of PEEK surface at different mold temperatures: (**a**) 220 °C; (**b**) 240 °C; (**c**) 260 °C; and (**d**) 280 °C.

The microscopic morphology corresponding to the shear damage of SCF-PEEK/CCF-PAEK in Figure 8 is the same as that of PEEK/CCF-PAEK, and only SCF-PEEK can be observed at a mold temperature of 220 °C. As the mold temperature increases, as shown in Figure 8b, the appearance of continuous carbon fibers in the red circle indicates that melting begins to occur at the interface. As the mold temperature increases to 260 °C, i.e., Figure 8c, only continuous fibers of CCF-PAEK and its resin can be observed at the interface.
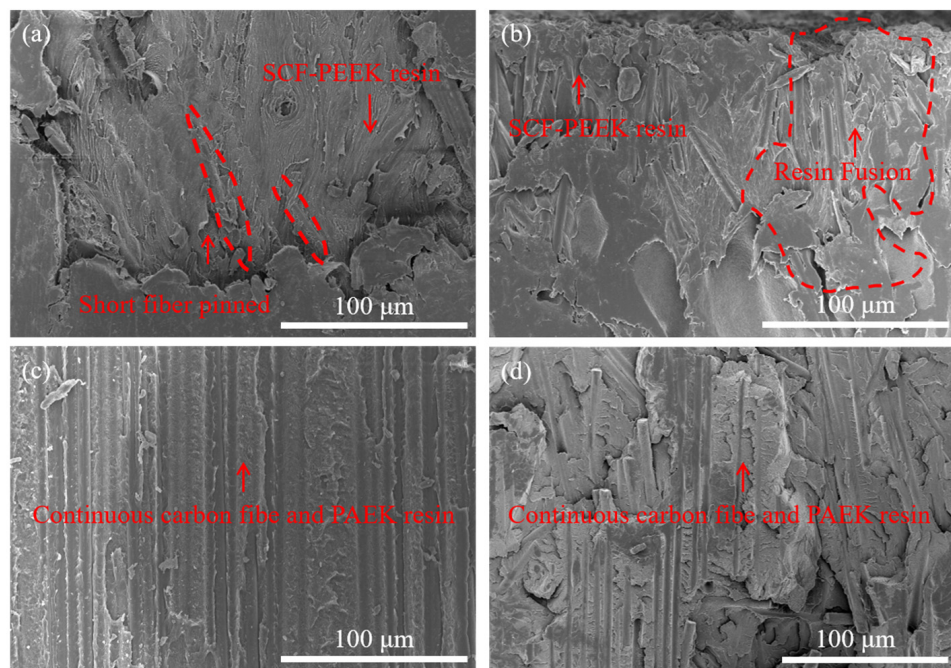


**Figure 8.** Failure morphology of SCF-PEEK surface at different mold temperatures: (**a**) 220 °C; (**b**) 240 °C; (**c**) 260 °C; and (**d**) 280 °C.

The experimental results show that the interface failure mode of the composite changes with the increase in mold temperature. When it is low, the temperature at the interface is low, the injection mold melt cools rapidly, and the molecular diffusion is relatively slow, resulting in poor adhesion [29]. Shear failure is manifested as an interface failure. Interfacial bonding is manifested as mechanical bonding. With the increase in the mold temperature, the fracture surface area of PEEK increased gradually. Higher mold temperature increased the interface temperature between PEEK resin and PAEK and increased the blending time before curing, which was beneficial to the fusing process of the resin. When the interface temperature is higher than the melting temperature of PAEK, the resin eutectic layer is formed at the interface [30], which improves the interfacial bonding strength.

The interfaces of PEEK/CCF-PAEK and SCF-PEEK/CCF-PAEK before failure are shown in Figures 9 and 10, respectively. Optical microscope observations were made at different mold temperatures, with CCF-PAEK on the upper side and PEEK and SCF-PEEK on the lower side. In Figure 9a, when the mold temperature was 220 °C, PEEK resin was poorly combined with PAEK resin, resulting in obvious interface stratification and even pores. When the mold temperature is 220 °C, there is also a boundary at the interface, but no pores are observed (Figure 10a). With the increase in mold temperature, the boundary line slowly disappears. Although there was no obvious gap between PAEK and PEEK, a clear boundary could still be observed (Figures 9a,b and 10a,b). The interface between the two completely disappears when the mold temperature reaches 260 °C. The results show that resin melting can significantly improve the shear strength of short beams, which is of great significance. After adding the short carbon fiber, they cross the boundary and are nailed in the PAEK resin layer (Figure 10b,c).

Adding staple fibers enhances the stiffness and strength of the injection layer but also influences the interfacial bonding strength [31]. However, when the mold temperature was raised to 280 °C, holes appeared at the interface (Figure 10d). In the process of overmolding, when the mold temperature is 280 °C, the resin adheres to the mold cavity, and the difficulty of demolding leads to defects at the interface layer, which reduces the interlayer shear strength.
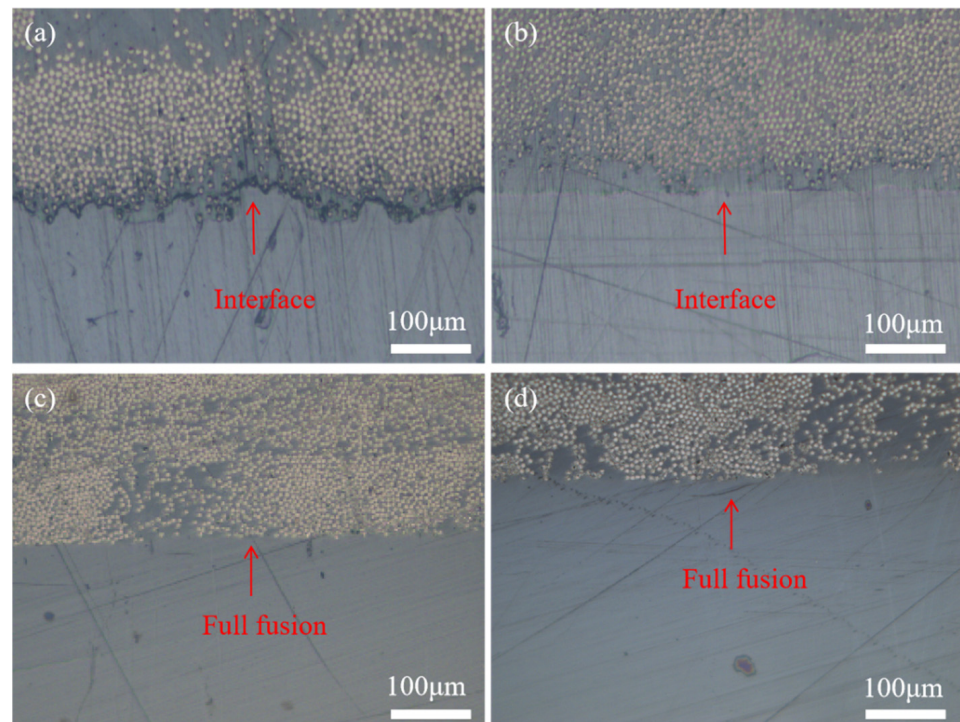


**Figure 9.** The interface of PEEK/CCF-PAEK before failure at different mold temperatures: (**a**) 220 °C; (**b**) 240 °C; (**c**) 260 °C; and (**d**) 280 °C.
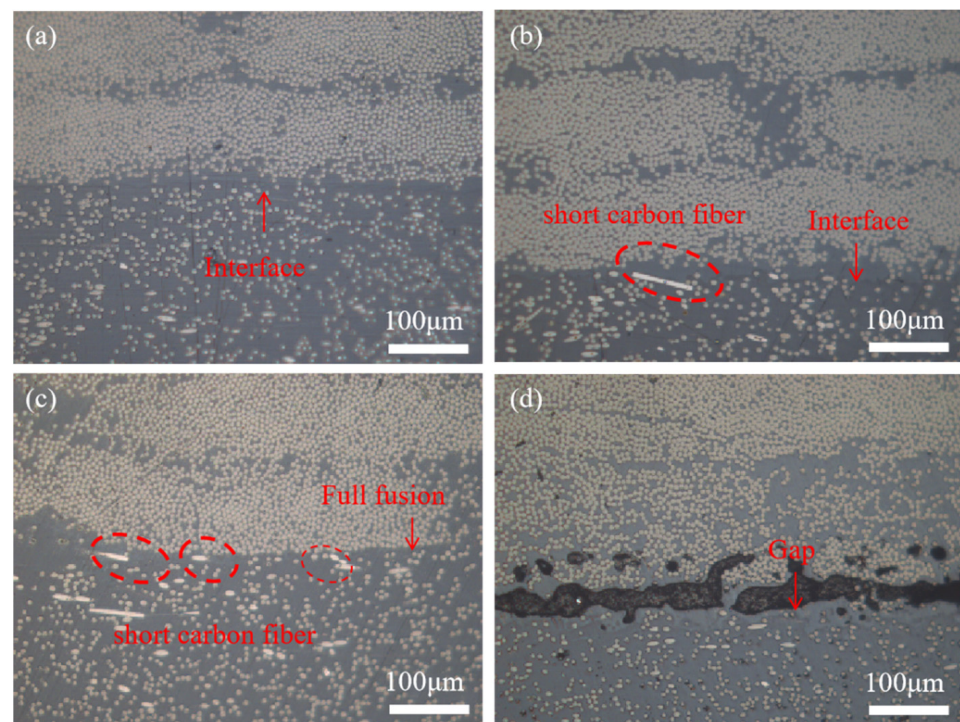
**Figure 10.** The interface of SCF-PEEK/CCF-PAEK before failure at different mold temperatures: (**a**) 220 °C; (**b**) 240 °C; (**c**) 260 °C; and (**d**) 280 °C.

The results show that the interface between the injection and insert layers will change with different mold temperatures. With the increase in mold temperature, the melt can have a longer contact time before consolidation. Thus, changing the melting state of PAEK resin at low melting temperatures promotes the heat transfer between the injection molding layer and the insert layer, making the PAEK and PEEK interface disappear while forming the resin eutectic layer. The boundary line between the injection mold melt and the insert interface gradually disappears, forming a strong and reliable connection and increasing the shear strength. The mold temperature is still lower than the melting temperature of PAEK. Still, the heat transferred by PEEK at high melting temperatures combines the injection and insert layers. It can solve the problem that the composite material of overmolding cannot be molded at high temperatures.

The nanoindentation load-depth curves of the secondary molded composites at different mold temperatures are shown in Figure 11a. Observing the curves in the Figure, we know that for the same indentation load, the indentation depth gradually becomes smaller as the mold temperature increases, indicating that the bearing capacity of the resin at the interface gradually becomes stronger as the mold temperature increases. For the PEEK/CCF-PAEK composite, the load capacity of the interface resin is similar to that of PEEK when the mold temperature is 260 °C, indicating that the preform and the injection layer resin have reached a state of molten resin intermixing, which is consistent with the strength of PEEK. The higher loads at the SCF-PEEK/CCF-PAEK composite interface compared to PEEK indicate that adding short-cut carbon fibers enhances the resin at the interface, allowing it to carry higher loads.

It can be observed that the modulus decreases rapidly with the increase in the indentation depth when the indentation depth is small in Figure 11b, and the modulus curve changes more at this time. After the depth exceeds 250 nm, the modulus value gradually becomes smooth with the increase in depth. When the indentation depth exceeds 500 nm, the modulus curve becomes smooth, and the material modulus is calculated at this time. The depth-modulus curve of the PEEK/CCF-PAEK secondary composite at a mold temperature of 220 °C is relatively unstable, and the modulus at this time is low at 4.2 GPa. This indicates that the melt can form a resin intergradation layer with the preform

surface resin at a mold temperature of 260 °C and, therefore, has the same modulus as PEEK. For the SCF-PEEK/CCF-PAEK secondary molding composite, the depth–modulus curve is relatively smoother, and the addition of short-cut carbon fibers can improve the modulus of the resin at the interface. With the increase in mold temperature, the modulus also gradually increased. The increase was higher at the mold temperature of 260 °C. In the previous paper, the modulus reached 5.5 GPa, related to transforming the interfacial bonding state at the mold temperature of 260 °C, i.e., the interfacial resin can melt and diffuse into one. The short-cut carbon fiber can be embedded in the interfacial layer, which benefits the modulus increase.
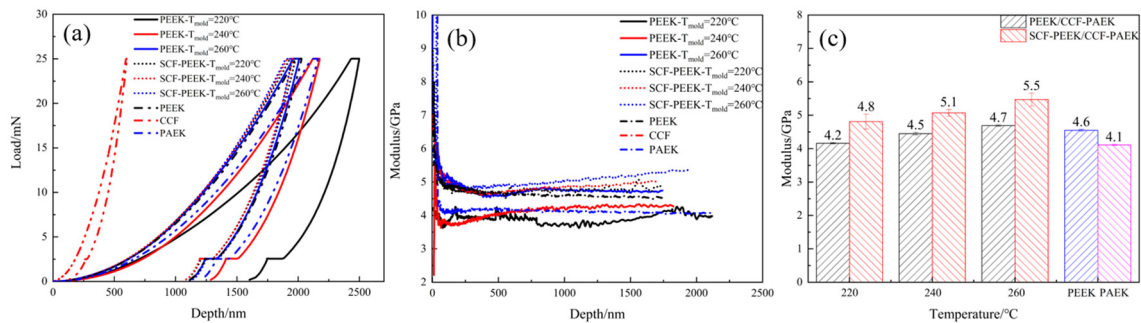


**Figure 11.** Nanoindentation analysis of composite materials formed by secondary molding at different mold temperatures: (**a**) load depth curve; (**b**) modulus depth curve; (**c**) modulus.

### 3.2. Influence of Melt Temperature on the Interfacial Bonding Strength

Figure 12 shows the shear strength of PEEK/CCF-PAEK and SCF-PEEK/CCF-PAEK short beams at different melting temperatures. The shear strength of PEEK/CCF-PAEK was 69 MPa, 67 MPa, 71 MPa, 67 MPa, and 66 MPa, respectively. The shear strength of the SCF-PEEK/CCF-PAEK short beam was 84 MPa, 84 MPa, 85 MPa, 87 MPa, and 83 MPa, respectively. Comparing the shear strength data of the short beam of the two resin overmolding samples shows that the melt temperature has little influence on the PEEK/CCF-PAEK interfacial bonding strength when the mold temperature is 260 °C. Figure 13 shows the interfacial bonding state of the SCF-PEEK/CCF-PAEK composite at different melt temperatures, and the boundary between PAEK and PEEK becomes unclear when the mold temperature is 260 °C. As the melt temperature increases, more and more short carbon fibers are pinned into the resin; as shown in the red circle in the figure, the short carbon fibers cross the boundary to connect the two matrix resins and improve the interfacial bonding strength. The fluidity of the SCF-PEEK resin can be improved by increasing the melt temperature when a resin interfusion zone forms at the interface. More short carbon fibers can be inserted into the resin-rich region to strengthen the interface.
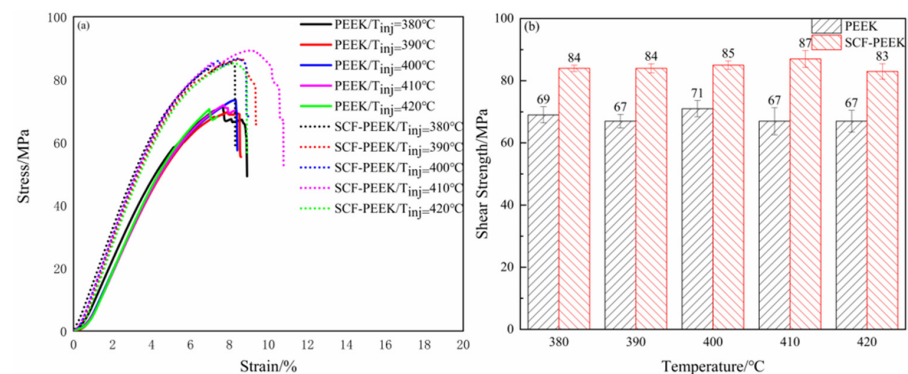


**Figure 12.** Influence of melt temperature on short-beam shear strength: (**a**) stress–strain curves of overmolding samples at different melt temperatures; (**b**) melt temperature and shear strength of the short beam.
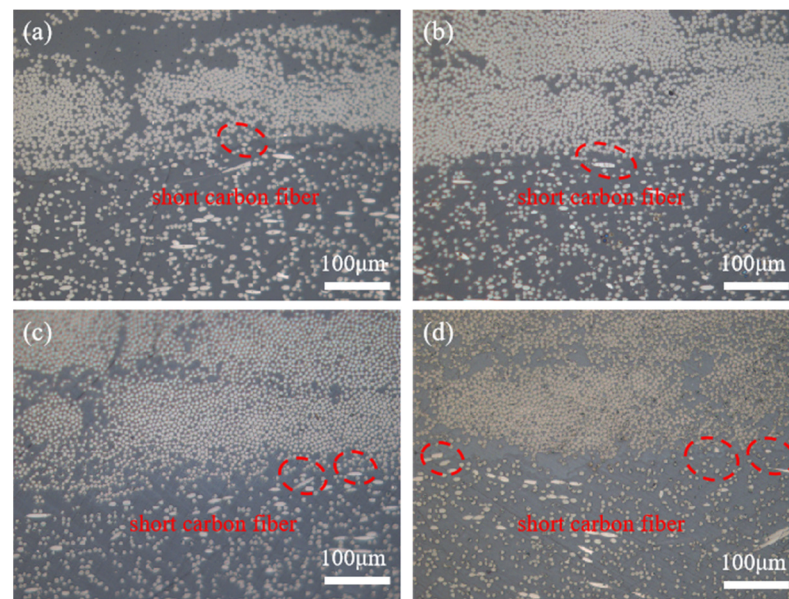
**Figure 13.** The interface of SCF-PEEK/CCF-PAEK before failure at different melt temperatures: (**a**) 380 °C; (**b**) 390 °C; (**c**) 410 °C; and (**d**) 420 °C.

The final conditions chosen were a mold temperature of 260 °C, the highest shear strength at a melt temperature of 400 °C for PEEK/CCF-PAEK, and a higher melt temperature of 410 °C for SCF-PEEK/CCF-PAEK. According to Figure S1. For the relationship between interface temperature and shear strength for PEEK/CCF-PAEK, below the interface temperature of 320 °C, the shear strength of the melt is lower than at the interface temperature of 320 °C. When the interface temperature is raised to 320 °C and above, the shear strength at low mold temperature and high melt temperature is lower than that at high mold temperature. At high mold temperatures, the melt temperature has less influence on the shear strength.

### 3.3. Molecular Dynamics Simulation

PAEK was painted brown to observe the intermolecular diffusion and interface formation process, and PEEK was painted green, as shown in Figure 14. According to the results, the mold temperature significantly affects the interfacial bonding strength. In contrast, melt temperature has nearly no effect. Therefore, this simulation used only mold temperature as the influencing factor. The injection molding temperature is set at 400 °C, and the mold temperature is set at 220 °C, 240 °C, 260 °C, and 280 °C, respectively. The simulation showed that as the mold temperature increased, some molecular chains crossed the interface and became entangled with another layer of molecular chains.

Figure 15 shows the radius of gyration, mean square displacement of the whole system during the interface bonding process at different mold temperatures. In PEEK/PAEK over-molding, the formation of the interface depends not only on the mutual motion of the two molecular chains but also on the self-motion of the molecules. Figure 14 shows the rotation radius and mean azimuth shift data at different mold temperatures at the PAEK and PEEK interfaces. It can be seen that the rotation radius of PEEK and PAEK increases with the increase in mold temperature as can be seen in Figure 14a that under different processing conditions, the rotation radius of the total system gradually increases when it reaches a stable state at 300 ps. Figure 14b shows the mean azimuth shift–time curve at different mold temperatures. At higher values, the total mean azimuth shift increases rapidly with time. This means that as the temperature increases, the molecules move faster. However, when the temperature change is the same, especially when the mold temperature is 220 °C, the change in MSD is slower. It was found that under the processing conditions, the mechanical properties of the prepared samples and the microstructure observation after failure

showed slow molecular movement and poor interfacial bonding strength. The molecular motion rate increases gradually with the increase in mold temperature, and the interface bonding strength increases. However, the mean azimuth shift value is small when the mold temperature gradually increases to 260 °C and 280 °C. The experimental results show that the interfacial bonding strength does not increase after the mold temperature increases.
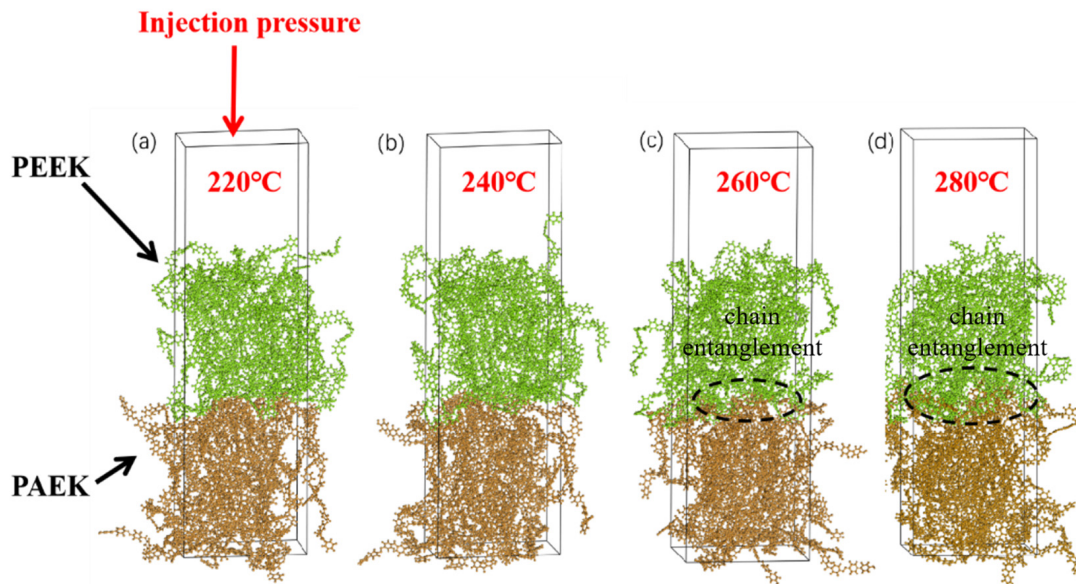


**Figure 14.** Adhesion of PEEK and PAEK interfaces at different mold temperatures: (**a**) 220 °C; (**b**) 240 °C; (**c**) 260 °C; and (**d**) 280 °C.
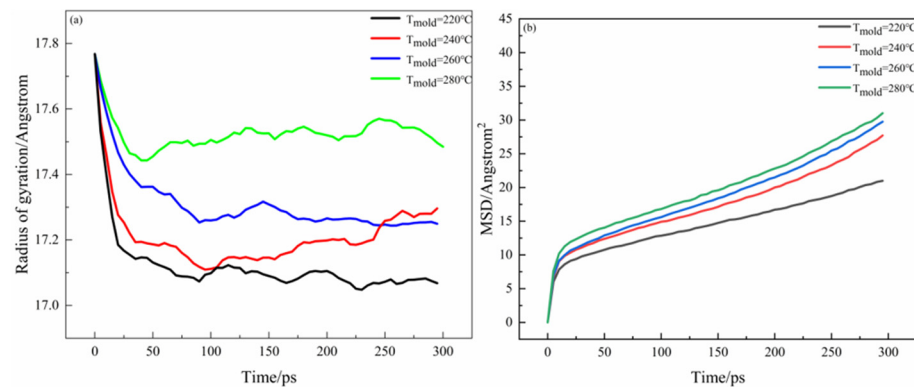


**Figure 15.** $R_g$ and MSD at PEEK and PAEK interfaces: (**a**) rotation of gyration; (**b**) mean square displacement.

Figure 16 shows the two systems' interface bonding energy and diffusion coefficient at different mold temperatures. It can be seen that when the mold temperature increases from 220 °C to 280 °C, the diffusion coefficient increases from $7.3 \times 10^{-10}$ m$^2 \cdot$s$^{-1}$ to $14.0 \times 10^{-10}$ m$^2 \cdot$s$^{-1}$, and the absolute value of the interface energy increases sharply from 233.4 kcal$\cdot$mol$^{-1}$ to 450.8 kcal$\cdot$mol$^{-1}$. Compared with other temperature changes, the diffusion coefficient changes are larger when the mold temperature increases from 220 °C to 240 °C. At this time, the molecular diffusion rate increased, which was in the same trend as the shear strength of the short beam, as shown in Table 5. It is proved that the resin began to melt and bond at the interface within the mold temperature range from 220 °C to 240 °C. It can be concluded that the non-bonding free energy at the interface increases when the mold temperature increases, and the mutual diffusion of the two systems at the interface is enhanced, thus improving the interface energy.
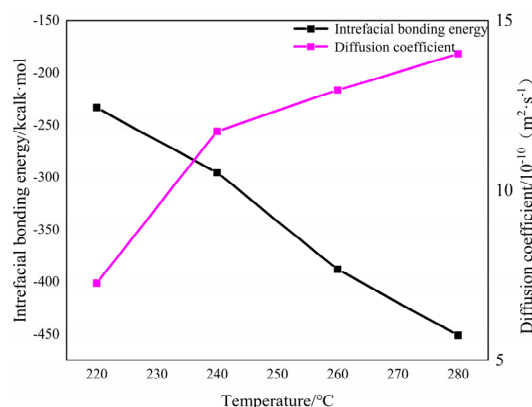
**Figure 16.** The two systems interfacial bonding energy and diffusion coefficient at different mold temperatures.

**Table 5.** Interfacial bonding energy, diffusion coefficient, and shear strength of PEEK and PAEK short beam.

| $T_{mold}$ /°C | Diffusion Coefficient /$10^{-10}m^2 \cdot s^{-1}$ | Bonding Energy /kcal·mol$^{-1}$ | PEEK/CCF-PAEK ILSS/MPa | SCF-PEEK/CCF-PAEK ILSS/MPa |
|---|---|---|---|---|
| 220 | 7.2 | 233.3 | 56 | 77 |
| 240 | 11.8 | 295.4 | 65 | 79 |
| 260 | 13.0 | 388.0 | 70 | 83 |
| 280 | 14.0 | 450.8 | 68 | 71 |

In the molecular dynamics simulation, the interfacial bonding energy and diffusion coefficient will continue to increase when the mold temperature increases. Only the injection process is calculated without considering processes such as holding pressure, and only the resin molecular chain is simulated without involving fibers. The simulation results do not match the experimental results at the final mold temperature of 280 °C, as the interfacial bonding energy is higher in the simulation. Still, the actual interfacial bonding strength is highest at the mold temperature of 260 °C due to the internal stress at the interface of the overmolding composite at the high mold temperature, so the final mold temperature is 260 °C.

## 4. Conclusions

(1) In this paper, carbon-fiber-reinforced composite material (CCF-PAEK) with a low melting temperatures was prepared via PAEK. PEEK and SCF-PEEK resin with high melting temperatures were used as injection resin. The results show that the interface bonding strength is greatly affected by mold temperature, whereas the melting temperature has little effect on the interface bonding strength. When the mold temperature was 220 °C, the shear strength of the PEEK/CCF-PAEK short beam was 56 MPa, and when the mold temperature was increased to 260 °C, the shear strength of the PEEK/CCF-PAEK short beam was 70 MPa, which increased by 25%. The shear strength of short-beam SCF-PEEK/CCF-PAEK was 77 MPa when the mold temperature was 220 °C and 85 MPa when the mold temperature was raised to 260 °C. When the mold temperature was lower than the melt temperature of PAEK, the overmolding composites can form a good bond. The melt temperature had little effect on the shear strength of the PEEK/CCF-PAEK short beams, but as the melt temperature increased from 380 °C to 410 °C, the shear strength of the SCF-PEEK/CCF-PAEK short beams increased from 83 MPa to 87 MPa. For the SCF-PEEK/CCF-PAEK, the increase in melt temperature can promote more short carbon fibers to cross the boundary and nail more short carbon fibers in the matrix interfusion zone to improve the shear strength of short beams.

(2) The interfacial bonding of overmolding composites includes mechanical meshing, resin fusion, and short carbon fiber interfacial nailing. The molecular dynamics simulation and experiments prove that the interface bonding strength mainly depends on mechanical meshing when the mold temperature is less than 220 °C. The resin melts at the interface when the mold temperature is 220–240 °C. Mechanical meshing and resin fusion affect the interface bonding strength in this case. When the mold temperature reaches 260 °C, the resin at the interface is completely fused, forming the matrix interfusion zone. The short carbon fiber can cross the interface and connect the two resin matrices, improving the bonding strength.

(3) Through the molecular dynamics simulation, it was found that the interface bonding energy and diffusion coefficient are in good agreement with the experimental results. The mold temperature had a positive effect on PAEK-PEEK interface bonding. The diffusion coefficient and bonding energy of the interface increased with the increase in mold temperature. Therefore, a higher mold temperature will result in higher interface bonding strength.

## References

1. Stewart, R. Thermoplastic composites—Recyclable and fast to process. *Reinf. Plast.* **2011**, *55*, 22–28. [CrossRef]
2. Sonnenfeld, C.; Mendil-Jakani, H.; Agogue, R.; Nunez, P.; Beauchene, P. Thermoplastic/thermoset multilayer composites: A way improve the impact damage tolerance of thermosetting resin matrix to composites. *Compos. Struct.* **2017**, *171*, 298–305. [CrossRef]
3. Cheon, J.; Kim, M. Impact resistance and interlaminar shear strength enhancement of carbon fiber reinforced thermoplastic composites by introducing MWCNT-anchored carbon fiber. *Compos. Part B-Eng.* **2021**, *217*, 108872. [CrossRef]
4. Marsh, G. Airbus takes on Boeing with reinforced plastic A350 XWB. *Reinf. Plast.* **2007**, *51*, 26–27, 29. [CrossRef]
5. Marsh, G. Bombardier throws down the gauntlet with CSeries airliner. *Reinf. Plast.* **2011**, *55*, 22–26. [CrossRef]
6. Donaldson, S.L. Fracture toughness testing of graphite/epoxy and graphite/PEEK composites. *Composites* **1985**, *16*, 103–112. [CrossRef]
7. Farahani, R.D.; Dube, M. Novel Heating Elements for Induction Welding of Carbon Fiber/Polyphenylene Sulfide Thermo-plastic Composites. *Adv. Eng. Mater.* **2017**, *19*, 1700294. [CrossRef]
8. Vieille, B.; Chabchoub, M.; Bouscarrat, D.; Keller, C. Prediction of the notched strength of woven-ply PolyPhenylene Sulfide thermoplastic composites at a constant high temperature by a physically-based model. *Compos. Struct.* **2016**, *153*, 529–537. [CrossRef]
9. Hron, R.; Kadlec, M.; Růžek, R. Effect of the Test Procedure and Thermoplastic Composite Resin Type on the Curved Beam Strength. *Materials* **2021**, *14*, 352. [CrossRef]
10. Yu, T.; Gao, H.; Wang, B.; Guo, C.; Jiang, F. Research Progress of Molding Process of Carbon Fiber Reinforced Thermo-plastic Composites. *Eng. Plast. Appl.* **2018**, *46*, 139–144.
11. Brauner, C.; Nakouzi, S.; Zweifel, L.; Tresch, J. Co-curing behaviour of thermoset composites with a thermoplastic boundary layer for welding purposes. *Adv. Compos. Lett.* **2020**, *29*, 2633366X20902777. [CrossRef]
12. Ageorges, C.; Ye, L.; Hou, M. Advances in fusion bonding techniques for joining thermoplastic matrix composites: A review. *Compos. Part A Appl. Sci. Manuf.* **2001**, *32*, 839–857. [CrossRef]

13. Du, B.; Chen, L.; Liu, H.; He, Q.; Qin, W.; Li, W. Resistance welding of glass fiber reinforced thermoplastic composite: Experimental investigation and process parameter optimization. *Chin. J. Aeronaut.* **2020**, *33*, 3469–3478. [CrossRef]

14. Murray, R.E.; Roadman, J.; Beach, R. Fusion joining of thermoplastic composite wind turbine blades: Lap-shear bond characterization. *Renew. Energy* **2019**, *140*, 501–512. [CrossRef]

15. Silva, F.J.G.; Soares, M.R.; Ferreira, L.P.; Alves, A.C.; Brito, M.; Campilho, R.D.S.G.; Sousa, V.F.C. A Novel Automated Sys-tem for the Handling of Car Seat Wires on Plastic Over-Injection Molding Machines. *Machines* **2021**, *9*, 141. [CrossRef]

16. Kong, B. Development of the overmolding instrument panel. In Proceedings of the Asia Pacific Automotive Engineering Conference, Bangkok, Thailand, 1–3 April 2013.

17. Park, D.K.; Kong, B.S.; Kim, B.C. Development of Crash Pad Using Overmolding Technology. *Int. J. Automot. Technol.* **2022**, *23*, 1739–1745. [CrossRef]

18. Yu, L.; Xia, B.; Zhang, J.; Peng, B. Effect of temperature related processing parameters on the interface bonding strength of automotive overmolding injection parts. *Mater. Test.* **2019**, *61*, 960–964. [CrossRef]

19. Aurrekoetxea, J.; Castillo, G.; Cortes, F.; Sarrionandia, M.A.; Urrutibeascoa, I. Failure of multimaterial fusion bonding inter-face generated during over-injection molding/thermoforming hybrid process. *J. Appl. Polym. Sci.* **2006**, *102*, 261–265. [CrossRef]

20. Boros, R.; Tatyana, A.; Golcs, A.; Krafcsik, O.H.; Kovacs, J.G. Plasma treatment to improve the adhesion between ABS and PA6 in hybrid structures produced by injection overmolding. *Polym. Test.* **2022**, *106*, 107446. [CrossRef]

21. Matsumoto, K.; Ishikawa, T.; Tanaka, T. A novel joining method by using carbon nanotube-based thermoplastic film for injection overmolding process. *J. Reinf. Plast. Compos.* **2019**, *38*, 616–627. [CrossRef]

22. Sun, H.; Yao, J.; Zhang, J.; Gu, Y.; Wang, W.; Liu, G. Preparation of Continuous Carbon Fiber Reinforced Poly ether ether ketone Composite and Its Mechanical Properties. *China Plast. Ind.* **2021**, *49*, 110–113.

23. *ASTM D2344-00*; Standard Test Method for Short-Beam Strength of Polymer Matrix Composite Materials and Their Laminates. ASTM International: West Conshohocken, PA, USA, 2000.

24. Zhou, M.; Xiong, X.; Drummer, D.; Jiang, B. Molecular Dynamics Simulation on the Effect of Bonding Pressure on Thermal Bonding of Polymer Microfluidic Chip. *Polymers* **2019**, *11*, 557. [CrossRef]

25. Zhang, M.; Jiang, B.; Chen, C.; Drummer, D.; Zhai, Z. The Effect of Temperature and Strain Rate on the Interfacial Behavior of Glass Fiber Reinforced Polypropylene Composites: A Molecular Dynamics Study. *Polymers* **2019**, *11*, 1766. [CrossRef] [PubMed]

26. Wang, Q.; Sun, L.; Li, L.; Yang, W.; Zhang, Y.; Dai, Z.; Xiong, Z. Experimental and numerical investigations on microstructures and mechanical properties of hybrid fiber reinforced thermoplastic polymer. *Polym. Test.* **2018**, *70*, 215–225. [CrossRef]

27. Wang, Z.; Li, S.; Wang, J.; Han, E.; Tian, G.; Wu, D. Dielectric and mechanical properties of polyimide fiber reinforced cyanate ester resin composites with varying resin contents. *J. Polym. Res.* **2020**, *27*, 160. [CrossRef]

28. Sauer, B.B.; Kampert, W.G.; Wakeman, M.D.; Yuan, S. Screening method for the onset of bonding of molten polyamide resin layers to continuous fiber reinforced laminate sheets. *Compos. Sci. Technol.* **2016**, *129*, 166–172. [CrossRef]

29. Jiang, B.; Fu, L.; Zhang, M.; Weng, C.; Zhai, Z. Effect of thermal gradient on interfacial behavior of hybrid fiber reinforced polypropylene composites fabricated by injection overmolding technique. *Polym. Compos.* **2020**, *41*, 4064–4073. [CrossRef]

30. Deng, T.; Huang, Z.; Zheng, B.; Jiang, W.; Chen, L.; Chen, C.; Zhou, H.; Zhou, H. Bond strength and bond mechanism of in-jection over-molded woven carbon fiber/PEEK-short carbon fiber/PEEK composite components. *J. Appl. Polym. Sci.* **2022**, *139*, e53222. [CrossRef]

31. Ning, N.; Fu, S.; Zhang, W.; Chen, F.; Wang, K.; Deng, H.; Zhang, Q.; Fu, Q. Realizing the enhancement of interfacial interaction in semicrystalline polymer/filler composites via interfacial crystallization. *Prog. Polym. Sci.* **2012**, *37*, 1425–1455. [CrossRef]

# Parametric Investigation into the Shear Strength of Adhesively Bonded Single-Lap Joints

**Quanlong Chen [1,2], Bing Du [3,*], Xiaodong Zhang [4], Hai Zhong [4], Conggang Ning [3], Huimin Bai [3], Qian Li [3], Ruqing Pan [3], Baocheng Zhou [2] and Hanjie Hu [1,2,*]**

[1] School of Aeronautics, Chongqing Jiaotong University, Chongqing 400074, China
[2] The Green Aerotechnics Research Institute of CQJTU, Chongqing 401120, China
[3] Chongqing Key Laboratory of Nano–Micro Composite Materials and Devices, School of Metallurgy and Materials Engineering, Chongqing University of Science and Technology, Chongqing 401331, China
[4] Innovation Center, Chongqing Polycomp International Corp., Chongqing 401321, China
[*] Correspondence: dubing@cqust.edu.cn (B.D.); huhj@gatri.cn (H.H.)

**Abstract:** In this paper, the shear strength of adhesively bonded single-lap joints were experimentally and numerically investigated. Based on the validated simulation, the effects of lap length, adhesive layer thickness, adhesive layer shape, adhesive layer overflow length, and laminate lay-up on the shear strength of adhesively bonded single-lap joints were studied. The load-displacement curves and shear strength under different parameters were compared. It was shown that the shear strength of single-lap joints gradually decreases with the increase of lap length and adhesive layer thickness, which were 53.83% and 16.15%, respectively. Considering the potential condition in fabrication, the adhesive layer shape and adhesive layer overflow length were also investigated. The adhesive with normal and triangle shape owned the comparable shear strength, which was higher than the arc one. The shear strength increased by 19.37% from 18.43 MPa to 22.00 MPa with increasing the adhesive layer overflow length to 50% of lap length. It was beneficial for shear strength to increase the adhesive layer overflow length to 50% of lap length. Among the selected four lay-ups, $[0]_{16s}$ had the highest shear strength, which was nearly 3 times greater than the one of $[90]_{16s}$. In the real process preparation, increasing the number of $0°$ layers, selecting the appropriate lap length and thickness of the adhesive layer, and controlling the shape and length of the adhesive layer overflow are of great help to improve the tensile shear strength of the single-lap glue joint.

**Keywords:** composite laminate; single lap joint; adhesively bonding; geometric parameters; failure strength

## 1. Introduction

Composite materials are widely used in aerospace, shipbuilding, wind power generation, and other industries because of their high specific strength and specific modulus. Although composite materials have good integrity, the problem of connection between structures is inevitable due to a series of factors such as structural design and manufacturing cost. The main connection methods of composite materials are adhesive connections, mechanical connections, stitching connections, Z-Pin connections, and hybrid connections [1]. Adhesive joint, as a form of connection, is the most widely used type of composite material connection compared to several other types of connections, as it maintains the integrity of the structure, reduces the weight of the joint, and enhances the sealing of the structural joint. There are various types of lap structures for adhesive joint, mainly single-lap [2–4], flat-fold-flat type [5], wave type [6], etc. Damage failure occurs when the strength of the adhesive joint itself cannot support the strength of the outside world. According to the location where the damage occurs, the failure form of the joint can be divided into four forms: parent material fracture, cohesive failure, interfacial failure, and mixed failure [7].

Chen et al. [8] studied the experimental shear strength of single-lap joints prepared by three different forming processes, RTM, RTM with the introduction of sewing and adhesive joint under ambient temperature, and hot and humid high-temperature environments, and analyzed the shear damage mechanism of single lap joints under the three preparation methods and the effect of ambient temperature on the shear strength of single-lap joints based on the experimental phenomena. Li [9] prepared a new self-inserting adhesive joint structure and studied the effects of lap length, inflection point, and lap surface on the bearing capacity of the joint. Zhang et al. [10] studied the shear damage test of the adhesive surface of the composite single-lap adhesive structure and obtained the ultimate shear strength of the structure. Wu et al. [11] studied various forms of adhesive joints of composites and analyzed the stresses in the adhesive joints. Liang et al. [12] conducted experimental studies and numerical simulations on adhesive joints of laminates with different lap lengths and found that the failure modes and ultimate loads of adhesive joints are related to the length of the adhesive joint and the thickness of the adhesive parts based on the damage morphology of the joints. The use of the finite element method for parametric study and analysis of composite adhesive joint is more common. The study includes the factors affecting the stresses in the adhesive layer and the strength of the joint, such as the lap length [12], the thickness of the adhesive layer [13–16], the lay-up angle [17], the design of the joint end [18], etc. It also includes the models for the analysis of the damage of the adhesive layer and the prediction of the joint strength. In particular, finite element methods based on cohesion and continuum damage models have been developed recently to analyze the damage of adhesive layers and the damage of composite interfaces [19,20]. Xu et al. [21] investigated flat-fold-flat (FJF) adhesive joints by ABAQUS software and compared the strength of flat single-lap adhesive joints and found that FJF lap joints have a larger damage tolerance compared to the flat-lap method.

From the above, it can be concluded that many factors, such as lap length, adhesive layer thickness, and laminate lay-up, have influence on the shear strength of the single-lap joint. However, the factors named lap overflow adhesive layer shape and lap overflow length, which can be met in the fabrication process, are investigated relatively less. In this paper, the shear strength of adhesively bonded single-lap joints were experimentally and numerically investigated. Based on the validated simulation, the effects of lap length, adhesive layer thickness, adhesive layer shape, adhesive layer overflow length, and laminate lay-up on the shear strength of adhesively bonded single-lap joints were studied. The load-displacement curves and shear strength under different parameters were compared. Moreover, the interaction between the above factors was studied to select the key factor by the Design of Experiment (DOE) method.

## 2. Methods

### 2.1. Fabrication and Experiment

The laminate material is ZPNPREG®2551/150/37 carbon fiber/epoxy prepreg, provided by Shangwei (Shanghai, China) Carbon Fiber Composites Company Limited (SWCFC). The specific material mechanical property parameters are shown in Table 1; the single-lap zone bonding material is LORD®320/322 epoxy structural adhesive, and the performance parameters are shown in Table 2; the reinforcing sheet zone bonding material is 3M epoxy structural adhesive.

**Table 1.** ZPNPREG®2551/150/37 parameters.

| Mechanical Performance Parameters | Symbol | Value |
|---|---|---|
| Longitudinal tensile modulus | $E_1$ | 111 GPa |
| Transverse tensile modulus | $E_2$ | 7.3 GPa |
| In-plane shear modulus | $G_{12}$ | 3.7 GPa |
| Longitudinal tensile strength | $X_t$ | 1690 MPa |
| Longitudinal compression strength | $X_c$ | 1070 MPa |
| Transverse tensile strength | $Y_t$ | 35 MPa |
| Transverse compression strength | $Y_c$ | 134 MPa |
| In-plane shear strength | $S$ | 49 MPa |

**Table 2.** Adhesive performance parameters.

| Types of Adhesives | $K_{nn}$ MPa | $K_{ss}$ MPa | $K_{tt}$ MPa | $\sigma_n$ MPa | $\sigma_s$ MPa | $\sigma_t$ MPa | $G_{nn}$ N/mm | $G_{ss}$ N/mm | $G_{tt}$ N/mm |
|---|---|---|---|---|---|---|---|---|---|
| LORD®320/322 | 1586 | 1586 | 1586 | 30.6 | 30.6 | 30.6 | 0.3 | 1.2 | 1.2 |

$K_{nn}$, $K_{ss}$, and $K_{tt}$ refer to stiffnesses in the normal direction, the first shear direction, and the second shear direction, respectively. $\sigma_n$, $\sigma_s$, and $\sigma_t$ refer to peak values of the nominal stress in the normal direction, the first shear direction, and the second shear direction, respectively. $G_{nn}$, $G_{ss}$, and $G_{tt}$ refer to separation energies in the normal direction, the first shear direction, and the second shear direction, respectively. The laminate lay-up design was $[0/90]_{4s}$; the laminate was prepared by molding process, and the single-lap specimen was prepared by cutting with 4060 CNC engraving machine, as shown in Figure 1. The geometry of the single-lap specimen is $100 \times 25 \times 2.4$ mm, the length of the lap area is 12.5 mm, and the geometry of the reinforced sheet specimen is $82.5 \times 25 \times 2.5$ mm, as shown in Figure 2.
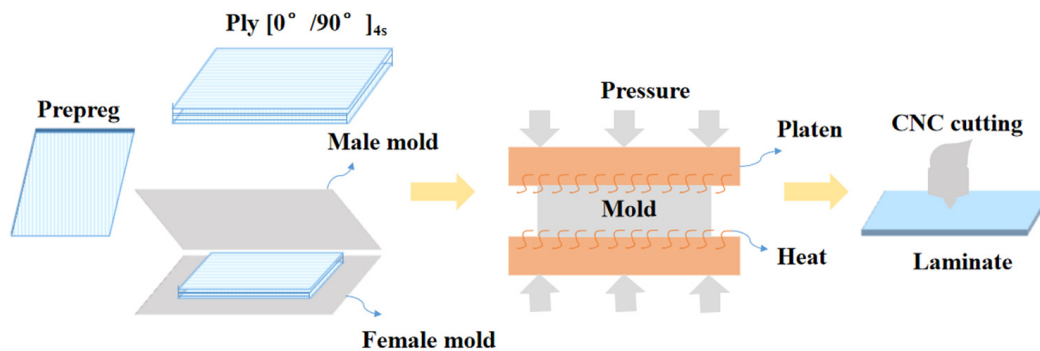


**Figure 1.** Fabrication of single-lap laminate.
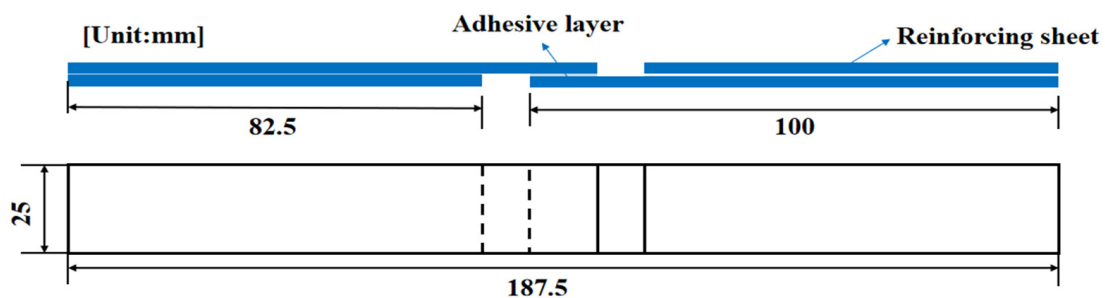


**Figure 2.** Schematic diagram of single-lap specimen.

The specimens were prepared in two steps, the first for gluing of the lap zone and the second for gluing of the reinforcement piece. Each process contains three parts: surface grinding, application of epoxy structural adhesive, and curing at room temperature $(23 \pm 5)$ °C for 24 h. Surface treatment was conducted as in reference [22]: firstly, random sanding with 220-grit sandpaper, followed by alcohol wiping of impurities on the adhesive surface after sanding; application of structural adhesive was completed within 20 min; the fixing pressure was applied using long-tail clamps with a pressure of less than 0.1 MPa. The laminate single-lap adhesive specimens are shown in Figure 3.



**Figure 3.** The fabricated single-lap specimen.

The lap shear testing was conducted on a UTM5105X electronic universal testing machine according to GB/T 3334-2016 with the speed of 1.3 mm/min [23,24]. The specimen is fixed as shown in Figure 4. Tensile shear strength of the specimen can be calculated by

$$\tau = F_m / (B \times L) \tag{1}$$

where $\tau$ is tensile shear strength in MPa (MPa); $F_m$ is test maximum force in Newtons (N); $B$ is bonding area width in millimeters (mm); $L$ is bonding area length in millimeters (mm).



**Figure 4.** Tensile shear test of single-lap specimen.

## 2.2. Simulation

The finite element part uses ABAQUS/Explicit to establish the single-lap tensile shear model. The model includes the establishment of laminate and adhesive layer; the laminate adopts 4-node quadrilateral linear-reduced integral form of shell cells (S4R), which can effectively ensure the accuracy and efficiency of the calculation; the adhesive layer is divided by three-dimensional cohesive cells (COH3D8); and the adhesive layer is meshed by sweeping in the mesh partitioning. The parameters in Tables 1 and 2 are used for composite and adhesive layer, respectively. The cohesive bilinear model is chosen where the Quads Damage criterion and B-K mixed-mode energy criterion are used. After the convergence test, the mesh size of 1 mm and step time of 0.1 s are chosen. In this paper, the mesh size is chosen to be 1 mm, the laminate is connected to the adhesive layer by face-to-face binding, the displacement is loaded along the *X*-axis by establishing the reference point and coupling constraint to the edge, and the fixed end is completely fixed by establishing the reference point. The end is completely fixed in degrees of freedom, and the specific modeling is shown in Figure 5.
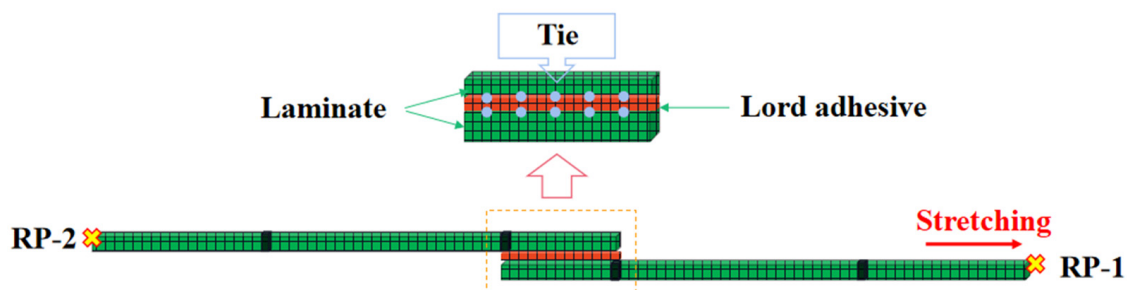


**Figure 5.** Simulation set-up.

## 3. Results and Discussion

### 3.1. Validation of Simulation Results

The experimental results of LORD adhesive are shown in Table 3, and the load-displacement curves and specimen cross-sections obtained from the experiments are shown in Figure 6. From the cross-sectional view of the specimens in Figure 6, the specimens all have both structural adhesive and plate interface failure and structural adhesive cohesive failure, which are mixed failure modes, where the failure mode of the adhesive joint is mainly cohesive failure, i.e., the adhesive layer is damaged internally due to insufficient shear strength. The load displacement curve is linear-elastic at the initial tension, and the adhesive layer undergoes linear-elastic deformation. After reaching the peak load, the internal stress of the adhesive layer meets the damage initiation criterion, and local failure starts to occur. Then, the failure area of the adhesive layer expands until the final total failure. The average peak load of the adhesive joint specimen is 5342.07 N, and the average tensile shear strength is 17.00 MPa, with the average maximum displacement of failure at 0.48 mm. As shown in specimen cross-sectional diagram, adhesive cohesive failure happened, indicating that the adhesive layer is damaged internally due to insufficient shear strength.

**Table 3.** Experimental results of tensile shear test.

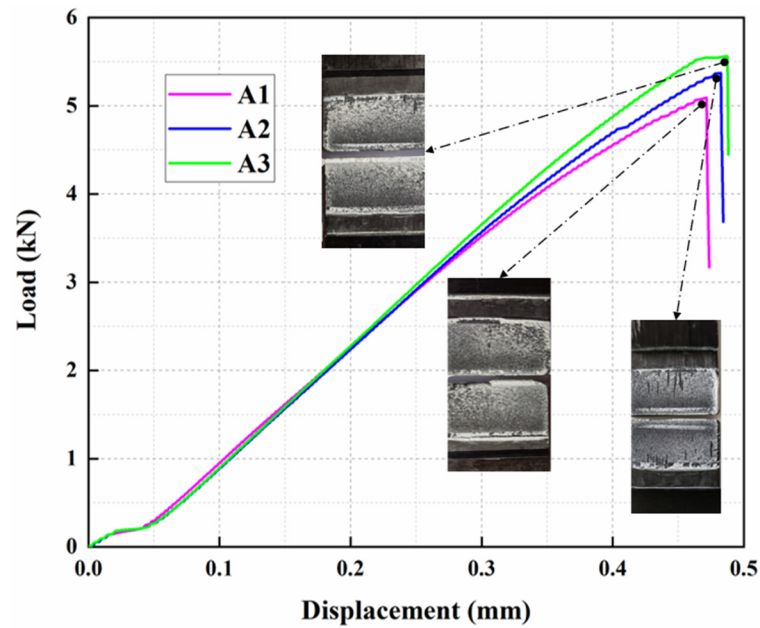| Experimental Parts | Failure Load (N) | Tensile Shear Strength (MPA) |
|---|---|---|
| A1 | 5091.36 | 16.25 |
| A2 | 5371.08 | 16.93 |
| A3 | 5563.76 | 17.82 |
| Average value | 5342.07 ± 237.53 | 17.00 ± 0.10 |

**Figure 6.** The load-displacement curves of single-lap specimens.

The simulated and experimental curves are compared as in Figure 7, from which it is found that there is a difference between the displacement of the simulated curve and the experimentally obtained displacement. The average failure load error between simulation and experiment is 7.83%, which is within the reasonable range and proves the validity of simulation.
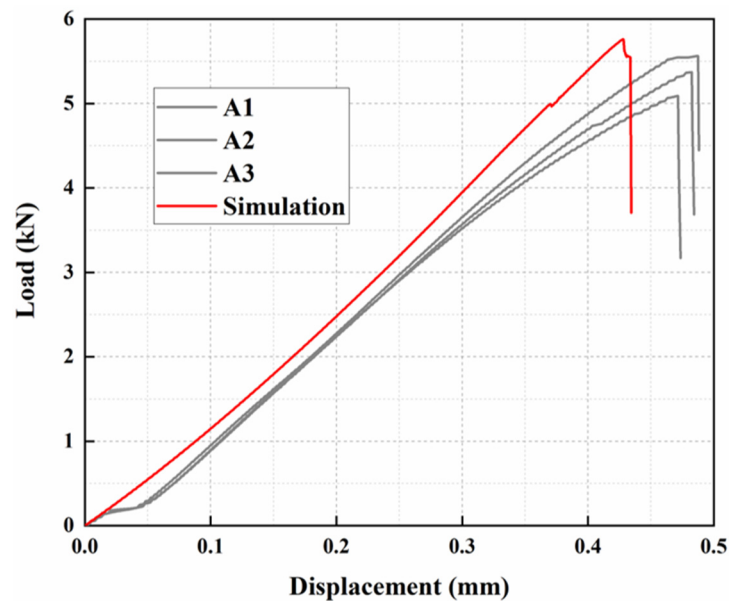


**Figure 7.** Comparison of experimental and FE simulation results.

*3.2. Effect of Lap Length*

In order to study the effect of lap length on the strength of composite adhesive joint, the lap length *L* was varied with other parameters identical, and four lap lengths were set as 12.5 mm, 25 mm, 37.5 mm, and 50 mm, respectively. From Figure 8, it is found that the shear strength of single-lap joints gradually decreases with the increase in lap length, and this decline is slowing down. Although decreasing the lap length is beneficial for improving the shear strength, special attention should also be paid to choosing this parameter, considering the fabrication problem and requirements of other properties.
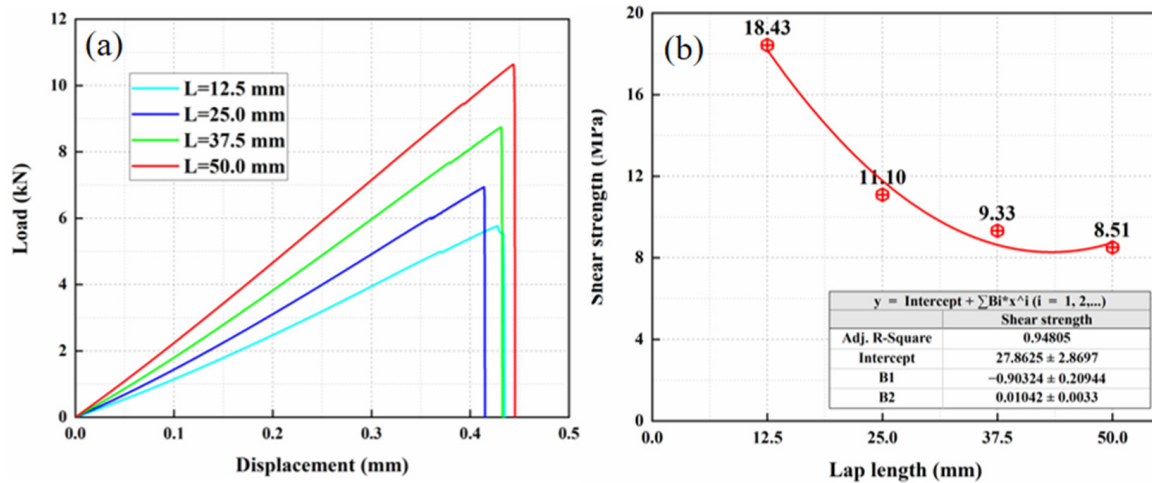
**Figure 8.** The result of different lap lengths: (**a**) load displacement curves and (**b**) shear strength.

### 3.3. Effect of Adhesive Layer Thickness

In order to study the effect of the adhesive layer thickness on the shear strength of the composite adhesive joint, the thickness *t* of the adhesive layer was varied with the other identical parameters, and four adhesive layer thicknesses were set as 0.25 mm, 0.5 mm, 0.75 mm, and 1.00 mm, respectively. The load displacement curves and shear strength of the single-lap specimen with a different adhesive layer thickness is depicted in Figure 9. It is shown that the shear strength of single-lap joints gradually decreases with the increase in adhesive layer thickness. When adhesive thickness increases from 0.25 mm to 1.00 mm, the 16% drop of the shear strength is found, which is from 19.81 MPa to 16.62 MPa, where a similar result has been found in [25]. Qin et al. [26] found that when the adhesive layer thickness increased from 2.0 mm to 5.0 mm, the damage load of the adhesive joint decreased overall.
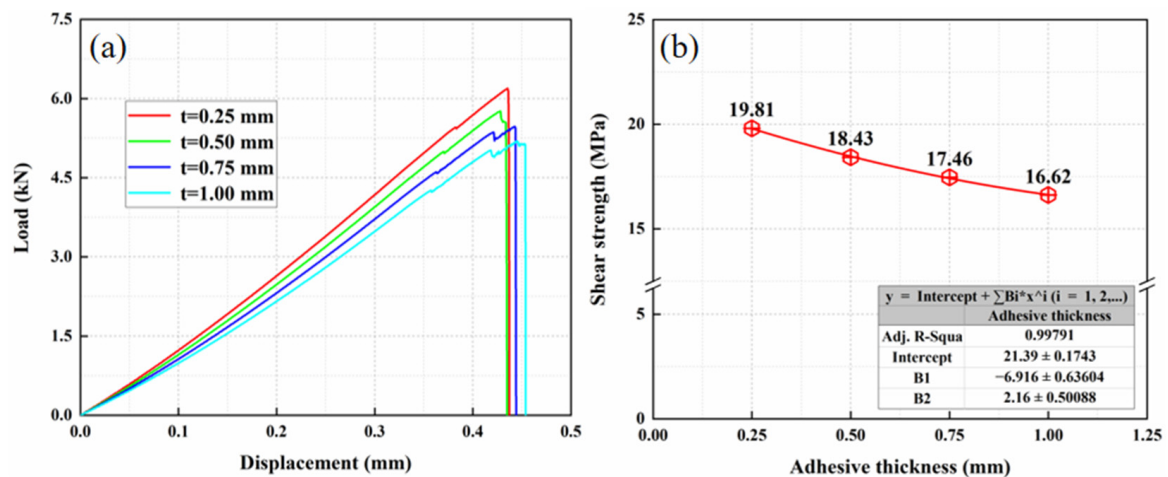


**Figure 9.** The result of different adhesive layer thickness: (**a**) load displacement curves and (**b**) shear strength.

### 3.4. Effect of Adhesive Layer Shape

Considering the potential condition in fabrication, the squeezing of adhesive layer will be found as the forms of contact of laminate end and overflow onto the surface. Investigation on the influence of adhesive layer shape and adhesive layer overflow length were conducted. The lap shape of overflow was changed under the other identical parameters, and three shapes were named circular, triangular, and unoverflowed, and their schematic diagram is shown in Figure 10. In Figure 11, it is shown that the adhesive with the normal

and triangle shape owned the comparable shear strength, which was 2 times greater than that of the arc one. Meanwhile, the initial stiffness in load-displacement curves are nearly the same.
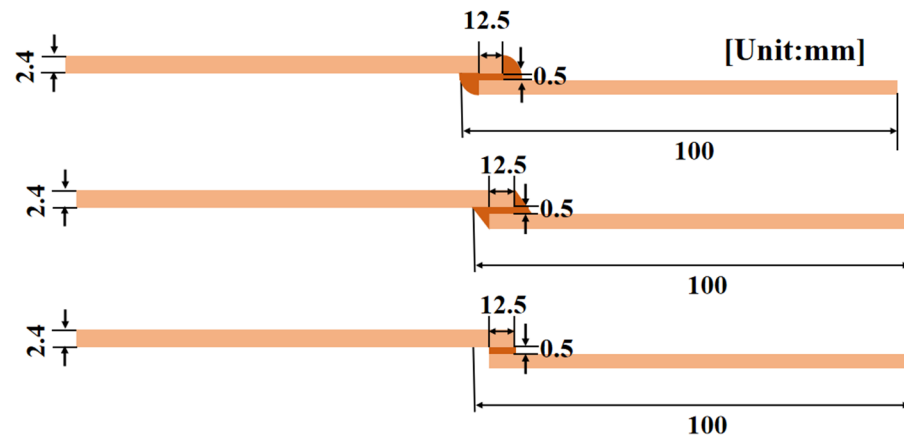


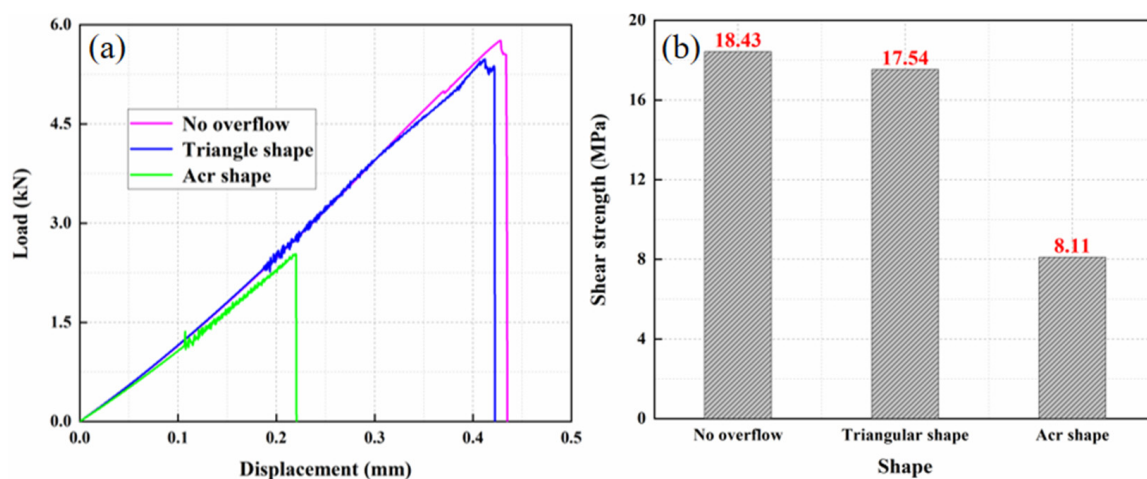**Figure 10.** Schematic diagram of different adhesive layer shapes.



**Figure 11.** The result of different adhesive layer shapes: (**a**) load displacement curve and (**b**) shear strength.

### 3.5. Effect of Adhesive Layer Overflow Length

In order to study the influence of the overflow length of structural adhesive on the strength of composite adhesive joint during lap joint, the overflow length *l* was changed under the premise that other parameters were the same, and three lengths were set as 0, 0.5*L*, *L*. The schematic diagram is shown in Figure 12, the load displacement curves of the adhesive head under three overflow lengths are shown in Figure 13a,b is the shear strength under three overflow lengths. It was beneficial for shear strength to increase the adhesive layer overflow length to 50% of lap length.
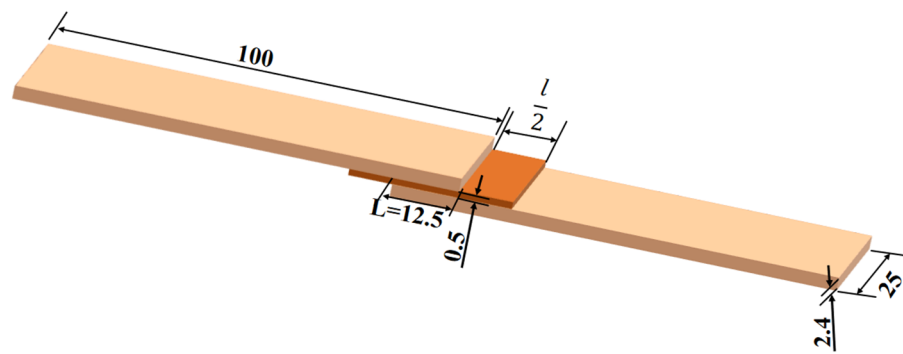
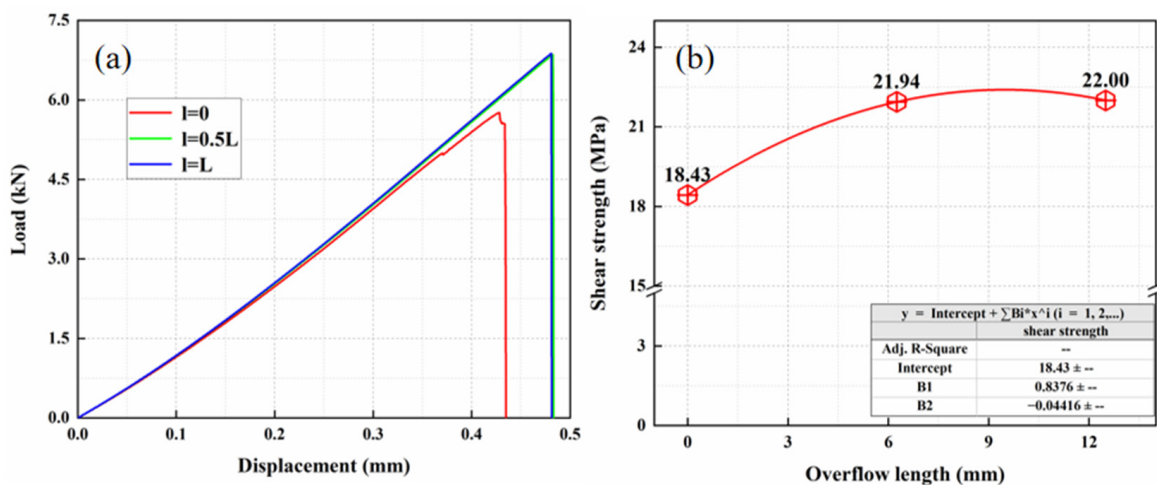**Figure 12.** Schematic diagram of different adhesive layer overflow length.



**Figure 13.** The result of adhesive layer overflow length: (**a**) load displacement curves and (**b**) shear strength.

In the real fabrication process, it is inevitable that the structural adhesive will overflow onto the part of the lap area length. The overflow lengths under each lap length are defined as 0*L*, 0.5*L*, *L*. As shown in Figure 14, tensile shear strength increases with the increase in overflow length when the lap length is 12.5 mm; when the lap length is 25 mm, the tensile shear strength first decreases and then increases; when the lap length is 37.5 mm and 50 mm, the tensile shear strength decreases with the increase in overflow length. Neto et al. [2] used a cohesive zone model to simulate the adhesive layer and established a prediction criterion for joint failure. It was found that the joints with brittle adhesives (AV138) undergo damage in the adhesive when the lap length is in the range of 10–20 mm. The damage of the joints exhibits interlaminar damage of the bonded composite when the lap length is between 30–80 mm. For the results shown in Figure 14, a potential reason is that the distribution of the shear stress is influenced by the overflow length. An increase in the overflow length leads to a decrease in the Mode II toughness of the interface [27–29]. As a result, earlier cracking starts and extends at the interface, leading to a reduction in the strength of the joint.
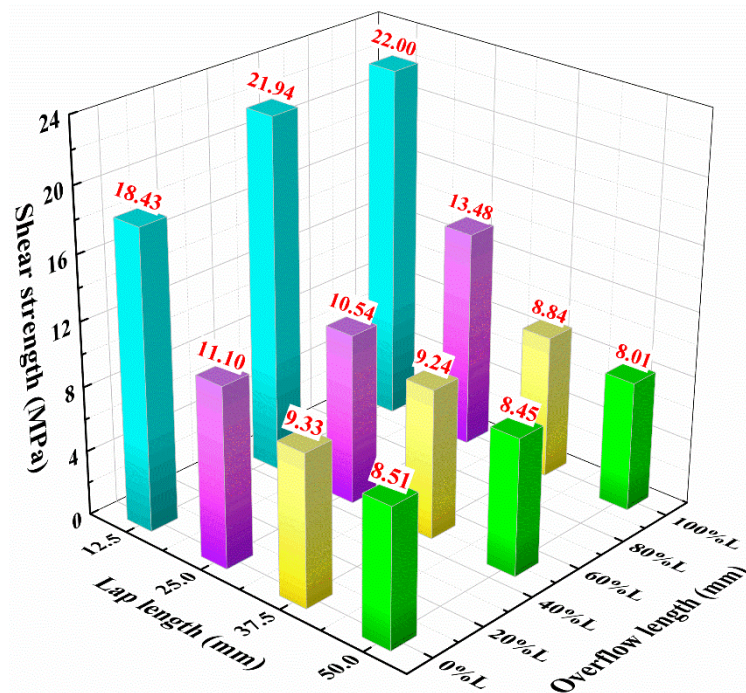
**Figure 14.** Effect of overflow length on tensile shear strength at different lap lengths.

*3.6. Effect of Laminate Lay-Up*

In order to study the influence of the lay-up angle of the laminate on the strength of the composite adhesive joint, four lay-ups were set up with $[0]_{16s}$, $[90]_{16s}$, $[0/90]_{4s}$, and $[0/\pm 45/90]_{2s}$ by changing the lay-up angle while keeping the other parameters identical, and Figure 15a shows the load displacement curves of the adhesive head under the four lay-ups, and Figure 15b shows the shear strength. According to the results, the higher the proportion of $0°$ lay-up, the greater the shear strength of single-lap. Among the selected four lay-ups, $[0]_{16s}$ had the highest shear strength, which was nearly 3 times greater than the one of $[90]_{16s}$.
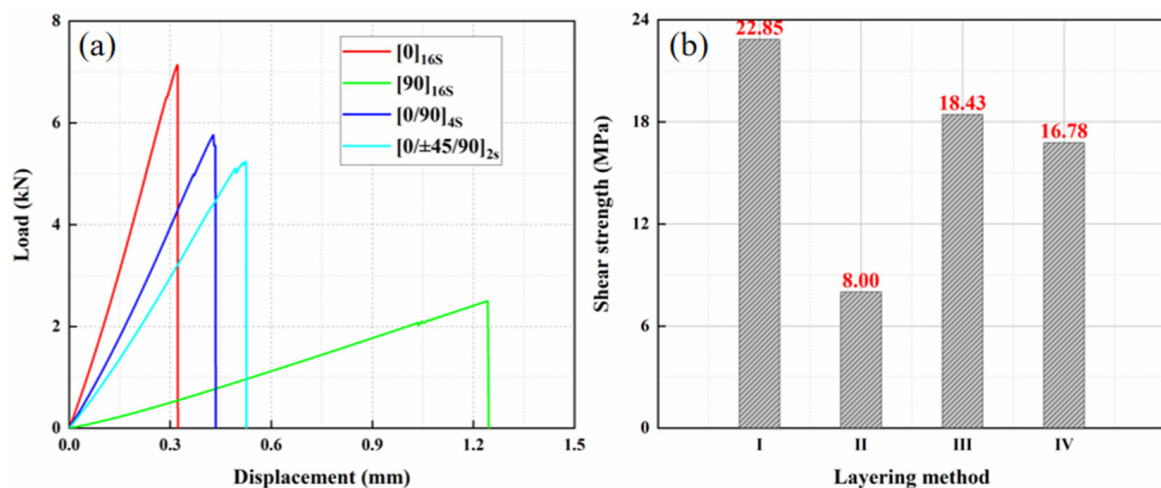


**Figure 15.** The result of different lay-ups: (**a**) load displacement curves and (**b**) shear strength.

It is known from other scholars that the higher the proportion of $0°$ plies, the higher the single-lap glued tensile shear strength of the laminate [30], and the maximum tensile shear strength under $[0]_{16s}$ plying method is due to the fact that the plying fiber direction of the CFRP composite laminate adjacent to the adhesive layer is $0°$, and the laminate can withstand larger tensile loads; the minimum tensile shear strength under $[90]_{16s}$ plying

method is due to the fact that the plying fiber direction of the CFRP composite laminate adjacent to the adhesive layer is 90°, and the laminate cannot withstand larger tensile loads.

### 3.7. Multifactor Interaction

Based on the original study of a single factor, an orthogonal experimental table was designed, and the results were obtained by model calculations in Table 4 and analyzed in Table 5 to study the interactive effects of each factor of lap length, adhesive layer thickness, adhesive layer overflow length, and laminate lay-up method on tensile shear strength.

**Table 4.** Orthogonal experimental design and results.

| No. | Lap Length (mm) | Adhesive Layer Thickness (mm) | Adhesive Layer Overflow Length | Laminate Lay-Up | Tensile Shear Strength (MPa) |
|---|---|---|---|---|---|
| 1 | 12.50 | 0.25 | 0$L$ | $[0]_{16s}$ | 25.09 |
| 2 | 12.50 | 0.50 | 0.5$L$ | $[90]_{16s}$ | 5.91 |
| 3 | 12.50 | 0.75 | $L$ | $[0/90]_{4s}$ | 16.73 |
| 4 | 12.50 | 1.00 | 0$L$ | $[0/\pm45/90]_{2s}$ | 15.27 |
| 5 | 25.00 | 0.25 | 0.5$L$ | $[0/90]_{4s}$ | 12.33 |
| 6 | 25.00 | 0.50 | 0$L$ | $[0/\pm45/90]_{2s}$ | 10.11 |
| 7 | 25.00 | 0.75 | 0$L$ | $[0]_{16s}$ | 12.18 |
| 8 | 25.00 | 1.00 | $L$ | $[90]_{16s}$ | 3.19 |
| 9 | 37.50 | 0.25 | $L$ | $[0/\pm45/90]_{2s}$ | 9.54 |
| 10 | 37.50 | 0.50 | 0$L$ | $[0/90]_{4s}$ | 9.33 |
| 11 | 37.50 | 0.75 | 0$L$ | $[90]_{16s}$ | 4.71 |
| 12 | 37.50 | 1.00 | 0.5$L$ | $[0]_{16s}$ | 8.84 |
| 13 | 50.00 | 0.25 | 0$L$ | $[90]_{16s}$ | 4.33 |
| 14 | 50.00 | 0.50 | $L$ | $[0]_{16s}$ | 9.22 |
| 15 | 50.00 | 0.75 | 0.5$L$ | $[0/\pm45/90]_{2s}$ | 6.99 |
| 16 | 50.00 | 1.00 | 0$L$ | $[0/90]_{4s}$ | 7.39 |

**Table 5.** Multifactor analysis of variance results for orthogonal experiments.

| Source | Sum of Squares | df | Mean Square | F Value | p |
|---|---|---|---|---|---|
| Intercept distance | 1367.847 | 1 | 1367.847 | 326.051 | 0.000 ** |
| Lap length (mm) | 184.15 | 3 | 61.383 | 14.632 | 0.013 * |
| Adhesive layer thickness (mm) | 46.295 | 3 | 15.432 | 3.678 | 0.12 |
| Adhesive overflow length | 17.984 | 2 | 8.992 | 2.143 | 0.233 |
| Laminate lay-up | 187.397 | 3 | 62.466 | 14.89 | 0.012 * |
| Residuals | 16.781 | 4 | 4.195 | | |

$R^2 = 0.963$; * $p < 0.05$ ** $p < 0.01$.

The closer $R^2$ is to 1, the better the model fits the results. The model variance $R^2 = 0.963$ indicates that 96% of the experimental data can be explained by this model. The larger the $F$ value of the model, the less the $p$-value represents the more significant effect of the correlation coefficient. The 4-factor ANOVA was used to analyze the relationship between the effects of lap length, adhesive layer thickness, lap spillage length, and laminate lay-up on tensile shear strength. From Table 4, the lap length showed a significant effect on the tensile shear strength with $F = 14.632$, $p = 0.013 < 0.05$; the adhesive layer thickness and overflow length did not show significance on the tensile shear strength with $F = 3.678$, $p = 0.12 > 0.05$ and $F = 2.143$, $p = 0.233 > 0.05$, respectively; the laminate lay-up method shows a significant effect ($F = 14.89$, $p = 0.012 < 0.05$).

## 4. Conclusions

In this paper, the shear strength of adhesively bonded single-lap joints were experimentally and numerically investigated. Based on the validated simulation, the effects of lap length, adhesive layer thickness, adhesive layer shape, adhesive layer overflow length, and laminate lay-up on the shear strength of adhesively bonded single-lap joints were studied. The load-displacement curves and shear strength under different parameters were compared. Moreover, the interaction between the above factors was studied to select the key factor by the Design of Experiment (DOE) method. The following conclusions were obtained:

The shear strength of single-lap joints gradually decreases with the increase in lap length. The shear strength of single-lap joints gradually decreases as the thickness of the adhesive layer increases. The shear strength gradually increases with the increase in the overflow length of the adhesive layer.

By comparing the shear strength of three overflow shapes, the shear strength of the normal-shaped adhesive layer is the largest, and the different overflow shapes have a greater effect on the shear strength of single-lap joints. According to the results, the higher the proportion of $0°$ lay-up, the greater the shear strength of single lap, and the maximum shear strength of the laminate with the lay-up of $[0]_{16s}$, which was nearly 3 times larger than the one of $[90]_{16s}$.

The lap length, adhesive layer thickness, lap overflow length, and laminate lay-up method in the interaction of each factor on tensile shear strength, the lap length, and laminate lay-up method will have a significant effect on the tensile shear strength. It will be beneficial for the selection of parameters in the design and fabrication process.

## References

1. Fox, D.E.; Swaim, K.W. *Static Strength Characteristics of Mechanically Fastened Composite Joints*; BiblioGov: Washington, DC, USA, 1999.
2. Neto, J.; Campilho, R.D.S.G.; da Silva, L.F.M. Parametric study of adhesive joints with composites. *Int. J. Adhes. Adhes.* **2012**, *37*, 96–101. [CrossRef]
3. Anyfantis, K.N.; Tsouvalis, N.G. Loading and fracture response of CFRP-to-steel adhesively bonded joints with thick adherents—Part I: Experiments. *Compos. Struct.* **2013**, *96*, 850–857. [CrossRef]
4. Ozel, A.; Yazici, B.; Akpinar, S.; Aydin, M.D.; Temiz, Ş. A study on the strength of adhesively bonded joints with different adherends. *Compos. Part B Eng.* **2014**, *62*, 167–174. [CrossRef]
5. Kishore, A.N.; Prasad, N.S. An experimental study of Flat-Joggle-Flat bonded joints in composite laminates. *Int. J. Adhes. Adhes.* **2012**, *35*, 55–58. [CrossRef]
6. Nosouhi, F.; Farahani, M.; Ansari, M. Experimental and numerical study on the composite adhesive joint reinforcement using wavy edge. *J. Adhes. Sci. Technol.* **2018**, *32*, 1007–1017. [CrossRef]
7. Xiong, D. *A Study on Adhesive Strength of Single Lap Structural Adhesive Join of Glass Fiber Reinforced Composites*; Hunan University: Changsha, China, 2018. (In Chinese)

8.  Lie, C.; Xiong, J.-J.; Cheng, Z.-L. Experimental Investigation on Shear Strength of Composite Single-lap Joints. *J. Mater. Eng.* **2009**, *11*, 31–35. (In Chinese)

9.  Li, J. *Self-Inserting Adhesive Bonding and Mechanical Properties of GFRP Laminates*; Harbin Engineering University: Harbin, China, 2019. (In Chinese)

10. Zhang, S.-F.; Zhang, B.; Luo, Q.; Ou, Y. Shear Tests and Stress Analysis of Single Lap Adhesive Joint of Composite Material. *Environ. Technol.* **2017**, *35*, 39–44. (In Chinese)

11. Wu, X.; Li, J.; Jiao, Y. Design of Joint Forms of Composite. *J. Text. Res.* **2003**, *24*, 92–94+6. (In Chinese) [CrossRef]

12. Liang, Z.; Yan, Y.; Zhang, T.; Li, J.; Meng, X.; Liao, B. Experimental investigation and numerical simulation of composite laminate adhesively bonded single-lap joints. *J. Beijing Univ. Aeronaut. Astronaut.* **2014**, *40*, 1786–1792. (In Chinese) [CrossRef]

13. Liao, L.; Huang, C.; Sawa, T. Effect of adhesive thickness, adhesivetype and scarf angle on the mechanical properties of scarf adhesive joints LJ. *Int. J. Solids Struct.* **2013**, *50*, 4333–4340. [CrossRef]

14. Fernández-Cañadas, L.M.; Ivañez, I.; Sanchez-Saez, S.; Barbero, E.J. Effect of adhesive thickness and overlap on the behavior of composite single-lap joints. *Mech. Adv. Mater. Struct.* **2021**, *28*, 1111–1120. [CrossRef]

15. Xu, W.; Wei, Y. Strength and interface failure mechanism of adhesive joints. *Int. J. Adhes. Adhes.* **2012**, *34*, 80–92. [CrossRef]

16. Ji, G.; Ouyang, Z.; Li, G.; Ibekwe, S.; Pang, S.S. Effects of adhesive thickness on global and local Mode-I interfacial fracture of bonded joints. *Int. J. Solids Struct.* **2010**, *47*, 2445–2458. [CrossRef]

17. Peng, H.; Qin, Z.; Wang, J.; Yang, K. Analysis of interface ply angle effects on stress distribution and failure force of composite joint. *FRP Compos. Mater.* **2017**, *4*, 29–34. (In Chinese) [CrossRef]

18. Campilho, R.D.S.G.; de Moura, M.; Domingues, J. Numerical prediction on the tensile residual strength of repaired CFRP under different geometric changes. *Int. J. Adhes. Adhes.* **2009**, *29*, 195–205. [CrossRef]

19. Campilho, R.D.S.G.; Banea, M.D.; Neto, J.; da Silva, L.F. Modelling adhesive joints with cohesive zone models: Effect of the cohesive law shape of the adhesive layer. *Int. J. Adhes. Adhes.* **2013**, *44*, 48–56. [CrossRef]

20. Ye, J.; Yan, Y.; Li, J.; Hong, Y.; Tian, Z. 3D explicit finite element analysis of tensile fail-ure behavior in adhesive-bonded composite single-lap joints. *Compos. Struct.* **2018**, *201*, 261–275. [CrossRef]

21. Xu, C.; Liu, Z.-M. Numerical Study on the Failure of CFRP Flat-Joggle-Flat Bonded Joints. *Comput. Integr. Manuf. Syst.* **2020**, *37*, 199–205. (In Chinese)

22. Guanxia, Y.; Tao, Y.; Wenhui, Y.; Du, Y. The influence of surface treatment on the tensile properties of carbon fiber-reinforced epoxy composites-bonded joints. *Compos. Part B* **2019**, *160*, 446–456.

23. Koutras, N.; Villegas, I.F.; Benedictus, R. Influence of temperature on the strength of resistance welded glass fibre reinforced PPS joints. *Compos. Part A Appl. Sci. Manuf.* **2018**, *105*, 57–67. [CrossRef]

24. Villegas, I.F.; Palardy, G. Ultrasonic welding of thermoplastic composite coupons for mechanical characterization of welded joints through single lap shear testing. *JoVE J. Vis. Exp.* **2016**, *108*, e53592. [CrossRef] [PubMed]

25. Arenas, J.M.; Narbón, J.J.; Alía, C. Optimum adhesive thickness in structural adhesives joints using statistical techniques based on Weibull distribution. *Int. J. Adhes. Adhes.* **2010**, *30*, 160–165. [CrossRef]

26. Kumar, S.; Tampi, S. Modeling of single-lap composite adhesive joints under mechanical and thermal loads. *J. Adhes. Sci. Technol.* **2016**, *30*, 759–783. [CrossRef]

27. Wagih, A.; Tao, R.; Yudhanto, A.; Lubineau, G. Improving mode II fracture toughness of secondary bonded joints using laser patterning of adherends. *Compos. Part A Appl. Sci. Manuf.* **2020**, *134*, 105892. [CrossRef]

28. Wagih, A.; Lubineau, G. Enhanced mode II fracture toughness of secondary bonded joints using tailored sacrificial cracks inside the adhesive. *Compos. Sci. Technol.* **2021**, *204*, 108605. [CrossRef]

29. Wagih, A.; Tao, R.; Lubineau, G. Bio-inspired adhesive joint with improved interlaminar fracture toughness. *Compos. Part A Appl. Sci. Manuf.* **2021**, *149*, 106530. [CrossRef]

30. Mao, Z.G.; Hou, Y.L.; Li, C.; Tie, Y.; Sun, L. Effect of lap length and stacking sequence on strength and damage behaviors of adhesively bonded CFRP composite laminates. *J. Compos. Mater.* **2020**, *37*, 121–131. (In Chinese) [CrossRef]

**MDPI**